

# **Shape transformations in optically trapped particles and minimal surfaces: An experimental and theoretical study**

Liam Collard

Department of Mathematics and Department of Chemistry  
University of Leicester

Thesis submitted for the degree of  
Doctor of Philosophy  
at the University of Leicester  
April 23, 2018

# Shape transformations in optically trapped particles and minimal surfaces: An experimental and theoretical study

Liam Collard

## Abstract

Optical tweezing can be used to isolate single, micrometre sized particles. This is facilitated by a gradient force from a tightly focussed laser beam. The optical tweezing microscope at the University of Leicester has been integrated with instrumentation for spectroscopic detection. In this work, both elastic and inelastic light scattering techniques are used to monitor physical changes in lipid vesicles and liquid aerosol droplets. Alongside this experimental work, numerical methods and mathematical models have been used to produce images of the coalescence of liquid droplets. The goal of this project was to refine mathematical models for shape transformations in microparticles and further develop elastic light scattering techniques.

Individual unilamellar vesicles have been optically trapped and, by measuring the intensity modulation of elastic back scattered light, changes in the biophysical properties of lipid bilayers were revealed. Our approach offers unprecedented temporal resolution and, uniquely, physical transformations of lipid bilayers can be monitored on a length scale of micrometers. As an example, the deformation of a membrane bilayer following the gel to fluid phase transition in a pure phospholipid vesicle was observed to take place across an interval of  $54 \pm 5$  ms.

The binary coalescence of liquid microdroplets is investigated by both experimental and computational methods in chapter 6. Different theoretical models are explored for simulating the shape transformations occurring during aerosol droplet coalescence. A finite element model was identified as most suitable for precisely mapping the morphological changes. This model was then compared to experimental recordings of elastic light scattering over a coalescence, for droplets of different viscosity and coalescence trajectory.

The visualization software was explored further in an investigation of shape transformations of minimal surfaces. By expressing a minimal surface as the real part of a holomorphic function, the surface may be transformed to create new families of minimal surfaces. In chapter 7 these transformations are applied to the minimal surface known as the  $k$ -noid. The properties of the resulting surfaces are then investigated.

## Publications

- (i) L. Collard, D. Perez-Guaita, B. H. A. Faraj, B. Wood, R. Wallis, P. W. Andrew, and A. J. Hudson, “Light scattering by optically-trapped vesicles affords unprecedented temporal resolution of lipid-raft dynamics,” *Scientific Reports*, 2017
- (ii) B. R. Bzdek, L. Collard, J. E. Sprittles, A. J. Hudson, and J. P. Reid, “Dynamic measurements and simulations of airborne picolitre-droplet coalescence in holographic optical tweezers,” *Journal of Chemical Physics*, vol. 145, no. 5, 2016

## **Acknowledgements**

This thesis would not have been possible without the support of my supervisors Dr Andrew Hudson and Dr Katrin Leschke. Their guidance over the last four years has been invaluable in my development as a researcher. I would also like to thank James Sprittles, Bryan Bzdek and Jonathan Reid for their work on our collaborative paper.

Thanks also must be given to all colleagues from the optical tweezing laboratory and Michael Atiyah building who have helped to make my work much more enjoyable.

I am also grateful to EPSRC and the college of science at the University of Leicester for their financial support during my study.

Finally, I must thank my family and friends for their support and encouragement. They have been a continuous source of motivation to me.

# Contents

<b>1</b>	<b>Overview of project</b>	<b>18</b>
<b>I</b>	<b>Preliminaries</b>	<b>25</b>
<b>2</b>	<b>Introduction</b>	<b>27</b>
2.1	Optical trapping . . . . .	27
2.1.1	First demonstrations of optical trapping . . . . .	27
2.1.2	Single-beam gradient force optical trap . . . . .	28
2.2	Light scattering . . . . .	34
2.2.1	Elastic light scattering . . . . .	35
2.2.2	Inelastic light scattering . . . . .	38
2.3	Colloids . . . . .	42
2.3.1	Liposomes . . . . .	43
2.3.2	Liquid aerosol . . . . .	50
2.4	Mathematical modelling of the coalescence of aqueous droplets . . . . .	55
2.4.1	The initial point of contact . . . . .	55
2.4.2	A finite element based analysis of coalescence . . . . .	59
2.5	Summary . . . . .	61
<b>3</b>	<b>Minimal surfaces</b>	<b>64</b>

3.1	Preliminaries . . . . .	64
3.1.1	Manifolds . . . . .	64
3.1.2	Surfaces . . . . .	68
3.1.3	Riemann surfaces . . . . .	71
3.2	Minimal surfaces . . . . .	77
3.2.1	Conformal maps . . . . .	77
3.2.2	Holomorphic null curves . . . . .	80
3.2.3	The Weierstrass-Enneper representation . . . . .	84
3.3	The simple factor dressing . . . . .	99
3.3.1	Quaternions . . . . .	100
3.3.2	Willmore surfaces . . . . .	101
3.3.3	The simple factor dressing . . . . .	104
<b>4</b>	<b>Experimental and computational methods</b>	<b>112</b>
4.1	Introduction . . . . .	112
4.2	Detailed description of optical tweezing apparatus . . . . .	113
4.2.1	The optical tweezers . . . . .	115
4.2.2	Light scattering source (488 nm laser) . . . . .	120
4.2.3	Bright field imaging and measurements of the intensity of elastic light scattering . . . . .	121
4.2.4	The Raman spectroscopy configuration . . . . .	123

4.3	Other experimental techniques . . . . .	124
4.3.1	Dynamic light scattering . . . . .	125
4.3.2	Liposome preparation . . . . .	126
4.4	Computational analysis . . . . .	127
4.4.1	Multivariate analysis of Raman spectra . . . . .	127
 <b>II Results and discussion</b>		<b>129</b>
 <b>5 Monitoring phase behaviour and the mechanical properties of optically trapped liposomes using light scattering</b>		<b>131</b>
5.1	Introduction . . . . .	132
5.1.1	The main gel to liquid transition . . . . .	132
5.1.2	The liquid crystalline state in multi-component lipid bilayers and mixed phase behaviour . . . . .	137
5.2	Experimental details . . . . .	141
5.2.1	Microscope apparatus . . . . .	142
5.3	Results and discussion . . . . .	143
5.3.1	The gel-to-liquid crystalline transition of an optically trapped DPPC liposome . . . . .	144
5.3.2	Raman measurements of liposomes . . . . .	153
5.3.3	Dynamic light scattering . . . . .	155

5.3.4	Microdomain behaviour in fluid POPC/chol bilayers . . . . .	157
5.3.5	Microdomain behaviour in fluid POPC/chol/SM bilayers . . . . .	163
5.4	Conclusions and future work . . . . .	167
<b>6</b>	<b>Elastic light scattering and mathematical modelling of the coalescence of aerosol microdroplets</b>	<b>172</b>
6.1	Experimental and computational techniques . . . . .	173
6.1.1	Optical tweezers measurements . . . . .	173
6.1.2	Computer simulations . . . . .	175
6.2	A comparison of mathematical modelling with previous light scattering results .	176
6.3	Results and discussion . . . . .	179
6.3.1	Analysis of low viscosity droplets, the affect of droplet orientation . . . .	180
6.3.2	Viscous aerosol . . . . .	187
6.4	Conclusions . . . . .	195
<b>7</b>	<b>The simple factor dressing of the k-noid</b>	<b>200</b>
7.1	Constructing the k-noid . . . . .	200
7.1.1	The behaviour of the poles . . . . .	205
7.1.2	The geodesics of the k-noid . . . . .	208
7.1.3	Constructing the <i>k</i> -noid from its symmetries . . . . .	211
7.2	The periodicity of the simple factor dressing of the k-noid . . . . .	222

7.3	Symmetries of the simple factor dressing of the k-noid . . . . .	229
7.4	Conclusions . . . . .	231
<b>8</b>	<b>Conclusions</b>	<b>234</b>
	<b>Appendices</b>	<b>238</b>
<b>A</b>	<b>Customised heating stage plate</b>	<b>238</b>
<b>B</b>	<b>Code relating to coalescence of aqueous droplets</b>	<b>242</b>
<b>C</b>	<b>An implementation of the k-noid</b>	<b>244</b>
	<b>Bibliography</b>	<b>252</b>

## List of Figures

2.1	A focussed Gaussian laser . . . . .	30
2.2	A microparticle entering an optical trap in the ray optical regime . . . . .	32
2.3	An optically trapped microparticle in the ray optics regime . . . . .	33
2.4	The angular dependence of Rayleigh scattering . . . . .	36
2.5	The angular dependence of Mie scattering . . . . .	38
2.6	Energy level diagram for infrared absorption, Rayleigh scattering, Stokes Raman scattering and Anti-Stokes Raman scattering regimes. . . . .	40
2.7	Chemical formulas for POPC top, a cerebroside and cholesterol . . . . .	44
2.8	The three main lipid components of a cell . . . . .	45
2.9	Unilamellar, multilamellar and multivesicular liposomes . . . . .	47
2.10	A unilamellar liposome . . . . .	48
2.11	Elastic scattered light over a coalescence . . . . .	53
2.12	The first 4 modes of an oscillation of a sphere . . . . .	54
2.13	The meniscus between two coalescing droplets . . . . .	57
3.1	Charts and a transition map for a manifold . . . . .	65
3.2	An immersion from manifold $M$ to $\tilde{M}$ . . . . .	67
3.3	A minimal immersion, and the Gauss map . . . . .	86
3.4	Four minimal surfaces . . . . .	88
3.5	The associated family of the catenoid . . . . .	95

3.6	The Lopez-Ros deformation of the catenoid . . . . .	97
3.7	The simple factor dressing with parameter $\mu$ for the catenoid . . . . .	106
3.8	The simple factor dressing of the catenoid in $\mathbb{R}^3$ . . . . .	107
4.1	A simplified optical trap . . . . .	113
4.2	Schematic of optical tweezers at the University of Leicester . . . . .	115
4.3	The path of the 1070 nm trapping laser . . . . .	116
4.4	A Keplerian telescope . . . . .	117
4.5	An infinity corrected microscope and finite correction optical system . . . . .	119
4.6	The 488 nm laser path . . . . .	121
4.7	The path of the light scattered onto the photodiode or CCD . . . . .	122
4.8	The path of the light scattered onto the spectrograph . . . . .	124
4.9	Schematic of spectrograph . . . . .	125
5.1	Lateral and rotational diffusion of a lipid bilayer . . . . .	133
5.2	The gel, ripple and fluid phases of a bilayer . . . . .	135
5.3	Ordered and disordered lipid bilayers . . . . .	138
5.4	Phase boundary diagram for POPC/cholesterol lipid bilayers . . . . .	139
5.5	Phase diagram for POPC/cholesterol/SM lipid bilayers . . . . .	141
5.6	Low temporal resolution light scattering over the temperature ramp of DPPC liposome . . . . .	146
5.7	The heating rate of the heating plate . . . . .	147

5.8	Differential scanning calorimetry thermograms for a DPPC suspension . . . . .	147
5.9	Further examples of light scattering from a DPPC liposome over a temperature ramp . . . . .	148
5.10	Supplementary examples of light scattering from a DPPC liposome as it was heated and cooled. . . . .	149
5.11	High temporal resolution light scattering over the temperature ramp of DPPC liposome . . . . .	150
5.12	Images of back scattered light immediately before and after the main gel-to- liquid phase transition . . . . .	151
5.13	Further images of back scattered light immediately before and after the main gel-to-liquid phase transition . . . . .	152
5.14	A prolate spheroid . . . . .	152
5.15	Raman spectra for a DPPC liposome in gel, ripple and fluid phases . . . . .	154
5.16	The number distribution of a 1 ml sample of DPPC liposomes at 20 °C red, and 50 °C green calculated using dynamic light scattering. . . . .	156
5.17	High and low temporal resolution elastic light scattering of a POPC/cholesterol liposome over a temperature ramp . . . . .	158
5.18	Differential scanning calorimetry thermograms of POPC/cholesterol liposome suspension . . . . .	159
5.19	Supplementary low resolution light scattering for a POPC/cholesterol liposome over a temperature ramp . . . . .	159
5.20	Raman spectra for a POPC/cholesterol liposome . . . . .	161

5.21	Number distribution of a POPC/cholesterol suspension at 20 °C and 50 °C . . . . .	163
5.22	High and low temporal resolution elastic light scattering of a POPC/cholesterol/SM liposome over a temperature ramp . . . . .	164
5.23	Differential scanning calorimetry thermogram of a POPC/cholesterol/SM liposome suspension . . . . .	165
5.24	Supplementary low temporal resolution elastic light scattering of a POPC/cholesterol/SM liposome over a temperature ramp . . . . .	165
5.25	Raman spectra for POPC/cholesterol/SM . . . . .	167
5.26	A microfluidic device . . . . .	169
6.1	A simplified schematic of the optical tweezers used at the University of Bristol. . . . .	174
6.2	Elastic light scattering over a coalescence of aqueous droplets . . . . .	177
6.3	Simulated aspect ratio and elastic light scattering over a coalescence of aqueous droplets . . . . .	178
6.4	Images of the simulated coalescence of aqueous aerosol droplets . . . . .	179
6.5	Transverse and parallel coalescence . . . . .	181
6.6	Observation of a transverse coalescence . . . . .	182
6.7	Observation of a parallel coalescence . . . . .	184
6.8	Simulated aspect ratio of composite drop from both orientations . . . . .	185
6.9	Coalescence viewed from a millisecond time-scale . . . . .	186
6.10	Images and light scattering of coalescence of sucrose droplets at 89% RH . . . . .	190

6.11	The simulated aspect ratio and aspect ratio of images for the coalescence of sucrose droplets at 89% RH . . . . .	191
6.12	Images and light scattering of coalescence of sucrose droplets at 86% RH . . . . .	192
6.13	The simulated aspect ratio and aspect ratio of images for the coalescence of sucrose droplets at 86% RH . . . . .	193
6.14	Images and light scattering of coalescence of sucrose droplets at 82% RH . . . . .	194
6.15	The simulated aspect ratio and aspect ratio of images for the coalescence of sucrose droplets at 82% RH . . . . .	195
6.16	Coalescence of droplets with viscosity estimated at 0.67 mPas . . . . .	196
6.17	Simulated aspect ratio of droplets with viscosity estimated at 0.67 mPas . . . . .	197
7.1	The domain on which the 4-noid has been implemented . . . . .	212
7.2	Construction of the domain of the $k$ -noid . . . . .	213
7.3	The fundamental domain $D_0$ of the $k$ -noid. . . . .	214
7.4	A fundamental piece of the trinoid. . . . .	215
7.5	The construction of the trinoid from one fundamental piece. . . . .	216
7.6	The $k$ -noid for $k = 3, 4, 5, 6$ . . . . .	217
7.7	The interior and exterior of the conjugate surface to the $k$ -noid . . . . .	219
7.8	The construction of the periodic conjugate surface using its rotational symmetries. . . . .	221
7.9	The Lopez-Ros deformation of the $k$ -noid . . . . .	223
7.10	The simple factor dressing of the trinoid preserving one catenoidal end . . . . .	225
7.11	The simple factor dressing of the 4-noid preserving two catenoidal ends . . . . .	226

7.12	The simple factor dressing of the trinoid with multiple periods . . . . .	228
A.1	Schematic of the heating plate. . . . .	238
A.2	Comparison of the temperature recorded at the thermocouple and the estimated temperature of the sample. . . . .	241

## List of Tables

2.1	The eight different types of colloidal dispersions. . . . .	42
3.1	The Weierstrass data for four minimal surfaces. . . . .	87
5.1	Transition temperatures for different tail length lipids . . . . .	134
5.2	The average diameter $z_{avg}$ and polydispersity index of a sample of a 1ml DPPC liposomes at 20 °C and 50 °C. . . . .	157
5.3	Average size and polydispersity index of a POPC/cholesterol suspension at 20 °C and 50 °C . . . . .	163

## List of abbreviations

BB	Beam block
BS	Beam splitter
CCD	Charged coupling device
CMC	Constant mean curvature
DC	Dichroic mirror
DLS	Dynamic light scattering
DPPC	1,2-Dipalmitoyl-sn-glycero-3-phosphocholine
DSC	Differential scanning calorimetry
L	Lens
LED	Light emitting diode
LUV	Large unilamellar vesicles
M	Mirror
MO	Microscope objective
NA	Numerical aperture
ND	Neutral density
NF	Notch filter
PBS	Phosphate saline buffer
PDI	Polydisperisty index
PH	Pin hole
POPC	1-palmitoyl-2-oleoyl-sn-glycero-3-phosphocholine
RH	Relative humidity
SLM	Spatial light modulator
SM	Sphingomeylin

# **Chapter One - Overview of project**

# 1 Overview of project

Initially, the goal of this project was to investigate the coalescence of aqueous microdroplets both experimentally and theoretically. Two liquid droplets dispersed in air of micrometer size can be held stably in 3 dimensions using modern optical tweezers. The position of the optical traps can be adjusted on a micrometer scale. This allows coalescence to be induced by dragging one optically trapped droplet toward another. This was initially investigated in [1]. The composite droplet will become fully relaxed after several microseconds, therefore, even with modern high frame rate cameras imaging the coalescence of aqueous micrometer sized droplets is challenging. Despite this, elastic back scattered light can be sampled at a much quicker rate. In [1] the intensity of light scattering is observed to oscillate over the coalescence.

This oscillation can be corresponded with the classical theory of Lord Rayleigh [2]. When the droplets initially make contact, they pass from a state of low potential energy to high potential energy. Largely, the energy is dissipated through a viscously damped oscillation. The theory developed by Rayleigh describes the amplitude and period of this oscillation depending on the surface tension and viscosity of the fluid, however it does not provide images. One goal of this project was to correspond the light scattering results with a mathematical simulation of coalescence, capable of producing images of the relaxing droplet.

Optical tweezers are used to isolated micrometer sized particles, the technique was first developed by Arthur Ashkin in the 1980's [3]. They are constructed from a tightly focused Gaussian laser beam. The intensity gradient of the beam creates a force propelling the particle toward the center of the beam. The particle eventually becomes stably trapped above the beams focus. In this thesis holographic optical tweezers are used, here the phase pattern of the beam is controlled using a spatial light modulator. This allows for multiple traps to be constructed and for

the position to be adjusted on a micrometer scale. The optical tweezers used at the University of Leicester have also been integrated with spectroscopic apparatus capable of recording elastic and inelastically scattered light.

The coalescence phenomena has also received considerable attention as a fluid mechanics problem. The coalescence is initiated by a handle forming between two touching droplets. This has been observed to form experimentally [4]. The growth of this handle has been resolved analytically [5], however to give a complete description of the evolution of the composite droplet numerical methods are required.

Recently, a finite element based programme has been developed at the University of Warwick to numerically resolve various different wetting problems [6]. A solution for the coalescence is produced by numerically solving Navier-Stokes type equations in the bulk of the fluid and at the boundary. This can produce coordinates for the coalescence over time. In this work, we consider the effect of the viscosity of the droplet on the dynamics of coalescence.

Alongside our interest in using optical tweezers to analyse coalescence, another goal of the project was to develop the optical tweezers to observe morphological changes in biological membranes. Generally, in a cell membrane there are several different components which can significantly complicate physical interactions in the membrane. The cell membrane is composed of lipids and proteins. Of particular importance to the composition of the cell membrane are phospholipids.

To study specific physical interactions in cell membranes liposomes are used as they have the same structure as a cell membrane, but do not have the complex interior. Liposomes are largely composed of phospholipids but can be prepared so that they are composed of the lipids and proteins involved in a certain physical interaction. Because of this, liposomes are often used as

simplified models for cells.

As well as their role as models for cell membranes, liposomes can be used as carriers for medicine. There are several ways by which a liposome can release an interior solution to the body allowing for a highly targeted drug delivery. One example is through a temperature transition [7]. As a liposome is heated, it is known to pass from a gel like state where the liposome has low permeability to a liquid crystalline state where the permeability has been increased. This is due to a decrease in the electrostatic attraction between the lipid tails. Therefore, as the liposome is heated it will release part of the interior solution. The transition from the gel to liquid phase decreases the rigidity of the bilayer.

Spectroscopy has been used to analyse the gel-to-liquid crystalline transition for samples of liposomes [8], however characterizing the properties of individual cells and liposomes remains a challenging problem. In chapter five we investigate the gel-to-liquid crystalline transition for a single optically trapped liposome. Previously it has been shown by calorimetry that the gel-to-liquid crystalline transition occurs over approximately 1 °C [9]. We are able to show that for a single liposome the change in rigidity of the bilayer occurs on a millisecond time-scale corresponding to a significantly smaller temperature difference.

Raman spectroscopy has been used to observe the gradual decrease in molecular ordering for optically trapped liposomes. Most scattered light is scattered elastically, whereby the momentum and wavelength of the light is unchanged. However, it is also possible for a molecule to change the momentum of an incident photon, the light is said to be scattered inelastically. As momentum is inversely proportional to wavelength, the wavelength is also changed. The momentum of scattered photon is dependent on the vibrational modes of the incident molecule. Therefore by recording the intensity of inelastic scattering at multiple wavelengths the chemical composition

of a material can be characterized. This technique is known as Raman spectroscopy.

Inelastic scattering techniques are often used to characterize the composition of cells and liposomes. The Raman scattered light corresponding to vibrational modes of the C-H bonds of a lipid tail are known to provide a way to measure the molecular ordering of a bilayer [10]. In chapter 5, sets of Raman spectra for optically trapped vesicles of different lipid blends are presented. This allowed for the change in molecular packing order over temperature transitions to be characterized.

The visualization software used to produce images of the coalescence was also used to investigate shape transformations of minimal surfaces. Minimal surfaces locally take on the smallest possible area on a given boundary. Because of this they are of significance in engineering and physics. Lagrange, who coined the term minimal surface found the plane as an example [11]. Later on, Meusnier discovered that the helicoid and catenoid were also examples. Minimal surfaces are now one of the best understood classes of surfaces due to links with complex analysis. As a conformal minimal immersion  $f : M \rightarrow \mathbb{R}^3$ , where  $M$  is a Riemann surface, is a harmonic map, a minimal surface may be thought of as the real part of certain holomorphic functions  $\Phi : M \rightarrow \mathbb{C}^3$ . Further conditions are needed to ensure that the converse holds. A holomorphic function  $\Phi$  satisfying these conditions is called a *holomorphic null curve*. One way to generate holomorphic null curves is the *Weierstrass-Enneper formula*. By specifying a meromorphic function  $g : M \rightarrow \mathbb{C}$  and a holomorphic 1-form  $\omega : TM \rightarrow \mathbb{C}$  an integral formula produces a holomorphic null curve. The formula was independently discovered by Weierstrass [12] and Enneper [13].

There are several transformations that may be applied to a holomorphic null curve to create new examples of minimal surfaces. Multiplication of a holomorphic null curve by a complex constant

preserves holomorphicity, the conformality condition and the immersion condition. The resulting family of minimal surfaces is known as the *associate family*. The special case when the constant is  $i$  gives the imaginary part of  $\Phi$  as the minimal surface, this surface is called the *conjugate surface*. Since multiplication by a real number is only a scaling of the surface one restricts to unit complex numbers.

As well as the associate family matrix transformations have also been used to give new examples of minimal surfaces. Any multiplication of the holomorphic null curve by a complex orthogonal matrix gives a new holomorphic null curve. This is referred to as a *Goursat transformation*. Of particular interest is the special case of the Lopez-Ros deformation. It was used to show that the only complete, embedded, finite total curvature minimal surface with genus zero is either the catenoid or plane [14].

Minimal surfaces may also be thought of as examples of *Willmore surfaces*. Willmore surfaces are critical points of the Willmore energy which physically depicts the bending energy of the surface. A family of flat connections  $d_\mu$  with  $\mu \in \mathbb{C}^*$  may be associated with a Willmore surface, and conversely, every family of flat connections of an appropriate form describes a Willmore surface. A *dressing* may then be applied to this family of connections to give new Willmore surfaces. By dressing we denote a gauge of the family  $d_\mu$  by a matrix-valued map depending smoothly on a point on the surface and meromorphically on the spectral parameter  $\mu$ . Generally, finding explicit dressings for a Willmore surface is not possible. However, in the case of a minimal surface and a dressing matrix with a simple pole, the resulting minimal immersion may be given explicitly by a quaternionic formulation. This transformation is known as the simple factor dressing [15]. It turns out that the Lopez-Ros deformation is a special case of the simple factor dressing.

In chapter 7 of this thesis we apply the simple factor dressing to a special class of minimal surface, the  $k$ -noids. The simplest case of a  $k$ -noid is the catenoid for  $k = 2$ , for higher  $k$ , the  $k$ -noid has  $k$  ends asymptotically approaching the end of a catenoid. We construct  $k$ -noids from their symmetries. The visualization software JReality, which has also been used to create videos of the coalescence, allowed to implement this to obtain highly detailed images of a  $k$ -noid. The software is also compatible with the transformations of minimal surfaces and hence, the simple factor dressing can be applied to our implementation of the  $k$ -noid. The periodicity and symmetry of the simple factor dressing of the  $k$ -noid is analysed and illustrated.

Our interest in minimal surfaces is linked to the interest in coalescence of liquid microdroplets. Both phenomena are described by the Young-Laplace equation, it is given by

$$\Delta p = 2\sigma H,$$

where  $\Delta p$  is pressure difference across the interface,  $\sigma$  is the surface tension at the interface and  $H$  is the mean curvature. Therefore if the minimal surface is considered as a soap film, there is equal pressure either side of the film. In the case of a liquid sphere, pre-coalescence there is a constant pressure difference around the sphere. Spheres are part of the related class of constant mean curvature (CMC) surfaces. Constant mean curvature surfaces minimize surface area around a given volume. In the case of coalescence, once contact is made between the droplets, the composite droplet is no longer CMC. The droplet attempts to recover the spherical shape and minimize the surface area.

Chapter 2 of this thesis provides an introduction to colloidal dispersions and the experimental techniques which have been used to observe morphological changes in colloidal particles. In chapter 3, the preliminary theory of minimal surfaces is recapped. Shape deformations that have

been applied to the  $k$ -noid are also discussed. The optical tweezers used at the University of Leicester are described in detail in chapter 4. Other experimental and computational techniques are also described in chapter 4. In chapter 5, temperature transitions and microdomain formation and dissolution are analysed for a single optically trapped lipid vesicle. To do so, changes in elastic and inelastic scattered light were observed. Chapter 6 contrasts experimental observations of the coalescence of optically trapped microdroplets with a finite element based simulation. Modulations in elastic scattering are compared with the simulated aspect ratio over the coalescence. The  $k$ -noid has been implemented so that the transformations discussed in chapter 3 may be applied to it to create new families of minimal surfaces. The geometric properties of the resultant surfaces are investigated in chapter 7. Chapter 7 also describes how the  $k$ -noid has been constructed from its symmetries.

## **Part I**

# **Preliminaries**

# **Chapter Two - Introduction**

## **2 Introduction**

An introduction to the experimental techniques of optical tweezing and microspectroscopy is given below. In the first section, the initial work on optical trapping by Arthur Ashkin and the theory of modern optical tweezers is discussed. In the subsequent section, the spectroscopic techniques that can be used in conjunction with optical trapping are described. Section 2.3 gives a general introduction to the types of colloidal particles that have been studied in this thesis, and the changes in morphology that have been observed. In the last section classical and modern mathematical models that can be used to describe the coalescence of two aqueous aerosol droplets are discussed.

### **2.1 Optical trapping**

Optical trapping is a technique whereby a laser beam can be used to manipulate dielectric objects of nanometre to micrometer size. The technique was first developed by Arthur Ashkin at Bell laboratories in the 1970s [16]. He demonstrated that radiation pressure could affect the motion of micron sized droplets and latex spheres. He developed the technique to create a single-beam 3D gradient force optical trap which is now known as optical tweezers [3]. Optical tweezers are now commonly used in chemistry, biology and physics to study the physical properties of single particles, such as emulsion droplets, aerosol droplets, vesicles and biological cells.

#### **2.1.1 First demonstrations of optical trapping**

Arthur Ashkin designed several experiments to observe radiation pressure that led him to create optical tweezers. In his initial experiment he demonstrated that micron sized beads could be

accelerated by photons from a laser beam. An aqueous suspension of 1  $\mu\text{m}$  diameter latex spheres was placed in a glass cell into which a continuous wave TEM<sub>00</sub> mode of an argon-ion (514.5 nm) laser was focused to a tight waist [16]. He observed that the spheres would flow along the propagation of the laser light and deposit at the edge of the glass window from which the laser exited the chamber. The spheres would also be drawn toward the waist of the laser beam. The force responsible for drawing particles into the beam waist would later be exploited by Ashkin to develop gradient force trapping that became known as optical tweezing.

In the same paper, he also demonstrated that the radiation pressure along the axis of the propagation of light could be used to isolate a microsphere in the centre of the sample if an identical beam from a counter propagating laser entered from the opposite side of the cell. This type of trap was referred to as an “optical bottle”; the radiation pressure from the counter propagating lasers is balanced in order for the particle to become trapped in the centre of the cell [16].

In 1971 Ashkin created another form of optical trap capable of levitating water droplets dispersed in air [17]. In this experiment, a focused TEM<sub>00</sub> argon-ion laser with a wavelength of 514.5 nm was directed vertically at a sample of water droplets in a glass cell. The water droplets were generated using a nebulizer. The radiation pressure is controlled by adjusting the lasers power. By balancing the radiation pressure from the laser against gravity an equilibrium could be reached where the droplet would be stably trapped in the centre of the cell.

### **2.1.2 Single-beam gradient force optical trap**

In [3] Ashkin developed the first single-beam gradient force optical trap. Rather than using the linear radiation pressure from counter-propagating lasers, this trap is created by a gradient force that draws the particle to the waist of the beam. This type of trap is preferable to the optical bottle

and levitation trap as it creates a potential energy minimum in all 3 dimensions (i.e perpendicular and parallel to the direction of propagation of the laser). The experimental setup is also easier to configure and only uses a single laser beam. The single-beam gradient force trap is now referred to as optical tweezers.

To create optical tweezers, a high numerical aperture microscope is used to focus the laser beam tightly. Ashkin used a 1.25 numerical aperture water-immersion objective and an argon-ion laser with wavelength of 514.5 nm. The high numerical aperture lens focuses the laser beam to a tight waist, significantly increasing the gradient of the intensity profile of the Gaussian beam at the focus. He demonstrated that the single-beam gradient force could trap droplets of diameter from 25 nm to 10  $\mu\text{m}$ .

The phenomenon of optical tweezing can be rationalized by considering the change in momentum of the photons interacting with a dielectric particle possessing a high refractive index compared to the surrounding medium. However, to accurately describe the forces involved, a more detailed approach than given below is needed in order to take account of the size of the droplet compared with the wavelength of the trapping laser. When the laser interacts with a droplet, a fraction of the light will either be absorbed or scattered. The latter creates a scattering force  $f_{scat}$ , along the direction of propagation of light. Transmitted light will be refracted by the droplet from the initial direction of propagation. As the direction of these photons has changed, the momentum of the photons has also changed. Due to Newton's third law, there will be an equal and opposite reaction on the droplet. The reaction against the change in the direction of the refracted photons can account for the force pulling the particle toward the centre of the beam. This force is called the gradient force  $f_{grad}$ ; this is shown in figure 2.1.

The figure shows a dielectric particle with a high refractive index interacting with a tightly

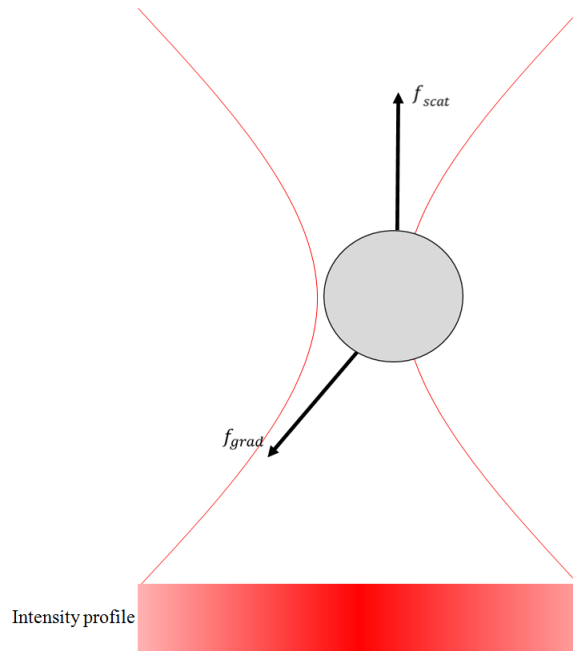


Figure 2.1: A tightly focused Gaussian laser interacting with a transparent particle (grey circle). The intensity profile is shown the gradient red line. The laser applies forces onto the particle  $f_{scat}$  and  $f_{grad}$ .

focused Gaussian laser beam. The beam applies two forces to the particle  $f_{scat}$  and  $f_{grad}$ . In Ashkin's initial experiment, the scattering force  $f_{scat}$  pushes the particle along the direction of propagation of light to the edge of the cell. In the design illustrated in figure 2.1, the gradient force  $f_{grad}$  is pushing the droplet toward the centre of the beam. The force  $f_{scat}$  depends on the intensity of the beam and  $f_{grad}$  on the intensity gradient (dictated by the numerical aperture of the objective lens).

The magnitude of the forces involved in an optical trap depend on the size of the particle relative to the wavelength of the trapping laser. This gives rise to three different trapping regimes, the Rayleigh regime where the particle size is small compared to the laser wavelength, the Mie regime where the particle size is similar to the laser wavelength, and the geometric regime where the particle is significantly larger than the laser wavelength. To quantify the strength of the forces

involved in an optical trap each regime needs its own consideration.

In the Rayleigh case, the trapped droplet can be seen as an infinitesimal point dipole in an inhomogeneous electromagnetic field [3]. By applying Maxwells equations to the Lorentz force, the following equations for  $f_{scat}$  and  $f_{grad}$  can be derived,

$$f_{scat} = \frac{I_0}{c} \frac{128\pi^5 r^6}{3\lambda^4} \left( \frac{m^2 - 1}{m^2 + 2} \right)^2 n_b, \quad (1)$$

and

$$f_{grad} = -\frac{n_b^3 r^3}{2} \left( \frac{m^2 - 1}{m^2 + 2} \right) \delta E^2, \quad (2)$$

where  $I_0$  is the initial intensity of the beam,  $r$  is the particle radius,  $m$  is the refractive index of the particle,  $n_b$  is the refractive index of the medium,  $\lambda$  is the wavelength of the light,  $c$  is the speed of light in a vacuum and  $E$  is the electric field. Typically the Rayleigh regime is considered an appropriate description for optical traps with  $2r < \frac{1}{10}\lambda$ .

For stable trapping, these forces must be balanced, that is  $f_{scat} = f_{grad}$ . As the force  $f_{scat}$  depends on intensity of the beam and  $f_{grad}$  depends on the gradient of the beam intensity, this can be accomplished by adjusting the laser power. Ashkin initially postulated that Rayleigh trapping could be used for optically trapping of atoms. Several groups are now using optical tweezers to trap and cool atoms [18] [19].

In the geometric regime, the wavelength of the scattered light is significantly larger than the particle diameter, and the radiation forces can be described using a ray optics model. In figure 2.2, a dielectric sphere of high refractive index is shown interacting with a tightly focused Gaussian laser beam. The intensity gradient is illustrated on the figure indicating that the beam intensity increases towards the centre line. The black lines (1) and (2) show two rays within the aperture

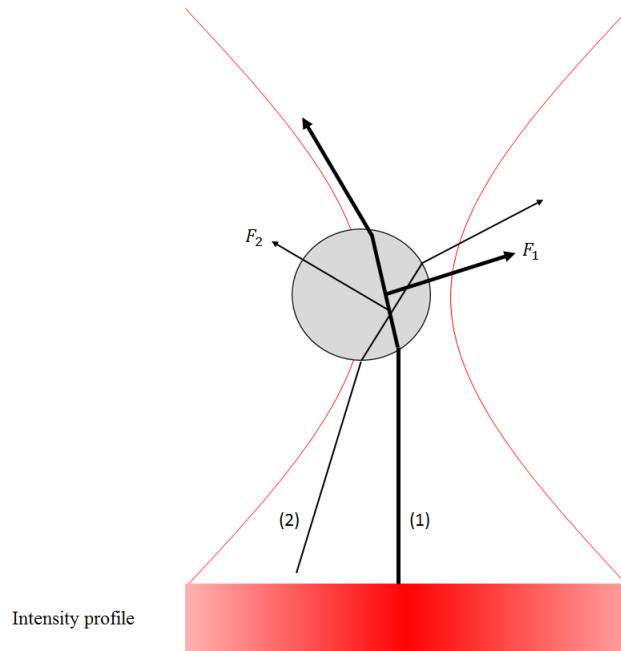


Figure 2.2: A spherical microparticle entering the optical trap in the ray optics regime. The laser has been focussed to a narrow waist by the objective lens, the intensity profile of the beam is shown below the laser. Due to the gradient of the intensity profile, the ray (1) at the centre of the beam puts a greater force,  $F_1$  onto the droplet than ray (2). The total force causes the droplet to move toward the central axis.

of the lens. Due to the intensity profile of the Gaussian beam ray (1) has a higher intensity than (2). The sphere refracts both rays of light, and there is a change in the momentum of the refracted photons in each ray. As a consequence of an equal and opposite reaction forces  $F_1$  and  $F_2$  there is an overall force that will act on the droplet,  $f_{grad}$ , which will propel the droplet towards the centreline of the axis of propagation of the laser. The ray tracing model allows the refractive force from a single ray on the droplet to be calculated. To calculate the total force on the sphere, Ashkin numerically integrated across all possible rays in [20].

The high refractive index sphere will become stably trapped at a position above the laser beams focus. The condition for equilibrium is illustrated in figure 2.3. As the position of the sphere

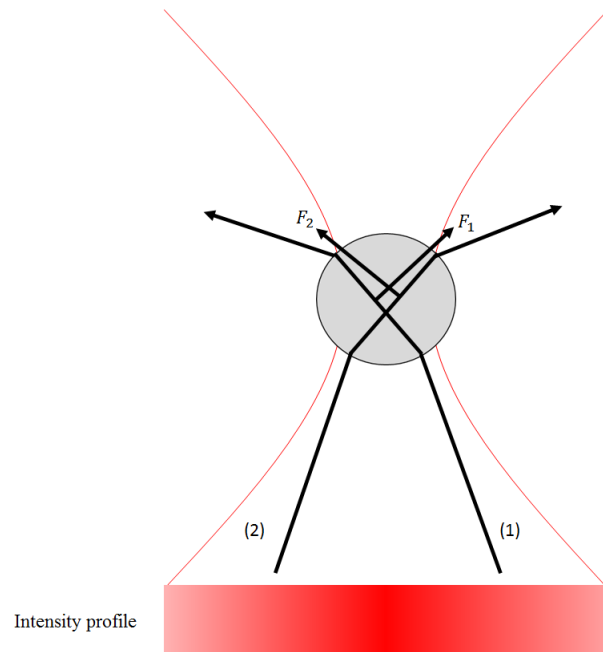


Figure 2.3: A stably trapped microparticle in the ray optics regime. The refractive forces due to rays (1) and (2),  $F_1$  and  $F_2$  are equal due to the symmetry of the intensity gradient. This causes the droplet to become stable in the optical trap slightly above the focus of the laser beam.

is also symmetric about the centreline of the beam, the refractive forces labelled  $F_1$  and  $F_2$  are equal in magnitude. By considering all rays acting on the particle the refractive forces will balance in the horizontal plane. The gradient and gravitational forces can counterbalance the radiation pressure leading to a stable optical tweezing.

In the Mie regime, the diameter of the droplet is similar to the wavelength of light. Neither the ray optics model or the point dipole model (described later) are suitable to describe the forces of the optical tweezers. The Mie-Lorenz theory can be applied to give values for the forces,  $f_{scat}$  and  $f_{grad}$  [21], if the incident light is expressed as a series of transverse electric and magnetic waves. Simulations utilizing the Mie-Lorenz theory have been compared to experimental data and shown to be in reasonable agreement [22]. The optical trapping based experiments in this

thesis fall into the Mie trapping regime.

Ashkin later used the optical tweezers to trap yeast cells, red blood cells and spirogyra [23]. He demonstrated that an infrared laser caused significantly less optical damage to a cell than the 514.5 nm laser used in previous studies [24]. This can be attributed to reduced absorption leading to lower heating or photochemical damage to the cell. Previously, there were few methods to study single living cells without causing significant damage to them, Ashkin's work demonstrated that optical trapping could potentially be used as a new method to isolate single cells.

Optical trapping has previously been used at the University of Leicester to analyse the binary coalescence process of two micron sized aqueous droplets [1]. In chapter six these results are compared with both traditional and modern mathematical models. Optical trapping has been shown to have many applications in physics, chemistry and biology. Once integrated with spectroscopic techniques, it can be used to study cells, aerosol and other colloidal particles. Optical tweezers have also been particularly useful for measuring piconewton forces on microparticles. A detailed review of these types of studies can be found at [25]. In chapter 5 of this thesis optical tweezers are used in a new study of the biophysical properties of lipid vesicles.

## **2.2 Light scattering**

Optical trapping can facilitate a wide range of spectroscopic measurements on single microparticles. Spectroscopic methods have been shown to be capable of probing many different physical properties of single particles such as morphology [26] and molecular structure [27]. For example, changes in morphology have been observed by monitoring elastic light scattering from the optically trapped particle. This type of measurement can be made in the direction of the propagation of light (i.e. forward scattered), or in the opposite direction (i.e. back scattered). In

addition, a photon can be scattered inelastically and the wavelength of the scattered light can be used to deduce information on the composition and structure [27]. Measurements of both elastic and inelastic light are discussed in this thesis.

### 2.2.1 Elastic light scattering

In elastic scattering, the scattered light has the same wavelength as the incident light. Similar to the theory of optical trapping, elastic light scattering by microspheres needs to be considered in three different regimes based on the particle size compared to the wavelength of the incident light. The theory of elastic light scattering is not limited to spheres and is also well understood for other shapes despite the increased complexity of mathematical modelling.

As described earlier, the Rayleigh scattering regime refers to when the wavelength of the incident light is significantly larger than the diameter of the scattering particle; the Mie regime, when the wavelength of the incident light is comparable to the diameter of the particle; and, the geometric regime, when the particle is much larger than the wavelength of the incident light.

In the Rayleigh regime, the intensity and angular dependency of the elastic light scattering can be modelled by representing the scattering particle as a point dipole inside an electric field. The intensity of the scattered light from a spherical particle is given by

$$I = I_0 \frac{1 + \cos^2(\theta)}{2R^2} \left( \frac{2\pi}{\lambda} \right)^4 \left( \frac{m^2 - 1}{m^2 + 2} \right)^2 \left( \frac{d}{2} \right)^6, \quad (3)$$

where  $I$  is the intensity of the scattered light,  $I_0$  is the intensity of the incident light,  $\theta$  is the scattering angle,  $R$  is the distance from the particle to the detector,  $\lambda$  is the wavelength of light,  $m$  is the refractive index of the particle and  $d$  is the diameter of the particle. Typically this model

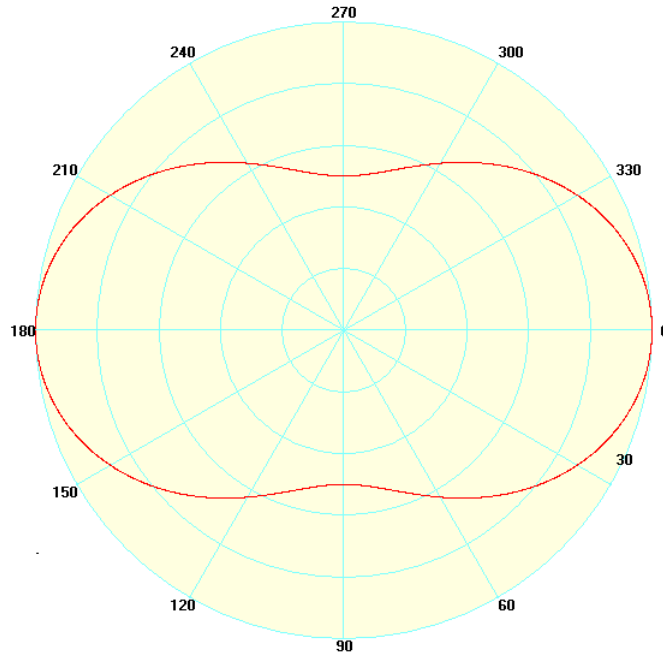


Figure 2.4: A polar plot of the Rayleigh scattering angular dependency for a  $0.1 \mu\text{m}$  diameter water droplet dispersed in air scattering  $1070 \text{ nm}$  unpolarized light, the plot was created using the MiePlot software [29].

is considered suitable for a particle with  $d < \frac{1}{10}\lambda$ .

Equation (3) highlights some significant properties of the angular dependence of the Rayleigh scattering. As  $I$  is inversely proportional to  $\lambda^4$ , the intensity of Rayleigh scattering is higher for shorter wavelengths of light; this was originally derived by Lord Rayleigh in [28]. The intensity  $I$  is also proportional to  $d^6$  indicating that larger particles scatter significantly more than smaller ones. The symmetry of the scattering pattern is also illustrated by equation (3). As  $I(\theta) = I(\theta + \pi)$  and  $I(\theta) = I(-\theta)$  there are equal proportions of light scattered in the forward and backward hemisphere scattered, as shown in figure 2.4. The scattering pattern in figure 2.4 was generated using the software MiePlot [29].

Mie scattering requires more sophisticated modelling than the Rayleigh or geometric regimes as neither the point dipole model of a scattering particle or a ray optics consideration can provide an accurate description. To model Mie scattering, the Mie-Lorenz theory must be used. Although the solutions are complex, there are several software packages available in Mathematica and Matlab to model this scattering regime. The intensity of the Mie scattering in spherical coordinates is given as the solution to the scalar wave differential equation:

$$\frac{1}{r^2} \frac{\delta}{\delta r} \left( r^2 \frac{\delta \psi}{\delta r} \right) + \frac{1}{r^2 \sin(\theta)} \frac{\delta}{\delta \theta} \left( \sin(\theta) \frac{\delta \psi}{\delta \theta} \right) + \left( \frac{1}{r^2 \sin(\theta)} \frac{\delta^2 \psi}{\delta \phi^2} \right) + k^2 \psi = 0,$$

where  $k^2 = \omega^2 \mu \epsilon$ ;  $\omega$  is the frequency of the incident field;  $\mu$  is the magnetic permeability; and  $\epsilon$  is the electric permittivity.

Though the theory of Mie scattering is complex, the fundamental characteristics for the nature of the scattering and its angular dependency are known. The intensity and angular dependency of Mie scattering are not strongly affected by the wavelength of the incident light. It is also well known that in the limiting case of  $d \approx \lambda$ , the Mie and Rayleigh regimes converge. A standard Mie scattering pattern is shown in figure 2.5, which was created using the programme MiePlot [29]; the same programme has been used to model many different Mie scattering problems [30]. The plot shows a particle scattering more light in the forward hemisphere; this is a characteristic property of Mie scattering. The programme used to create the plot has a wide range of functions and is also capable of plotting Rayleigh scattering.

In geometric light scattering, the diameter of the droplet is significantly larger than the wavelength of the incident light. Geometric scattering can be modelled by consideration of a ray tracing diagram. To calculate the angular dependence of the geometric scattering is challenging but there are various models proposed in the literature [31]. In the geometric regime more light

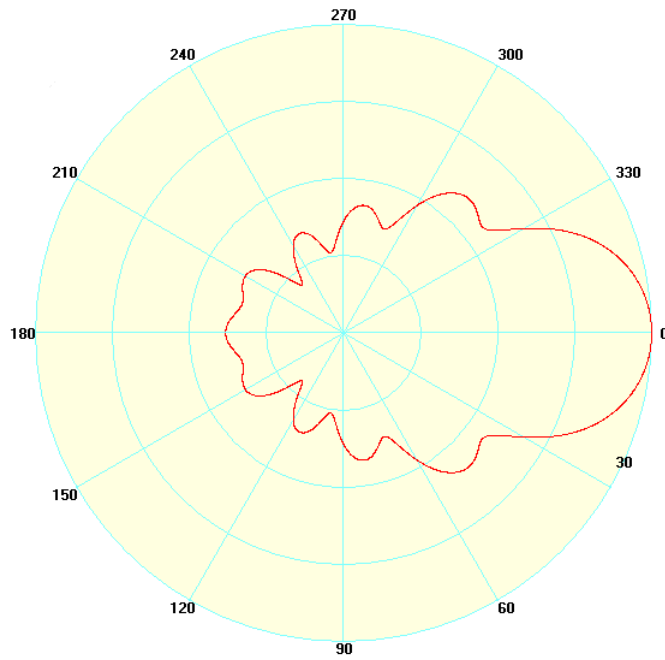


Figure 2.5: A polar plot on a logarithmic scale of the Mie scattering angular dependency for a  $1\mu\text{m}$  water droplet dispersed in air scattering  $1070\text{ nm}$  unpolarized light. The plot was created using the MiePlot software [29].

is scattered in the forward hemisphere. Although this is similar to the Mie regime, the effect is stronger in the geometric regime.

### 2.2.2 Inelastic light scattering

In inelastic scattering, the momentum of the incident photons is not conserved. The molecules exchange energy with the photon and, therefore, the momentum of the scattered photon is changed. Both the energy and momentum of a photon is inversely proportional to wavelength, and, therefore, the wavelength of the photon is also changed. This is given by equation 4, where  $\lambda$  is the wavelength,  $p$  is the momentum of the photon and  $h$  is Planck's constant

$$\lambda = \frac{h}{p}. \quad (4)$$

By measuring the intensity of the inelastically scattered light at different wavelengths information describing the molecular structure of the scattering material can be obtained. This is because the change in photon energy can be correlated to the separation of vibrational energy levels. Raman scattering was first observed by Chandrasekhara Venkata Raman, for which he was awarded the Nobel prize for physics in 1930 [32].

Raman scattering can occur by two different mechanisms, where the wavelength of the photon can be increased or decreased. Figure 2.6 is a vibrational energy level diagram illustrating the transfer of energy by both infra-red absorption of light, and the different Raman scattering mechanisms. The elastic Rayleigh scattering process is also illustrated in the diagram. In infra-red absorption, the frequency of the incident light must be resonant with the energy gap between the vibrational levels of the molecule. Techniques for measuring the frequencies of absorbed infra-red light are known as infra-red spectroscopy [33]. In Rayleigh scattering, the vibrational energy of the molecule is unchanged and the scattered photon has the same wavelength as the incident light. In Stokes Raman scattering, the molecule is excited into a higher vibrational energy state, and the scattered photon has lower energy and hence a longer wavelength. In anti-Stokes Raman scattering, the vibrational energy of the molecule is decreased and the photon energy is increased and the wavelength shortened.

By measuring the intensity of the inelastically scattered light at different wavelengths, a Raman spectrum can be produced. As the vibrational frequencies of molecules depend on the connectivity of atoms and their environment, Raman can be used to characterize the molecular structure of materials. Not all vibrational motion in molecules can be excited to induce Raman scattering.

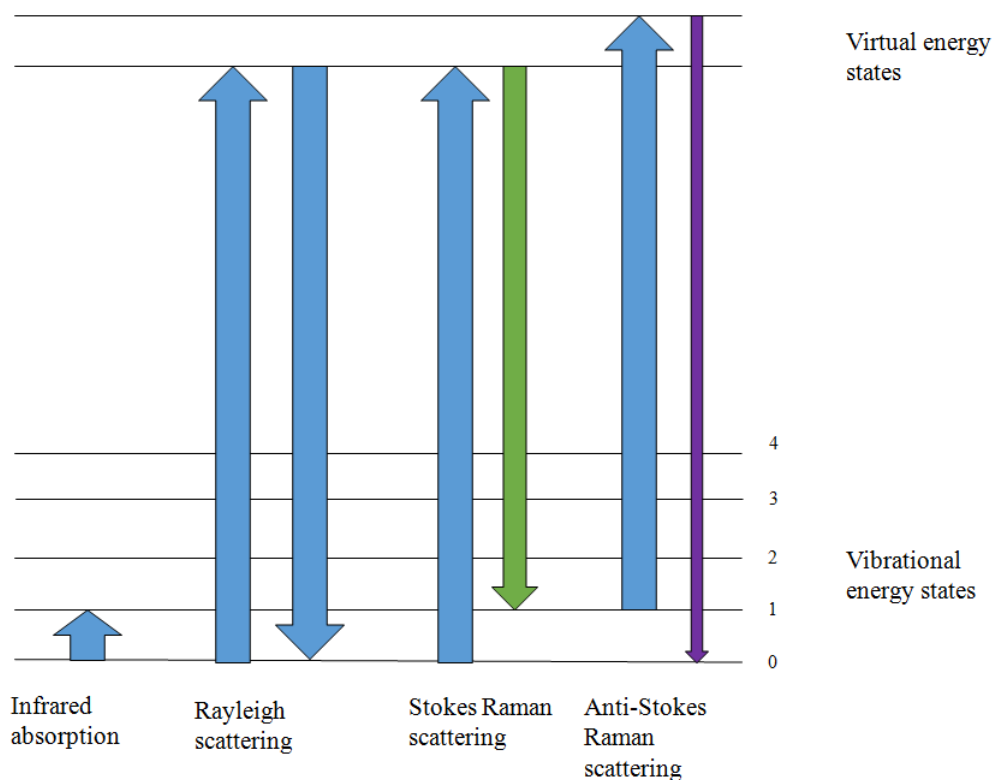


Figure 2.6: Energy level diagram for infrared absorption, Rayleigh scattering, Stokes Raman scattering and Anti-Stokes Raman scattering regimes.

The vibrational modes that can be excited are referred to as Raman active.

Only about 1 in  $10^7$  photons are scattered inelastically meaning that the Rayleigh scattering is much more stronger than Raman. Because of this, high sensitivity detectors are used to measure Raman scattering, and Rayleigh scattered light must be filtered ahead of the detector.

As well as providing a unique fingerprint, the individual Raman peaks can reveal several important details of molecular properties of a material. The relative intensity of a peak is proportional to the concentration of a component. The width of the peak can often be related to the homogeneity of the molecular packing. The polarization of the Raman scattered light is not necessarily the same as the incident light. The ratio of polarized to unpolarized or perpendicular to parallel

Raman scattered light is dependent on the incidence angle and the symmetry of the molecular packing.

The intensity of the Raman scattering  $I$ , is inversely related to  $\lambda^4$  where  $\lambda$  is the wavelength of the incident light. Shorter wavelength excitation lasers produce higher intensity Raman scattering. However shorter wavelength lasers also can also cause significant optical damage to cells and induce auto-fluorescence. The choice of wavelength of the laser in a Raman measurement will depend on the material being analysed.

There are several forms of Raman spectroscopy allowing for a microscopic analysis. Optical tweezers have previously been used in conjunction with Raman to record spectra for a single microparticle in an emulsion [34]. This type of Raman configuration is referred to as Raman tweezers. This has been particularly useful for studying biological cells. Both Raman scattering and optical trapping can be configured to cause minimal optical damage to the single cell. If a single trapping and spectroscopic laser are used, selecting an appropriate wavelength laser can be challenging. In [35], a 785 nm laser is used as a Raman tweezer for red blood cells and yeast. The laser was shown not to cause significant optical damage allowing Raman spectra of living cells to be recorded. Raman tweezers can also be configured to allow separate lasers for trapping and Raman excitation. Higher wavelength lasers are often favoured for optical tweezing experiments but this results in reduced Raman scattering. By using a shorter wavelength excitation laser at a low power combined with higher wavelength trapping laser, high resolution Raman spectra can be recorded without optical damage. This is shown in [36] for yeast cells.

Raman scattering is highly dependant on the polarization of the incident light, typically in Raman spectroscopy unpolarized light is used to excite the vibrational modes of the molecules. If the light is polarized it will only activate certain active vibrational modes depending on the ori-

		Dispersed phase		
		<b>Gas</b>	<b>Liquid</b>	<b>Solid</b>
Continuous phase	<b>Gas</b>	None known	Liquid aerosol	Solid aerosol
	<b>Liquid</b>	Foam	Emulsion	Sol
	<b>Solid</b>	Solid foam	Gel	Solid sol

Table 2.1: The eight different types of colloidal dispersions.

entation of the molecule. This means that the Raman spectra generated from unpolarized light will ensure a complete spectrum of all Raman active modes.

## 2.3 Colloids

A colloidal suspension is a mixture in which microparticles are dispersed in a continuous phase. Table 2.1 shows the different types of colloidal suspensions. To be classified as a colloid the microparticles in the dispersed phase must be significantly larger than a molecule in the continuous phase. Colloidal particles can have a diameter of approximately 1 nm-1000 nm. There are many examples of colloids in everyday life such as milk (an emulsion), smoke (solid aerosol) and clouds (liquid aerosol).

There are several physical and chemical interactions within a colloidal suspension. Despite the diversity and importance of colloidal chemistry, the interactions of individual microparticles are poorly characterized. Optical trapping provides an opportunity to isolate transparent microparticles in a colloid. In this thesis, optical trapping is used to study liquid aerosol (water droplets dispersed in air) and lipid vesicles (liposomes) dispersed in an aqueous solution. These two types of colloids will be described below.

### 2.3.1 Liposomes

A liposome consists of a lipid bilayer enclosing an aqueous core. Liposomes were first created in Cambridge in the 1960s [37]. Liposomes mimic the structure of a cell membrane. Because they do not have the same complex interior structure as a cell, they can be used as simple models to explore the physical interactions and processes taking place within a cell's membrane. Liposomes are also of interest for drug delivery, where the therapeutic agent can be packaged in the interior solution. There are many ways that a liposome can be made to release part of its interior contents allowing for a targeted drug delivery. Several techniques have been used to isolate single cells and liposomes including micropipette manipulation [38], microfluidics [39] and magnetic selection [40]. In chapter five, the techniques described in the previous sections have been used to study temperature transitions of single optically trapped liposomes.

A cell membrane is composed of a lipid bilayer containing several different lipid molecules. Lipids comprise a broad group of molecules that are insoluble in water but soluble in organic solvents. The lipids in a cell membrane can be classified into three major groups: phospholipids, glycolipids and cholesterol.

The principal component of a cell membrane is the phospholipid group. Phospholipids have a non-polar hydrophobic tail and a negatively charged hydrophilic head. The head group is approximately 1 nm in diameter and the tail group is approximately 1.6 nm long. Glycolipids are similar to phospholipids with the addition of a carbohydrate chain attached to the head group. Cholesterol is significantly smaller than the other lipids in a cell membrane, it is approximately 1.6 nm long and 0.5 nm wide. Cholesterol is largely hydrophobic, and embeds in the membrane between lipid tails, increasing the rigidity of the bilayer. Figure 2.8 shows the hydrophilic and hydrophobic parts of the important membrane lipids. It is also possible to create membrane like

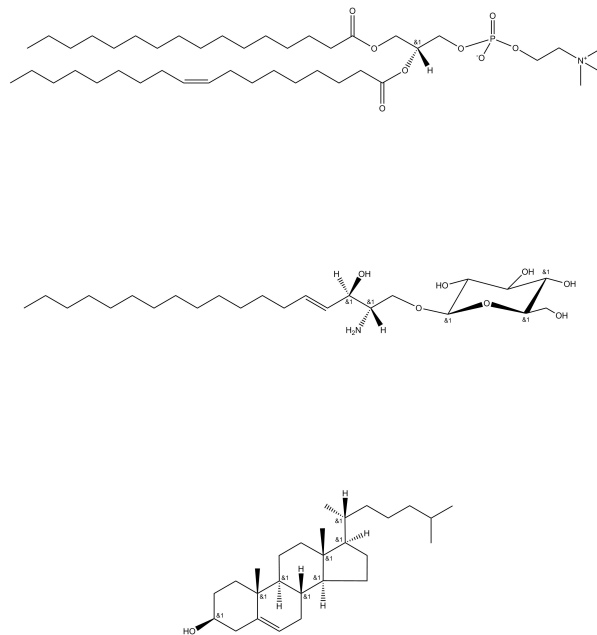


Figure 2.7: Chemical formulas for POPC top, a cerebroside (middle) and cholesterol (bottom).

structures from just phospholipids. Phospholipids can arrange themselves in various energetically favourable ways:

- (i) As a monolayer consisting of a single layer of lipids. The head groups must be located at an interface with an aqueous solution and the tails at the interface with the non-aqueous solution (i.e. oil).
- (ii) As a bilayer consisting of two layers of lipids formed by placing the hydrophobic tails together. The lipid bilayer has a thickness of roughly 5 nm.
- (iii) As a micelle consisting of lipids in a spherical structure with the hydrophobic tails directed to the interior of the sphere and the heads on the exterior surface, interfacing with an

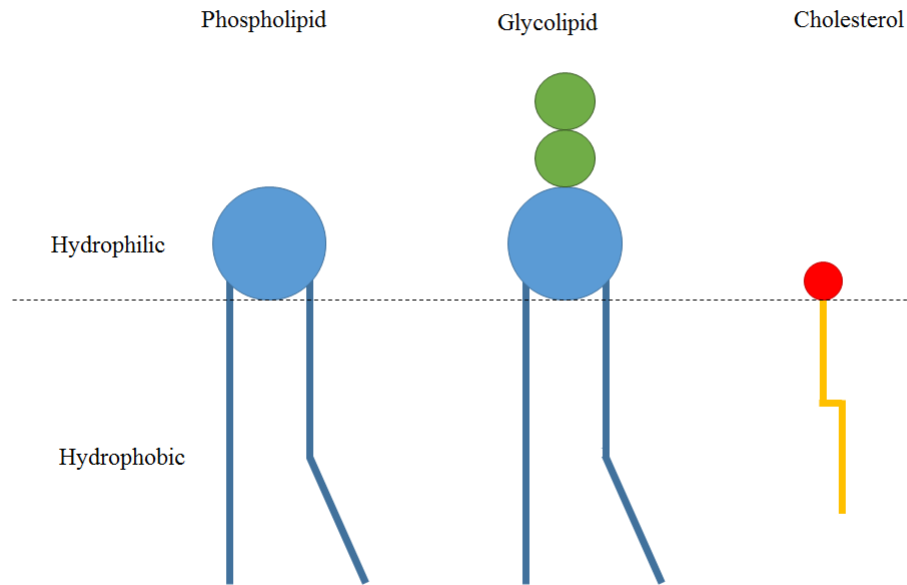


Figure 2.8: The three main lipid components of a cell membrane, phospholipids, glycolipids and cholesterol (left to right). The phospholipid has a large hydrophilic head and two fatty acid chains forming the hydrophobic tail. The glycolipid is similar to a phospholipid, there is a carbohydrate chain (green circles) attached to the head. The cholesterol head is significantly smaller than the other lipid heads, making cholesterol largely hydrophilic.

aqueous solution.

- (iv) As a liposome/vesicle consisting of a spherical bilayer (as in ii) encapsulating an aqueous core. Though the bilayer is primarily made of phospholipids it can also be enriched with other lipids; these structures are still referred to as liposomes. The external surface of the liposome also interfaces with an aqueous phase.

Liposomes typically have diameter between 20 nm-200  $\mu\text{m}$ . Below 100 nm they are known

as small vesicles, 100 nm-1  $\mu\text{m}$  as large vesicles, greater than 1  $\mu\text{m}$  as giant vesicles. In the work presented in this thesis we focus on large unilamellar vesicles (typically with diameter of 1  $\mu\text{m}$ ). This vesicle size is straightforward to optically trap and sensitive to light scattering measurements.

A liposome can be multilamellar, unilamellar or multivesicular; they are illustrated in figure 2.9. A unilamellar vesicle has one bilayer encapsulating the interior solution; this type of liposome can be utilized as a cell membrane model. In a multilamellar or multivesicular liposome, other bilayers form within the interior. Multilamellar refers to the existence of multiple layers of lipid molecules and multivesicular to the existence of smaller vesicles encapsulated by an outer lipid bilayer. Multilamellar and multivesicular liposomes can be used to encapsulate and separate several solutions within the outer bilayer.

Figure 2.10 shows a phospholipid unilamellar liposome. The individual lipids are tightly packed together and separating the interior and exterior solutions. The hydrophobic heads are orientated toward the aqueous exterior and interior solutions and the tails are enclosed within the bilayer.

Liposomes can be used to model cell membrane behaviour and can be used to study specific membrane components within the cell. For example liposomes have been used to model exocytosis [41], endocytosis [42], and cell adhesion [43]. Typically giant unilamellar vesicles are most appropriate models because they are similar in size to a mammalian cell. There are large levels of complexity in cells depending on which organism they are found in. Liposomes offer an opportunity to study the permeability and physical properties of the cell membrane without interference from the structures within the cell. To do so, liposomes can be enriched with other lipids and proteins found in cell membranes.

Liposomes are also of great interest in drug delivery, they can allow for highly targeted drug

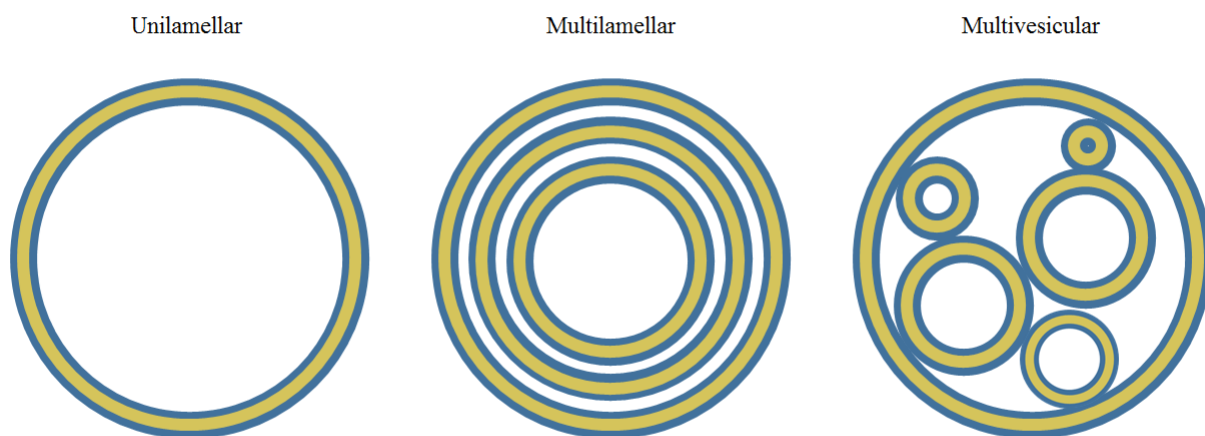


Figure 2.9: A unilamellar, multilamellar and multivesicular liposome (left to right). The unilamellar liposome consists of a single bilayer (blue and yellow circle) encapsulating the interior solution. In the multilamellar case multiple vesicles are encapsulated within each other. In the multivesicular case the outer bilayer encapsulates multiple vesicles.

delivery. They have been shown to be efficient carriers for anti-cancer drugs [44], antifungal agents [45] and DNA [46]. Once a solution of liposomes with different exterior and interior solutions has been prepared there are many ways that the liposomes can release their interior contents. Liposomes are capable of gradually or rapidly releasing their interior solution. In [47] release rates are investigated for several lipid blends. Faster release can be achieved with ultrasound techniques [48], photosensitive release [49], and a pH sensitive release [50]. Another mode of release is through a temperature-induced phase transition. The review article [51] gives

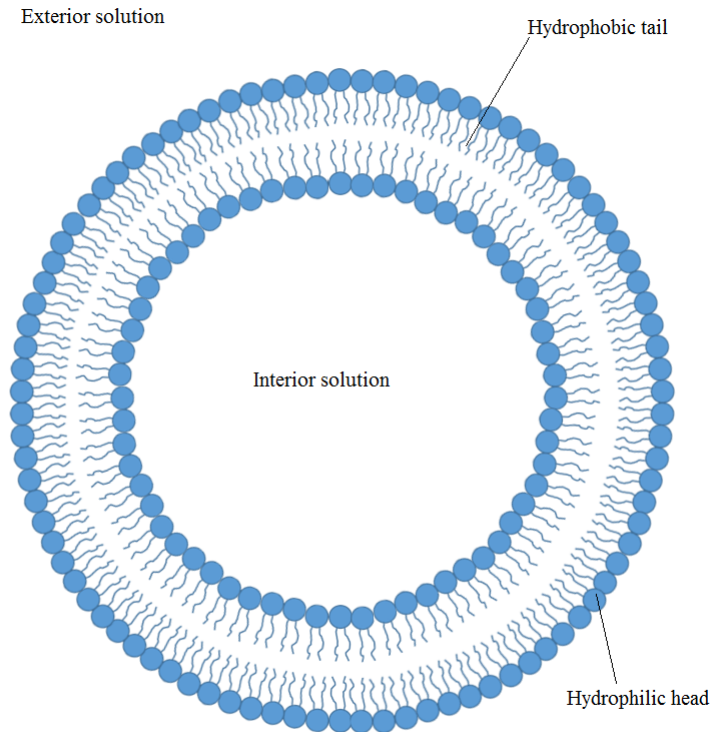


Figure 2.10: A unilamellar liposome, the bilayer is arranged as an energetically favourable sphere. The hydrophilic heads face toward the aqueous interior and exterior solutions and the tails are attracted to each other. The bilayer has low permeability and the lipid solution can be prepared so that there are different interior and exterior solutions.

an overview of temperature based drug release. Chapter 5 of this thesis focuses on analysing temperature induced phase transitions for a single optically trapped vesicle, a detailed discussion of phase transitions will be given in the introduction to that chapter. Aside from phase transitions, there are other methods allowing for highly targeted drug delivery. One such example is by fusion of a liposome onto a cell membrane, facilitated by the addition of a fusion agent. Under these conditions, the liposome can merge with another bilayer and transfer part of its interior solution to the cell [52]. Liposome fusion was investigated as part of this research work for single vesicles using elastic light scattering and fluorescence techniques, and some details are provided about

these experiments at the end of chapter 5.

Though the principal component of a cell membrane is the phospholipids, the cell membrane will typically be enriched with other lipids, cholesterol and proteins. This can create complex interactions within the bilayer affecting the physical properties of the cell membrane which is an enriched lipid bilayer. The fluid-mosaic model describes the self-organisation, and lateral and rotational diffusion, of lipids and proteins embedded in the bilayer structure of cellular membranes [53]. The model explains how the presence of certain proteins or cholesterol limit the ability of lipid molecules to interchange with each other, thus increasing the rigidity of a lipid bilayer.

Optical trapping has previously been used to study the physical properties of liposomes and cells. As discussed in section 2.1 Ashkin first demonstrated that long wavelength lasers could be used to optically trap a cell without significant damage [23]. In [54], it was demonstrated that giant unilamellar vesicles could be captured using optical trapping; the vesicles had a diameter of 10  $\mu\text{m}$  which is an appropriate model for a mammalian cell. It has also been demonstrated that small unilamellar vesicles with a diameter of 50 nm vesicles can also be optically trapped [55]; as the vesicles are below the diffraction limit they are monitored using fluorescence techniques.

Elastic light scattering measurements have also previously been made on optically trapped vesicles and cells. The angular dependence of the scattering of an optically trapped cell was considered in [56]. The scattering was compared to the Mie-Lorenz theory of scattering for spheres to study the cells orientational dynamics within the optical trap. In [57] a clearing agent (glycerol/glucose water) was added to red blood cells which reduced the scattering intensity. By reconciling the angular scattering of an optically trapped red blood cell with Mie theory, the authors obtained values for the refractive index of a red blood cell.

There is a large amount of literature on the Raman scattering from lipid bilayers of synthetic vesi-

cles. It has been shown to be a powerful method for characterizing the structure of lipid bilayers and to identify healthy cells. In [58] and [59], the authors show that there is a significant decrease in the size of the Raman peaks attributed to DNA and protein for dead cells. A set of spectra for 35 different lipids is presented in [60]. Raman spectra have previously been recorded for pure phospholipid liposomes containing hydrocarbon chains with different degrees of saturation using confocal Raman tweezers [61]. A method is also being developed to use Raman scattering to identify cancerous cells in skin and breast tissue. Cancerous cells produce visibly different Raman spectra to healthy cells [62]. This approach has the advantage over current methods in tissue pathology as Raman measurement and analysis can be carried out significantly quicker.

### **2.3.2 Liquid aerosol**

An aerosol consists of a liquid or solid phase dispersed in a gas phase. Aerosols are of interest in many areas of science: environmental science (clouds or fog), medicine (inhalers) and industry (fuel injection systems). The coalescence and agglomeration of liquid aerosol microdroplets is also an important phenomena in such areas. The interactions between individual droplets can affect the properties of the entire aerosol. The coalescence of micrometer sized droplets has been suggested to affect cloud formation [63], ink-jet printing [64] and spray drying [65]. In chapter 6, the binary coalescence is analysed for micrometer sized droplets by making a comparison between mathematical models and optical tweezers based experiments.

The average size of droplets within an aerosol can vary widely. For example, in clouds or fog, the average diameter is on a micrometer scale, however, in rain, the droplets are on a millimetre scale. Different methods are required to study different sized aerosol droplets. The dynamics of the coalescence process are also strongly dependant on droplet size. Using high speed imag-

ing, a frame rate of 10 kHz is required to observe droplet coalescence on a millimetre scale. To accurately characterize the coalescence process for droplets on a micrometer scale, a MHz frame rate camera would be required. Even at this frame rate, the coalescence process would be complete after just a few frames of the video recording. Illumination of the coalescence event to obtain a clear contrast of the droplets in video images also becomes increasingly challenging at microsecond exposure times. In addition, high-speed cameras capable of recording sequences of images at MHz frame rates are expensive. Elastic light scattering can be sampled much faster (GHz rates) so can often be a more suitable way to probe shape deformations occurring during the coalescence of aerosol droplets.

There are several methods which may be used to isolate pairs of aerosol droplets and then induce and measure coalescence. A review of techniques for isolating micrometer sized particles can be found in [66]. Typically these methods are only suitable for droplets of diameter smaller than  $100\ \mu\text{m}$  as for droplets larger than this the coalescence cannot be resolved by video imaging due to the short coalescence time. One such method is through the use of microfluidic devices. In [67], aqueous droplets with radius greater than  $100\ \mu\text{m}$  are dispersed in oil in a microfluidic device. The flow allows the droplets to be isolated such that they are separated by a small film. Coalescence is then induced by removing the film.

Electrostatic levitation can be used to isolate charged aerosol particles. In Milikans oil drop experiment, a negatively charged and a positively charged plate are used to create a DC electric field in an isolated chamber. The electric field balances the gravitational force on the oil droplet against gravity leading to stable levitation. To create an electrodynamic balance, another electrode is added to form an AC electric field, which provides lateral and axial trapping capability. The electrodynamic balance can be integrated with a spectroscopic apparatus to measure physical and chemical properties of the isolated aerosol droplets. It has been shown that an

electrodynamic balance is capable of trapping micro particles of radius  $1\ \mu\text{m}$  to  $100\ \mu\text{m}$ .

An electrodynamic balance has also been used in conjunction with Raman spectroscopy to characterize the chemical composition of aerosol droplets [68]. In [69], the electro-dynamic balance was used to analyse collisions of microdroplets, two droplets of different chemicals were collided and Raman spectra were then taken to observe if any chemical reaction had taken place.

In previous work at the University of Leicester, a pair of liquid aerosol droplets of radii  $1\ \mu\text{m}$  -  $6\ \mu\text{m}$  have were isolated using optical tweezers [1]. The position of the optical traps was then adjusted, using a spatial light modulator, to induce coalescence. The time from initial contact of the two droplets to a fully relaxed spherical droplet was recorded by measuring changes in elastic back scattered light. Light scattered as a result of photons from the trapping laser was recorded on a photodiode connected to an oscilloscope capable of recording data points every 100 ns. The modulation of the intensity of light scattering during the coalescence event is shown in figure 2.11 (the data was taken from [1]). The experiment shows an overall decline in the intensity of light scattering over the course of the coalescence. This can be explained by Mie theory due to an increase in droplet size. The initial point of contact is marked by a large increase in scattering between  $t=0\ \mu\text{s}$  and  $t=1\ \mu\text{s}$ . Between  $t=1\ \mu\text{s}$  and  $t=17\ \mu\text{s}$  six periods of an oscillation were observed. This experimental result is analysed using mathematical modelling techniques in chapter 6.

The periodicity and damping of the oscillation can be quite accurately described by the theory of Lord Rayleigh. When two liquid droplets first coalesce they pass from a low potential energy state to a high potential energy state, this energy is lost through a viscously damped oscillation. Rayleigh showed that the period of oscillation caused by surfaces forces alone was given by,

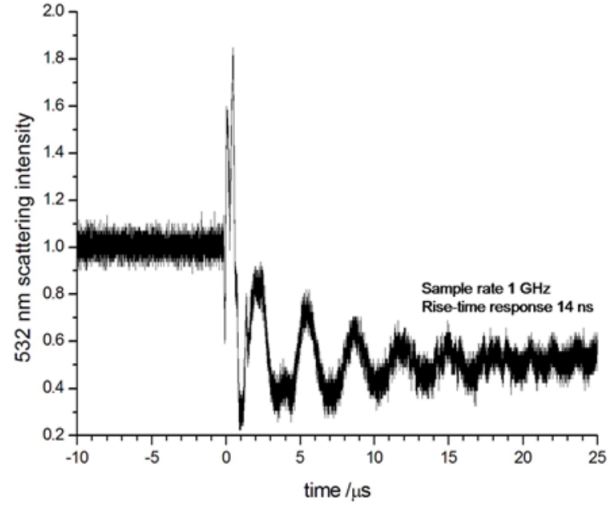


Figure 2.11: The 532 nm elastic back scattered light over the coalescence of two aqueous aerosols, taken from [1].

$$\omega_l = \frac{l(l-1)(l+2)\sigma}{r^3\rho}$$

where  $\omega_l$  is the period of the oscillation,  $l$  is the mode of the oscillation,  $\sigma$  is the surface tension of the droplet,  $\rho$  is the droplets density and  $r$  is the droplet radius [2]. The mode of the oscillation  $l$ , describes the shape of the oscillating droplet. Each mode produces a distinct shape deformation described by the Legendre polynomial. The  $l = 2, 3, 4, 5$  modes of an oscillation of a circular shape are shown in figure 2.12, the image was taken from [70]. The shape oscillates between the blue and red curves before eventually becoming a stable circle.

The effect of viscosity on the rate of damping was later considered by Lamb [71], the damping constant  $\tau_l$  is given by

$$\tau_l = \frac{r^2\rho}{(l-1)(2l+1)\eta},$$

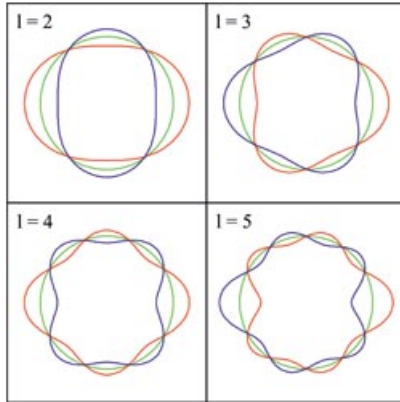


Figure 2.12: The  $l = 2, 3, 4, 5$  modes of an oscillation of a sphere, the figure was taken from [70].

where  $\eta$  is the dynamic viscosity. The amplitude of the oscillation is given by

$$A(t) = \sum_l \exp\left(-\frac{t}{\tau_1}\right) A_{0,l} \cos(\omega_l t),$$

where  $A_{0,l}$  is the initial amplitude of the  $l^{\text{th}}$  oscillation.

The theory of Rayleigh and Lamb provides a description of the period and damping rate of the oscillation undergone by the composite droplet, however it does not describe the magnitude of the deformations of the oscillating droplet. To give a complete image of the coalescence, a complete consideration of the Navier-Stokes type equations is required. Analytic methods can resolve parts of the coalescence, however in order to provide a complete description, numerical methods are needed.

Raman tweezers have previously been used to compare the initial and final states in the binary coalescence of aqueous microparticles [72]. The volume of two optically trapped droplets was measured using cavity enhanced Raman spectroscopy (the droplets had radii  $3.014 \mu\text{m}$  and  $4.083 \mu\text{m}$ ). After coalescence was induced, the volume of the composite droplet was measured in the

same way showing that volume is conserved. In [73], Raman spectra taken from optically trapped aerosol were used to characterize the size and composition of micrometer sized droplets.

## **2.4 Mathematical modelling of the coalescence of aqueous droplets**

As discussed above, characterizing the dynamics of the coalescence of aqueous aerosols with diameters of less than 100  $\mu\text{m}$  remains a challenging problem due to the speed of the process. The elastic light scattering data shows that the oscillation predicted by Rayleigh can be observed experimentally. However neither the theory of Rayleigh or the elastic light scattering results can be used to produce a visual representation of the process.

Alongside the attention the problem has received experimentally, it has also been of significant interest in computational fluid mechanics. Under certain assumptions, the early stages of coalescence can be described reasonably well without the use of numerical simulations. Recently a purpose built finite element based simulation has been developed at the University of Warwick describing both the early stages of coalescence and the subsequent shape transformations that take place prior to equilibration [74]. Chapter 6 presents a comparison of the elastic light scattering data recorded from an optical tweezers experiment and the finite element simulation.

### **2.4.1 The initial point of contact**

In this work we are primarily interested in the internal capillary forces acting during the coalescence event, however we will also note the conditions for coalescence. The conditions for coalescence after a collision is also a significant area of study [75]. After a collision of unequal sized droplets, there are 4 possible types of events.

- (i) Coalescence, where the droplets merge into a single larger droplet.
- (ii) Bouncing, where the droplets do not make full contact and instead, the impact causes the droplets to repel each other.
- (iii) Head on separation, where the kinetic energy of the collision is too high to be dissipated through oscillations in surface deformation and the composite droplet subsequently breaks apart.
- (iv) Off centre separation, where rather than a head on collision, one droplet grazes the other, and the grazing causes a rotation, increasing centrifugal forces on the composite droplet which causes it to break apart.

The outcome is dependant on the ratio of the Weber number to the impact factor. The Weber number  $We$  and impact factor  $B$  are defined as follows,

$$We = \frac{2r\rho u^2}{\sigma}, \quad B = \frac{\chi}{2r},$$

where  $u$  is the relative velocity and  $\chi$  is the distance from the centres of droplet projected in the direction normal to the relative velocity vector. For a figure showing the boundaries of these domains, and more detailed discussion of the theory of droplet collision, the reader is referred to [75].

In this section, the effect of initial velocity will not be considered. This is because the approach of a pair of droplets takes place with a low speed in the optical tweezing experiment. After the initial contact it is a standard assumption that a meniscus forms connecting the two droplets. The mechanism for the formation of the meniscus is unknown, however it has been observed experimentally [76] and is widely considered to be a reasonable assumption, though an interface

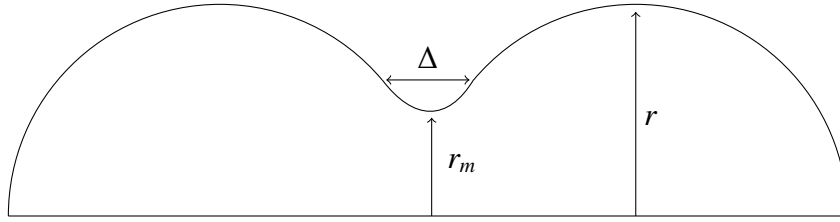


Figure 2.13: The meniscus between two merging droplets, adapted from [5].

formation model has also recently been considered [77]. The meniscus is shown in figure 2.13, two droplets of radius  $r$  have made contact, a meniscus of height  $r_m$  and width  $\Delta$  has formed between them.

Once a meniscus is formed the dynamics of the coalescence event are determined by the Reynolds number, the Reynolds number describes the ratio of inertial to viscous forces. It is given by

$$Re = \frac{\sigma r_m}{\rho \nu^2},$$

where  $\sigma$  is the surface tension of the fluid,  $\rho$  is the density,  $\nu$  is the kinematic viscosity and  $r_m$  is the height of the meniscus. Therefore in the initial stages of coalescence, where  $r_m$  is small, the flow is driven by the viscous forces and the inertial forces may be neglected. Once  $r_m$  has grown sufficiently, so that inertial forces may no longer be neglected, the flow is said to be in the inertial driven stage. The stage occurs when the Reynolds number  $Re \gg 1$ , or once  $r_m$  is greater than the viscous length scale,

$$l_v = \frac{\rho \nu^2}{\sigma}.$$

Typically the value of  $l_v$  is very low, in [78] the author calculates that, for water,  $l_v = 13.8$  nm and, for mercury  $l_v = 0.42$  nm.

In the viscously driven domain, the evolution of the shape of the meniscus over time depends on whether the exterior fluid may be modelled as inviscid. Hopper found that in the case of an inviscid exterior fluid, the height of the meniscus,  $r_m$ , evolves according to:

$$r_m(t) = -\frac{1}{\pi}t \ln(t), \quad (5)$$

for  $t \rightarrow 0$  [79]. The flow is initially driven by the region of high curvature at the meniscus. To find a value for  $r_m(t)$  an expression for the force distribution around the meniscus (over length  $\Delta$ ) is integrated in [5]. The following expression is derived by the same method for a viscous exterior fluid,

$$r_m(t) = -\frac{1}{4\pi}t \ln(t), \quad (6)$$

which is four times slower than Hopper's solution. In [5], the author also uses the same computation to derive Hopper's solution.

After the initial stage of coalescence, the flow may be modelled as being inviscid, hence the Euler equations may be applied. Egger's proposed the following proportionality expression for  $r_m$  for  $r_m \gg l_v$ ,

$$r_m(t) \propto \left(\frac{\sigma r}{\rho}\right)^{\frac{1}{4}} t^{\frac{1}{2}}, \quad (7)$$

where the proportionality constant  $C_i$  is generally considered to be between 1 and 1.7. A numerical investigation by the same author found that  $C_i = 1.62$  [80] however experimentally it has been predicted that  $C_i$  is significantly lower. For example, an analysis of the coalescence of a pendant and sessile droplets (millimetre dimension scale) found a prefactor of 1.14 for water. In

[81], two water droplets of approximately 0.1 cm in diameter are brought into contact by use of syringes, and a prefactor of  $C_i = 1.09 \pm 0.08$  was determined.

#### **2.4.2 A finite element based analysis of coalescence**

The descriptions of the early stages of coalescence outlined above, give expressions for the growth of the meniscus. The initial stages of coalescence are challenging to visualize experimentally for the sub-10  $\mu\text{m}$  sized aerosol droplets we wish to study. Our objective is to reconcile the oscillations seen in figure 2.11 with a visual representation of the coalescence. To do so, the experimental data will be compared with results from a finite element based simulation originally presented in [74]. The bulk flow of the liquid is governed by the incompressible Navier-Stokes equations with classical boundary conditions applied at the free-surface. The complexity of the problem is such that numerical methods are required to obtain a solution for the profile of the droplet surface. Ultimately the code produces sets of coordinates for the boundary of the surface for each time stamp giving a complete description of the coalescence.

The finite element model used to produce images of the coalescing droplet solves Navier-Stokes equations at the boundary (free surface) and in the bulk flow. We will recap the main principles of the procedure, for a complete exposition on the numerical method the reader is referred to [82] and for details on the initial conditions [74]. The problem is firstly normalized against the initial radii of the droplets so that the precursor droplets are both of radii 1. It is assumed that, instantaneously, the two touching spheres transform to two spheres connected by a small handle of height  $10^{-12}$ . The handle is assumed to be circular. Due to the symmetry of the problem only one quadrant needs to be considered with symmetry and smoothness conditions at the boundaries.

The flow is then discretized into triangular elements with the condition that nodes on the free surface stay on the free surface and nodes in the bulk flow are free to move around. The mesh uses bipolar coordinates  $(\rho, \sigma)$  which are related to the Cartesian coordinates  $(x, y)$  by the transformation,

$$x = a \frac{\sinh(\rho)}{\cosh(\rho) - \sin(\sigma)}, \quad y = a \frac{\sin(\sigma)}{\cosh(\rho) - \sin(\sigma)}.$$

The transformation creates smaller elements around the meniscus which drives the coalescence.

Initially, the velocity of the flow at  $t = 0$  is assumed to be zero. The flow is driven by the region of high curvature at the meniscus. The pressure and velocity of all nodes are then transformed into the weak form, that is, they are approximated by their value at each node and an interpolating function associated with the node. The interpolating functions are quadratic for velocity and linear for pressure. The interpolating functions have value one at the node they are associated with and zero at every other node. A solution is approximated by multiplying the interpolating function by the value at each node. This solution is then substituted into the Navier-Stokes equations governing the problem. As the solution is not exact this gives a residual.

The aim of the finite element model is to reduce these residuals to zero. To do so the Galerkin method is used. The residuals are multiplied by a series of weighting functions, which are the same form as the interpolating functions. By insisting that the integrals vanish, the coefficients of the interpolating functions can be found and hence an approximate piecewise solution that is linear for pressure and quadratic for velocity is found. These equations are then solved using a Gaussian quadrature method. It is important to ensure that the solution is independent of the temporal resolution. The chosen time-step is adaptive, the error can be estimated and if it is greater than a certain threshold, a smaller time-step is chosen.

The mathematical modelling in [74] has been compared with the scaling law given by equation 7 in [6]. Firstly, the problem is formulated so that it is dimensionless, that is the droplets have initial radii 1, and the height of the dimensionless meniscus is given by  $\bar{r}_b$ . The finite element model is then fitted against equation 7 for different values of  $C_i$ . For the early stages ( $\bar{r}_b < 0.15$ ), a value of  $C_i = 1.5$  gives a reasonable approximation to equation 7, however, the error quickly becomes significant. For  $C_i = 1.25$ , a reasonable fit is made for  $0.1 < \bar{r}_b < 0.75$ , however, the error is significant for  $\bar{r}_b < 0.1$ . The viscosity driven phase is also examined using the finite element based solution [83]. By comparing when the finite element simulations coincide with the equations 5, 6 and 7 boundaries for the viscously driven regime, the inertial regime and the "transition regime" are established.

Outside of the standard coalescence, where the merging droplets are surrounded by another fluid, the finite element based simulation has also been used to analyse the jumping phenomena [84]. This is where two spherical droplets coalesce on an ultra hydrophobic surface coalesce and the resulting droplet is observed to jump from the surface. The process has been called coalescence-induced jumping. In this example, the excess energy which is normally lost through viscously-damped oscillations is converted into translational kinetic energy causing the droplet to detach from the surface.

## 2.5 Summary

The aim of the research undertaken for this thesis was to compare the elastic light scattering results for the coalescence of optically trapped aerosol droplets previously reported in [1] with a mathematical model of the process. The results of a finite element based method were shown to be in strong agreement with both the classical theory and elastic light scattering results. This was

then applied to droplets of varying viscosity. During the project the optical tweezing apparatus was also developed to analyse the shape transformations and phase transitions of unilamellar, micron-sized lipid vesicles. The experiments showed that the change morphology of a single vesicle over the phase transition takes place across a very narrow range of temperature, which is much narrower than the width of the thermotropic transition observed in bulk samples of lipids. Alongside the computer simulations of coalescence of aerosol droplets, the visualization software was used to implement the minimal surface known as the " $k$ -noid". New minimal surfaces can be generated from others if a Weierstrass representation for the surface is known. For the  $k$ -noid, new minimal surfaces were generated using the Lopez-Ros deformation and the simple factor dressing. The symmetries and periodicity of these surfaces was then considered. The next chapter will give a short introduction to the theory of minimal surfaces.

# Chapter Three - Minimal surfaces

## 3 Minimal surfaces

This chapter provides an introduction to the theory of minimal surfaces. In the first section some elementary results from manifold theory and differential geometry are recapped. Following this, links between minimal surface theory and complex analysis are discussed. The final section explains how new minimal surfaces may be created by applying a simple factor dressing to a known minimal surface.

### 3.1 Preliminaries

A minimal surface is given by an immersion of a Riemann surface into  $\mathbb{R}^3$ . The Riemann surface significantly contributes to the geometry of a minimal surface. We will briefly recap the notion of smooth manifolds and Riemann surfaces, for a detailed discussion the reader is referred to [85]. This section also gives a brief introduction to the basics of differential geometry, for a more detailed discussion the reader is referred to [86].

#### 3.1.1 Manifolds

Surfaces can be thought of as two dimensional manifolds. Therefore before we define a minimal surface, we shall recap the notion of a manifold.

**Definition 3.1.1.** *A topological space  $M$  is called a manifold of dimension  $n$ , if every point  $p \in M$  has a neighbourhood homeomorphic to  $\mathbb{R}^n$ . A two dimensional manifold is called a surface.*

To define a notion of smoothness we will also need to consider the charts and transition maps of a manifold.

**Definition 3.1.2.** A chart for a manifold  $M$  is a pair  $(U, \varphi)$ , such that  $U$  is open in  $M$  and  $\varphi: U \rightarrow V$  is a homeomorphism, where  $V$  is an open subset of  $\mathbb{R}^n$ . An atlas is a collection of charts,  $(U_i, \varphi_i)$  such that  $\bigcup_{i \in I} U_i = M$ . A parametrization is a homeomorphism  $\phi: V \rightarrow U$ .

**Definition 3.1.3.** A transition map of manifold  $M$  is a map,

$$r = \varphi \circ \tilde{\varphi}^{-1} = \tilde{\varphi}(U \cap \tilde{U}) \rightarrow \varphi(U \cap \tilde{U}),$$

where  $(U, \varphi)$  and  $(\tilde{U}, \tilde{\varphi})$  are charts of  $M$ , and  $U \cap \tilde{U} \neq \emptyset$ .

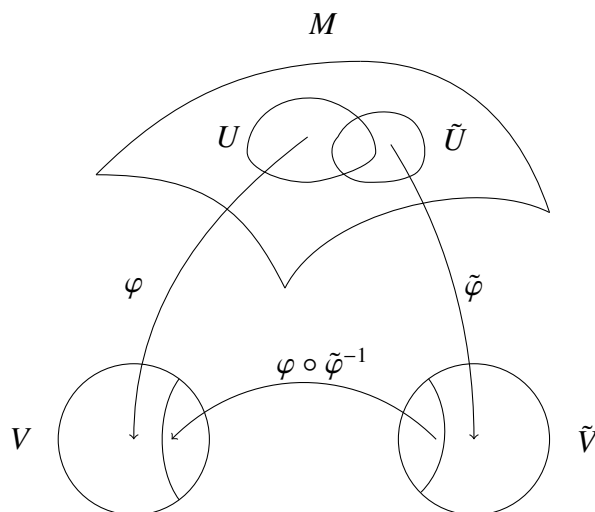


Figure 3.1: Two charts and a transition map for manifold  $M$ .

**Definition 3.1.4.** A smooth manifold is a manifold such that all transition maps are smooth.

The use of transition maps also allows other geometric properties of a manifold to be described. This notion of smoothness will allow a tangent space to be defined at each point on the manifold.

**Definition 3.1.5.** Let  $p$  be a point on a smooth manifold  $M$ , with chart  $\varphi: U \rightarrow V$ , where  $U$  is a neighbourhood of  $p$  and  $V \subset \mathbb{R}^2$  is open. If  $\lambda_1: (-\epsilon, \epsilon) \rightarrow M$  and  $\lambda_2: (-\epsilon, \epsilon) \rightarrow M$  are

curves on  $M$  with  $\lambda_1(0) = \lambda_2(0) = p$ , they are said to be equivalent at  $p$  if their derivatives at  $t = 0$  are equal. The set of equivalence classes of such curves is said to be the tangent space to  $M$  at  $p$ , and is denoted by  $T_pM$ . The differential  $d_p\varphi: T_pM \rightarrow \mathbb{R}^n$  of a chart  $\varphi$  is defined, as  $d_p\varphi(v) = \frac{d}{dt}(\varphi \circ \lambda)|_{t=0}$ , where  $\lambda: (-\epsilon, \epsilon) \rightarrow M$ ,  $\lambda(0) = p$ ,  $\lambda'(0) = v$ .

The notion of a tangent space allows us to define a differential of smooth maps between smooth manifolds.

**Definition 3.1.6.** A map  $f: M \rightarrow \tilde{M}$  is said to be smooth at  $p$  if for charts  $(U, \varphi)$  and  $(\tilde{U}, \tilde{\varphi})$  of  $M$  and  $\tilde{M}$  respectively, with  $p \in U$  and  $f(p) \in \tilde{U}$ , the map

$$\tilde{\varphi} \circ f \circ \varphi^{-1}: \varphi(U) \rightarrow \tilde{\varphi}(\tilde{U}),$$

is smooth.

**Definition 3.1.7.** Consider two smooth manifolds  $M$  and  $\tilde{M}$ , and a smooth map  $f: M \rightarrow \tilde{M}$  between them. In this case, the differential of  $f$ , at point  $p \in M$ ,  $df_p: T_pM \rightarrow T_{f(p)}\tilde{M}$  is given by:

$$df_p(v) = (f \circ \lambda)'(0),$$

where  $v \in T_pM$ , and  $\lambda$  is a curve in  $M$  with  $\lambda(0) = p$ ,  $\lambda'(0) = v$ .

This allows us to define an immersion from a manifold to  $\mathbb{R}^3$ . We will look at the case of minimal surfaces immersed in  $\mathbb{R}^3$ , however the definition is given for any differentiable map between two manifolds.

**Definition 3.1.8.** A map  $f: M \rightarrow \tilde{M}$  is said to be an immersion if its differential is everywhere injective.

In the study of minimal surfaces, embedded minimal surfaces are also of special interest.

**Definition 3.1.9.** An immersion  $f: M \rightarrow \tilde{M}$  is said to be an embedding if  $f$  is injective.

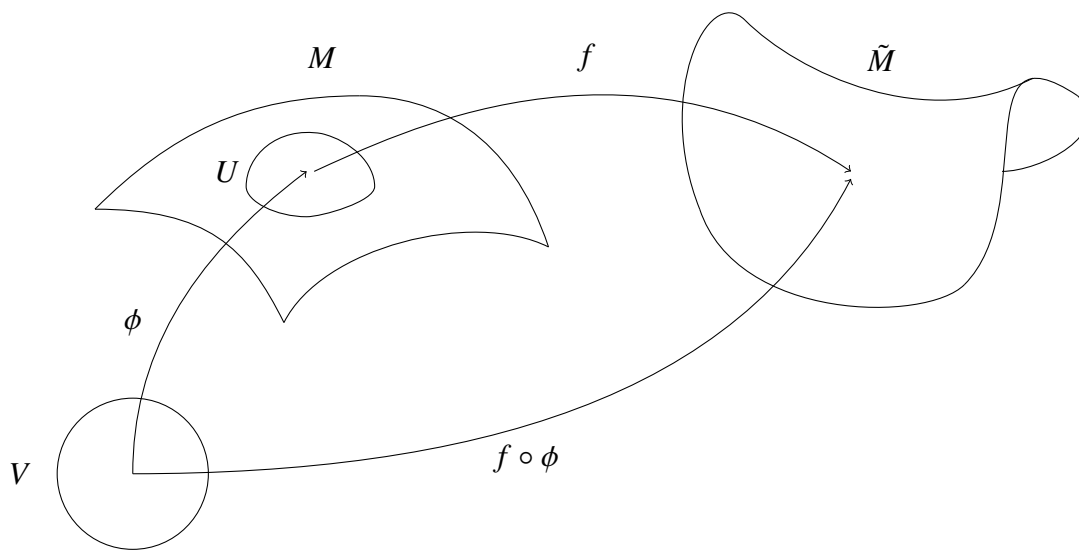


Figure 3.2: An immersion from manifold  $M$  to manifold  $\tilde{M}$ , and the composition map,  $f \circ \phi: \mathbb{R}^n \rightarrow \tilde{M}$ , where  $\phi: V \rightarrow U$  is a parametrization for the manifold.

By composing the immersion with a parametrization of  $M$ , local coordinates are given on  $\tilde{M}$ .

By defining the notion of an inner product on the tangent space several geometric properties such as angles and lengths can be defined on the tangent space of a manifold.

**Definition 3.1.10.** A Riemannian manifold is a smooth manifold  $M$ , with an inner product  $g_p$  on  $T_pM$ , such that for all vector fields  $X, Y \in \Gamma(TM)$  the function  $p \rightarrow g_p(X(p), Y(p))$  is smooth.

Later on we will often need to consider the universal cover of a manifold.

**Definition 3.1.11.** *The universal cover of a connected topological space  $M$ , is the simply connected topological space  $\tilde{M}$  together with the mapping  $\pi: \tilde{M} \rightarrow M$  which is continuous and surjective, such that every point  $p \in \tilde{M}$  has a neighbourhood homeomorphic to a disjoint union of open sets in  $M$ .*

Note that the universal cover will always exist if  $M$  is connected, locally pathwise connected and semilocally simply connected, see [87] for details.

### 3.1.2 Surfaces

For surfaces immersed in  $\mathbb{R}^3$ , the notion of curvature comes from looking at how the normal varies across the surface.

**Definition 3.1.12.** *For an immersion  $f: M \rightarrow \mathbb{R}^3$ , a Gauss map  $N: M \rightarrow S^2$  is a smooth map such that  $N(p)$  is perpendicular to  $d_p f(T_p M)$  for every point  $p \in M$  and  $\|N(p)\| = 1$ . If  $f$  has a Gauss map the surface is called orientable.*

From now on, we assume that the surfaces we consider are orientable. For an immersion  $f: M \rightarrow \mathbb{R}^3$  it is well known that the normal can be expressed in terms of the partial derivatives of  $f \circ \phi$ , where  $\phi$  is a parametrization of  $M$ . From now, in abuse of notation we identify a map  $F: M \rightarrow \tilde{M}$  with the map with coordinates,  $F \circ \phi: V \rightarrow \tilde{M}$ , where  $\phi$  is a parametrization of  $M$ . In  $\mathbb{R}^3$  there are two choices for the normal. We will assume without loss of generality that the surface is parametrized so that the Gauss map is given by

$$N = \frac{f_u \times f_v}{\|f_u \times f_v\|}.$$

**Definition 3.1.13.** *The first fundamental form of an immersion  $f: M \rightarrow \mathbb{R}^3$  is the induced metric*

on  $M$ . That is,

$$I(X, Y) = \langle df_p(X), df_p(Y) \rangle,$$

where  $X, Y \in T_pM$ .

**Definition 3.1.14.** The second fundamental form of an immersion  $f: M \rightarrow \mathbb{R}^3$  is the bilinear form

$$II(X, Y) = -\langle dN_p(X), df_p(Y) \rangle,$$

where  $X, Y \in T_pM$ .

Given a parametrization  $\phi$  of  $M$  at  $p$ , the coefficients of the first fundamental form are given by

$$E = \langle f_u, f_u \rangle, \quad F = \langle f_u, f_v \rangle, \quad G = \langle f_v, f_v \rangle,$$

so that  $I = \begin{pmatrix} E & F \\ F & G \end{pmatrix}$  is a matrix representation of the first fundamental form with respect to the basis  $f_u, f_v$ .

Similarly, the coefficients of the second fundamental form given by

$$e = \langle f_{uu}, N \rangle, \quad f = \langle f_{uv}, N \rangle, \quad g = \langle f_{vv}, N \rangle,$$

give  $II = \begin{pmatrix} e & f \\ f & g \end{pmatrix}$ , a matrix representation for the second fundamental form.

To define a notion of curvature the Weingarten map (or shape operator) must be defined.

**Definition 3.1.15.** For an immersion  $f: M \rightarrow \mathbb{R}^3$  with Gauss map  $N$  the Weingarten map at point  $p$  is the map from the tangent space (when identifying  $T_pM$  and  $df_p(T_pM)$ ) defined by

$$W_p = -dN_p.$$

This allows us to define the mean and Gaussian curvature:

**Definition 3.1.16.** For an immersion  $f: M \rightarrow \mathbb{R}^3$  the mean curvature  $H$  is given by the trace of the Weingarten map  $W$  and the Gaussian curvature  $K$  is given by the determinant:

$$H = \text{tr}(W), \quad K = \det(W).$$

By use of the Weingarten equations, the Weingarten map can be expressed in terms of the first and second fundamental forms locally. This can be used to compute the mean and Gaussian curvature:

$$H = \frac{eG - 2fF + gE}{2(EG - F^2)}, \quad K = \frac{eg - f^2}{EG - F^2}.$$

We also have a special interest in the average Gaussian curvature across the surfaces.

**Definition 3.1.17.** For any immersion  $f: M \rightarrow \mathbb{R}^3$  the total curvature  $K_T$ , is defined as

$$K_T = \int_M K dA,$$

where  $K$  is the Gaussian curvature of  $f$ . If the total curvature is finite, the surface is said to be of finite total curvature.

There are several possible definitions of a minimal surface. We use the definition of vanishing

mean curvature.

**Definition 3.1.18.** Let  $f: M \rightarrow \mathbb{R}^3$  be an immersion from a two dimensional manifold. Then  $f$  is said to be minimal if  $H = 0$ .

Geodesics on a surface describe the shortest path between two points on the surface. Later on, we will use geodesics to extend minimal surfaces by reflection. To do so we extend the well known Schwarz reflection principle for holomorphic maps to minimal surfaces.

**Definition 3.1.19.** For a surface  $S$  parametrized by immersion  $f: M \rightarrow \mathbb{R}^3$  a curve  $\lambda: (-\epsilon, \epsilon) \rightarrow S$  is said to be a geodesic if its geodesic curvature given by  $\kappa_g = \frac{\langle \lambda'', N \times \lambda' \rangle}{\langle \lambda', \lambda' \rangle^{\frac{3}{2}}}$  vanishes.

Geodesics also allow us to define complete surfaces.

**Definition 3.1.20.** A surface  $S$  is said to be complete if the induced metric space on  $S$  is complete in the usual sense.

### 3.1.3 Riemann surfaces

To define a minimal surface using harmonic maps an underlying Riemann surface is used. Riemann surfaces are a case of the larger class of complex manifolds:

**Definition 3.1.21.** A manifold is said to be complex if the transition maps between charts are holomorphic. That is, if  $U, \tilde{U} \in M$  are open sets and  $\varphi: U \rightarrow V$  and  $\tilde{\varphi}: \tilde{U} \rightarrow \tilde{V}$  are charts of  $M$ , with  $V, \tilde{V} \subset \mathbb{C}^n$ , then the transition map

$$\varphi \circ \tilde{\varphi}^{-1}: \tilde{\varphi}(U \cap \tilde{U}) \rightarrow \varphi(U \cap \tilde{U}),$$

is holomorphic.

Restricting to the two dimensional manifold case, the manifold locally resembles  $\mathbb{C}$ . In this case the manifold is called a *Riemann surface*. As the inverse of a transition map is also a transition map, all transition maps of a complex manifold must be biholomorphic.

**Example 3.1.1.** As an example consider the 2-sphere  $S^2$ , which will become important later on since the  $k$ -noid is an immersion from a punctured  $S^2$  to  $\mathbb{R}^3$ . The 2-sphere  $S^2$  is described by the two charts  $(U, \varphi)$  and  $(\tilde{U}, \tilde{\varphi})$  where

$$U = S^2 \setminus \left\{ \begin{pmatrix} 0 \\ 0 \\ 1 \end{pmatrix} \right\}, \quad \tilde{U} = S^2 \setminus \left\{ \begin{pmatrix} 0 \\ 0 \\ -1 \end{pmatrix} \right\}.$$

Writing

$$S^2 = \left\{ \begin{pmatrix} x_1 \\ x_2 \\ x_3 \end{pmatrix} \in \mathbb{R}^3 : x_1^2 + x_2^2 + x_3^2 = 1 \right\},$$

the charts  $\varphi : U \rightarrow \mathbb{C}$  and  $\tilde{\varphi} : \tilde{U} \rightarrow \mathbb{C}$  are given by

$$\varphi(x_1, x_2, x_3) = \frac{x_1 + ix_2}{1 - x_3}, \quad \tilde{\varphi}(x_1, x_2, x_3) = \frac{x_1 - ix_2}{1 + x_3},$$

which are the stereographic projections of the sphere from the north and south pole respectively.

The map  $r : \varphi(U) \rightarrow \tilde{\varphi}(\tilde{U})$  with  $r(z) = \frac{1}{\bar{z}}$  is the transition map for these charts as,

$$r\left(\frac{x_1 + ix_2}{1 - x_3}\right) = \frac{1 - x_3}{x_1 + ix_2} = \frac{(1 - x_3)(x_1 - ix_2)}{x_1^2 + x_2^2} = \frac{(1 - x_3)(x_1 - ix_2)}{1 - x_3^2} = \frac{x_1 - ix_2}{1 + x_3}.$$

Thus,  $S^2$  is a Riemann surface.

For a complex manifold  $M$  it is possible to canonically define an *almost complex structure*  $J$  on the tangent space  $T_pM$ , that is a linear operator on the tangent space, with  $J^2 = -1$ . Manifolds that admit an almost complex structure  $J$ , that is, a smooth section  $J \in \Gamma(\text{End}(TM))$  with  $J^2 = -1$ , are said to be *almost complex*. Generally, it is not the case that almost complex manifolds are complex. If the manifold  $M$  is complex and has a chart  $\varphi: U \rightarrow V$  and a vector  $X$  in the tangent space, the complex structure  $J$  is given by  $d_p\varphi(JX) = id_p\varphi(X)$ . In this case the almost complex structure is referred to as the *complex structure*.

In the case of a two dimensional real manifold, almost complex manifolds are known to be complex manifolds. To prove this the Newlander-Nirenberg theorem is used [88].

**Theorem 3.1.22.** *An almost complex manifold  $M$  is complex if and only if the Nijenhuis tensor,*

$$N(X, Y) = 2([JX, JY] - [X, Y] - J[X, JY] - J[JX, Y])$$

*vanishes, where  $X, Y \in \Gamma(TM)$  and  $[A, B]$  indicates the Lie bracket on vector fields, where  $A, B \in \Gamma(TM)$ .*

To prove this theorem, a detailed description of manifold theory is required. A proof can be found in [89].

**Theorem 3.1.23.** *If the real dimension of a manifold  $M$  is two, then  $M$  is complex if and only if  $M$  is almost complex.*

*Proof.* Assume that  $M$  is almost complex and let  $J$  be the almost complex structure on  $M$ , and  $N$  the Nijenhuis tensor as defined above. In the two dimensional case,  $X$  and  $JX$  form a basis for

$T_pM$ , and we only need to show that  $N[X, JX] = 0$ , to do this we use the property that the Lie bracket is anticommutative. We have

$$\begin{aligned} N[X, JX] &= 2([JX, -X] - [X, JX] - J[X, -X] - J[JX, JX]) \\ &= 2([X, JX] - [X, JX] + J[X, X] - J[JX, JX]) \\ &= 0. \end{aligned}$$

Therefore, if  $M$  is an almost complex manifold of dimension two, then  $M$  is complex. The converse is also clear.  $\square$

We will often need to consider holomorphic maps from complex manifolds into  $\mathbb{C}$ .

**Definition 3.1.24.** A map  $f: M \rightarrow \mathbb{C}$  from a complex manifold  $M$  to  $\mathbb{C}$  is holomorphic if  $df$  is complex linear. That is  $df(JX) = idf(X)$ .

**Example 3.1.2.** For a holomorphic map  $f: \mathbb{C} \rightarrow \mathbb{C}$  where  $f(x, y) = u(x, y) + iv(x, y)$  the Cauchy-Riemann equations can be derived from the above definition. Let  $z = x + iy$ , then the vectors  $\frac{\partial}{\partial x}$  and  $\frac{\partial}{\partial y}$  form a basis for  $T\mathbb{C} \cong \mathbb{C}$  with  $J\frac{\partial}{\partial x} = \frac{\partial}{\partial y}$ . Therefore

$$df\left(\frac{\partial}{\partial y}\right) = df\left(J\frac{\partial}{\partial x}\right) = idf\left(\frac{\partial}{\partial x}\right),$$

which implies that  $\frac{\partial f}{\partial y} = i\frac{\partial f}{\partial x}$ . This can be written in terms of  $u$  and  $v$  giving that

$$u_y + iv_y = iu_x - v_x.$$

By comparing real and imaginary parts we recover the Cauchy-Riemann equations.

Holomorphic maps may be extended by reflection, this is known as the Schwarz reflection principle. We will later extend this to a reflection principle for minimal surfaces, allowing a  $k$ -noid to be constructed from its symmetries.

**Theorem 3.1.25.** *Let  $f: G \rightarrow \mathbb{C}$  be a holomorphic function where  $G \subset \mathbb{C}$ , such that the boundary of  $G$  contains a line segment  $\delta$  and assume  $\Delta = f(\delta)$  is also a line segment. Let  $G^*$  be the reflection of  $G$  in the boundary  $\delta$  and  $z^*$  be the reflection of point  $z$  across  $\delta$ . Consider  $f^*: G^* \rightarrow \mathbb{C}$  such that  $f^*(\delta) = f(\delta)$  and  $f^*(z)$  is the reflection of  $f(z)$  across  $\Delta$ . Then  $f^*: G^* \rightarrow \mathbb{C}$  is holomorphic.*

*Proof.* Without loss of generality we may assume that  $\delta$  is part of the real line and so for  $z \in G$  we have  $z^* = \bar{z}$ . We may also assume that  $\Delta$  is part of the real axis as  $G$  and  $G^*$  may be transformed by a Mobius transformation preserving the holomorphicity and continuity of  $f$  so that  $\Delta$  is mapped to a straight line on the real axis. We also have that  $f^*(z^*) = \overline{f(z)}$ . Therefore, the analytic expansion of  $f^*(z^*)$  around  $z_0^*$ , where  $z_0 \in G$ , is

$$f^*(z^*) = \overline{f(z)} = \sum_{n=0}^{\infty} \overline{a_n(z - z_0)^n} = \sum_{n=0}^{\infty} \bar{a}_n(\bar{z} - \bar{z}_0)^n = \sum_{n=0}^{\infty} \bar{a}_n(z^* - z_0^*)^n.$$

Hence, we see that  $f^*: G^* \rightarrow \mathbb{C}$  is holomorphic. □

The notions of poles, zeroes and meromorphic functions can be extended to complex manifolds by considering the parametrization of the manifold.

**Definition 3.1.26.** *Let  $M$  and  $\tilde{M} = M \setminus \{\phi(p)\}$  be Riemann surfaces with parametrizations  $\phi: V \rightarrow U$  and  $\tilde{\phi}: V \setminus \{p\} \rightarrow U \setminus \{\phi(p)\}$  respectively. Consider a map  $f$  such that  $f: \tilde{M} \rightarrow \mathbb{C}$  is holomorphic but  $f: M \rightarrow \mathbb{C}$  is not. Then  $f$  is said to have a pole at  $\phi(p)$  if  $f \circ \tilde{\phi}: V \setminus \{p\} \rightarrow \mathbb{C}$*

has a pole at  $p$  in the usual sense. That is, if  $V \setminus \{p\}$  is an open subset of  $\mathbb{C}$  and  $F: V \setminus \{p\} \rightarrow \mathbb{C}$  is a holomorphic map, then  $F$  has a pole of order  $n$  at  $p$  if there exists holomorphic function  $g: V \rightarrow \mathbb{C}$ , with  $g(p) \neq 0$ , such that,

$$f(z) = \frac{g(z)}{(z-p)^n},$$

where  $z$  is a coordinate of  $V$ . If the pole has order 1 it is called a simple pole.

**Definition 3.1.27.** If  $M$  is a Riemann surface with parametrization  $\phi: V \rightarrow U$  and  $f: M \rightarrow \mathbb{C}$  is a holomorphic map and coordinate  $z$ , then  $f$  is said to have a zero at  $\phi(p)$  if  $f \circ \phi: V \rightarrow \mathbb{C}$  has a zero at  $p$  in the usual sense. That is, if  $V$  is an open subset of  $\mathbb{C}$  and  $F: V \rightarrow \mathbb{C}$  is a holomorphic map, then  $F$  has a zero of order  $n$  at  $p$  if there exists a holomorphic function  $g: V \rightarrow \mathbb{C}$  with  $g(p) \neq 0$ , and

$$f(z) = g(z)(z-p)^n,$$

where  $z$  is a coordinate of  $V$ . If the zero has order 1, it is called a simple zero.

**Definition 3.1.28.** A function  $f: M \rightarrow \mathbb{C}$  is said to be meromorphic if it is holomorphic on  $M$  except a set of isolated poles.

**Definition 3.1.29.** For a Riemann surface  $M$ , a linear map  $\alpha: TM \rightarrow \mathbb{C}$ , is called a holomorphic 1-form if it can be described locally as  $\alpha = f(z)dz$ , where  $f$  is a holomorphic function and  $z = u + iv$  is a local coordinate on  $M$ .

## 3.2 Minimal surfaces

This section will focus on how holomorphic and meromorphic functions can be used to generate minimal surfaces. Before we can do so, we must briefly recap the notion of a conformal map.

### 3.2.1 Conformal maps

Conformal maps can be thought of as maps that preserve angles and orientation of vectors on the tangent space of a Riemannian manifold. Formally this condition is given by the following definition.

**Definition 3.2.1.** *Consider two Riemannian manifolds  $(M, g)$  and  $(\tilde{M}, \tilde{g})$ , and let  $f: M \rightarrow \tilde{M}$  be an immersion between them. Then  $f$  is said to be conformal if it preserves angles and maps equal length vectors to equal length vectors, that is, if  $\|X\| = \|Y\|$  then  $\|df_p(X)\| = \|df_p(Y)\|$  and  $\theta_g(X, Y) = \theta_{\tilde{g}}(df_p(X), df_p(Y))$ , where  $X, Y \in T_pM$  and  $\theta_g(X, Y)$  is the angle between  $X$  and  $Y$ , with respect to the metric  $g$ .*

The following theorem provides a simple way to check if an immersion is conformal.

**Theorem 3.2.2.** *Let  $(M, g)$  and  $(\tilde{M}, \tilde{g})$  be Riemannian manifolds, and  $f: M \rightarrow \tilde{M}$  be an immersion between them. Let  $m = \dim M$  and  $\{X_1, \dots, X_n\}$  be an orthonormal basis of  $T_pM$  for  $p \in M$ . Then  $f$  is conformal at  $p$  if and only if for all  $p$ , we have that,*

$$\|df_p(X_i)\| = \|df_p(X_j)\| \quad \forall i, j, \quad \text{and} \quad \tilde{g}_{f(p)}(df_p(X_i), df_p(X_j)) = 0, \quad \forall i \neq j.$$

*Proof.* If  $f$  is conformal then  $f$  preserves angles and lengths, therefore the orthonormal basis is mapped to an orthogonal basis with  $\|df_p(X_i)\| = \|df_p(X_j)\|$ , for all  $i, j$ .

Conversely, consider two vectors  $X$  and  $Y$  in  $T_pM$  with,  $\|X\| = \|Y\|$  and the angle between them  $\theta_g(X, Y)$  which is given by,  $\cos(\theta_g(X, Y)) = \frac{g_p(X, Y)}{\|X\|\|Y\|}$ .

Let  $X = \sum x_i X_i$  and  $Y = \sum y_i X_i$  where  $X_i$  are the basis vectors for  $T_pM$ , then by the linearity of  $df_p$  we have,

$$\tilde{g}_{f(p)}(df_p(X), df_p(Y)) = \sum_{i,j} x_i y_j \tilde{g}_{f(p)}(df_p(X_i), df_p(X_j)).$$

By assumption all terms with  $i \neq j$  are equal to zero, this gives that:

$$\tilde{g}_{f(p)}(df_p(X), df_p(Y)) = \sum_i x_i y_i \tilde{g}_{f(p)}(df_p(X_i), df_p(X_i)).$$

We also have that  $\tilde{g}_{f(p)}(df_p(X_i), df_p(X_i)) = \tilde{g}_{f(p)}(df_p(X_j), df_p(X_j))$  for all  $i, j$ , with  $\lambda = \tilde{g}_{f(p)}(df_p(X_i), df_p(X_i)) > 0$  so therefore,

$$\tilde{g}_{f(p)}(df_p(X), df_p(Y)) = \lambda \sum_i x_i y_i = \lambda g_p(X, Y).$$

Now consider the function  $\theta_{\tilde{g}}(df_p(X), df_p(Y))$

$$\cos(\theta_{\tilde{g}}(df_p(X), df_p(Y))) = \frac{\tilde{g}_{f(p)}(df_p(X), df_p(Y))}{\|df_p(X)\| \|df_p(Y)\|} = \frac{\lambda g_p(X, Y)}{\lambda \|X\| \|Y\|} = \frac{g_p(X, Y)}{\|X\| \|Y\|} = \cos(\theta_g(X, Y)),$$

showing that angles are preserved. We also need to show that is if  $\|X\| = \|Y\|$  then  $\|df_p(X)\| = \|df_p(Y)\|$ . Consider a pair of equal length vectors  $X, Y \in T_pM$ , then

$$\|df_p(X)\|^2 = \tilde{g}_{f(p)}(df_p(X), df_p(X)) = \lambda\|X\|^2 = \lambda\|Y\|^2 = \|df_p(Y)\|^2,$$

shows the claim. □

**Definition 3.2.3.** For a Riemann surface  $M$  a coordinate  $(x, y)$  is called a conformal coordinate, if the parametrization map  $\phi: V \rightarrow M$ , with  $\phi(u, v) = (x, y)$ , is conformal.

Given a conformal coordinate  $\phi$  of  $M$ , an immersion  $f: M \rightarrow \mathbb{R}^3$  is conformal if and only if  $|f_u| = |f_v|$  and  $\langle f_u, f_v \rangle = 0$ . This follows from theorem 3.2.2 since for a conformal coordinate,  $X = \phi_u$  and  $Y = \phi_v$  are perpendicular tangent vectors of  $M$ , and  $df_p(\phi_u) = (f \circ \phi)_u$  and  $df_p(\phi_v) = (f \circ \phi)_v$ . Note that we have equipped the manifold  $\mathbb{R}^3$  with the standard metric. Therefore for a conformal immersion into  $\mathbb{R}^3$ , the coefficients of the first fundamental form can be reduced to

$$E = \langle f_u, f_u \rangle = \langle f_v, f_v \rangle = G, \quad F = 0.$$

Therefore in the case of a conformal immersion the mean curvature  $H$  is given by,

$$H = \frac{e + g}{2E}.$$

This allows us to show that harmonic, conformal immersions are minimal immersions.

**Theorem 3.2.4.** If an immersion  $f: M \rightarrow \mathbb{R}^3$  is conformal then  $\Delta f = 0$  if and only if  $H = 0$ .

*Proof.* Let  $(u, v)$  be a conformal coordinate on  $M$ , as  $f$  is conformal we have that  $E = G$  and  $F = 0$ . Now consider  $\langle f_{uu} + f_{vv}, f_u \rangle$ ,

$$\begin{aligned}
\langle f_{uu} + f_{vv}, f_u \rangle &= \langle f_{uu}, f_u \rangle + \langle f_{vv}, f_u \rangle \\
&= \frac{1}{2} \langle f_u, f_u \rangle_u - \langle f_{uv}, f_v \rangle \\
&= \frac{1}{2} (\langle f_u, f_u \rangle_u - \langle f_v, f_v \rangle_u) \\
&= 0.
\end{aligned}$$

A similar argument can be used to show that  $\langle f_{uu} + f_{vv}, f_v \rangle = 0$ . This implies that  $\Delta f$  is parallel to  $N$ . Since  $f$  is conformal we have  $H = \frac{e+g}{2E}$ , so that

$$2EH = \langle f_{uu}, N \rangle + \langle f_{vv}, N \rangle,$$

which shows that  $2EHN = \Delta f$ . So if  $H = 0$  we have a harmonic map and vice versa.

□

### 3.2.2 Holomorphic null curves

It is a well known result in complex analysis that a harmonic map  $f: M \rightarrow \mathbb{R}$  can be thought of as the real part of a holomorphic function. In this section a discussion of the link between holomorphic and harmonic maps is given. This can be used to generate minimal surfaces from holomorphic functions.

**Theorem 3.2.5.** *If  $\Phi: \Omega \rightarrow \mathbb{C}$  is a holomorphic function, where  $\Omega$  is an open subset of  $\mathbb{C}$ , with  $\Phi(x, y) = u(x, y) + iv(x, y)$ , then  $u(x, y)$  and  $v(x, y)$  are real valued harmonic functions.*

*Proof.* Since  $\Phi$  is a holomorphic function, the Cauchy-Riemann equations hold, that is,  $u_x = v_y$

and  $u_y = -v_x$ , so that,

$$u_{xx} = v_{yx} = v_{xy} = -u_{yy}.$$

This gives that  $u_{xx} + u_{yy} = 0$ , which is the harmonicity condition. A similar argument can be applied for  $v$ .

□

**Theorem 3.2.6.** *If  $u: \Omega \rightarrow \mathbb{R}$  is a harmonic function on simply connected region  $\Omega$ , then  $u$  is the real part of holomorphic function  $\Phi$  on  $\Omega$ .*

*Proof.* The function  $\psi = u_x - iu_y$  satisfies the Cauchy-Riemann relations since  $u$  is harmonic.

Let  $\Phi = U + iV = \int \psi dz$  be the primitive of  $\psi$ , and note that,

$$\frac{\partial}{\partial z}(\Phi(z)) = \frac{1}{2} \left( \frac{\partial}{\partial x} - i \frac{\partial}{\partial y} \right) (U(x, y) + iV(x, y)) = \frac{1}{2} \left( \left( \frac{\partial U}{\partial x} + \frac{\partial V}{\partial y} \right) + i \left( \frac{\partial V}{\partial x} - \frac{\partial U}{\partial y} \right) \right).$$

By applying the Cauchy-Riemann equations we get that,

$$\Phi' = U_x - iU_y. \tag{8}$$

We also have that  $\Phi' = \psi$  so,

$$U_x(x, y) - iU_y(x, y) = \Phi' = \psi = u_x - iu_y.$$

Therefore  $U = u + c$  where  $c$  is a real constant, giving that  $u = \operatorname{Re}(\Phi + c)$ . As  $\Phi$  is holomorphic  $\Phi + c$  will also be holomorphic giving that  $u$  is the real part of holomorphic function. □

Therefore for a simply connected region  $\Omega$ , the real part of a holomorphic function  $\Phi: \Omega \rightarrow \mathbb{C}^3$  will generate a minimal surface if the real part of  $\Phi$  is a conformal immersion. To ensure that  $\text{Re}(\Phi)$  is conformal,  $\Phi$  is also required to satisfy the null condition.

**Theorem 3.2.7.** *If  $\Phi: \Omega \rightarrow \mathbb{C}^3$  is a holomorphic function then  $f = \text{Re}(\Phi)$ , is conformal if and only if the null condition*

$$\langle \Phi', \Phi' \rangle = \Phi_1'^2 + \Phi_2'^2 + \Phi_3'^2 = 0,$$

is satisfied, where  $\Phi_i' = \frac{\partial}{\partial z} \Phi_i$ . Here,  $\langle, \rangle$  denotes the standard bilinear complex form on  $\mathbb{C}^3$ .

*Proof.* Firstly, let  $\Phi(z) = f(x, y) + ig(x, y)$  where  $z = x + iy$ , we wish to show that if the null condition is satisfied then  $\|f_x\| = \|f_y\|$  and  $2\langle f_x, f_y \rangle = 0$ . By using (8) and the Cauchy-Riemann equations we have,

$$\frac{\partial}{\partial z}(\Phi(z)) = \frac{\partial f}{\partial x} + i \frac{\partial g}{\partial x}.$$

Therefore, we can compute  $\langle \Phi', \Phi' \rangle$  using the Cauchy-Riemann equations,

$$\begin{aligned} \langle \Phi', \Phi' \rangle &= \langle \Phi_x, \Phi_x \rangle \\ &= \langle f_x + ig_x, f_x + ig_x \rangle \\ &= \langle f_x, f_x \rangle - \langle g_x, g_x \rangle + 2i\langle f_x, g_x \rangle \\ &= \langle f_x, f_x \rangle - \langle f_y, f_y \rangle - 2i\langle f_x, f_y \rangle \\ &= \|f_x\|^2 - \|f_y\|^2 - 2i\langle f_x, f_y \rangle. \end{aligned}$$

By comparing real and imaginary parts, we see that  $\langle \Phi', \Phi' \rangle = 0$  is equivalent to  $\|f_x\| = \|f_y\|$  and  $2\langle f_x, f_y \rangle = 0$  which are the conformality conditions.  $\square$

We also wish to ensure that  $\text{Re}(\Phi)$ , is an immersion, to do so the following result is used.

**Theorem 3.2.8.** *Let  $\Phi: M \rightarrow \mathbb{C}^3$  be a holomorphic null curve from a Riemann surface  $M$ . Then  $f = \text{Re}(\Phi)$  is an immersion if*

$$|\Phi'_1|^2 + |\Phi'_2|^2 + |\Phi'_3|^2 \neq 0. \quad (9)$$

*Proof.* Firstly note that (9) is equivalent to  $\langle \Phi', \bar{\Phi}' \rangle \neq 0$ . Recall that  $\Phi' = f_x - if_y$ , hence we have that

$$\langle \Phi', \bar{\Phi}' \rangle = \langle f_x - if_y, f_x + if_y \rangle = \|f_x\|^2 + \|f_y\|^2.$$

So that (9) holds if and only if  $\|f_x\|^2 = \|f_y\|^2 \neq 0$  (as  $f$  is conformal). Now,  $df = f_x dx + f_y dy$  is injective if  $\ker df = \{0\}$ . Since  $f$  is conformal this is equivalent to  $\|f_x\| = \|f_y\| \neq 0$ .  $\square$

This now allows us to generate minimal immersions using holomorphic null curves.

**Definition 3.2.9.** *Let  $M$  be a Riemann surface and  $\tilde{M}$  be its universal cover. A function  $\Phi: \tilde{M} \rightarrow \mathbb{C}^3$  is said to be a holomorphic null curve, if  $\Phi$  is holomorphic with  $|\Phi'_1|^2 + |\Phi'_2|^2 + |\Phi'_3|^2 \neq 0$  and the null condition,*

$$\langle \Phi', \Phi' \rangle = 0,$$

*is satisfied. The real part of  $\Phi$ ,  $f = \text{Re}(\Phi)$  is a minimal immersion.*

Note that we have defined the holomorphic null curve  $\Phi$  on the universal cover  $\tilde{M}$  of the Riemann surface  $M$ . In general the minimal immersion  $f = \text{Re}(\Phi): \tilde{M} \rightarrow \mathbb{R}^3$  is also only defined on the

universal cover  $\tilde{M}$ . However, if  $\text{Re}(\Phi \circ \pi^{-1}): M \rightarrow \mathbb{R}^3$  is well defined we say that  $\text{Re}(\Phi)$  is single-valued on  $M$ , then in abuse of notation we will write  $f = \text{Re}(\Phi \circ \pi^{-1}): M \rightarrow \mathbb{R}^3$ .

### 3.2.3 The Weierstrass-Enneper representation

The problem of finding minimal surfaces is therefore reduced to finding holomorphic null curves. The celebrated Weierstrass-Enneper parametrization provides a method to generate holomorphic null curves from a meromorphic function  $g$  and holomorphic 1-form  $\omega$ . It was discovered by Weierstrass [12] and independently by Enneper [13].

**Theorem 3.2.10.** *Consider a meromorphic function  $g$  and holomorphic 1-form  $\omega$  on a Riemann surface  $M$ , such that when  $g$  has a pole of order  $m$  at  $p$ , then  $\omega$  has a zero of order greater than or equal to  $2m$ . Then,*

$$\Phi = \begin{pmatrix} \Phi_1 \\ \Phi_2 \\ \Phi_3 \end{pmatrix} = \int \begin{pmatrix} \frac{1}{2}\omega(1 - g^2) \\ \frac{i}{2}\omega(1 + g^2) \\ g\omega \end{pmatrix},$$

*is a holomorphic null curve, and  $f: \tilde{M} \rightarrow \mathbb{R}^3$  with  $f = \text{Re}(\Phi)$  is a minimal surface (if  $g$  has a pole of order  $m$  at  $p$  and the corresponding zero of  $\omega$  has order greater than  $m$  then  $f$  is a branched immersion).*

*Proof.* As  $\frac{1}{2}\omega(1 - g^2)$ ,  $\frac{i}{2}\omega(1 + g^2)$  and  $g\omega$  are all holomorphic  $\Phi$  will also be holomorphic. Next we check the null condition, consider,

$$\langle \Phi', \Phi' \rangle = \left(\frac{1}{2}\omega(1 - g^2)\right)^2 + \left(\frac{i}{2}\omega(1 + g^2)\right)^2 + (g\omega)^2 = 0.$$

If the order  $m$  of the pole of  $g$  is twice the order of the zero of  $\omega$  then:

$$|\Phi'_1|^2 + |\Phi'_2|^2 + |\Phi'_3|^2 = \frac{1}{4}|\omega|^2|1 - g^2|^2 + \frac{1}{4}|\omega|^2|1 + g^2|^2 + |g|^2|\omega|^2 = \frac{1}{2}|\omega|^2(1 + |g|^2)^2 \neq 0.$$

If the order of the zero of  $\omega$  is greater than  $m$  then this condition will no longer be satisfied and  $f$  will no longer be an immersion, therefore the pole  $p$  is a branch point of  $f$ .  $\square$

There are multiple forms of the Weierstrass representation, often it is convenient to write it in terms of the height differential  $dh = g\omega$ , giving,

$$\Phi = \begin{pmatrix} \Phi_1 \\ \Phi_2 \\ \Phi_3 \end{pmatrix} = \int \begin{pmatrix} \frac{1}{2}\left(\frac{1}{g} - g\right) \\ \frac{i}{2}\left(\frac{1}{g} + g\right) \\ 1 \end{pmatrix} dh.$$

Conversely, if  $\Phi$  is a holomorphic null curve, the Weierstrass data  $(g, \omega)$  is given by,

$$g = \frac{d\Phi_3}{d\Phi_1 - id\Phi_2}, \quad \omega = d\Phi_1 - id\Phi_2. \quad (10)$$

We can also write the Gauss map  $N$ , and Gaussian curvature  $K$  in terms of the Weierstrass data [90].

**Theorem 3.2.11.** *For any minimal surface generated by Weierstrass data  $(g, \omega)$  the normal  $N$  and Gaussian curvature  $K$  can be expressed as follows,*

$$N = \frac{1}{|g|^2 + 1} \begin{pmatrix} 2 \operatorname{Re}(g) \\ 2 \operatorname{Im}(g) \\ |g|^2 - 1 \end{pmatrix}, \quad K = \left( \frac{-4|dg|}{|\omega||1 - g^2|^2} \right)^2.$$

The theorem shows that for a minimal surface generated by Weierstrass data  $(g, \omega)$ , the normal  $N$  does not depend on  $\omega$ . It is also apparent that  $g$  is the stereographic projection of the normal, because of this  $g$  is sometimes also referred to as the Gauss map.

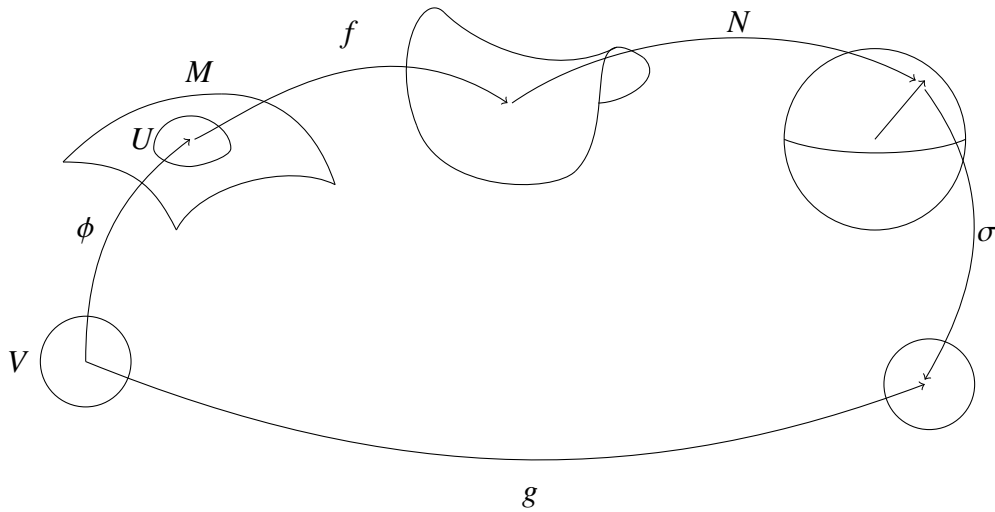


Figure 3.3: A minimal immersion, the Gauss map  $N$  and Gauss map  $g$ . The minimal surface is generated by immersion  $f: M \rightarrow \mathbb{R}^3$  where  $M$  is a Riemann surface with parametrization  $\phi: V \rightarrow U$ . The Gauss map  $N$  is the map  $N: \mathbb{R}^3 \rightarrow S^2$ , and  $\sigma$  is the stereographic projection from  $S^2$  into  $\mathbb{R}^2$ . Therefore the Gauss map  $g$  can be considered as the composition of functions  $g = \sigma \circ N \circ f \circ \phi$ .

Minimal surface	$\omega(z)$	$g(z)$
Enneper's surface	1	$z$
Catenoid	$\frac{1}{(z^2-1)^2}$	$z$
Scherk's surface	$\frac{4}{1-z^4}$	$iz$
Helicoid	$\frac{i}{(z^2-1)^2}$	$z$

Table 3.1: The Weierstrass data for four minimal surfaces.

Table 3.1 gives Weierstrass data for four minimal surfaces, images of the surfaces are shown in figure 3.4, all pictures of minimal surfaces shown in this chapter were produced using the software "Surface Lab" created at the University of Leicester [91]. The surface lab software utilizes the software package "JReality" [92] to produce an image of a surface from a parametrization. The software package "jTEM (Java tools for experimental mathematicians)" [93] was also used to create the parametrization. The surface lab has been extended to show the coalescence of aqueous aerosols and generate images of the minimal surface known as the  $k$ -noid. These are shown in chapters 6 and 7 respectively.

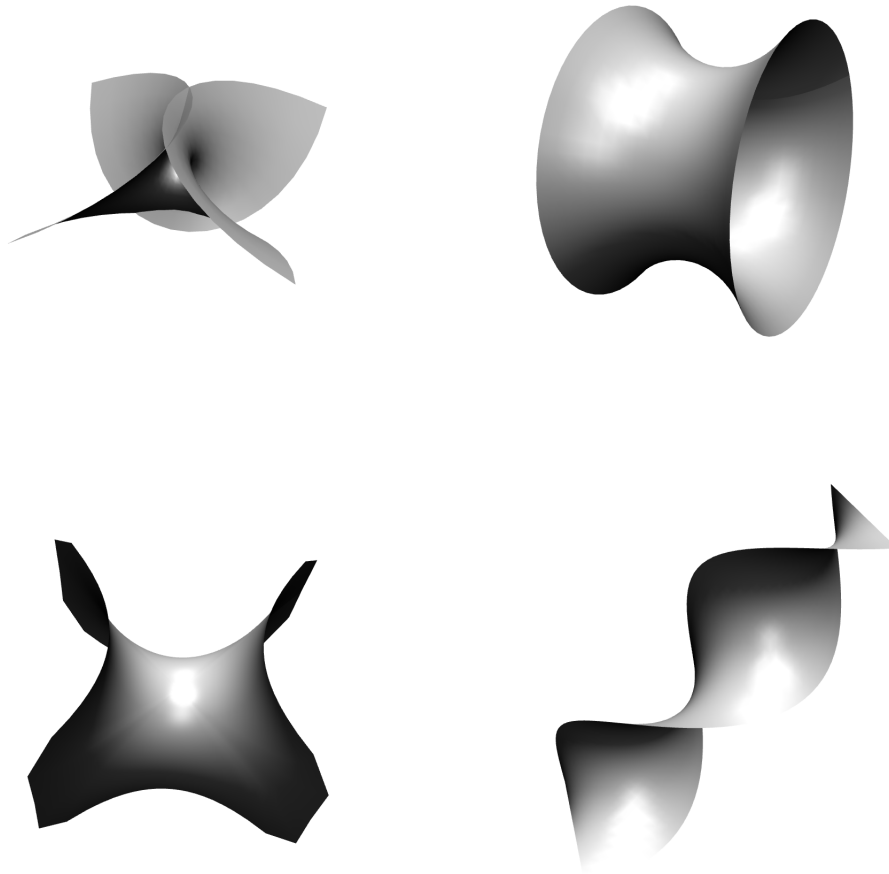


Figure 3.4: Four examples of minimal surfaces. They are Enneper's surface (top left), the catenoid (top right), Scherk's surface (bottom left) and the helicoid (bottom right).

The surfaces shown in the figure, are the Enneper surface, catenoid, Scherk's surface and the helicoid. It is notable that for the catenoid if  $(g, \omega)$  is the Weierstrass data, then  $(g, i\omega)$  is the Weierstrass data for the helicoid. This is because if  $\Phi$  is a holomorphic null curve the imaginary part  $\text{Im}(\Phi)$ , also generates a minimal surface, that is:

**Definition 3.2.12.** *If  $\Phi: \tilde{M} \rightarrow \mathbb{C}^3$  is a holomorphic null curve and  $f: M \rightarrow \mathbb{R}^3$  is a minimal*

surface where  $\operatorname{Re}(\Phi) = f$ , then the imaginary part of  $\Phi$ ,  $\operatorname{Im}(\Phi)$  is also a minimal surface. The minimal surface  $f^* = \operatorname{Im}(\Phi)$  is called the conjugate surface to  $f = \operatorname{Re}(\Phi)$ .

Hence, the helicoid is the conjugate surface to the catenoid (and vice versa), as a transformation of the Weierstrass data  $(g, \omega) \rightarrow (g, i\omega)$  is equivalent to multiplying holomorphic null curve  $\Phi$  by  $i$ . Note that if  $f$  is defined on  $M = \mathbb{C} \setminus \{0\}$  the conjugate surface may be defined on the universal cover  $\tilde{M}$ . This is the case for the catenoid and helicoid. The catenoid is defined on a Riemann surface  $M$  and the helicoid on its universal cover  $\tilde{M}$ , hence the helicoid is multivalued on  $M$  and is a periodic surface.

**Definition 3.2.13.** Let  $M$  be a compact Riemann surface, and  $\{p_1, \dots, p_k\}$  a finite number of points in  $M$ . Consider a minimal immersion  $f: \hat{M} \rightarrow \mathbb{R}^3$ , where  $\hat{M} = M \setminus \{p_1, \dots, p_k\}$ . The image  $E_j = f(B_j)$  of a punctured disk around  $B_j$  around  $p_j$  is called an end of  $f$ .

The behaviour of the ends is determined by the residue at the poles, this is due to the following theorem, see [15].

**Theorem 3.2.14.** Let  $f: M \rightarrow \mathbb{R}^3$  be a minimal surface with a complete end at  $p$ . Let  $z$  be a conformal coordinate of  $M$  at the end  $p$  which is defined on a punctured disc  $D_* = D \setminus \{0\}$  and is centred at  $p$ .

Then the following statements are equivalent:

- $f$  has an embedded finite total curvature end at  $p$ .
- $d\Phi$  has order -2 at  $z = 0$  and  $\operatorname{Res}(d\Phi, 0)$  is real.

If  $\operatorname{Res}(d\Phi, 0) = 0$  then the end is planar, otherwise, it is catenoidal.

The residues at the poles of the holomorphic null curve  $\Phi: \tilde{M} \rightarrow \mathbb{C}^3$  can also be used to calculate the translation periods of possibly multivalued conjugate surface  $f^*: \tilde{M} \rightarrow \mathbb{R}^3$ .

**Theorem 3.2.15.** *Let  $f: M \rightarrow \mathbb{R}^3$  be a minimal surface and  $\Phi: \tilde{M} \rightarrow \mathbb{C}^3$  its holomorphic null curve. Let  $f^*: \tilde{M} \rightarrow \mathbb{R}^3$  be the conjugate surface of  $f$ . Then for any end at  $p_j$  of  $M$  either  $f^*$  is defined on  $M$  near  $p_j$ , or  $f^*$  has translational period  $\tau_j^* = 2\pi \operatorname{Res}(\Phi', p_j)$ .*

*Proof.* If  $p_j$  is a pole of holomorphic function  $\Phi: \tilde{M} \rightarrow \mathbb{C}^3$  then the integral of  $\Phi'$  of curve  $\lambda$  around  $p_j$  is given by

$$\oint_{\lambda} \Phi'(z) dz = 2\pi i \operatorname{Res}(\Phi', p_j).$$

If  $f$  is single valued on  $M$  then  $\oint_{\lambda} \Phi'(z) dz$  is an imaginary number so  $\oint_{\lambda} \Phi'(z) dz = ai$  where  $a \in \mathbb{R}^3$ . Therefore either  $a = 0$  in which case  $f^*$  is defined on  $M$  near  $p_j$ , or the translational period of  $f^*$  is given by  $2\pi \operatorname{Res}(\Phi', p_j)$ .  $\square$

The introduction of the conjugate surface allows us to formulate the reflection principle for minimal surfaces. It will be used in our construction of the  $k$ -noid and its conjugate surface. It is a consequence of the Schwarz reflection principle for holomorphic maps outlined in the previous section.

**Lemma 3.2.16.** *Suppose that  $f: M \rightarrow \mathbb{R}^3$  is a minimal surface and  $f^*: \tilde{M} \rightarrow \mathbb{R}^3$  is its conjugate surface, then the planar geodesics on  $f$  correspond to straight lines on  $f^*$ . Moreover, the straight line is perpendicular to the plane containing the geodesic.*

*Proof.* To show this consider the shape operator  $W_p^*$  of the conjugate surface, and note that due to the Cauchy-Riemann relations of  $\Phi = f + if^*$  we have that  $df(X) = f_x dx(X) + f_y dy(X) = f_y^* dx(X) - f_x^* dy(X) = -df^*(JX)$ , hence  $df^*(X) = -df(JX)$ . Therefore, since  $df_p(W_p(X)) = -dN_p(X)$  and  $f^*$  has the same Gauss map as  $f$  we have that  $W_p^* = JW_p$ .

To show that planar geodesics on the surface correspond to straight lines on the conjugate we must consider the curvature  $\kappa$  and torsion  $\tau$  of a curve on the surface. We can assume that  $\lambda = f(\tilde{\lambda})$  is a unit speed curve, where  $\tilde{\lambda}$  is a curve on  $M$ . We denote by  $g$  the induced metric of  $f$  on  $M$ . For a unit speed space curve, curvature and torsion are given by,

$$\kappa = \langle n, t' \rangle \quad \tau = \langle -n, (t \times n)' \rangle,$$

where  $n$  is the normal to the curve and  $t$  is the tangent (this is known as the Frenet frame). In the case of a geodesic we have that  $\langle \lambda'', (N \circ \tilde{\lambda}) \times \lambda' \rangle = \langle (N \circ \tilde{\lambda}), \lambda' \times \lambda'' \rangle = 0$ . Since the binormal to  $\lambda$  is given by  $\frac{\lambda' \times \lambda''}{\|\lambda' \times \lambda''\|}$  we see that for a geodesic the normal  $n$  is equal to the normal  $\pm N$  to the surface (up to change of sign). Since  $t$  is also tangent to the surface, that is  $\langle t, N \circ \tilde{\lambda} \rangle = 0$ , we see that  $\langle N \circ \tilde{\lambda}, t' \rangle = -\langle (N \circ \tilde{\lambda})', t \rangle$ . Therefore

$$\kappa = \pm \langle N \circ \tilde{\lambda}, t' \rangle = \mp \langle (N \circ \tilde{\lambda})', t \rangle = \mp \langle df(W_p(\tilde{\lambda}')), df(\tilde{\lambda}') \rangle = \mp g_p(W_p(\tilde{\lambda}'), \tilde{\lambda}'),$$

and

$$\tau = \pm \langle (N \circ \tilde{\lambda})', (t \times N) \rangle = \mp \langle df(W_p(\tilde{\lambda}')), df(J\tilde{\lambda}') \rangle = \mp g_p(W_p(\tilde{\lambda}'), J\tilde{\lambda}').$$

Here we used that in the case of a conformal map we have  $df(JX) = N \times df(X)$  for  $X \in TM$  and thus  $(t \times N) = -(N \times t) = -df(J\tilde{\lambda}')$ . It is also known that for a curve having  $\kappa = 0$  implies the curve is a straight line and  $\tau = 0$  implies the curve is a planar curve, where the plane is perpendicular to the binormal. As we have that  $W_p^* = JW_p$  we see that

$$\kappa = \mp g_p(W_p(\tilde{\lambda}'), \tilde{\lambda}') = \mp g_p(JW_p(\tilde{\lambda}'), J\tilde{\lambda}') = \mp g_p(W_p^*(\tilde{\lambda}'), J\tilde{\lambda}') = \mp \tau^*,$$

and

$$\tau = \mp g_p(W_p(\tilde{\lambda}'), J\tilde{\lambda}') = \pm g_p(JW_p(\tilde{\lambda}'), \tilde{\lambda}') = \pm g_p(W_p^*(\tilde{\lambda}'), \tilde{\lambda}') = \pm \kappa^*.$$

Therefore in the case of a minimal surface  $f$ , if a curve  $\lambda$  on  $f$  has vanishing torsion the corresponding curve  $\lambda^*$  on the conjugate  $f^*$  must have vanishing curvature and vice versa. Hence planar geodesics on minimal surface  $f$  correspond to straight lines on the conjugate. We also wish to show that the straight line  $\lambda^*$  is perpendicular to the plane containing the planar geodesic  $\lambda$ . It is known that a curve with torsion zero lies in the plane perpendicular to the binormal [86], thus we need to show that the tangent  $t^*$  to  $\lambda^*$  is essentially the binormal to  $\lambda$ . Consider the binormal  $b = t \times n$  to the planar geodesic,

$$b = t \times (\pm(N \circ \tilde{\lambda})) = \mp df(J\tilde{\lambda}') = \pm df^*(\tilde{\lambda}') = \pm t^*.$$

□

**Theorem 3.2.17.** *Suppose a minimal surface  $f : M \rightarrow \mathbb{R}^3$  contains a straight line or a planar geodesic. Then the surface can be rotated  $180^\circ$  around the line, or reflected in the plane containing the geodesic continuing the minimal surface.*

*Proof.* Without loss of generality it may be assumed that the geodesic  $\lambda$  lies in the  $x - y$  plane and  $\lambda = f \circ \tilde{\lambda}$ . Then  $f^* \circ \tilde{\lambda}$  is a straight line in the  $z$  axis. Consider the image of  $\tilde{\lambda}$  under the holomorphic null curve  $\Phi$ ,

$$\Phi \circ \tilde{\lambda} = \begin{pmatrix} f_1 \circ \tilde{\lambda} + i(f_1^* \circ \tilde{\lambda}) \\ f_2 \circ \tilde{\lambda} + i(f_2^* \circ \tilde{\lambda}) \\ f_3 \circ \tilde{\lambda} + i(f_3^* \circ \tilde{\lambda}) \end{pmatrix} = \begin{pmatrix} f_1 \circ \tilde{\lambda} \\ f_2 \circ \tilde{\lambda} \\ i(f_3^* \circ \tilde{\lambda}) \end{pmatrix}$$

We may assume that  $\Phi_3$  is the conformal coordinate on  $M$  as it is a holomorphic on  $M$  and therefore  $\tilde{\lambda}$  is a segment of the imaginary axis. Therefore, the standard reflection principle can be applied. The Schwarz reflection principle allows us to extend  $\Phi_1$  and  $\Phi_2$  by reflection across the real axis and  $\Phi_3$  across the imaginary axis, that is, there is an extension of  $\Phi(z)$  given by  $\tilde{\Phi}(z^*)$

$$\tilde{\Phi}(z^*) = \begin{pmatrix} \overline{\Phi_1(z)} \\ \overline{\Phi_2(z)} \\ -\overline{\Phi_3(z)} \end{pmatrix} = \begin{pmatrix} f_1(z) - if_1^*(z) \\ f_2(z) - if_2^*(z) \\ -f_3(z) + if_3^*(z) \end{pmatrix},$$

which is a reflection of  $f$  in the  $x - y$  plane and a  $180^\circ$  rotation of  $f^*$  around the  $z$  axis.

□

There are several transformations that can be applied to a holomorphic null curve to create new minimal surfaces. The most simple of these is the one parameter deformation known as the associate family.

**Theorem 3.2.18.** *Let  $\Phi: \tilde{M} \rightarrow \mathbb{C}^3$  be a holomorphic null curve, then the function  $\Phi_\theta: \tilde{M} \rightarrow \mathbb{C}^3$  with  $\Phi_\theta = e^{i\theta}\Phi$  where  $\theta \in [0, 2\pi]$ , is also a holomorphic null curve. Hence  $f_\theta = \text{Re}(\Phi_\theta)$  is also a minimal surface.*

*Proof.* As  $e^{i\theta}$  is a complex constant, it is clear that  $\Phi_\theta$  will also be holomorphic. To check the null condition is also straightforward, consider,

$$\langle \Phi'_\theta, \Phi'_\theta \rangle = \langle e^{i\theta}\Phi', e^{i\theta}\Phi' \rangle = e^{2i\theta}\langle \Phi', \Phi' \rangle = 0.$$

To check the immersion condition is also straightforward,

$$|\Phi'_{1\theta}|^2 + |\Phi'_{2\theta}|^2 + |\Phi'_{3\theta}|^2 = |e^{i\theta}\Phi'_1|^2 + |e^{i\theta}\Phi'_2|^2 + |e^{i\theta}\Phi'_3|^2 = |\Phi'_1|^2 + |\Phi'_2|^2 + |\Phi'_3|^2,$$

showing that  $\Phi_\theta$  is a holomorphic null curve. □

In the case of  $\theta = \frac{\pi}{2}$  then  $f_\theta$  is the conjugate surface  $f^*$ . It can be useful computationally to express the associate family as a linear combination of  $f$  and  $f^*$ ,  $f_\theta = \cos(\theta)f + \sin(\theta)f^*$ . In terms of the Weierstrass data the associate family can be thought of as the transformation  $(g, \omega) \rightarrow (g, e^{i\theta}\omega)$ .

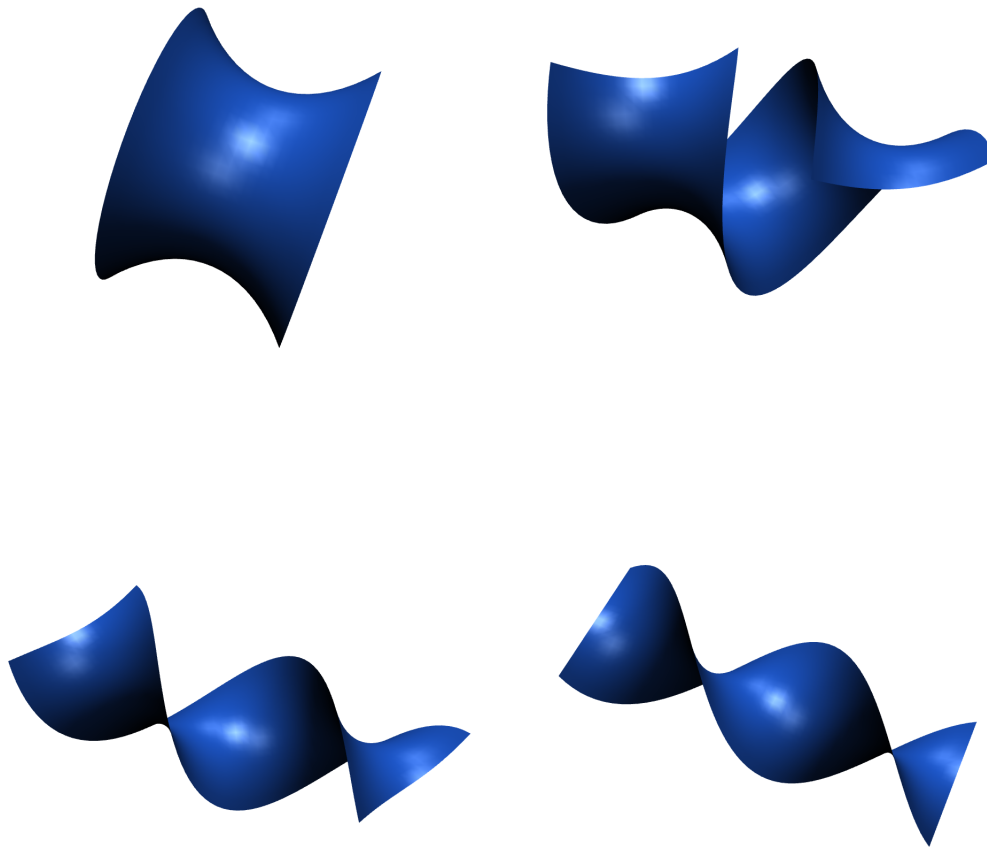


Figure 3.5: The catenoid (top left) and the associate family for  $\theta = \frac{\pi}{6}$  (top right),  $\theta = \frac{\pi}{3}$  (bottom left), and  $f^*$  (the helicoid) (bottom right).

The associate family has the property that the Gaussian curvature  $K$  is preserved across it.

**Theorem 3.2.19.** *The Gaussian curvature  $K$  is preserved throughout the associate family.*

*Proof.* With the Theorem Egregium it is sufficient to show that all immersions of the associate family are local isometries. Consider the first fundamental form of  $f$  in terms of the conformal

coordinate  $z = u + iv$ .

$$E = G = \langle f_u, f_u \rangle, F = 0$$

Consider the first coefficient of the first fundamental form  $E_\theta$  for the associate family and note that  $f_u^* = -f_v$  due to the Cauchy-Riemann relations.

$$\begin{aligned} E_\theta &= \langle f_u \cos(\theta) + f_u^* \sin(\theta), f_u \cos(\theta) + f_u^* \sin(\theta) \rangle \\ &= \langle f_u \cos(\theta) - f_v \sin(\theta), f_u \cos(\theta) - f_v \sin(\theta) \rangle \\ &= \cos^2(\theta) \langle f_u, f_u \rangle - 2 \cos(\theta) \sin(\theta) \langle f_u, f_v \rangle + \sin^2(\theta) \langle f_v, f_v \rangle \\ &= E \end{aligned}$$

A similar argument can be used to show that  $G_\theta = G$  and  $F_\theta = F$ , which shows that  $f_\theta$  is isometric to  $f$ . □

As well as the associate family there are several other ways to generate new holomorphic null curves from old. One such transformation is by the Lopez-Ros deformation originally described by Lopez and Ros in [14]. The authors used the deformation to show that the catenoid and plane are the only embedded complete minimal surfaces of genus zero and finite total curvature in  $\mathbb{R}^3$ .

**Theorem 3.2.20.** *Let  $\lambda$  be a positive real number and  $\Phi: \tilde{M} \rightarrow \mathbb{C}^3$  be a holomorphic null curve given by Weierstrass data  $(g, \omega)$ , generating a minimal immersion  $f: M \rightarrow \mathbb{C}^3$ , where  $f = \text{Re}(\Phi)$ . Then the Weierstrass data  $(\lambda g, \frac{1}{\lambda} \omega)$  generates a new holomorphic null curve  $\Phi_\lambda: \tilde{M} \rightarrow \mathbb{C}^3$ , and  $f_\lambda: \tilde{M} \rightarrow \mathbb{R}^3$  where  $f_\lambda = \text{Re}(\Phi_\lambda)$  is also a minimal surface.*

*Proof.* The Weierstrass data  $(\lambda g, \frac{1}{\lambda} \omega)$  will preserve the poles, holomorphicity and meromorphicity of  $g$  and  $\omega$  as  $\lambda$  is a non-zero real number. Therefore the Weierstrass data  $(\lambda g, \frac{1}{\lambda} \omega)$  can be

used to generate a new holomorphic null curve,  $\Phi_\lambda$ . □

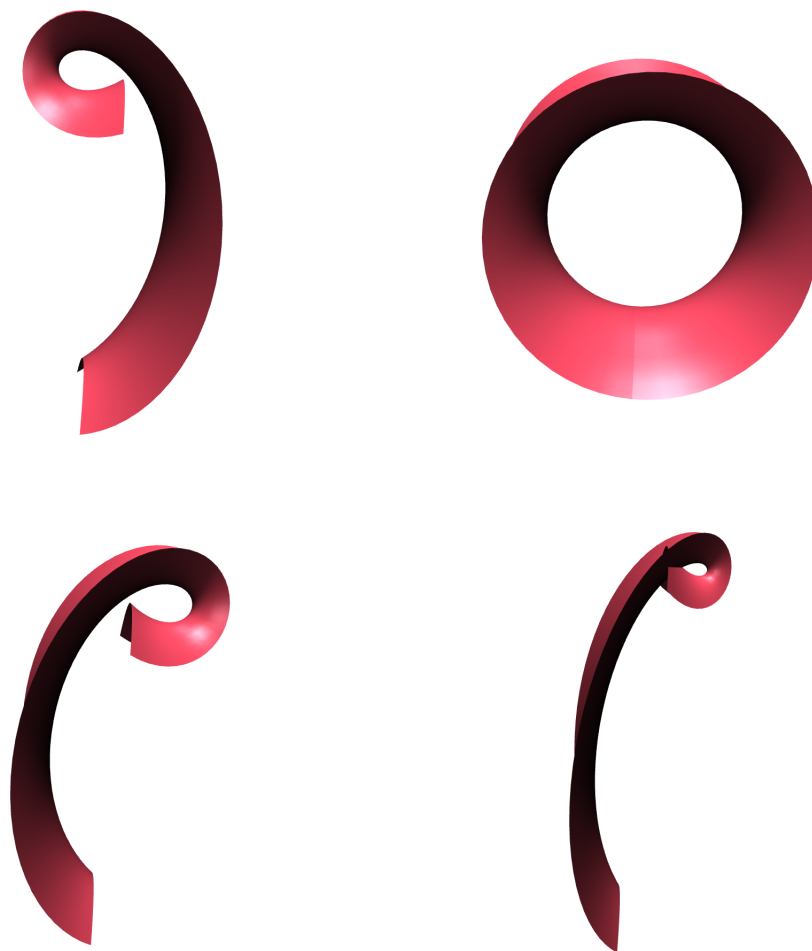


Figure 3.6: The Lopez-Ros deformation of the catenoid for  $\lambda = \frac{1}{2}$  (top left),  $\lambda = 1$  (top right),  $\lambda = 2$  (bottom left) and  $\lambda = 3$  (bottom right).

The Lopez-Ros deformation can be expressed in a much simpler form using matrix multiplication, this was shown in [15], the authors also show that the Lopez-Ros deformation is part of the larger class of simple factor dressings which are discussed in the next section.

**Theorem 3.2.21.** *If  $\lambda = e^s \in \mathbb{R}_+$ , and  $s \in \mathbb{R}$ , then the Lopez-Ros deformation with parameter  $\lambda$*

of holomorphic null curve  $\Phi: \tilde{M} \rightarrow \mathbb{C}^3$  is given by,  $\Phi_\lambda = A\Phi$ , where,

$$A = \begin{pmatrix} \cosh(s) & i \sinh(s) & 0 \\ -i \sinh(s) & \cosh(s) & 0 \\ 0 & 0 & 1 \end{pmatrix}.$$

Therefore  $f_\lambda: \tilde{M} \rightarrow \mathbb{R}^3$  with  $f_\lambda = \operatorname{Re}(A\Phi) = \begin{pmatrix} \cosh(s)f_1 - \sinh(s)f_2^* \\ \cosh(s)f_2 + \sinh(s)f_1^* \\ \tilde{f}_3 \end{pmatrix}$  is a minimal surface.

*Proof.* Consider  $\Phi_\lambda = A\Phi'$ , then

$$\Phi'_\lambda = A\Phi' = \begin{pmatrix} \cosh(s)\Phi'_1 + i \sinh(s)\Phi'_2 \\ \cosh(s)\Phi'_2 - i \sinh(s)\Phi'_1 \\ \Phi'_3 \end{pmatrix}$$

Recall that the Weierstrass data is given by (10). Therefore the Weierstrass data  $(g_\lambda, \omega_\lambda)$  for  $A\Phi'$  can be calculated,

$$\begin{aligned} \omega_\lambda &= (\Phi_\lambda)'_1 - i(\Phi_\lambda)'_2 \\ &= \Phi'_1(\cosh(s) - \sinh(s)) + i\Phi'_2(\sinh(s) - \cosh(s)) \\ &= \frac{1}{\lambda}(\Phi'_1 - i\Phi'_2) \\ &= \frac{1}{\lambda}\omega. \end{aligned}$$

For  $g_\lambda$  we compute that,

$$g_\lambda = \frac{(\Phi_\lambda)'_3}{\omega_\lambda} = \frac{\Phi'_3}{\frac{1}{\lambda}(\Phi'_1 - i\Phi'_2)} = \lambda g,$$

thus we obtain the Weierstrass data of the Lopez-Ros deformation.

□

This shows that the Lopez-Ros deformation is part of the much larger class of Goursat deformations.

**Theorem 3.2.22.** *Let  $\Phi: M \rightarrow \mathbb{C}^3$  be a holomorphic null curve and  $A \in O(3, \mathbb{C})$ . Then  $\Phi_A = A\Phi$  is also a holomorphic null curve and therefore  $Re(\Phi_A)$  generates a minimal surface.*

The matrix representation of the Lopez-Ros deformation can be used to show that it is an example of the more general simple factor dressing.

### 3.3 The simple factor dressing

So far we have focused on transforming holomorphic null curves to create new minimal surfaces. Aside from this certain harmonic maps associated to the minimal immersion can also be transformed to give new harmonic maps and therefore new minimal immersions. It can be shown that in some cases these transformations are Goursat deformations and therefore can be given a matrix representation.

From this point onwards it will be convenient to express minimal immersions as quaternions. This allows for straightforward computations of rotations. Therefore we will briefly recap some elementary results concerning quaternions.

### 3.3.1 Quaternions

The quaternions are a 4-dimensional extension of the complex numbers. We define them as follows.

**Definition 3.3.1.** *The space of quaternions  $\mathbb{H}$  is defined as  $\mathbb{H} = \text{span}(1, \mathbf{i}, \mathbf{j}, \mathbf{k})$  where:*

$$\mathbf{i}^2 = \mathbf{j}^2 = \mathbf{k}^2 = -1, \mathbf{i}\mathbf{j} = \mathbf{k}, \mathbf{j}\mathbf{i} = -\mathbf{k}.$$

*The space of imaginary quaternions is defined as  $\text{Im}(\mathbb{H}) = \text{span}(\mathbf{i}, \mathbf{j}, \mathbf{k}) = \mathbb{R}^3$ .*

As the space of imaginary quaternions can be identified with  $\mathbb{R}^3$  the immersion generating minimal surface  $f: M \rightarrow \mathbb{R}^3$  can be identified with the immersion  $f = f_1\mathbf{i} + f_2\mathbf{j} + f_3\mathbf{k}$ . There are several advantages to using this identification. One of these is that a rotation can be expressed in terms of quaternions using the following theorem, taken from [94].

**Theorem 3.3.2.** *Let  $p \in \text{Im} \mathbb{H}$  and  $q = \cos(\theta) + q_1 \sin(\theta) \in \mathbb{H}$  where  $q_1 \in \text{Im} \mathbb{H}$ . The operator  $R_q(v) = qpq^{-1}$  is a rotation of  $2\theta$  through the imaginary part of  $q$ .*

To prove this theorem the identity that for two imaginary quaternions  $a, b \in \text{Im} \mathbb{H}$  the quaternionic product  $ab$  may be written as  $ab = -\langle a, b \rangle + a \times b$ , this formula will later be relevant for our computation of the simple factor dressing. It is also worth noting that if  $|q| = 1$  then  $q^{-1} = \bar{q}$ . The theorem can also be extended for rotations in  $\mathbb{R}^4$ . That is if  $p \in \mathbb{H}$  represents a point in  $\mathbb{R}^4$  and  $m$  and  $n$  are quaternions the operator  $R_{m,n}(p) = n p m^{-1}$  represents a rotation in  $\mathbb{R}^4$ .

### 3.3.2 Willmore surfaces

To apply the simple factor dressing to a minimal surface we will consider minimal surfaces as examples of the more general Willmore surfaces.

**Definition 3.3.3.** *An immersion  $f: M \rightarrow \mathbb{R}^3$  is said to be a Willmore surface if it is a critical point of the Willmore energy*

$$\mathcal{W}(f) = \int_M (H^2 - K) dA.$$

The harmonic map which we apply the simple factor dressing to is the conformal Gauss map, we will use the result that in the case of a Willmore surface it is harmonic [95].

**Definition 3.3.4.** *For a surface in  $\mathbb{R}^3$  the conformal Gauss map  $S: \mathbb{H}^2 \rightarrow \mathbb{H}^2$  is given by,*

$$S = G \begin{pmatrix} N & 0 \\ H & -N \end{pmatrix} G^{-1},$$

where  $G = \begin{pmatrix} 1 & f \\ 0 & 1 \end{pmatrix}$ .

In the case of a minimal immersion the conformal Gauss map can be expressed in terms of the support function  $u = \langle N, f \rangle$ .

**Example 3.3.1.** Let  $f: M \rightarrow \mathbb{R}^3$  be a minimal immersion then the conformal Gauss map of  $f$ ,  $S$  is given by

$$S = \begin{pmatrix} N & 2u \\ 0 & -N \end{pmatrix}.$$

This follows, since for  $H = 0$  we have that

$$S = G \begin{pmatrix} N & 0 \\ 0 & -N \end{pmatrix} G^{-1} = \begin{pmatrix} N & -Nf - fN \\ 0 & -N \end{pmatrix},$$

however  $f$  and  $N$  are both imaginary quaternions so  $-Nf - fN = 2\langle N, f \rangle$ .

The following theorems characterize Willmore surfaces in terms of a condition on the conformal Gauss map, see [96], [95].

**Theorem 3.3.5.** *If  $f: M \rightarrow \mathbb{R}^3$  is a Willmore surface then its conformal Gauss map  $S$  is harmonic, that is if and only if*

$$d * A = 0,$$

where  $A$  the Hopf field of  $f$  given by  $4 * A = G \begin{pmatrix} 0 & 0 \\ \omega & 2(dN)'' \end{pmatrix} G^{-1}$ , with  $\omega = -dH - N * dH + H * (dN)''$  and  $d$  is the trivial connection.

Here,  $*$  is the negative Hodge star operator, that is if  $\delta$  is a one-form on the tangent bundle  $TM$  of a complex manifold  $M$ , then for  $X \in TM$  we have  $*\delta(X) = \delta(JX)$ .

**Theorem 3.3.6.** *If a conformal immersion  $f: M \rightarrow \mathbb{R}^3$  is minimal then it is Willmore.*

*Proof.* To prove this result we will show that in the case of  $f$  being a minimal conformal immersion we have that  $(dN)' = \frac{1}{2}(dN - N * dN) = 0$ . Firstly note that  $d * df = d(-f_x dy + f_y dx) = -\Delta f dx \wedge dy$  and then for a conformal coordinate  $x = x + iy$ ,

$$dN \wedge df = d * df = -\Delta f dx \wedge dy = 0.$$

On the one hand

$$dN \wedge df = dN * df - *dNdf = dN * df + *dNN * df = (dN - N * dN) * df = (dN)' * df,$$

so therefore  $(dN)'' = dN$ . Thus, the Hopf field  $*A$  has, since  $H = 0$ , the explicit form,

$$2d * A = \frac{1}{2}G \begin{pmatrix} 0 & 0 \\ 0 & 2(dN)'' \end{pmatrix} G^{-1} = \begin{pmatrix} 0 & f \\ 0 & 1 \end{pmatrix} dN.$$

Thus,

$$2d * A = d \left( \begin{pmatrix} 0 & f \\ 0 & 1 \end{pmatrix} dN \right) = \begin{pmatrix} 0 & df \\ 0 & 0 \end{pmatrix} \wedge dN = 0.$$

□

The above theorem shows that minimal surfaces have a harmonic conformal Gauss map. The following theorem allows us to generate a family of flat connections for any Willmore surface.

**Theorem 3.3.7.** *If  $f: M \rightarrow \mathbb{R}^3$  is a Willmore surface then the connection*

$$d_\mu = d + (\mu - 1)A^{1,0} + (\mu^{-1} - 1)A^{0,1}$$

*is flat for all  $\mu \in \mathbb{C}^* = \mathbb{C} \setminus \{0\}$ , where*

$$A^{1,0} = \frac{1}{2}(A - I * A) \quad A^{0,1} = \frac{1}{2}(A + I * A),$$

*and  $I$  indicates right multiplication by the unit quaternion  $\mathbf{i}$ .*

The Willmore surface can be recovered from its family of flat connections  $d_\mu$ . In particular if one can construct new families of flat connections with the same symmetries and reality conditions as  $d_\mu$ , then one can construct new Willmore surfaces. For many of these constructions one needs to find parallel sections of  $d_\mu$ . In the case of a minimal surface parallel sections  $\varphi$  of the flat connection  $d_\mu$  can be written in the form,

$$\varphi = \begin{pmatrix} 1 \\ 0 \end{pmatrix} \alpha + \begin{pmatrix} f \\ 1 \end{pmatrix} \beta,$$

where  $\alpha = -f^* - fm \frac{i(1+\mu)}{1-\mu}$  and  $\beta = Nm + m \frac{i(1+\mu)}{1-\mu}$  with  $\mu \in \mathbb{C}^*$  and  $m \in \mathbb{H}$ .

### 3.3.3 The simple factor dressing

The theory described in the previous subsection shows that new minimal surfaces may be generated by applying a dressing to the associated family of flat connections (if the minimal surface is thought of as a Willmore surface). In general the dressing of a Willmore surface is not straightforward to express, however for a simple factor dressing, that is a gauge of  $d_\lambda$  by a  $\lambda$  dependant matrix with simple pole, of a minimal surface the simple factor dressing  $\hat{f}$  of  $f$  may be expressed relatively simply.

So far this chapter has focussed on minimal immersions  $f: M \rightarrow \mathbb{R}^3$ , however it is also possible to define a minimal immersion  $f: M \rightarrow \mathbb{R}^4$ . In short if  $\phi: \tilde{M} \rightarrow \mathbb{C}^4$  is a holomorphic null curve then  $\text{Re}(\phi)$  can be thought of as a minimal immersion  $f: \tilde{M} \rightarrow \mathbb{R}^4$ . As we can identify the space of quaternions  $\mathbb{H}$  with  $\mathbb{R}^4$  in general the simple factor dressing of minimal immersion  $f: M \rightarrow \mathbb{R}^3$  will generate a minimal immersion  $\hat{f}: \tilde{M} \rightarrow \mathbb{R}^4$ . This is shown by the following expression for the simple factor dressing [15].

**Theorem 3.3.8.** *In the case of a minimal surface  $f: M \rightarrow \mathbb{R}^3$  with conjugate surface  $f^*: \tilde{M} \rightarrow \mathbb{R}^3$  the simple factor dressing of  $f$  is given by  $\hat{f}: \tilde{M} \rightarrow \mathbb{R}^4$  where*

$$\hat{f} = -f \frac{m(a-1)m^{-1}}{2} + f^* \frac{mbm^{-1}}{2} - n \frac{b}{a-1} n^{-1} \left( f \frac{mbm^{-1}}{2} + f^* \frac{m(a-1)m^{-1}}{2} \right),$$

where  $m, n \in \mathbb{H}$ ,  $a = \frac{\mu + \mu^{-1}}{2}$ ,  $b = i \frac{\mu^{-1} - \mu}{2}$  and  $\mu \in \mathbb{C} \setminus \{0, 1\}$ .

It is straightforward to show that if  $m = n$  then the simple factor dressing will generate a minimal immersion  $\hat{f}: \tilde{M} \rightarrow \mathbb{R}^3$  as if  $\hat{f}$  is considered as an imaginary quaternion then its real part is zero.

In the case of  $n = m = 1$  we refer to this as the *simple factor dressing with parameter  $\mu$* , we write the simple factor dressing with parameter  $\mu$  as  $f^\mu$ . Computationally it is convenient to express the simple factor dressing as a rotation of the simple factor dressing with parameter  $\mu$ .

**Theorem 3.3.9.** *The simple factor dressing with parameters  $(\mu, m, n)$ ,  $\hat{f}$  can be expressed as*

$$\hat{f} = R_{n,m}((R_{n,m}^{-1}(f))^\mu) = n((n^{-1}fm)^\mu)m^{-1}.$$

In [15] the authors also show that the simple factor dressing with parameter  $\mu$  can be expressed as a Goursat deformation.

**Theorem 3.3.10.** *Let  $\phi: \tilde{M} \rightarrow \mathbb{C}^3$  be a holomorphic null curve and  $f: M \rightarrow \mathbb{R}^3$  be a minimal immersion where  $f = \text{Re}(\phi)$ , then the function  $\phi^\mu: \tilde{M} \rightarrow \mathbb{C}^3$  with  $\phi^\mu = A\phi$  where*

$$A = \begin{pmatrix} 1 & 0 & 0 \\ 0 & \cosh(w) & i \sinh(w) \\ 0 & -i \sinh(w) & \cosh(w) \end{pmatrix}$$

with  $w \in \mathbb{C}$ , is also a holomorphic null curve. Hence  $f^\mu: \tilde{M} \rightarrow \mathbb{R}^3$  where  $f^\mu = \operatorname{Re}(\phi^\mu)$  is the simple factor dressing with parameter  $\mu$  and is also a minimal surface.

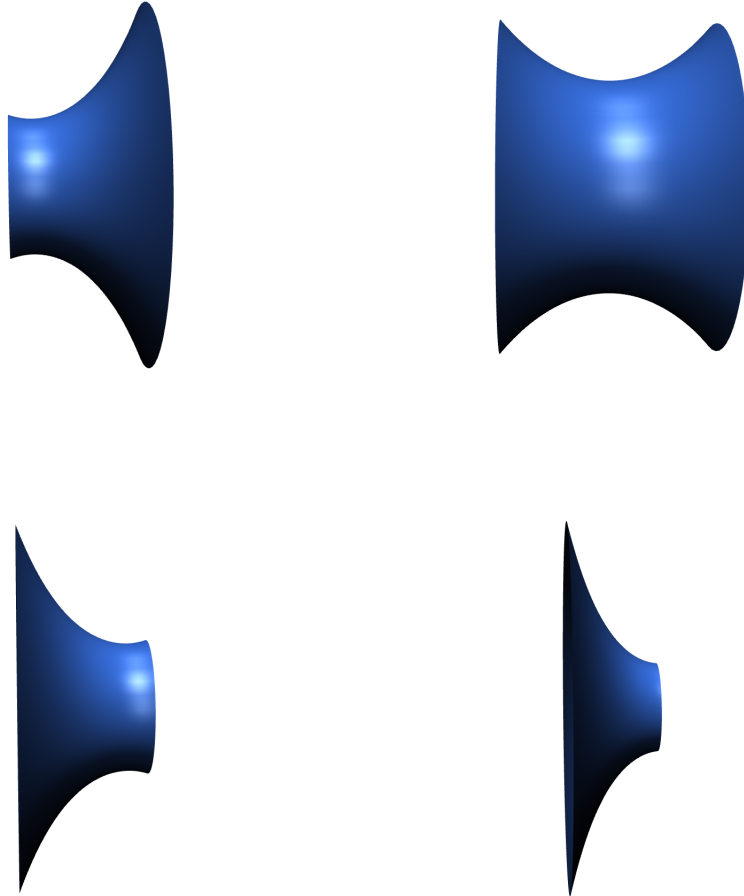


Figure 3.7: The simple factor dressing with parameter  $\mu$  for the catenoid and values of  $\mu = \frac{1}{2}$ ,  $\mu = 1$  top right,  $\mu = 2$  bottom left and  $\mu = 3$  top right.

It is a straightforward computation to see that the simple factor dressing with parameter  $\mu$  is a Goursat deformation.

**Theorem 3.3.11.** *The simple factor dressing with parameter  $\mu$  is a Goursat deformation.*

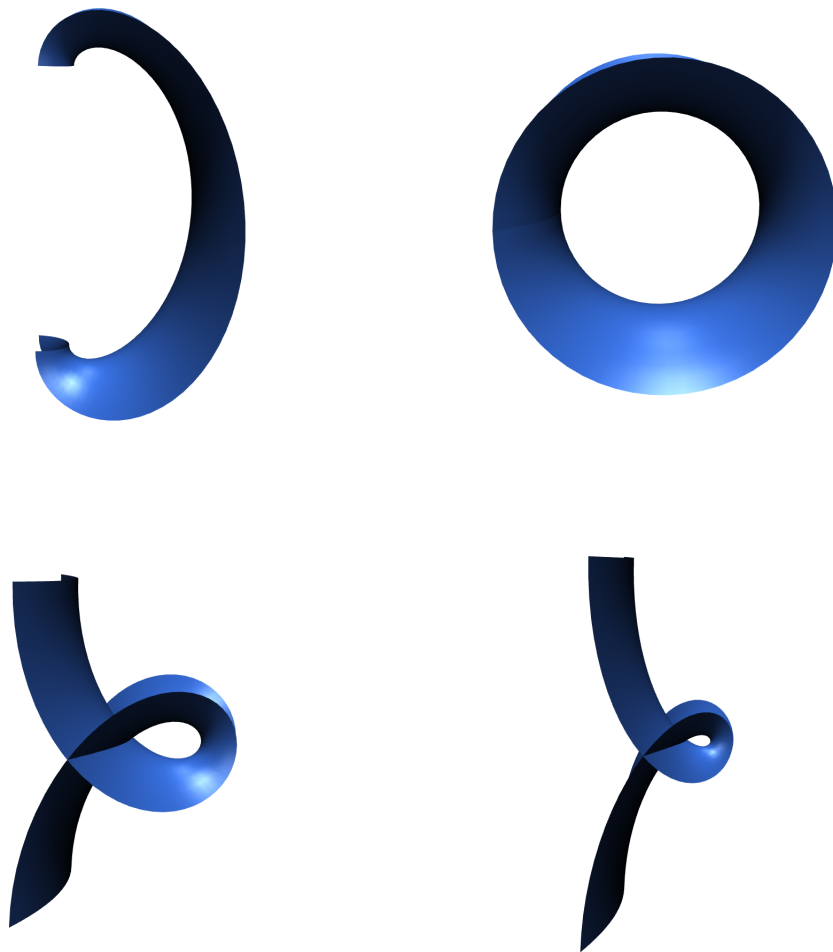


Figure 3.8: The simple factor dressing with  $m = n = 1 + \mathbf{k}$  for the catenoid and values of  $\mu = \frac{1}{2}$ ,  $\mu = 1$  top right,  $\mu = 2$  bottom left and  $\mu = 3$  top right.

*Proof.* As the simple factor dressing with parameter  $\mu$  can be thought of as a matrix transformation all that we need to show is that  $A \in O(3)$ , that is  $AA^T = 1$ . Consider

$$AA^T = \begin{pmatrix} 1 & 0 & 0 \\ 0 & \cosh(w) & i \sinh(w) \\ 0 & -i \sinh(w) & \cosh(w) \end{pmatrix} \begin{pmatrix} 1 & 0 & 0 \\ 0 & \cosh(w) & -i \sinh(w) \\ 0 & i \sinh(w) & \cosh(w) \end{pmatrix} = \begin{pmatrix} 1 & 0 & 0 \\ 0 & 1 & 0 \\ 0 & 0 & 1 \end{pmatrix}.$$

□

As  $R_{n,m}$  and  $R_{n,m}^{-1}$  are also complex orthogonal matrices it is clear that the simple factor dressing is a Goursat deformation.

The following theorem allows us to easily compute the translational period  $\hat{\tau}$  of the simple factor dressing of a minimal surface.

**Theorem 3.3.12.** *If  $f: M \rightarrow \mathbb{R}^3$  is a periodic minimal surface with translational period  $\tau$  then the simple factor dressing  $f^\mu: \tilde{M} \rightarrow \mathbb{R}^3$  with parameter  $\mu$  is periodic with translational period  $\tau^\mu$  where,*

$$\tau^\mu = \begin{pmatrix} \tau_1 \\ \cos(t)(\tau_2 \cosh(s)\tau_3^* \sinh(s)) - \sin(t)(\tau_3 \cosh(s) + \tau_2^* \sinh(s)) \\ \sin(t)(\tau_2 \cosh(s)\tau_3^* \sinh(s)) + \cos(t)(\tau_3 \cosh(s) + \tau_2^* \sinh(s)) \end{pmatrix}.$$

Here  $\tau^* = \begin{pmatrix} \tau_1^* \\ \tau_2^* \\ \tau_3^* \end{pmatrix}$  denotes the translational period of the conjugate surface.

It can also be shown that the Lopez-Ros deformation is an example of a simple factor dressing.

**Theorem 3.3.13.** *The simple factor dressing with  $m = n = \frac{1-i-j-k}{2}$  is the Lopez-Ros deformation.*

*Proof.* Firstly note that for the quaternions  $m = \frac{1-i-j-k}{2} \in \mathbb{H}$  and  $f = f_1\mathbf{i} + f_2\mathbf{j} + f_3\mathbf{k} \in \text{Im } \mathbb{H}$  the operators  $mfm^{-1}$  and  $m^{-1}fm$  are given as follows,

$$mfm^{-1} = f_2\mathbf{i} + f_3\mathbf{j} + f_1\mathbf{k}, \quad m^{-1}fm = f_3\mathbf{i} + f_1\mathbf{j} + f_2\mathbf{k}.$$

Therefore the simple factor dressing is given by,

$$\begin{aligned} m((m^{-1}fm)^\mu)m^{-1} &= m((f_3\mathbf{i} + f_1\mathbf{j} + f_2\mathbf{k})^\mu)m^{-1} \\ &= m(f_3\mathbf{i} + (\cosh(w)f_1 - \sinh(w)f_2^*)\mathbf{j} + (\sinh(w)f_1^* + \cosh(w)f_2)\mathbf{k})m^{-1} \\ &= (\cosh(w)f_1 - \sinh(w)f_2^*)\mathbf{i} + (\sinh(w)f_1^* + \cosh(w)f_2)\mathbf{j} + f_3\mathbf{k}. \end{aligned}$$

By theorem 3.2.21 this is the Lopez-Ros deformation. □

In the case of  $m \neq n$  the simple factor dressing gives a minimal immersion  $\hat{f}: \tilde{M} \rightarrow \mathbb{R}^4$ . As the simple factor dressing with parameter  $\mu$  may be represented as a matrix transformation similar to that shown in theorem 3.3.10 with

$$A = \begin{pmatrix} 1 & 0 & 0 & 0 \\ 0 & 1 & 0 & 0 \\ 0 & 0 & \cosh(w) & i \sinh(w) \\ 0 & 0 & -i \sinh(w) & \cosh(w) \end{pmatrix},$$

the simple factor dressing of a minimal surfaces in  $\mathbb{R}^4$  is straightforward to compute in terms of

quaternions via a rotation operator.

# **Chapter Four - Experimental and computational methods**

## 4 Experimental and computational methods

In this chapter the experimental methods used to monitor the morphological changes of liposomes is described. The apparatus was previously used to study the binary coalescence of aerosol droplets. Firstly, a description for the components of the optical tweezing set-up used at the University of Leicester is given. The optical tweezers have been integrated with a range of spectroscopic techniques, which is also described in this chapter.

The theory of dynamic light scattering is discussed. This technique has allowed us to measure the effect of temperature induced phase transitions on the average diameter of liposomes. A short description of the protocol used to make a large unilamellar (LUV) sample of liposomes in a bulk sample is also given.

Computational methods were also used to analyse Raman spectra obtained from optically trapped liposomes. Raman spectra could be split into multiple pure components using a multivariate analysis algorithm. The principles of this algorithm are outlined at the end of this chapter.

### 4.1 Introduction

The optical tweezing apparatus used in this work is a bespoke inverted microscope that enables spatial and temporal control of the trapping laser. The apparatus is configured for measurements of elastic light scattering, Raman scattering and fluorescence. The optical tweezing apparatus can be sub-divided into different functional components for optical manipulation.

A highly simplified illustration of optical tweezers is shown in figure 4.1. The path of the trapping laser is shown in red. Firstly a collimated laser is transmitted by a dichroic mirror onto a microscope objective. The laser beam must over-fill the back aperture of the microscope objec-

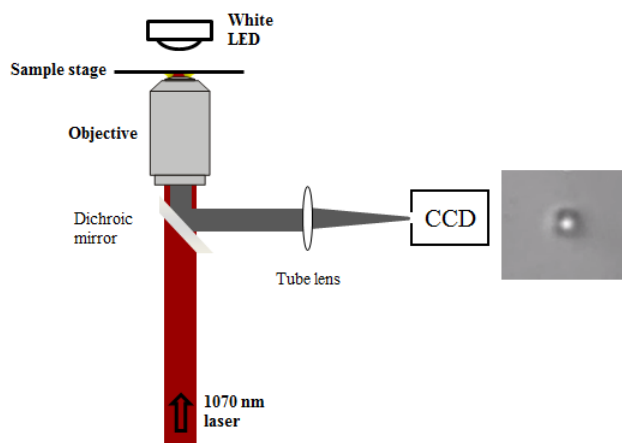


Figure 4.1: A simplified optical trap. The trapping lasers path is shown in red and the light from the LED is shown in grey, a dichroic mirror is allowing the trapping laser to pass but reflecting light from the LED to pass through to the CCD. A bright field image of an optically trapped particle taken on the CCD is also shown.

tive. The microscope objective focuses the beam to a tight waist, dependent on the objective's numerical aperture, creating the optical trap in the object plane of the microscope. The sample is illuminated from above by an LED. The light transmitted from the LED is reflected by the dichroic mirror onto a CCD for imaging of the optically trapped particle.

The addition of steering lenses and mirrors would allow the position of the trapping laser to be adjusted in 2 dimensions. The position of the trapping laser can be adjusted in 3 dimensions by use of a spatial light modulator (see below).

## 4.2 Detailed description of optical tweezing apparatus

This section gives a complete description of the optical tweezers and the spectroscopic apparatus used to make light scattering measurements on optically trapped microparticles. New exper-

imental data is reported later in this thesis that illustrates how the light scattering intensity is modulated during a temperature induced phase transition of a liposome. Earlier data recorded for the binary coalescence of aerosol droplets, using the same apparatus, was used to validate a theoretical model. Figure 4.2 is a schematic of the optical tweezing apparatus. The optical layout will be sub-divided into 4 components which will be described individually:

- (i) The optical tweezers utilizing a 1070 nm wavelength laser.
- (ii) The light scattering source utilizing a 488 nm wavelength laser.
- (iii) Bright field imaging and elastic light scattering measurement.
- (iv) Inelastic (Raman) light scattering spectrometer.

The optical tweezers apparatus is mounted on a optical table (Thorlabs) which rests on air springs to isolate the table from vibrations within the building. The optical elements in the system are attached to 30 mm cage mounts (ThorLabs), making it possible to precisely align the system.

In brief there are two lasers, at wavelengths of 488 nm (spectroscopy) and 1070 nm (trapping), overlapped in the sample plane. The lasers are both steered by a series of mirrors to the microscope objective where they are focussed to a narrow waist. Illumination from above the sample plane by an LED allows an image to be formed on a CCD. Elastic back scattered light from both the 488 nm and 1070 nm lasers can be recorded; however, Raman scattered light can only be recorded from the 488 nm laser as the spectrograph is insensitive to Raman scattering from the 1070 nm laser. For the elastic light scattering measurements, visible and near-infrared photodiodes can be used interchangeably. Each component will now be described in detail.



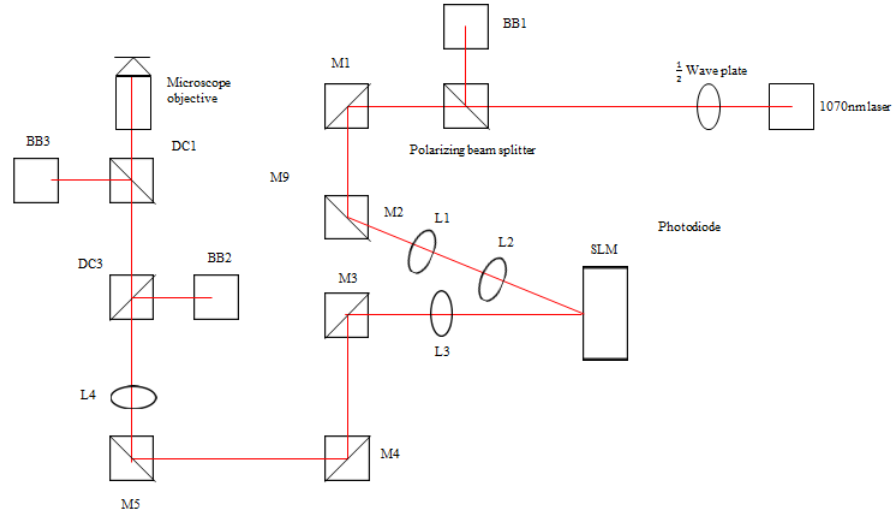


Figure 4.3: The path of the 1070 nm trapping laser, it is shown as a red line.

laser. The polarizing beam splitter used is Glen-Taylor polarizing beam splitter (Thorlabs), it reflects the vertically polarized light onto a beam block and transmits the horizontally polarized beam. Horizontally polarized light is required by the spatial light modulator.

The laser is then steered using mirrors M1 and M2 (all lenses and mirrors sourced from Thorlabs) onto a Keplerian telescope made up of two plano-convex lenses, L1 and L2 of focal lengths 5 cm and 15 cm respectively. Figure 4.4 shows a general Keplerian telescope made of two lenses labelled  $L_1$  with front focal distance  $f_1$ , and  $L_2$  with a back focal distance  $f_2$ . The telescope is configured so that the lenses are separated by a distance of  $f_1 + f_2$ . The telescope increases the beam diameter by a factor of  $\frac{f_2}{f_1}$  meaning that the diameter of the exit beam  $d_2$  is  $d_2 = d_1 \frac{f_2}{f_1}$  where  $d_1$  is the initial diameter of the beam. Thus, the lenses L1 and L2 are separated by a distance

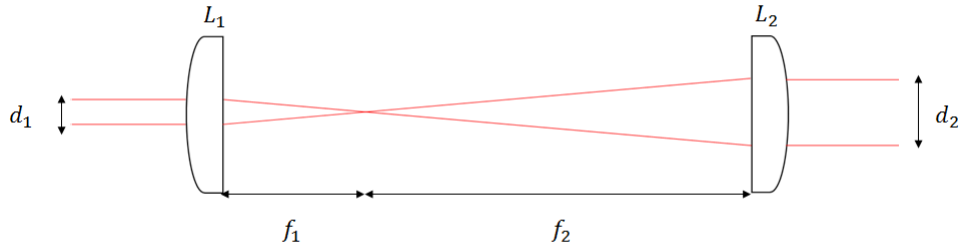


Figure 4.4: A general Keplerian telescope, the beam has initial diameter of  $d_1$ , lenses  $L_1$  and  $L_2$  have front and back focal planes at  $f_1$  and  $f_2$  respectively. This means that the emergent beams diameter  $d_2$  is given by  $d_2 = d_1 \frac{f_2}{f_1}$ . The lenses are separated by a length of  $f_1 + f_2$  so that their front and back focal planes coincide.

of 20 cm which results in a magnification factor of 3, creating a beam of diameter 21 mm. This beam diameter is matched to the screen of the spatial light modulator.

The spatial light modulator (SLM; Hamamatsu) imparts a phase-only pattern on the 1070 nm laser. The position of the optical tweezers can then be adjusted in three dimensions by changing the phase pattern. Different phase patterns can be used to create multiple optical traps which will be relevant to the work on the coalescence of aerosols presented in chapter 6. The SLM is an electrically addressed liquid crystal device consisting of a liquid crystal layer between a transparent electrode and a pixel arranged electrode. A voltage can be adjusted throughout the pixel arranged electrode causing the liquid crystals to rotate relative to the voltage, changing the phase pattern of the reflected light. A LabView computer program produced at the university of Glasgow was used to operate the SLM [97]. The position of the trap can be adjusted to

a nanometre scale in three dimensions. The SLM requires low angle of incidence to function optimally; in the set-up the angle of incidence is  $<10^\circ$ .

The SLM forms holographic optical tweezers. It creates a phase pattern on the trapping laser allowing multiple traps to be created. The technology was first developed by use of an addressable liquid crystal filter in [98], allowing an adjustable trap in two dimensions. The same group developed this technique to create multiple traps in three dimensions [99].

The SLM projects the beam onto lens L3 which forms another Keplerian telescope with lens L4. They have focal lengths of 40 cm and 20 cm respectively and are separated by a distance of 60 cm. This reduces the beams diameter to 10.5 mm, which over-fills the back aperture of the objective lens. Between the lenses L3 and L4 there are three steering mirrors M3, M4 and M5. The path length between the SLM and the back aperture of the objective lens corresponds to a  $4f$  optical system with lenses L3 and L4; i.e. the distance between the SLM and L3 is 40 cm and the distance between L4 and the back aperture is 20 cm.

DC3 and DC1 are dichroic mirrors, that allow longer wavelength light to pass but will reflect shorter wavelength light. DC3 allows 95% of the 1070 nm laser to pass through and DC1 transmits 50% of the 1070 nm laser. The function of the dichroic mirrors to enable imaging and spectroscopic measurements is explained later on.

The microscope objective used was a high numerical aperture (1.25) infinity-corrected microscope objective (MRP01902 CF1, Nikon UK). The high numerical aperture of the objective brings the laser beam to a tight waist. The diameter of the laser beams focus  $d$  can be calculated by the equation derived by Lord Rayleigh [100]:

$$d = \frac{1.2197\lambda}{NA} = \frac{1.2197 \times 1070\text{nm}}{1.25} = 1040\text{nm},$$

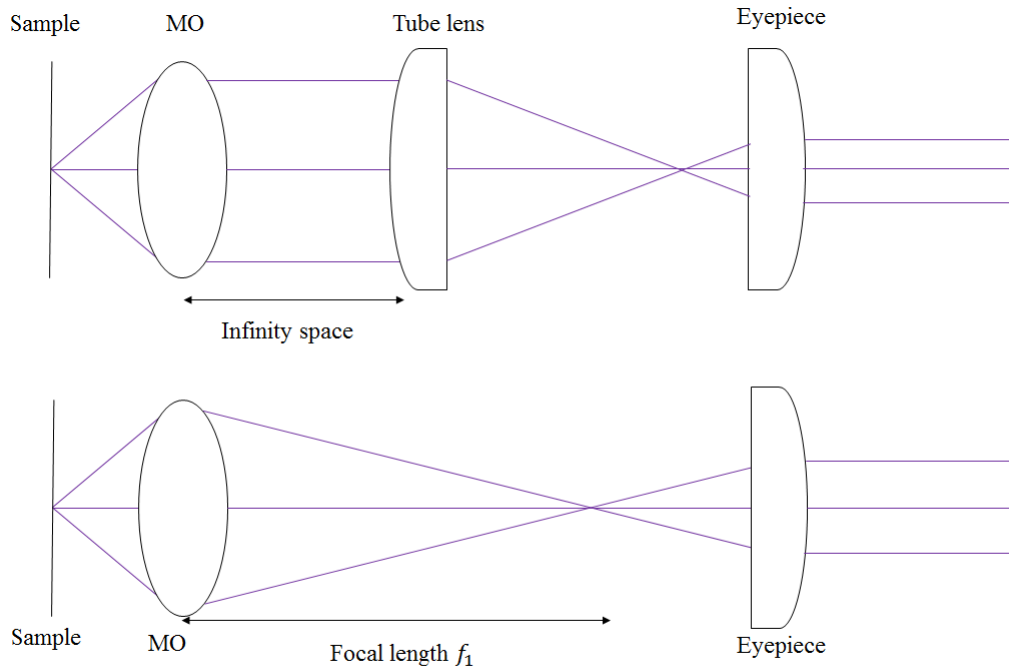


Figure 4.5: An infinity corrected optical system (top) and a finite correction optical system (bottom). In the finitely corrected optical system the microscope objective converges to the specified focal length  $f_1$ , in a typical finitely corrected system  $f_1$  would be 160 mm. In the infinity optical system the light does not converge, a tube lens is used to focus the light to the eyepiece.

where  $NA$  is the numerical aperture and the value 1.2197 is the first zero of the Bessel function divided by  $\pi$ . The equation shows that the higher the numerical aperture of the microscope objective, the tighter the focus of the beam and therefore the more powerful gradient force of the optical trap.

A small amount of immersion oil was placed on the objective lens to create an index match between the microscope objective and a cover glass.

As the microscope objective is infinity-corrected, it collimates transmitted light from the LED and scattered laser light from a trapped particle. As the light is collimated, it is easier to include additional components for spectroscopy-based experiments than it would be a for finite objec-

tives. Figure 4.5 shows a ray tracing diagram for a general infinity-corrected lens and a finitely corrected lens.

#### **4.2.2 Light scattering source (488 nm laser)**

A 488 nm laser is used for Raman spectroscopy and light scattering measurements. The model is a JDSU fibre based system with initial diameter of 1.4 mm. Firstly, the laser passes through a laser line filter (Semrock) which blocks other modes in the laser output. The blue laser light is initially linearly polarized however the  $\frac{1}{4}$  wave plate (Thorlabs) changes this to a circular polarization. In Raman analysis typically a circularly polarized excitation laser is used as it will excite all Raman active vibrations. If the excitation light is polarized then only vibrational modes in suitably orientated molecules will be excited.

The laser is then steered by mirrors M6 and M7 onto lens L5. A neutral density filter (Thorlabs) can be placed between mirror M7 and the lens L5 to attenuate the beam if required. L5 and L6 are also plano-convex lenses which form a Keplerian telescope to resize the diameter of the 488 nm beam to approximately the same size as the back aperture of the objective lens. L5 and L6 have focal lengths of 19 mm and 100 mm, respectively, expanding the beam to 7.5 mm, filling the back aperture of the objective. The expanded beam is then reflected onto beam splitter 50:50 BS1 by mirror M8. DC1 transmits 95% of the 488 nm laser light to the objective lens. The purpose of the 50:50 beam splitter is explained in the next section. The objective lens focuses the 488 nm beam to a tight waist which can be located inside the beam waist of the 1070 nm beam by adjusting the position of the near IR beam using the SLM.

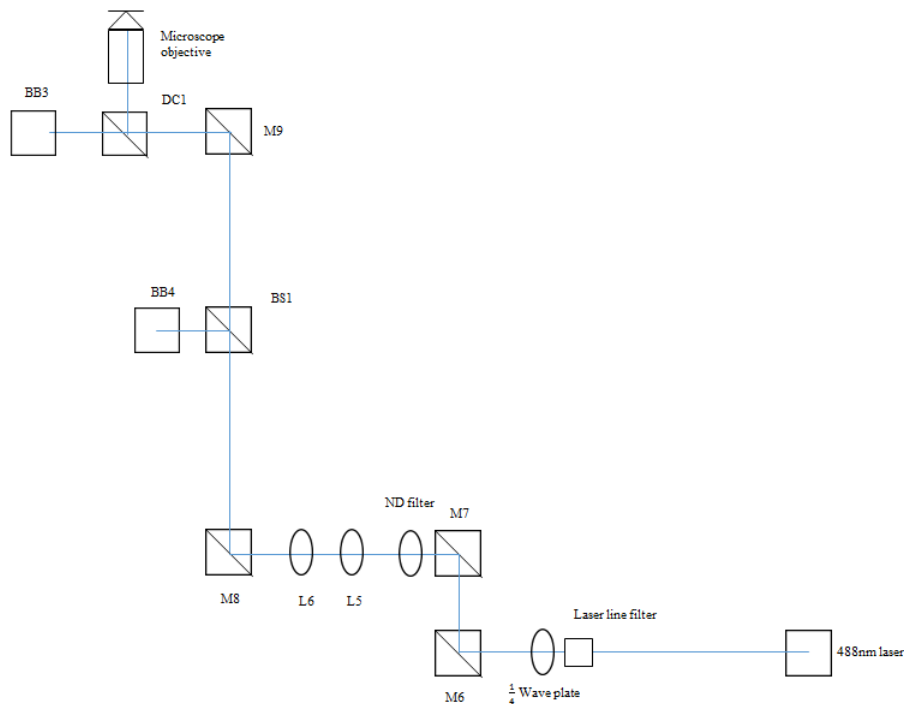


Figure 4.6: The 488 nm lasers path, it is shown as the blue line.

### 4.2.3 Bright field imaging and measurements of the intensity of elastic light scattering

A particle that is optically trapped above the microscope objective will scatter both the 1070 nm and 488 nm light. The back scattered component will then be collected by the objective. This can then be observed on a camera or photodiode. DC1 reflects 50% of the 1070 nm and 95 % of the 488 nm back scattered light toward the photodiode and camera. Mirror M9 reflects the light onto the beam splitter which reflects 50% of this light toward the camera. The light is then focused by a 16 cm tube lens L7, where an adjustable iris is placed in the front focal plane set onto an adjustable iris. This is used to isolate light scattered by the particle, and eliminate reflections from optical surfaces. L8 (a 16 cm tube lens) collimates the light before another tube lens, L9,

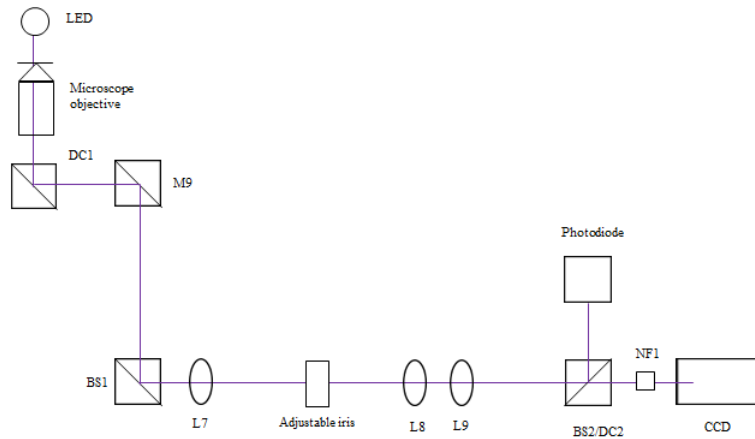


Figure 4.7: The path of the light scattered onto the photodiode or CCD, it is shown by the purple line.

focuses the light onto both the camera and the photodiode. The light can be split at different ratios, a 50% beam splitter can be used to give equal light on the camera and photodiode or a dichroic mirror can be used to reflect 95% of elastic scattered light at 488 nm or 1070 nm onto the photodiode if high sensitivity is required. Between the beam splitter/dichroic mirror and the charge coupled device (CCD) a notch filter can be placed to remove scattered light from the 1070 nm laser, allowing images of a trapped particle to be taken.

In this work, two photodiodes have been used to take light scattering measurements at high and low temporal resolution. For the low resolution measurements, an ordinary silicon photodiode (DET36A, ThorLabs) was used. This component is capable of recording both 1070 nm and 488 nm wavelengths of light. The low temporal resolution photodiode was connected to the data acquisition (DAQ) module (National Instruments, USB-6211) with a resistance load of 1 M $\Omega$ . The photodiode detector had a 0.1 ms rise-time response. For the high resolution measurements an

avalanche photodiode (APD 130A, ThorLabs) detector was used. This detector was not sensitive to the 1070 nm light. The detector had a rise-time response of 20 ns and was used to record data points every 4  $\mu$ s. The DAQ is connected to a computer and a custom LabView programme was used to record the light scattering data with a corresponding time stamp. Temperature was also recorded using a LabView compatible thermocouple module.

#### **4.2.4 The Raman spectroscopy configuration**

The inelastically scattered 488 nm laser light is used to measure the Raman spectrum of an optically trapped particle; see figure 4.8. Back scattered Raman wavelengths are collected by the objective lens. 95% of the light is transmitted by DC1 for  $\lambda > 490$  nm. Dichroic mirror DC3 transmits 95% of the Raman light onto the lens L10, which has a focal length of 16 cm. At the focal point the light passes through a 75  $\mu$ m pinhole PH, isolating the light scattered by the trapped particle from the background light. The Raman light is re-collimated by L11, a lens of focal length 20 cm, following reflection by mirror M10. Mirror M12 reflects the light onto NF2 which blocks out any residual light from the 488 nm laser. A lens of focal length 5 cm L13, focuses the Raman light onto the entrance slits of the spectrograph.

The spectrograph used was a SpectraPro 2500i, Acton Research Corporation. Figure 4.9 shows the configuration of the spectrograph. The light is reflected and collimated by the concave mirror M1 onto the grating. The grating has 1800 lines/mm and 500 nm blaze wavelength. The grating separates the light into its wavelength components. The light is then reflected and focused by concave mirror M2 onto the detector.

Spectral data points were measured in increments of 0.018 nm ( $0.5 \text{ cm}^{-1}$ ); the optical resolution of the spectrograph is  $2 \text{ cm}^{-1}$ , and the precision of a wave-number measurement is  $0.5 \text{ cm}^{-1}$ . The

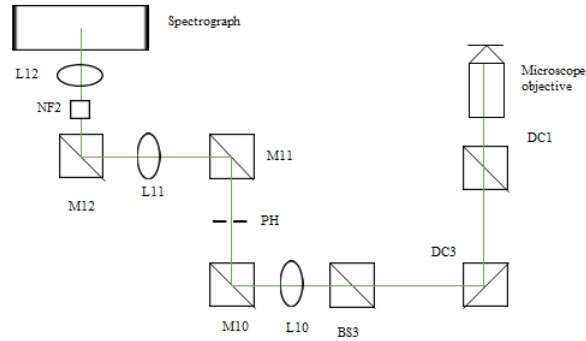


Figure 4.8: The path of the light scattered onto the spectrograph, it is shown by the green line.

acquisition time for the spectra presented in this thesis was 30 seconds. Spectra with a low signal to noise ratio could be recorded continuously at the shorter acquisition time of 1s. This could be used to align the optical pathway for the Raman-scattered light. Bright field illumination had to be halted during the acquisition of Raman spectra.

The detector (Princeton Instruments Inc., Pixis 100B) is a back illuminated CCD type detector with a  $1340 \times 100$  pixel array and  $20 \times 20 \mu\text{m}$  pixel size. It is cooled to  $-80^\circ\text{C}$  to reduce the dark current produced by the CCD. The spectrograph is connected to a laptop computer and the spectra are recorded using the programme WinSpec (Princeton instruments).

### 4.3 Other experimental techniques

In this section the experimental techniques used to support the information obtained from single droplet experiments are explained. As well as the optical trapping based experiments, dynamic

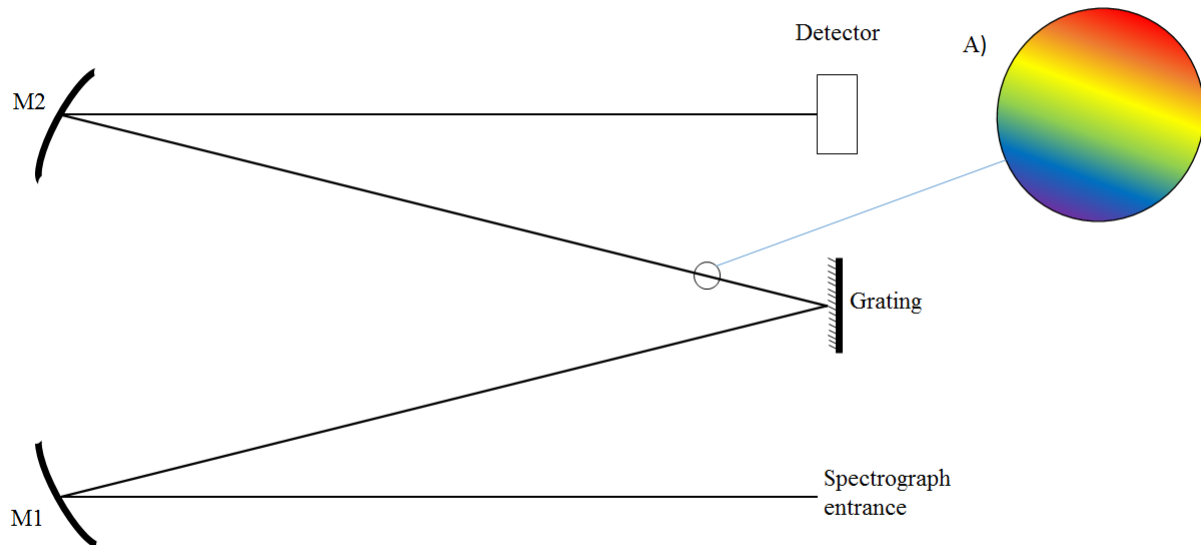


Figure 4.9: The mirrors grating and detector within the spectrograph. A) shows that the light has been split into its wavelength components by the diffraction grating.

light scattering was used to obtain size distributions, average size, and the polydispersity index for liposome samples. The method used to prepare large unilamellar vesicles is also described.

### 4.3.1 Dynamic light scattering

Dynamic light scattering (DLS) is a technique used to measure the size distribution of solid or liquid particles dispersed in a liquid solution. DLS can measure the size of particles to a nanometre scale. It can also measure the number of particles in a sample of a certain size. The apparatus used in this project for dynamic light scattering was a Malvern Zetasizer Nano ZS.

In dynamic light scattering, a laser is shone through a sample and the elastic light scattering

is measured at a fixed angle. Due to diffusion within the sample the intensity of the scattered light fluctuates at the fixed angle position. By considering the rate of fluctuations in scattering the diffusion constant can be calculated. This can then be used in conjunction with the Einstein relation to determine particle size. The equation relates the diffusion rate of the particles to size, is given by,

$$D = \frac{\kappa_i T}{6\pi\eta r}, \quad (11)$$

where  $D$  is the diffusion constant,  $T$  is the absolute temperature,  $\kappa_i$  is the Boltzmann constant,  $\eta$  is the dynamic viscosity and  $r$  is the particles radius. To calculate size using DLS, the dynamic viscosity of the sample must be known.

Dynamic light scattering is used in this work to calculate the size distribution in liposome samples. For all liposome samples used in this work, dynamic light scattering measurements were taken to ensure that the sample consisted of monodisperse large unilamellar vesicles.

#### **4.3.2 Liposome preparation**

The method used to prepare liposomes is based on the method described in [101]. Here, the method is described for making DPPC liposomes, the method was the same for the other lipid blends. 10 mg of the lipid DPPC (1,2-dipalmitoyl-sn-glycero-3-phosphocholine) (Avanti) was dissolved in 1 ml of chloroform. The chloroform was then evaporated off by placing the solution under a stream of dry nitrogen in a fume hood for two hours to yield a lipid film. The lipid film was then rehydrated with the buffer solution which in this case was Milli-Q water. The rehydrated lipid suspension was then heated to above the main phase transition temperature of 41 °C, to 50 °C and extruded through a 1  $\mu$ m polycarbonate membrane 25 times on an Avanti extruder stand to give large unilamellar vesicles (LUV). The lipid suspension was then stored in

a fridge and used within 2 weeks.

To produce the lipid sample of POPC (1-palmitoyl-2-oleoyl-sn-glycero-3-phosphocholine) (Avanti) and cholesterol (Avanti) at a molar ratio 1:1 molar mass, an identical method was used. For the lipid sample of POPC/cholesterol/sphingomyelin a molar ratio of 1:1:1 was used. In both cases the buffer used was PBS (Phosphate-buffered saline) and during the extrusion process both samples were heated to 50 °C.

## 4.4 Computational analysis

Sets of Raman spectra have been analysed using computational techniques. The set of spectra may be deconvolved into a multi-component form. By fitting the set of spectra into this form, gradual changes in molecular structure can be observed.

### 4.4.1 Multivariate analysis of Raman spectra

Raman spectra could be continuously recorded for a single optically trapped particle, the spectra were recorded every 30 seconds. Therefore as a liposome was being heated a set of spectra could be recorded. A multivariate-curve resolution (MCR) algorithm was then used to analyse this sequence of spectra. The algorithm has been described in [102]. By writing the set of spectra as a  $n \times m$  matrix  $D$ , with  $n$  data points per spectra and  $m$  spectra  $D$  can be written as,

$$D = CS^T = c_A s_A^T + c_B s_B^T \dots = A = \sum_{I=1}^k c_I s_I^T$$

where  $s_I^T$  is an intensity profile of the pure spectra ( $n$  dimensional row) and  $c_I$  corresponds to the concentration profiles for the sequence of recorded spectra ( $m$  dimensional vector),  $k$  corresponds

to the number of components.

The algorithm to find the optimal fit to the experimental data employed an iterative least-squares method to minimize the error matrix  $E = D - C_{fit}S_{fit}^T$ . The algorithm minimizes the variance in the components across the family of spectra. For the liposome experiments, the set of spectra were recorded in the C-H stretching band (2783.1 to 3028.9  $\text{cm}^{-1}$ ). The spectra were normalized and background subtracted before the analysis was done. The algorithm this is based on is described in [103].

## **Part II**

# **Results and discussion**

**Chapter Five - Monitoring phase behaviour  
and the mechanical properties of optically  
trapped liposomes using light scattering**

## **5 Monitoring phase behaviour and the mechanical properties of optically trapped liposomes using light scattering**

This chapter describes how the spectroscopic methods discussed in chapters 2 and 4 have been used to study phase behaviour of optically trapped liposomes. The optical tweezers were used to isolate an individual unilamellar 1  $\mu\text{m}$  diameter liposome, which was then heated on a custom designed microscope stage. Three different lipid blends were used in this work to observe the gel-to-liquid phase transition and changes in the microdomain structure of lipid bilayers. Elastic and inelastic light scattering techniques were used to report on these thermodynamic and structural changes in the liposome. These experimental measurements on singles liposomes are contrasted with dynamic light scattering and differential scanning calorimetry results taken on bulk samples of lipid suspensions. Although phase transitions in lipid bilayers have previously been observed in cells [104], the complexity of the cell membrane makes identifying these transitions challenging. Therefore, this chapter will focus exclusively on synthetic phospholipid based bilayer structures.

The first section of this chapter will give a general introduction to the different phase transitions in lipid bilayers. The second section will provide a detailed description of the specific spectroscopic techniques used in conjunction with the optical tweezers. In the third section the results of the experiments are presented with a discussion of their relevance to similar experiments reported in the literature. Finally some concluding remarks and suggestions for future work are given. The results presented in this chapter have previously been published in [105].

## 5.1 Introduction

It is well known that lipid bilayers exhibit temperature sensitive phase behaviour. Heating or cooling of a lipid bilayer is accompanied by a change in fluidity and rigidity of the membrane. In the fluid phase of a lipid bilayer the lipids are able to diffuse laterally and rotate about an axis perpendicular to the membrane. Whilst the lipid bilayer is in the gel phase, the molecules are constrained in a lattice. Transitions between the two phases can be induced by changing the temperature. The addition of cholesterol, proteins and lipids of other blends to the bilayer affects the intermolecular forces between lipid molecules and can change the nature of any phase transition or induce more complex phases in the lipid bilayer.

### 5.1.1 The main gel to liquid transition

The gel to fluid transition is observed in pure phospholipid bilayers. In this phase transition the lipid bilayer undergoes the main process from a gel state  $L_\beta$ , to liquid crystalline state  $L_\alpha$ . This process is known as melting. The main transition occurs at a characteristic temperature,  $T_m$ . There is also a pre-transition leading to the formation of a ripple phase  $P_\beta$ , the ripple phase is similar to the gel phase, and exists in a narrow range of temperature immediately below the main transition. The ripple phase is characterized by undulations on the bilayer surface.

The characteristic gel-to-liquid crystalline transition temperature is governed by the van der Waals interaction between the hydrophobic tails of lipid molecules. The hydrocarbon chains in two adjacent lipid molecules are attracted to each other due to the electrostatic forces between them. The van der Waals interaction is temperature sensitive, and as temperature is increased the attraction is weakened, due to increasing distance between the hydrocarbon chains of adjacent lipid molecules in the bilayer.

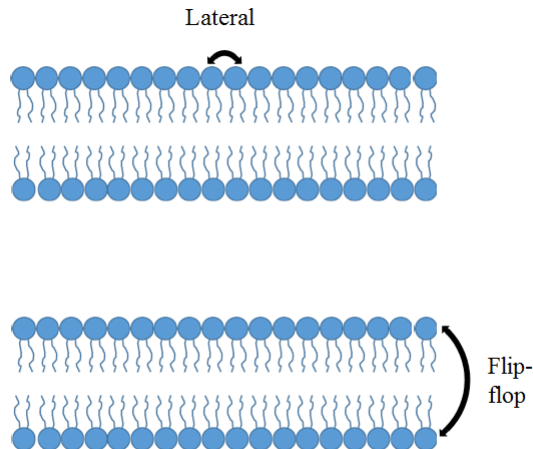


Figure 5.1: Fluid phase lipid bilayers showing a pair of lipid molecules diffusing across the membrane. The top image shows two lipids interchanging laterally, this is shown by a double arrow. The image below shows the flip-flop interchange of two lipid molecules, a significantly less energetically favourable way for the lipids to diffuse.

At the transition temperature  $T_m$ , the van der Waals forces of interaction have decreased sufficiently so that the lipids may interchange with each other. This can happen by a lateral interchange or by a flip-flop mechanism involving the opposing lipid molecule; this is illustrated in figure 5.1. A lateral interchange is common in the fluid phase, however, the flip-flop mechanism is not energetically favourable and is much less common.

The transition temperature  $T_m$  is determined by the length of the lipid tails. For a longer lipid tail with more carbon atoms so the van der Waals attraction is stronger and, therefore, more thermal energy must be supplied for the gel-to-liquid crystalline transition to take place. It is also possible for some lipids to contain a double bond between the carbon atoms. Lipids with a double bond are said to be unsaturated. The double bond causes a kink in the lipid tail, increasing the distance between the adjacent lipid molecules. This can significantly decrease the strength of the van der Waals attractions between the molecules and thus significantly reduce the transition temperature.

Tail length	Double bonds	Transition temperature °C
12	0	-1
14	0	23
16	0	41
18	0	55
20	0	66
22	0	75
24	0	80
18	1	1
18	2	-53
18	3	-60

Table 5.1: The transition temperature from the gel-to-liquid crystalline state for lipid bilayers depending on the tail lengths and the number of double bonds. The table was taken from [106].

Table 5.1 gives the transition temperature for different lipid tail molecules with variable lengths and number of double bonds. The table shows that the addition of one double bond can decrease the transition temperature by up to 54 °C.

As well as the main gel-to-liquid transition, there is also a pre-transition leading to a state called the ripple phase. The formation of the ripple phase is not well understood though there are several theories in the literature, reviewed in [107], it has also been suggested that there may be several types of ripple phase.

The gel, ripple and fluid phases are illustrated in figure 5.2. The top row shows a cross section of the lipid bilayer and the bottom row shows the packing order of the lipid heads. The gel and ripple phases are similar, where the lipids are tightly packed in a triangular lattice configuration and the tails are in an all-trans straight conformation. The lipid tails are not perpendicular to the bilayer and the angle to the normal of the bilayer is known as the tilt angle. Whilst the lipid bilayer is flat in the gel phase, it has a sawtooth structure in the ripple phase [108]. In the fluid phase, the packing order has been disrupted and the tails are no longer straight. The lipid tails

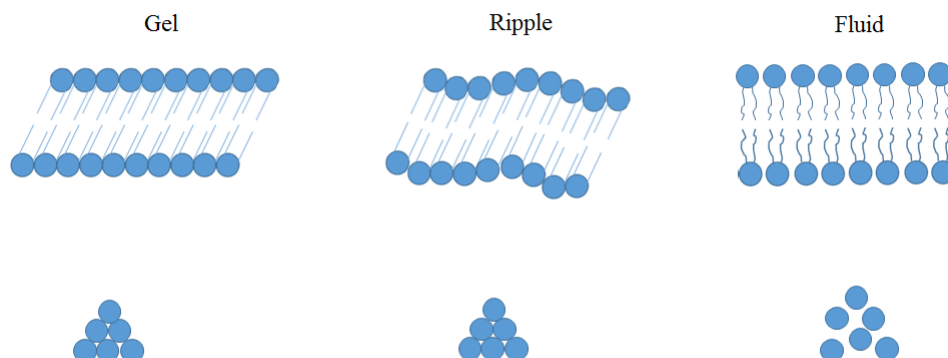


Figure 5.2: The gel, ripple and fluid phases of a liposome, the top row shows a cross section of the lipid bilayer and the bottom row shows the respective packing order.

have partially undergone trans-gauche isomerization at the C-C bonds. A sub-gel transition has also been identified in lipid bilayers which we have not explored. The sub-gel phase is similar to the gel, the area per lipid molecule is decreased and the tilt angle is increased [109].

The main transition temperature is an important consideration for liposomes prepared for drug delivery. In [7] the author investigated optimising a lipid blend to have a transition temperature slightly below body temperature. When liposomes transition from a gel state to a fluid state they become more permeable and can slow release their content to the exterior solution. The review article [110] provides an overview of temperature triggered drug release.

Differential scanning calorimetry (DSC) can be used to investigate the gel-to-liquid crystalline transition in a lipid bilayer. A DSC measurement is performed by parallel heating of a sample and a blank reference: maintaining both the sample and reference at the same temperature and recording the differential rate of heating. Thermocouples are used to independently regulate the

rate of heating of sample and reference so both are kept at the same temperature. The differential heat flux versus the temperature exhibits a sharp feature at the transition temperatures. Differential scanning calorograms for phospholipid bilayers are given in [9].

The gel-to-liquid crystalline transition has also been monitored using spectroscopic experiments. In [111] and [8], elastic light scattering was used to observe the transition in a suspension of liposomes. A 633 nm laser passed through suspensions of 100 nm liposomes [111]. By measuring the mean count rate of reflected photons at a 90° scattering angle the authors were able to see a change in intensity of scattered light when the gel-to-liquid crystalline transition occurred during a temperature ramp. The transition was observed at the known transition temperature of a saturated phosphocholine lipid across a full-width of 1°C.

Whilst earlier methods required dispersions of lipids, Raman spectroscopy has been used to monitor affects below and above the gel-to-liquid crystalline transition of a single optically trapped liposome. In [112], Raman spectra were recorded for an optically trapped DPPC liposome pre and post transition. Raman scattering is induced by the C-H and C-C vibrational frequencies. These are effected by the phase of the lipid bilayer, this will be discussed in detail in the results section.

Their experiment also investigated the permeability of the membrane and the release of the interior solution following the transition. The authors were able to show a gradual release of the interior solution after reaching the transition temperature  $T_m$ . The transition temperature can also be changed by binding a drug (tricyclic antidepressants ) to the membrane. Raman spectroscopy has also been used to fully characterize the release of a drug from a single optically trapped liposome [113].

### 5.1.2 The liquid crystalline state in multi-component lipid bilayers and mixed phase behaviour

In a cell, the phosphocholine bilayer will be enriched with proteins, sterols and other types of lipid molecule. Because of this, cell membranes tend not to have easily observable temperature transitions. It is well known that the presence of cholesterol lowers the gel-to-liquid crystalline transition temperature and broadens the temperature range over which the transition occurs [114]. In a cell, cholesterol is an essential component that adds rigidity to the bilayer. The addition of a sterol such as cholesterol to the lipid blend is known to induce the formation of other phases on the lipid bilayer, at certain temperatures.

Cholesterol disrupts the packing order and can limit the ability of the lipids to interchange laterally and rotationally. Cholesterol is largely hydrophobic and therefore becomes embedded between two lipids tails as shown in figure 5.3. As the attractions between the long chain lipid and cholesterol molecules are strongly dependent on temperature this induces new phase transitions of the fluid bilayer. Within the fluid state, the liquid ordered  $L_o$  and liquid disordered  $L_d$  phases can exist. The liquid ordered phase resembles the gel phase, in terms of the lipid molecules being predominately in an all-trans configuration, but unlike the gel phase, the lipid molecules are free to interchange and diffuse laterally in the membrane. In the liquid disordered phase, the local packing order is reduced and the tails undergo a trans-gauche isomerization. The liquid ordered and disordered phases are illustrated for a lipid bilayer enriched with cholesterol in figure 5.3.

In addition to the pure phases, the liquid ordered and disordered phases are believed to be able to co-exist together in a single thermotropic phase ( $L_d + L_o$ ). In a binary mixture of cholesterol and phospholipid, the phases  $L_o$ ,  $L_d$  and  $L_d + L_o$  have defined boundaries depending on the molar

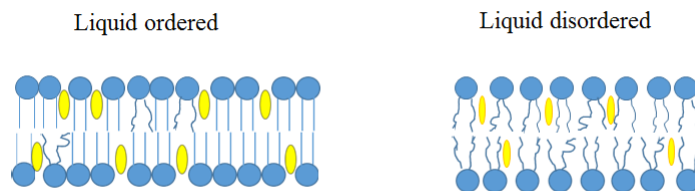


Figure 5.3: Two lipid bilayers enriched with cholesterol in the liquid-ordered and disordered phases. In the liquid-ordered phase (left), the cholesterol (yellow) is limiting the phospholipids ability to interchange. The tails are also in the all trans conformation. In the liquid-disordered phase (right), the tails are no longer in the trans configuration and the local packing order has been reduced.

properties of the different lipid components and temperature.

Figure 5.4 shows the boundaries between  $L_o$ ,  $L_d + L_o$  and  $L_d$  phases for a 1-palmitoyl-2-oleoyl-sn-glycero-3-phosphocholine (POPC) and cholesterol lipid blend. The figure shows that at lower proportions of cholesterol (or alternatively at higher temperature), the packing order will be decreased. The sharpness of the curves show that small increases in the ratio of cholesterol to POPC can significantly increase the transition temperature. The data shown in figure 5.4 was obtained by measuring changes in the diffusion constant for fluorescent-labelled lipid molecules embedded in the bilayer structure. It has not been possible to confirm thermotropic phase transitions  $L_o \leftrightarrow L_d + L_o \leftrightarrow L_d$  by directly measuring enthalpy changes (for instance by DSC).

A 1:1 molar ratio of POPC and cholesterol, at 20 °C, will produce a bilayer in the  $L_o$  phase. In this chapter we have used this lipid blend to observe the changes in structure in the vicinity of the proposed transition between liquid ordered and liquid disordered phases. The figure also suggests that the liquid disordered regime would be observed at a ambient temperature for POPC/cholesterol bilayers at low concentrations of cholesterol. However, it is preferable to use the ternary mixture POPC/cholesterol/sphingomyelin as a low concentration of cholesterol could

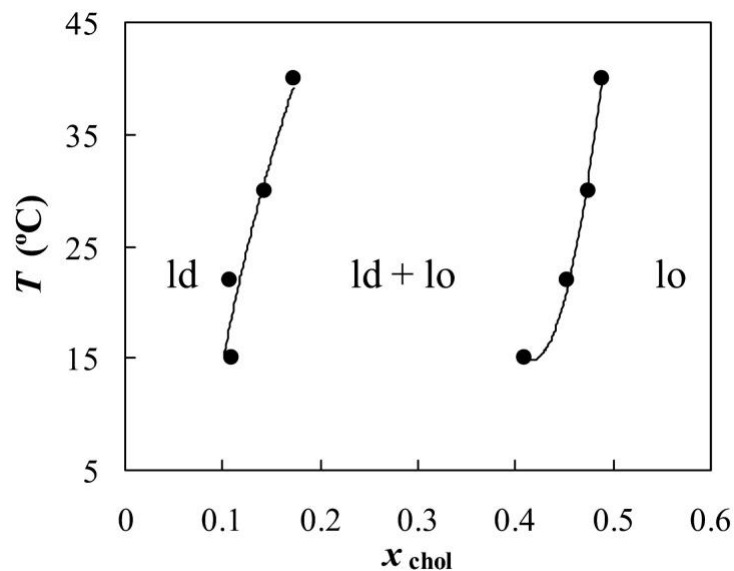


Figure 5.4: A phase boundary diagram for a POPC/cholesterol lipid blend taken from [115], the  $x$  axis shows the molar ratio of cholesterol to POPC.

result in a sample with an uneven distribution of lipid components.

The effect of the interaction between POPC, cholesterol and sphingomyelin (SM) on packing order and thermotropic phases is complex. In the work reported here, egg SM has been used which has an acyl chain length of 16, (similar to POPC). SM also has a hydrophilic head and hydrophobic tail, and the molecules are also able to diffuse readily in the bilayer. By the addition of SM to the lipid mix, the relative concentration of cholesterol has been reduced, this decreases the ordering of the lipid bilayer.

A phase diagram for the ternary mix of POPC/cholesterol/SM at 37 °C is shown in figure 5.5. The diagram shows that phase boundaries for the  $L_o$ ,  $L_o/L_d$ ,  $L_d$  and other complex phases relative to the proportions of POPC, cholesterol and SM. The diagram shows that reducing the proportion of either SM or cholesterol reduces the degree of ordering of the lipid bilayer, leading eventually

to a pure liquid-disordered phase. Reducing the concentration of cholesterol reduces ordering much more significantly than reducing the concentration of SM. As the temperature is increased the dashed lines shown in figure 5.5 will rise to higher values of  $x_{chol}$  and  $x_{SM}$ . For a 1:1:1 ternary mixture it is anticipated that a transition from  $L_o + L_d$  to  $L_d$  will occur between 30 °C and 60 °C. But as for the example of POPC/cholesterol bilayers the phase diagram shown in figure 5.4 was derived from measuring changes in the diffusion constant for fluorescent labelled lipid molecules embedded in the bilayer structure. It has not been possible to confirm thermotropic phase transitions between the liquid phases by directly measuring changes in enthalpy via calorimetry.

In addition to the phase behaviour described above, there can also be non-homogeneous diffusion leading to the segregation of lipid components in a fluid lipid bilayer. This can lead to ordered microdomains (which are also known as lipid rafts). These have been postulated to be involved in membrane signalling and trafficking [116]. Although ordered microdomain structures, enriched in cholesterol and sphingolipids, have been observed to float freely in the fluid matrix of artificial membranes, there is still controversy surrounding the dimensions of lipid rafts, and whether or not their existence is only transient in cellular membranes. The ordered microdomain structure of lipid rafts should not be equated to thermotropic phase-separation (i.e. to regions of  $L_o$  phase surrounded by a wider  $L_d$  phases), as the lipid rafts are not thermodynamically stable. Lipid rafts are microdomains with a lipid structure that only resembles the liquid-ordered ( $L_o$ ) phase of model membranes. These ordered raft microstructures could still exist in regions where a single homogeneous  $L_d$  phase is expected to be present. However, lipid rafts are anticipated to be more widely present in regions of  $L_o + L_d$  co-existence [117]. Thus, the model bilayers used to study the phenomena of lipid rafts will typically be comprised of lipid components in mole fractions expected to form a mixed phase  $L_o + L_d$  bilayer (i.e., in accord with figure 5.4 and 5.5).

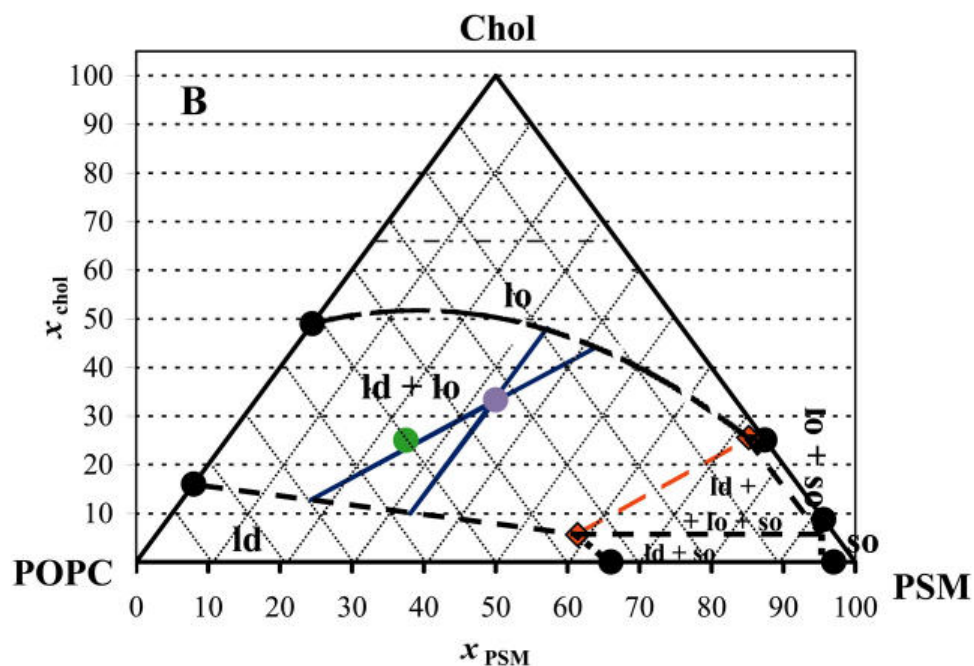


Figure 5.5: A phase diagram for a POPC/cholesterol/SM lipid blend at 37 °C taken from [115]. The black dashed lines show the boundaries between the  $L_o$ ,  $L_o + L_d$ ,  $L_d$  phases.

## 5.2 Experimental details

The experimental techniques used to observe the temperature induced phase transitions of individual vesicles will be described. An explanation of optical trapping, light scattering, Raman scattering and dynamic light scattering has already been given in the previous chapter. In this section, the specific experimental techniques relating to the set up of the optical tweezers for observing phase behaviour of liposomes and dynamic microdomain structures will be explained.

### 5.2.1 Microscope apparatus

This section describes the alignment of the microscopes stage, and the optical tweezing laser. The optimal position for optical trapping of a particle is at a height of approximately  $50\ \mu\text{m}$  above the surface of the cover glass. In the first instance, the 1070 nm filter NF1 shown in figure 3.2 was removed and the power of the laser was attenuated in order to view the Airy pattern on the camera, resulting from the reflection of the laser from the cover glass. By looking at the separation of the rings of the Airy pattern, the  $z$  position of the objective could be adjusted to place the focus of the laser beam at the upper surface of the cover glass and then raised to the required distance of  $50\ \mu\text{m}$  above.

A custom made heating plate was used to heat the sample. The design of the plate is specified in an appendix of this thesis. The appendix also details how the temperature of a trapped particle can be estimated from the recorded value for the temperature of the surface of the microscope stage.

The IR-trapping laser was always used at the highest possible power (10 W), as this condition leads to the most stable operation. To reduce the power of the beam to an optimal value for optical trapping, the  $\frac{1}{2}$ -wave plate could be adjusted so that the polarizing beam splitter would reflect more light onto the beam block. The power of the laser was measured in front of the spatial light modulator. The beam was attenuated so that the power measured approximately 150 mW at this position (see figure 3.3). The power was measured at this position for convenience in placing the power meter and ensuring consistent conditions in different experiments. Between the spatial light modulator and the sample plane there is a further attenuation in laser power. The final power of the laser in the sample plane is estimated to be approximately 20 mW. The output power of the 488 nm laser, used for light scattering experiments, was initially set internally to

12.5 mW. The final power in the sample plane was estimated to be 3 mW.

The dichroic mirror DC2 (see figure 3.3) was adjusted to optimize the back scattered light onto the photodiode. The adjustable iris was then reduced to a small aperture in order to isolate the scattered light originating from the trapped particle and eliminate reflected light from the optical surfaces. The position of the trapping laser was then adjusted in three dimensions (on a sub-micrometer scale) using the spatial light modulator. This was controlled with the LabView software on the computer. The position could be set on a sub-micrometre scale in three dimensions. By adjusting the position of the trapping laser, the particle could be located in the waist of the 488 nm laser.

To optimize the detection of Raman scattered laser the spectrometer was initially set to record at low time resolution (one spectra per second). Despite the weak intensity of the Raman peaks, by comparing the intensity of the C-H band due to molecules in the trapped particle against the background peak due to water, the alignment of the particle in the waist of the 488 nm laser could be refined.

### **5.3 Results and discussion**

Temperature-induced changes in the bending modulus and fluidity of the lipid bilayer in an isolated optically trapped vesicle have been determined by measuring the modulated intensity of elastic back scattered light. Morphological changes to the lipid vesicle that are a consequence of the formation or dissolution of microdomains in a fluid bilayer, or transitions between structures resembling the ideal lamellar phases, have been observed. Raman measurements on optically trapped vesicles are also reported. The latter technique has been widely used to report on the short-range packing order of the hydrocarbon chains and rotational diffusion of lipids in bilayer-

ers.

### 5.3.1 The gel-to-liquid crystalline transition of an optically trapped DPPC liposome

To observe the gel-to-liquid crystalline transition, liposomes containing a single lipid component, DPPC, were used. DPPC has an acyl chain length of 16 and no double bonds. Table 5.1 gives an expected main transition temperature of 41 °C. In the gel phase, the lipid heads are tightly packed and arranged in a triangular lattice configuration. The tilt angle of lipid molecules is 32° at 19 °C and the area occupied per lipid molecule on the bilayer is  $0.472 \pm 0.005 \text{ nm}^2$  [118]. The pre-transition from the gel to the ripple phase is known to occur between 33 °C and 35 °C causing a bilayer volume change of  $330 \pm 50 \times 10^{-5} \text{ ml/g}$  [119]. Over the main transition, the area occupied per lipid molecule increases to a value of  $0.64 \text{ nm}^2$  at 50 °C. A bilayer volume change of  $3700 \pm 200 \times 10^{-5} \text{ ml/g}$  [119] has also been reported.

The sample of liposomes was prepared using an extrusion based method as described in the previous chapter. The extruded sample was then diluted at a ratio of 1:1000 for the optical tweezing experiments. The stage was adjusted along the  $x$  and  $y$  axes in order to locate a liposome. The  $z$  position of the stage was then lowered a further 60 microns after optical trapping to allow for the thermal expansion of the heating plate. At room temperature, the liposome was located  $\sim 160 \mu\text{m}$  above the surface of the cover glass for these experiments. The position of the laser could then be adjusted in three dimensions using the spatial light modulator to optimize the light scattering signal recorded on the photodiode or spectrometer.

Figure 5.6 shows the temperature dependence of the back scattered light of the optically trapped liposome. At 44 °C, there is an increase of voltage from 0.235 V to 0.27 V. This is marked on the figure by the red dotted line labelled  $T_m$ .

The voltage was recorded every 0.25 seconds and the increase in light scattering at 44 °C occurs over only two data points, corresponding to a temperature difference of approximately 0.006 °C. 44 °C is approximately 3 °C higher than the reported temperature. This can be accounted for by a temperature difference between the sample and the thermocouple. It is conceivable that the reported temperature difference over this period is not entirely accurate due to small fluctuations in the heating rate as shown in figure 5.7. In the vicinity of the main transition, the ramp was approximately +29 m°C s<sup>-1</sup>. The heating rate was not regulated, leading to a non-linear increase but minimising transient fluctuations in temperature. The transition is significantly sharper than the value of 0.15 °C given in the literature for a bulk sample taken by differential dilatometry [120].

The pre-transition causes a small change in the intensity of back scattered light. In figure 5.6, it is shown as the red dotted line. It occurs between 40 °C and 40.5 °C which is also significantly higher than predicted in the literature. The pre-transition occurs over 4 seconds corresponding to a temperature difference of approximately 0.14 °C. The change in intensity is subtle compared to the large increase seen for the main transition.

The dramatic change in light scattering, indicating the main transition occurs at a similar temperature to that previously recorded by DSC. A DSC thermogram has been recorded for a DPPC sample and is shown in figure 5.8. The sharp change in heat flow at approximately 41 °C indicates the main transition, and is consistent with the literature. This is shown for both heating and cooling experiments. 41 °C is 3 °C lower than that shown by elastic scattering. This can be accounted for by a temperature difference between the value recorded at the thermocouple and at the waist of the beam. A detailed explanation of this is given in the appendices of this thesis.

The example shown in figure 5.6 is representative of the light scattering trace of several different

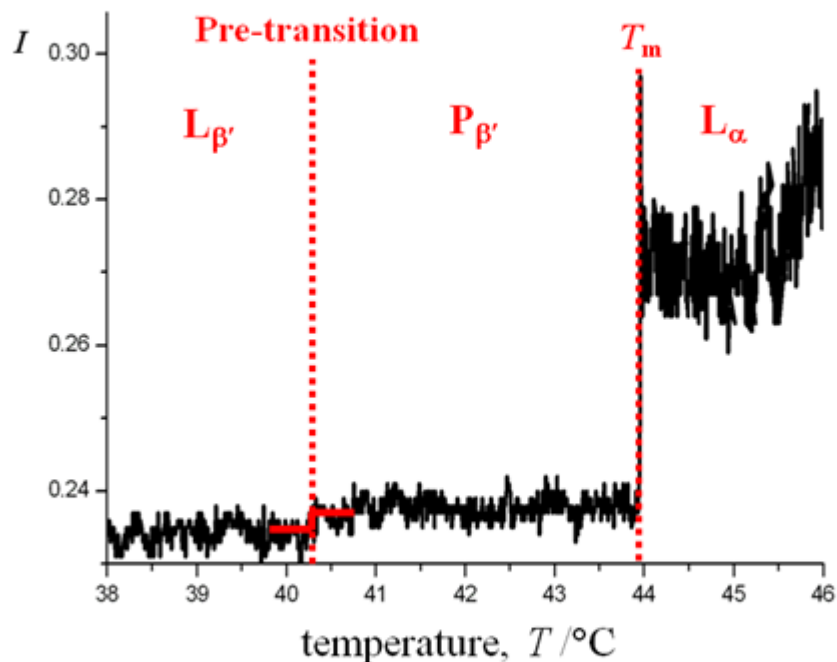


Figure 5.6: The back scattered 1070 nm light from an optically trapped DPPC liposome over the unregulated temperature ramp of 0.025 °C per second at low temporal resolution. A significant rise in light scattering is seen at 44 °C indicating the main transition from the ripple phase to fluid phase, this is marked by the red dotted line labelled  $T_m$ . The pre-transition between the gel phase and ripple phase is also indicated between 40 °C and 41 °C by a small increase in light scattering.

experiments. Seven examples are shown in figure 5.9 and 5.10. The examples shown in figure 5.10 also include the elastic light scattering (red) as the liposome was cooled. No temperature transition can be detected by light scattering as the liposome was cooled. The only explanation

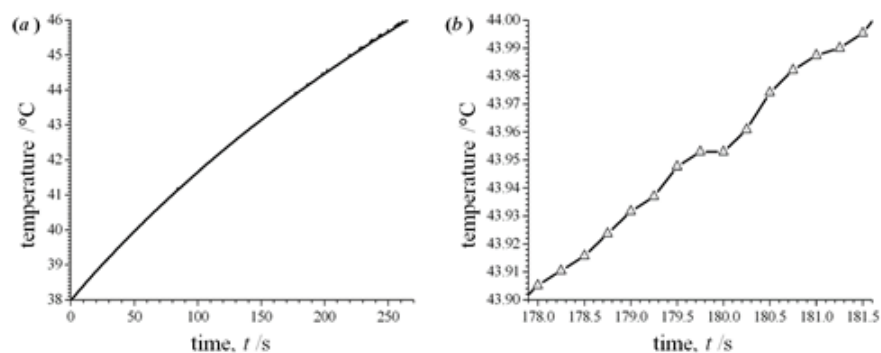


Figure 5.7: The heating rate of the aluminium plate, between 38 °C and 48 °C (left) and between 43.9 °C and 44 °C (right).

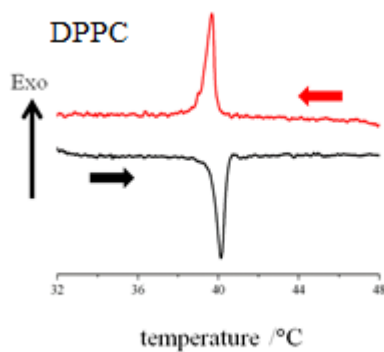


Figure 5.8: Differential scanning calorimetry thermograms of DPPC. A 20  $\mu\text{g}$  sample of the concentrated suspension of liposomes was used; the scan rate was 0.5 °C/min. The black line shows the heating trace and the red line shows the cooling trace.

for the absence of an abrupt change is supercooling of the fluid phase of the vesicle. This effect leads to a dramatic difference between the heating and cooling profiles for light scattering in comparison to the minor hysteresis in the main transition temperature observed by differential

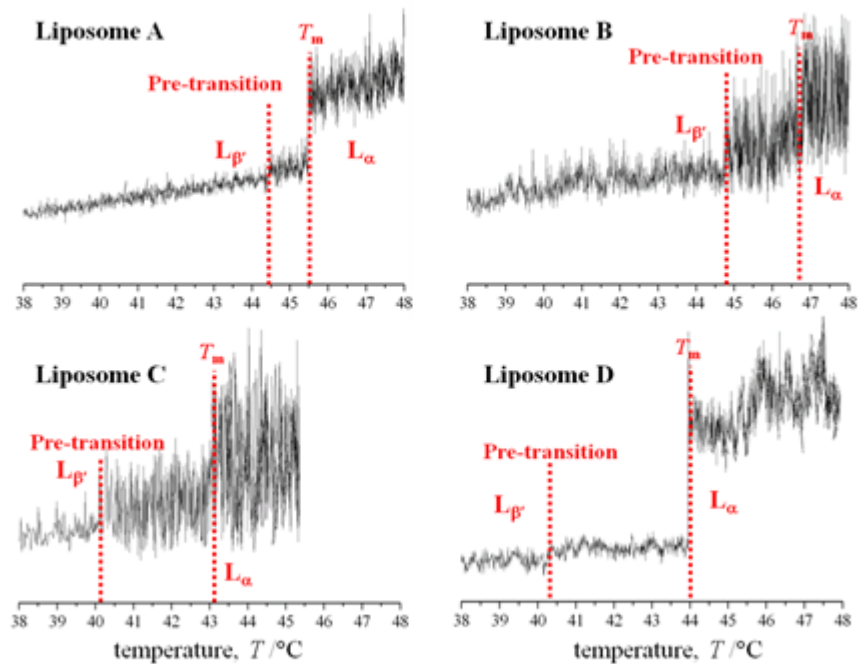


Figure 5.9: The profile of the back scattered intensity, at 1070 nm, measured for 4 different optically-trapped DPPC liposomes during the heating stage of a temperature ramp. The data for Liposome D is also shown in figure 5.6.

scanning calorimetry, shown in figure 5.8. The reason that the difference is pronounced must be the result of the small amount of lipid present in a single isolated vesicle, the relative high rate of cooling in the light scattering experiment and the absence of large numbers of discontinuities or defects in the lipid bilayer structure of a single vesicle. The light-scattering measurement would be insensitive to a liquid-to-gel transition that is delayed (by minutes) as the result of supercooling.

In figure 5.6 the main transition occurred over only one data point. To accurately time the length of the transition, a higher time resolution photodiode was used. This photodiode was not sensitive

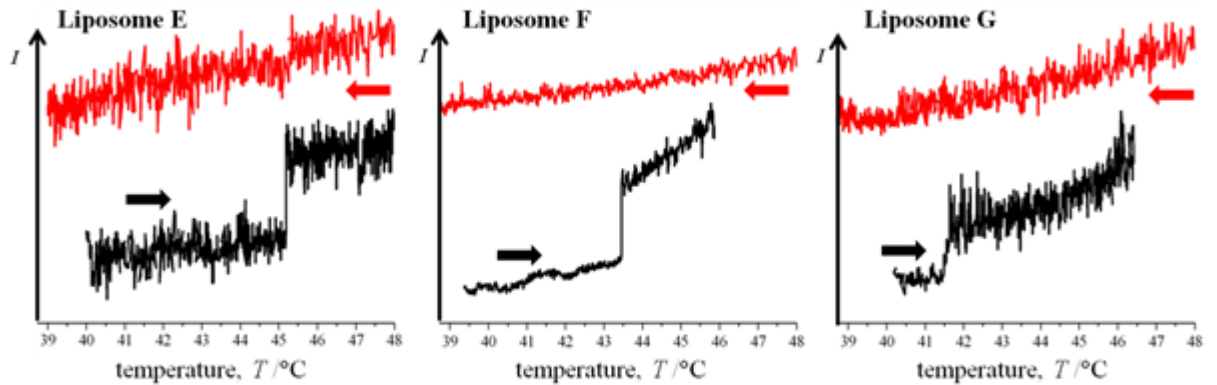


Figure 5.10: The profile of the back scattered intensity, at 1070 nm, measured for 3 different optically-trapped DPPC liposomes during the heating (black) and cooling (red) stages of a temperature ramp.

to infra-red laser light, and so the 488 nm laser was used as the scattering laser. The high resolution photodiode recorded 250000 data points per second. The 488 nm laser is significantly less powerful than the 1070 nm laser, so it is not capable of optical trapping, the 1070 nm laser was used to optically trap the liposome. As the pre-transition occurred over several data points there was no need to investigate this further.

Figure 5.11 shows the high temporal resolution scattering intensity against time over three seconds. An increase in scattering intensity is shown at  $\sim 1.1$  s. The time for the scattering intensity to go from minimum to maximum is  $54 \pm 5$  ms, corresponding to a temperature difference of  $0.001^\circ\text{C}$ . The figure also shows gaps in the scattering intensity corresponding to the time when the computer was acquiring the 250000 data points from the DAQ module, they are approximately 0.1 seconds in width.

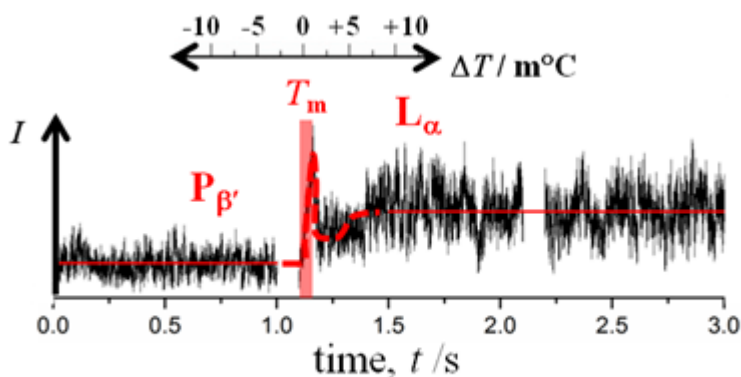


Figure 5.11: The 488 nm back scattered light of an optically trapped liposome against time and temperature taken at high temporal resolution. An increase in scattered light is seen just after 1 second, the width is highlighted in red to show the length of the transition  $54 \pm 5$  ms.

Both light scattering profiles, in figures 5.6 and 5.11, show an increase in intensity following the main transition, from ripple to fluid. An increase in the back scattered intensity appears to be a consequence of deformation of the lipid membrane during the course of the phase transition, resulting in a larger area of lipid bilayer located in regions of higher power density of the trapping laser; and a smaller vesicle diameter along the equatorial axis. Images of the light scattering profile, recorded on a charge-coupled device, from an optically-trapped DPPC liposome are shown in figures 5.13 and 5.12 just below and just above the temperature where the dramatic change in the intensity of light scattering is detected. The acquisition rate was 1 frame per second with an 80 ms integration time.

The change in the diameter of the diffraction rings observed in the images support a conclusion that the light scattering change could arise from deformation of the lipid membrane with an increase in the polar length and a concomitant decrease in the equatorial length. That is, the liposome deforms from a sphere to prolate sphere, a prolate spheroid is shown in figure 5.14. The image shown in figure 5.12 is a characteristic example of the change in elastic scattering

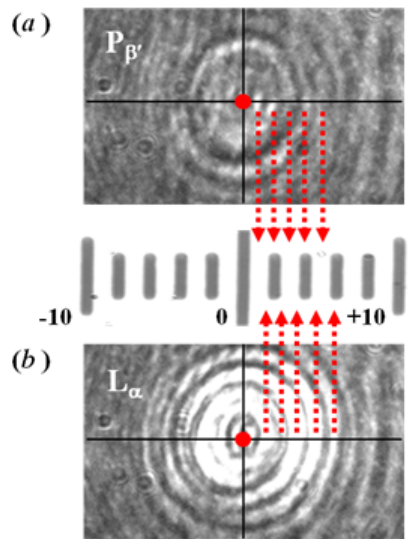


Figure 5.12: Images of the back scattered light, at 1070 nm, from an optically-trapped DPPC liposome. Snapshots of the diffraction pattern of scattered light were recorded at a 1 s interval during a temperature ramp. The images shown were recorded (a) immediately before, and (b) immediately after, a dramatic change in the overall scattering intensity was observed; i.e. across the ripple to fluid transition. A bright field image of a graticule (-10 to +10  $\mu\text{m}$ ) is reproduced in the centre panel.

seen on the camera, another example is shown in figure 5.13.

The magnitude of the gradient force exerted on a liposome in an optical trap is sub-pN, and this has been shown to be sufficient to deform liposomes, with a spherical diameter of approximately 1  $\mu\text{m}$ -diameter, to bring more lipid into the trap [121]. The gel-to-liquid crystalline transition significantly decreases the rigidity of the bilayer such that the sub-pN force may be sufficient to drag part of the bilayer toward the centre of the beam and thus increase the light scattering signal.

Recently it has been shown that for a fluid 100 nm DPPC liposome a 500 pN would be required

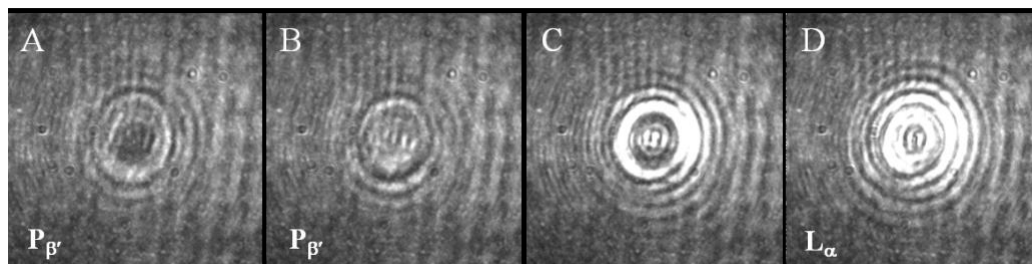


Figure 5.13: Images of the back-scattered light, at 1070 nm, from an optically-trapped DPPC liposome. Snapshots of the diffraction pattern of scattered light were recorded at a 1 s interval during a temperature ramp. The images shown were recorded (A) and (B) immediately before, (C) during and (D) immediately after, a dramatic change in the overall scattering intensity was observed.

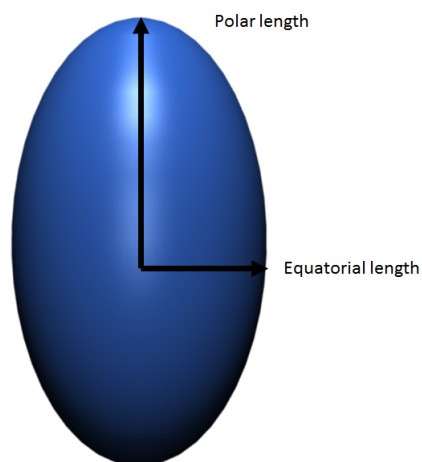


Figure 5.14: A prolate spheroid, the y axis is the polar length and the equatorial length is the x axis.

to produce a 1.5% elongation in size [122]. In our case of a 1  $\mu\text{m}$  liposome the curvature has been significantly reduced and so a much smaller force would be required to produce a deformation in size. As there is also 3-4 times increase in bending modulus when moving from the gel to liquid crystalline phase, it is conceivable that the increase in light scattering partly arises due to a deformation induced by the optical tweezers and increase in fluidity of the bilayer.

### 5.3.2 Raman measurements of liposomes

Raman spectroscopy was used to observe the changes in molecular structure over the temperature-induced transition. Figure 5.15 shows three Raman spectra in the C-H region for an optically trapped DPPC liposome in the gel (a), ripple (b) and fluid phases (c). For a DPPC liposome the C-H region comprises the symmetric ( $d^+$  2840  $\text{cm}^{-1}$ ) and antisymmetric ( $d^-$  2870  $\text{cm}^{-1}$ ) methylene stretch, the Fermi resonance of the symmetric methyl stretch ( $r_{FR}^+$  2920  $\text{cm}^{-1}$ ) and the antisymmetric methyl stretch ( $r^-$  2960  $\text{cm}^{-1}$ ). A weak band is also observed at 3030  $\text{cm}^{-1}$  for the antisymmetric  $\text{CH}_3$  stretch of the choline head group. The notation and values for these peaks are taken from [123]. Spectra a) is also consistent with the Raman spectra reported in [61] and [121]. Raman spectra for DPPC have previously been obtained for a supported lipid bilayer [124] and an optically trapped liposome [125] in the gel, ripple and fluid phases.

Some background on other spectral regions will be discussed here. The main features in Raman spectra of lipid molecules are analogous to those of long chain n-alkanes. There are distinct Raman bands within the C-C stretching region corresponding to tight and loose packing of the hydrocarbon chains in different thermotropic phases, namely: the asymmetric and symmetric C-C stretching bands at 1060  $\text{cm}^{-1}$  and 1130  $\text{cm}^{-1}$ , which originate from all-trans C-C bonds; and the skeletal C-C stretching band at 1080  $\text{cm}^{-1}$  from gauche segments of the alkyl chain. The relative intensity of the bands at 1130  $\text{cm}^{-1}$  and 1080  $\text{cm}^{-1}$  has been used to estimate the number of trans-conformational segments per alkyl chain [126]. The intensities of all the bands in the C-C stretching region are significantly lower than the bands in the C-H region, which is the reason why the latter was recorded in our experiments.

In a further spectral region, a blue-shift in the  $\text{CH}_2$  twisting mode at 1300  $\text{cm}^{-1}$  is also consistent with the disordered phase of lipid bilayers and structures that contain a broader distribution

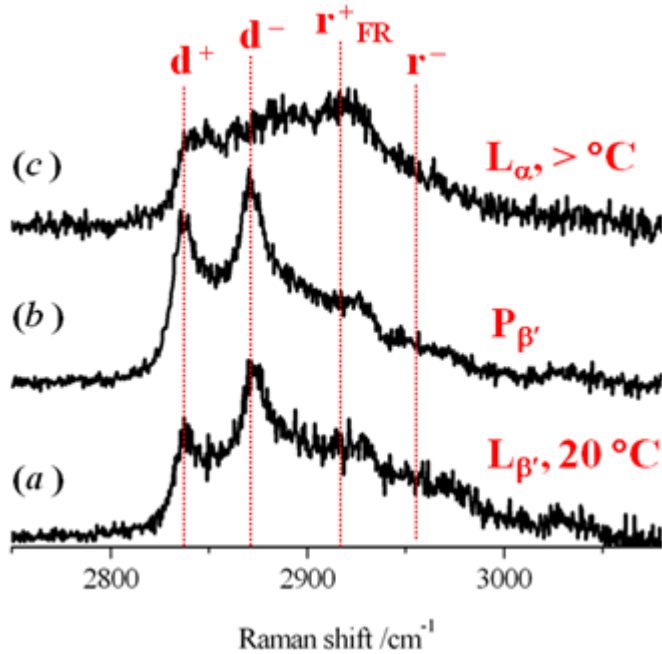


Figure 5.15: Three Raman spectra of an optically trapped DPPC liposome in the C-H region. Spectra a) is at 20 °C in the gel phase spectra b) is in the ripple phase and c) is in the liquid phase.

of gauche rotamers. The packing of the hydrocarbon chains also strongly affects the relative intensity of bands for the CH<sub>2</sub> twisting mode and the CH<sub>2</sub> scissor mode at 1440 cm<sup>-1</sup> but, unlike bands in the C-C stretching region, these methylene bands are not unique for trans and gauche segments, i.e. ordered and disordered lipid structures. The frequencies of the bending and stretching methylene modes are sensitive to the number of gauche segments. This is due to increasing steric repulsion between neighboring chains. However, the blue shift can be difficult to resolve in the C-H stretching region due to the overlapping band structure. All the methylene bands in this region are much weaker than the C-H stretching bands. The CH<sub>2</sub> wagging mode at 1370 cm<sup>-1</sup> is an extremely weak band.

The intensity ratio between the d<sup>-</sup> and d<sup>+</sup> bands,  $\frac{d^+}{d^-}$ , or, alternatively, the d<sup>-</sup> and r<sub>FR</sub><sup>+</sup> bands  $\frac{r_{FR}^+}{d^-}$ ,

has been reported in the literature to provide a qualitative measure of short-range packing order of the hydrocarbon chains, where a larger ratio is indicative of greater order [10]. In figure 5.15, the decrease in both of these ratios above the main transition for a single DPPC liposome is consistent with previous measurements. As with the elastic light scattering measurements, the gel-to-ripple pre-transition is subtle in comparison with the ripple-to-fluid transition. Raman measurements are unsuitable for high temporal resolution analysis and so the sharp width of the transition shown with the elastic scattering results cannot be reproduced for Raman.

### 5.3.3 Dynamic light scattering

The change in size and rigidity of the lipid bilayer was also investigated using dynamic light scattering. In both the high and low temporal resolution experiments, the droplet size is similar to the wavelength of the scattering laser. This means that the scattering falls into the Mie regime. In the Mie scattering regime, an increase in light scattering is expected when there is a decrease in droplet size. Figure 5.6 and figure 5.11 both show increases in light scattering. The change in size over the temperature-induced transition was recorded using dynamic light scattering. To record DLS, a 1 ml sample of a 1:100 diluted lipid solution was placed in a cuvette in the Zetasizer. The scattering intensity was recorded at 20 °C and 50 °C and used to calculate average liposome size, polydispersity index and a size by number distribution. This was calculated using software within the Zetasizer.

Figure 5.16 shows the number distribution for a sample of DPPC liposomes at 20 °C and 50 °C. The figure shows two peaks indicating the size distribution by number of the sample at 20 °C (red) and 50 °C (green). The values of the average diameter of the liposomes and polydispersity index are given in table 5.2. The dynamic light scattering results show that at room tempera-

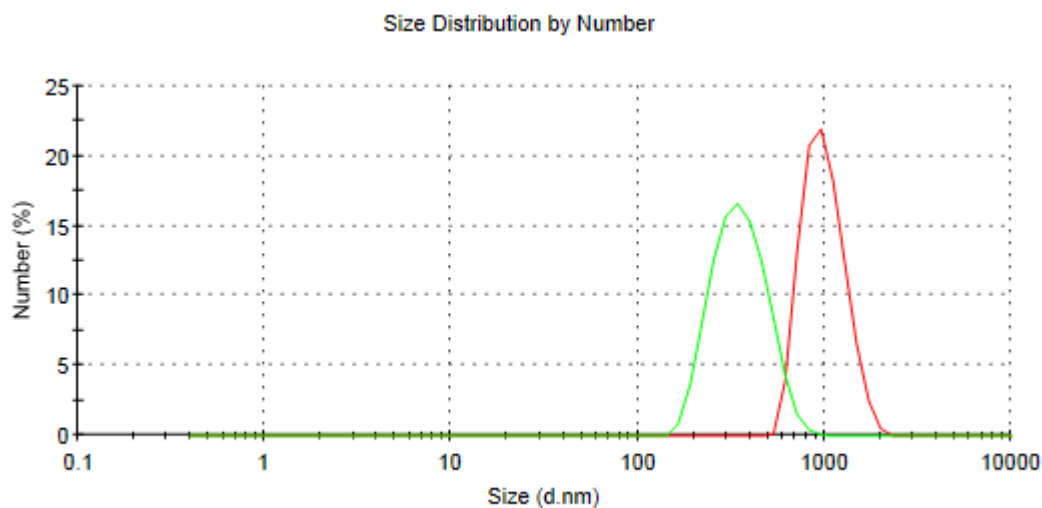


Figure 5.16: The number distribution of a 1 ml sample of DPPC liposomes at 20 °C red, and 50 °C green calculated using dynamic light scattering.

ture the average diameter of the liposomes was 973.1 nm, figure 5.16 also shows a single peak centred at approximately 1  $\mu\text{m}$  indicating that the extrusion process had been successful. The polydispersity index (PDI) describes homogeneity of the particle size. A PDI of less than 0.2 is considered to be a monodisperse sample. At both 20 °C and 50 °C, the PDI is below 0.2 indicating a monodisperse sample.

These results also show a significant decrease in the size of the liposome over the main transition of the lipid bilayer:  $z_{avg}$  decreases from 973.1 nm to 349.1 nm. This corresponds to the results from the optical tweezing experiments, where a significant increase in scattering is seen which implies a decrease in particle size in accord with the Mie scattering theory. The reduction in the interior aqueous volume could be attributed to a decrease in stiffness of the lipid bilayer and an increase in membrane permeability in the fluid phase leading to the partial collapse of the spherical shape of the vesicle.

Temperature	$z_{avg}$ nm	PDI
20 °C	973.1	0.177
50 °C	349.1	0.175

Table 5.2: The average diameter  $z_{avg}$  and polydispersity index of a sample of a 1ml DPPC liposomes at 20 °C and 50 °C.

### 5.3.4 Microdomain behaviour in fluid POPC/chol bilayers

The addition of cholesterol to the phosphocholine lipid vesicle results in more complex phase behaviour. A lipid bilayer can exist in a liquid ordered  $L_o$  phase and a mixed liquid ordered/disordered phase  $L_o/L_d$ , where transient ordered microdomains can also appear, and a liquid disordered  $L_d$  phase. In our experiments the lipid POPC was mixed with cholesterol to create binary 1:1 liposomal bilayers.

As shown in figure 5.3, the intercalation of cholesterol disrupts the triangular lattice configuration of the phosphocholine lipid molecules. In the fluid phase, a straight trans conformation of the hydrocarbon chains is favoured, where the lipids tilt angle is negligible. This results in a higher degree of short-range order than typical in the fluid phase of a lipid bilayer. For a single component POPC lipid bilayer the average area per lipid molecule is  $0.683 \text{ nm}^2$  [127], but this can decrease by 40% with a mole fraction of cholesterol of  $> 0.5$  [128].

The experimental details were similar to previous experiments. After the lipid sample of POPC/cholesterol had been extruded, a 1:1000 diluted sample of POPC/cholesterol and buffer (PBS) was prepared. A  $50 \mu\text{l}$  drop was then pipetted onto a 1.5 cover glass resting on the heating plate. The liposome was then optically trapped by adjusting the position of the stage.

As before the sample was heated and the 1070 nm light scattering was recorded at low temporal resolution. The left side of figure 5.17 shows the low time resolution temperature dependence of

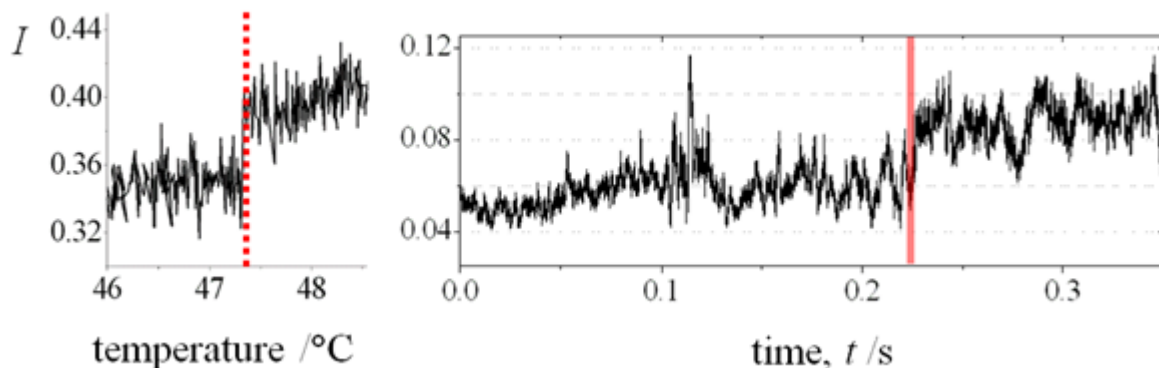


Figure 5.17: The back scattered 1070 nm light from an optically trapped POPC/cholesterol liposome over the unregulated temperature ramp of  $0.025\text{ }^{\circ}\text{C}$  per second at low temporal resolution (left). A small rise in light scattering is seen between  $47\text{ }^{\circ}\text{C}$  and  $47.5\text{ }^{\circ}\text{C}$ . The back scattered 488 nm light from an optically trapped POPC/cholesterol liposome taken at high temporal resolution (right). The full width of the transition is  $4\pm 2\text{ ms}$  illustrated by the red box, labelled  $T_m$ .

the 1070 nm light scattering for an optically trapped POPC/cholesterol liposome. An unregulated temperature ramp of approximately  $0.025\text{ }^{\circ}\text{C s}^{-1}$  was applied to observe the transition between the  $L_o$  phase and co-existing  $L_o/L_d$  phases. The example shown in figure 5.17 is a representative trace, it is shown for two liposomes in figure 5.19.

This increase in scattering can be considered as a cause of a deformation from a spherical shape to a prolate spheroid aligned along the propagation of light, this could be attributed to the force from the trapping laser. Like the gel-to-liquid transition the Young's modulus of lipid bilayers in disordered and ordered phases is considered in [122]. It is shown that for higher proportion cholesterol bilayers, larger forces are required to make a significant deformation of the bilayer.

A DSC trace is shown for a sample of POPC/cholesterol in figure 5.18. Although a change in membrane fluidity has been observed over a heating ramp for POPC/cholesterol in [115] and a change in elastic scattering has also been observed for a single optically trapped liposome in

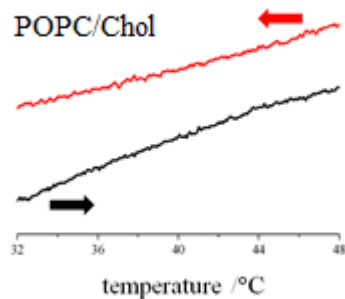


Figure 5.18: Differential scanning calorimetry thermograms of POPC/cholesterol. A 20  $\mu\text{g}$  sample of the concentrated suspension of liposomes was used; the scan rate was 0.5  $^{\circ}\text{C}/\text{min}$ . The black line shows the heating trace and the red line shows the cooling trace.

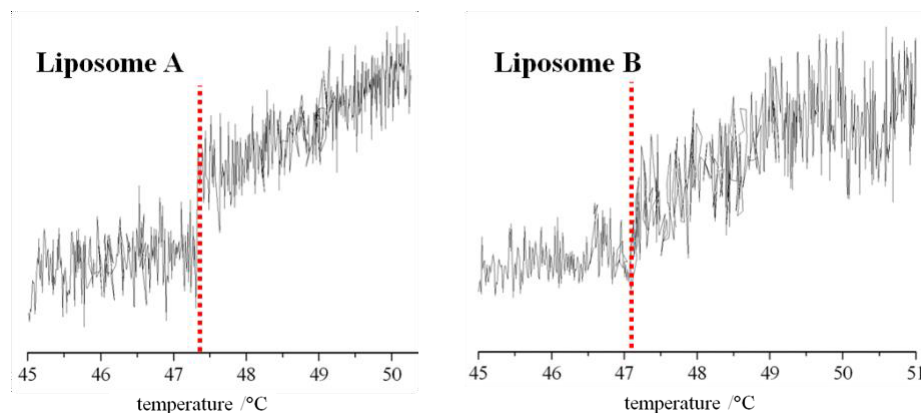


Figure 5.19: The profile of the back scattered intensity, at 1070 nm, measured for 2 different optically-trapped POPC/cholesterol liposomes during the heating stage of a temperature ramp. The data for Liposome A is also shown in Figure 5.17.

figure 5.17, no enthalpy change is detected by DSC. As such, a true thermotropic phase transition cannot be confirmed for the transition from an ordered lipid bilayer to the ordered/disordered bilayer.

A small rise in light scattering was observed over two data points corresponding to a temperature difference of 0.006  $^{\circ}\text{C}$ . The transition was observed at 47.3  $^{\circ}\text{C}$ , which is consistent with reported

diagrams shown in figure 5.4. The figure shows a small increase in intensity of the light scattering. In the Mie regime an increase in the intensity of back scattered light would normally be due to a decrease in the size of the vesicle. The magnitude of the intensity change, relative to the signal noise, is much lower than for the gel-liquid crystalline transition. This could be attributed to the subtle nature of transitions between liquid disordered and liquid ordered domains.

As the transition occurred over only two data points, to accurately time the morphological change of the liposome over the transition, the higher temporal resolution photodiode was used. The right side of figure 5.17 also shows the high resolution light scattering time dependence of the 488 nm light of an optically trapped POPC/cholesterol liposome. Like the low temporal resolution data, a small increase in scattering intensity is seen, between 0.2 s and 0.3 s. The transition was observed across  $4 \pm 2$  ms, which is highlighted in red, this corresponds to a temperature difference of  $0.0001$  °C.

Figure 5.20 shows a set of Raman spectra in the C-H stretching region, recorded from an optically trapped POPC/cholesterol liposome taken as it was heated from  $20$  °C to  $50$  °C. Raman spectra for lipid bilayers comprising of 1:1 POPC/cholesterol and 1:1 DPPC/cholesterol have been shown in [129] for a range of temperatures. For the POPC/cholesterol bilayer this work showed a decrease in the ratio of peaks,  $\frac{d^+}{d^-}$  between  $50$  K and  $315$  K, between  $200$  K and  $315$  K this decrease was from  $1.3$  to  $1$ . Figure 5.20 shows a small increase in the ratio  $\frac{d^+}{d^-}$  between temperatures  $298$  K and  $315$  K from  $0.95$  to  $1.1$ .

The small increase in the ratio  $\frac{d^+}{d^-}$  would normally indicate greater packing order across the bilayer, however it would be expected that between the  $L_o$  and  $L_o/L_d$  phases there would be a decrease in local packing order. This is perhaps due to the  $488$  nm laser only probing a relatively small layer of the bilayer.

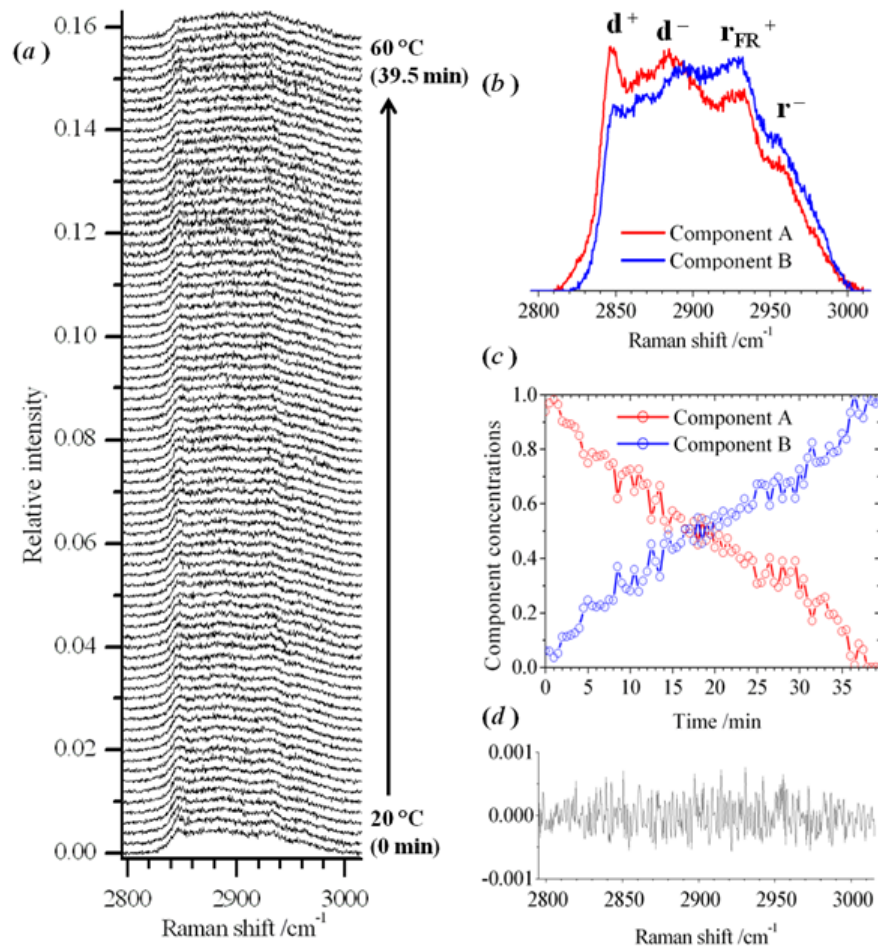


Figure 5.20: a) A set of Raman spectra for an optically trapped POPC/cholesterol heated from 20 °C to 60 °C. Spectra were recorded every 30 seconds. b) The two principle components of the set of spectra. c) The component concentrations for the set of spectra shown in (a). d) The residual for the 35th spectrum, recorded after 17 minutes, following optimisation of the component profiles.

The results of multivariate curve resolution on the sequence of Raman spectra is shown in the figure labelled (b) and (c). A fitting of two components captured 99.0% of the variance in the experimental data. In (d), the residual is shown for a representative example from the sequence of experimental spectra shown in (a). The residual in (d) corresponds to 19 minutes, where the

component concentrations are approximately equal. The signal remaining in (d) appears to be stochastic, without any trace of the C-H stretching band, and hence supports the suitability of the multivariate model. The chemometric analysis suggests that the Raman intensity profile changes continuously, and smoothly, between 20 and 60 °C. The fitted components, A and B, bear a close resemblance to the initial and final experimental spectra, respectively. The gradual change in the intensity profile for the sequence of Raman spectra in Figure(a) contrasts with the discrete change in the light-scattering profile assigned to the  $L_o \rightarrow L_o/L_d$  transition in figure 5.17. Hence elastic-light scattering and Raman spectroscopy are sensitive to different physical changes in the lipid bilayer. While a discrete phase transition can be determined by elastic-light scattering, the changes in ensemble-averaged properties of the lipid molecules in the bilayer are reported in the Raman spectra. The ensemble averages for the lateral packing of hydrocarbon chains and rotational diffusion of lipids appear to change continuously across a broad range of temperature near the phase boundary according to the Raman spectral profiles.

To characterize the change in size of POPC/cholesterol liposomes as they were heated dynamic light scattering was used. A sample of POPC/cholesterol and buffer at a dilution of 1:100 was used. Figure 5.21 shows the size distribution by number for a 1 ml sample of POPC/cholesterol at 20 °C (red) and 50 °C (green). As before the red peak is centred around 1  $\mu\text{m}$ , indicating a successful extrusion.

Table 5.3 shows the values of  $z_{avg}$  and PDI taken from the DLS experiment. The table shows a small increase in size from 811.9 nm to 869.5 nm between the two temperatures. As the change in size is small it is likely that the change in elastic scattering shown in figure 5.17 is largely due to a decrease in rigidity. The table also shows the PDI at 20 °C and 50 °C, at both temperatures it is low enough for the sample to be considered monodisperse. There is also a significant rise in the PDI between the two temperatures.

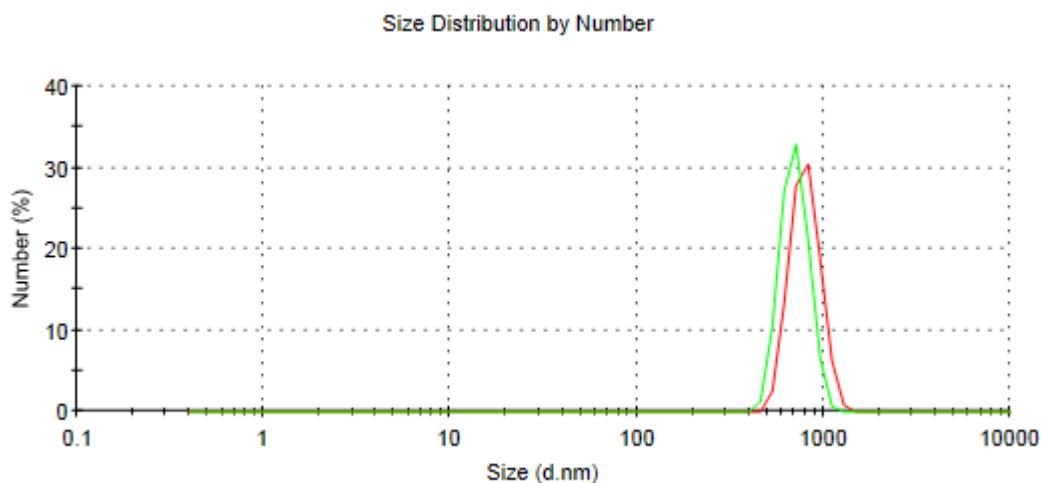


Figure 5.21: The number distribution of a 1 ml sample of POPC/cholesterol liposomes at 20 °C (red), and 50 °C (green) calculated using dynamic light scattering.

Temperature	$z_{avg}$ nm	PDI
20 °C	811.9	0.084
50 °C	869.5	0.15

Table 5.3: The average diameter  $z_{avg}$  and polydispersity index of a sample of 1:1 POPC/cholesterol liposomes at 20 °C and 50 °C.

### 5.3.5 Microdomain behaviour in fluid POPC/chol/SM bilayers

To observe the transition from the liquid ordered/disordered phase to liquid disordered phase a ternary mix of POPC, cholesterol and sphingomyelin (SM) was prepared with 1:1:1 molar mass. This gives a liquid ordered/disordered bilayer  $L_o/L_d$  at 20 °C and liquid disordered bilayer  $L_d$  at 50 °C. For the optical tweezing experiments, the extruded sample was diluted 1:1000 in PBS and a 50  $\mu$ l droplet of this solution was pipetted onto a No 1.5 thickness glass slide resting on the heating plate. A liposome was then optically trapped by adjusting the stages position in the  $x$  and  $y$  directions. The liposome was heated using an unregulated temperature ramp of 0.025 °C per second.

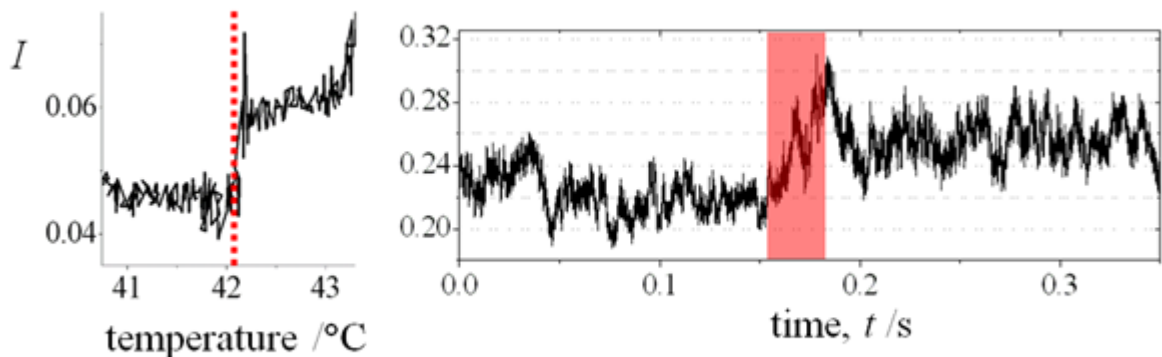


Figure 5.22: The back scattered 1070 nm light from an optically trapped POPC/cholesterol/SM liposome over the unregulated temperature ramp of 0.025 °C per second at low temporal resolution (left). A rise in light scattering is seen between 42 °C and 43 °C. The back scattered 488 nm light from an optically trapped POPC/cholesterol/SM liposome taken at high temporal resolution (right). The full width of the transition is  $30 \pm 5$  ms illustrated by the red box.

The left side of figure 5.22 shows the temperature dependency of 1070 nm light scattering at low temporal resolution from an optically trapped POPC/cholesterol/SM liposome. The increase in scattering occurs over only two data points corresponding to a temperature difference of 0.006 °C. Much like the liquid ordered to liquid ordered/disordered the change in intensity is much subtler than for the gel-to-liquid crystalline transition. The phase transition was observed at 42.1 °C, which is consistent with reported phase diagrams. The trace shown on the left side of figure 5.22 is a representative example, it is shown for two liposomes in figure 5.24. Again the increase in scattering can be attributed to a deformation of the bilayer from the decrease in rigidity as described in [122].

A DSC trace is shown for a sample of POPC/cholesterol/SM in figure 5.23. Like the POPC/cholesterol sample, no enthalpy change can be detected in the sample. Therefore no thermotropic

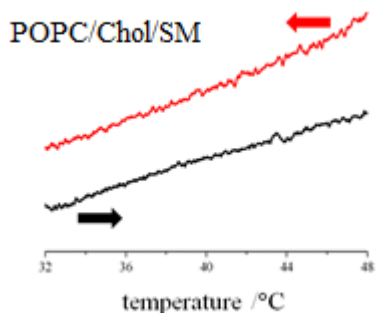


Figure 5.23: Differential scanning calorimetry thermogram of POPC/cholesterol/SM. A 20  $\mu\text{g}$  sample of the concentrated suspension of liposomes was used; the scan rate was 0.5  $^{\circ}\text{C}/\text{min}$ . The black line shows the heating trace and the red line shows the cooling trace.

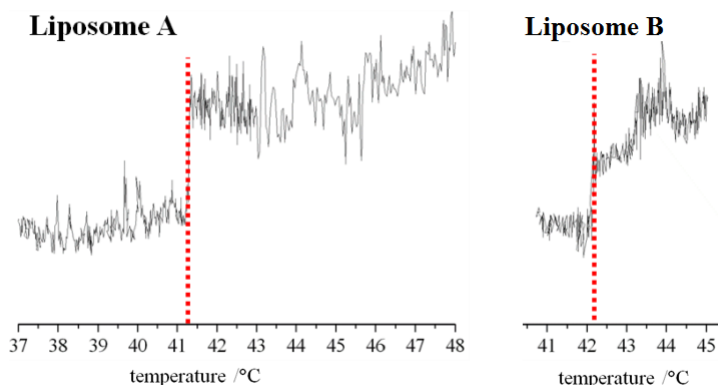


Figure 5.24: The profile of the back-scattered intensity, at 1070 nm, measured for 2 different optically-trapped POPC/cholesterol/sphingomyelin liposomes during the heating stage of a temperature ramp. The data for Liposome B is also shown in figure 5.22.

phase transition can be confirmed for the dissolution of ordered microdomains within the largely disordered bilayer.

The right side of figure 5.22 shows the time dependency of the 488 nm light scattering at high temporal resolution. The transition,  $L_o/L_d$  to  $L_d$ , is shown by an increase in scattering from

approximately 0.2 V to 0.24 V, the width of the transition is highlighted in red in the figure. The highlighted red area corresponds to a time of  $30 \pm 5$  ms and the lower limit for the full width is  $0.001$  °C. In [130], the width of this transition was measured using imaging techniques (iSCAT) as being less than 100 ms, though this was the limit of the experiments temporal resolution.

Figure 5.25 a) shows a set of Raman spectra recorded for a single optically trapped POPC/cholesterol/SM liposome as it was heated from  $20$  °C to  $60$  °C. Spectra were recorded every 30 seconds and there are a total of 66 spectra. The relative intensity of the spectra rises over the temperature ramp due to the thermal expansion of the heating plate. The difference in ratios  $\frac{d^-}{d^+}$ ,  $\frac{r_{FR}^+}{d^-}$  can again be used as a measure of packing order. There is a small increase in the ratio  $\frac{d^-}{d^+}$  between the first and last spectra. This is contrary to the expected result for a decrease in packing order. However there is also a strong increase in  $\frac{r_{FR}^+}{d^-}$ , which is known to indicate a decrease in packing order.

Using the multivariate Raman analysis algorithm the set of spectra shown in a) can be split into a component form. The algorithm splits the set of spectra into two components accounting for 99.4% of the variance of the fit. The fitted components, A and B, bear a close resemblance to the initial and final recorded spectra, respectively. The result of the multivariate analysis is shown in c), the spectra are marked with circles and the component concentrations are shown as red and blue lines. The analysis shows a gradual linear change in the concentration of the respective components.

In Figure 5.25 (d), the residual is shown for a representative example from the sequence of spectra to illustrate the quality of the analytical fit to the experimental data. The example in figure 5.25 (d) corresponds to the measurement at 17 minutes, which contains approximately equal concentrations of the two components and exhibits the most significant residual.

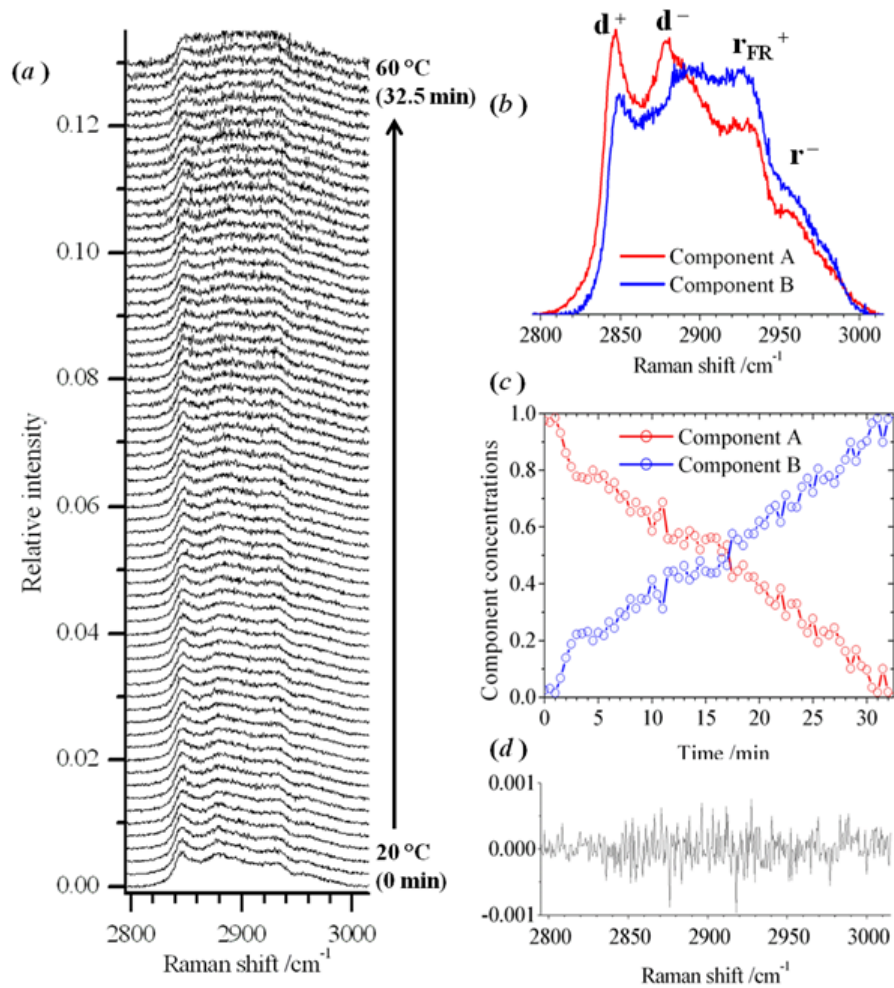


Figure 5.25: a) A set of Raman spectra for an optically trapped POPC/cholesterol/SM heated from 20 °C to 60 °C. Spectra were recorded every 30 seconds. b) The two principle component profiles of the set of spectra c) The component concentrations for the set of spectra shown in (a). d) The residual for the 35th spectrum, recorded after 17 minutes, following optimisation of the component profiles.

## 5.4 Conclusions and future work

The results described in this chapter demonstrate that the temperature-induced phase transitions and the formation and dissolution of ordered microdomains in a single liposome can be moni-

tored by light scattering.

A more complete study of the temperature-induced transitions could be undertaken for lipid mixes with different acyl chain lengths, different numbers of double bonds and of different sizes. To carry out this work a more refined system for controlling and recording temperature could be used to give a precise reading of the temperature difference over the transition. One possibility is to design a small environmental chamber that is compatible with the optical tweezers and can control the temperature ramp with high precision. This could potentially also resolve the problem of the heating plate expanding.

The Raman spectra shown in this chapter and the literature show a gradual change in the local molecular packing order of the lipid bilayers, over the temperature ramp, for three different lipid blends. This can be contrasted with the sharp changes in elastic light scattering occurring at the established transition temperatures. It can be inferred that there is a continuous change in packing order as a bilayer is heated, eventually leading to a sharp change in the droplets size or rigidity.

The experiments discussed in this chapter also investigate the formation and dissolution of ordered microdomains within a lipid bilayer. There is controversy surrounding the behaviour of lipid rafts, it is unclear whether the structure of POPC/cholesterol bilayers should be described by phase separated ordered and disordered regimes or a gradual change in homogeneity. By measuring an area of the spherical bilayer corresponding to a few micrometers we are able to show a change in elastic scattering corresponding to a change in bending modulus (a decline in rigidity) at the reported temperatures for the dissolution of ordered microdomains. It is likely that these abrupt changes correspond to the point when ordered microdomains cease to exist or appear in a largely disordered bilayer. The DSC results showed no change in heat flux at the correspond-

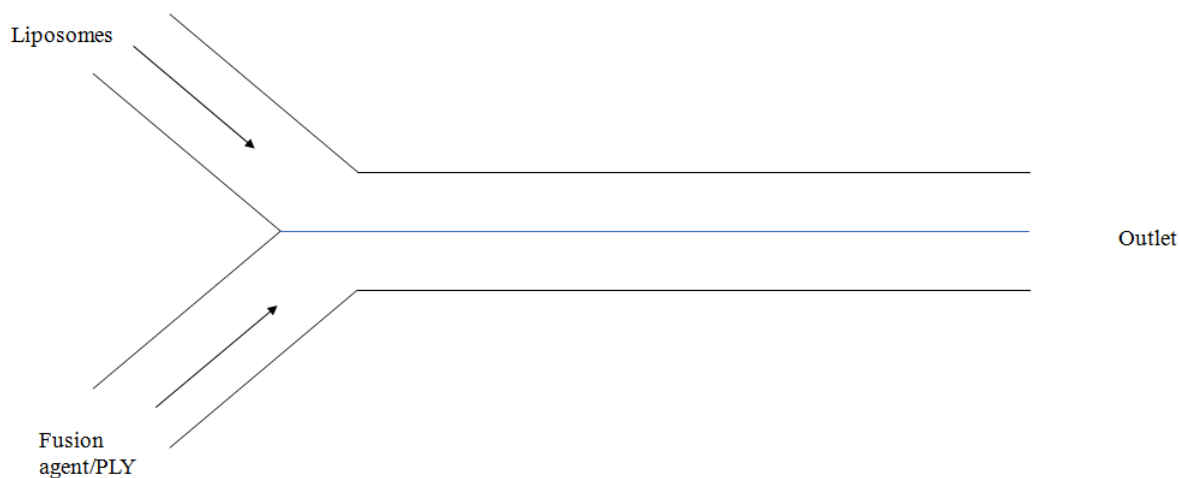


Figure 5.26: A microfluidic device, there are two inlets typically one is used for liposomes and the other filtered inlet is used for solutions of the toxin or a fusion agent. The speed of the inlet flows is configured so that the two solutions form a laminar flow, separating the two solutions. A liposome can then be optically trapped and dragged into the other solution.

ing temperatures, this can be compensated for as the ordered microdomains are continuously assembling and disassembling.

The bending rigidity for cholesterol enriched lipid bilayers has previously been investigated for giant unilamellar vesicles of approximately  $20\ \mu\text{m}$  diameter in [131]. By video microscopy, the bending modulus of the liposome is recorded for liposomes at different temperatures and different cholesterol concentrations. Though the experiment did not show a likely decrease in rigidity of the bilayer it is likely that the optical tweezing experiment is significantly more sensitive to the subtle change in rigidity. The optical tweezers are likely to deform the liposome to a prolate sphere and therefore induce an increase in light scattering. The molecular diffusion across a phosphocholine/cholesterol has previously been observed to exhibit a smooth change with increases in temperature [132], however it is relatively likely that the diffusion in the disordered bilayer is unaffected by the local formation of ordered microdomains within the bilayer.

Overall optical trapping has been shown to be a valuable method to study changes in an individual liposomes structure, elastic scattering and Raman scattering can be used to probe changes in molecular structure and morphology. Outside of temperature-induced transitions there are many other phenomena that could be observed for a single vesicle using optical tweezing. The absorption of a membrane protein on a liposomal bilayer could be observed using both elastic and inelastic techniques. The fusion of two liposomes could also be observed using elastic light scattering techniques, like temperature transitions liposome fusion is used as a method for drug delivery.

These types of experiment rely on being able to expose an optically trapped liposome to another solution, this can be accomplished using microfluidic devices. The optical tweezing group at the University of Leicester is currently investigating both protein absorption and liposome fusion. Silicon microfluidic devices have already been designed and built, a diagram showing the structure of such a device is shown in figure 5.26.

# **Chapter Six - Elastic light scattering and mathematical modelling of the coalescence of aerosol microdroplets**

## **6 Elastic light scattering and mathematical modelling of the coalescence of aerosol microdroplets**

This chapter contrasts experimental elastic light scattering measurements with the mathematical modelling of the coalescence of liquid aerosol droplets. The results presented in this chapter have previously been published in [133]. The introduction to this thesis describes how the coalescence process is driven by the Reynolds number which describes the ratio of inertial to viscous forces. The early stages of coalescence are divided into two regimes, an initial viscous regime and then an inertial regime [5]. After the two droplets make contact, the composite droplet undergoes a viscously damped oscillation [2]. In the case of a highly viscous droplet the oscillation is said to be over damped by viscosity, the spherical shape of the composite droplet is recovered by a gradual increase in the height of the handle. In this chapter both over damped and under damped droplets are considered.

The orientation of the coalescence event in the optical trap is also considered (i.e. transverse and parallel to the imaging plane). The elastic light scattering trace is dependant on the position of the droplet (relative to the propagation of light). These are shown to probe different modes of the oscillation with different sensitivities. Mathematical modelling allows for a complete analysis of this behaviour.

The results presented in this chapter focus on droplets of radius 6-10  $\mu\text{m}$ . The aspect ratio of the simulations is shown to correspond with the oscillation observed by elastic back scattered light measurements. In the viscous case, the gradual fall in light scattering following coalescence is also fitted against the aspect ratio. Here, images taken using a high frame rate camera can also be compared with simulated images. In this chapter, high frame rate camera images, elastic light

scattering and mathematical modelling techniques are compared to analyse the coalescence of aerosol droplets with different viscosities. The initial trajectory of the moving droplet relative to the optical trap is also considered.

## **6.1 Experimental and computational techniques**

This section will give a brief description of the experimental and computational techniques used to analyse the coalescence of liquid aerosol droplets. As a description of the design of holographic optical tweezers has already been given in chapter four this will not be discussed in depth again. The elastic light scattering measurements of the coalescence of optically trapped aerosol droplets shown in this chapter were taken at the University of Bristol. Rather than give a complete description of these optical tweezers the important differences between those used at the University of Leicester will be outlined.

Similarly, as the finite element procedure to used model the coalescence has been described in detail in chapter two this will not be described again. As the process produces a set of coordinates in two dimensions and a time stamp for each stage of the coalescence, the processes used to recover the aspect ratio over time of the droplet will be given. A description will be given of how the coordinates are used to produce videos of the coalescence using the JReality software package.

### **6.1.1 Optical tweezers measurements**

The optical tweezers used at the University of Bristol are similar to those used in the previous chapter. The trapping laser is guided by a series of mirrors and lenses onto a spatial light modulator which sets the phase pattern on the beam. The trap is created by an inverted high numerical

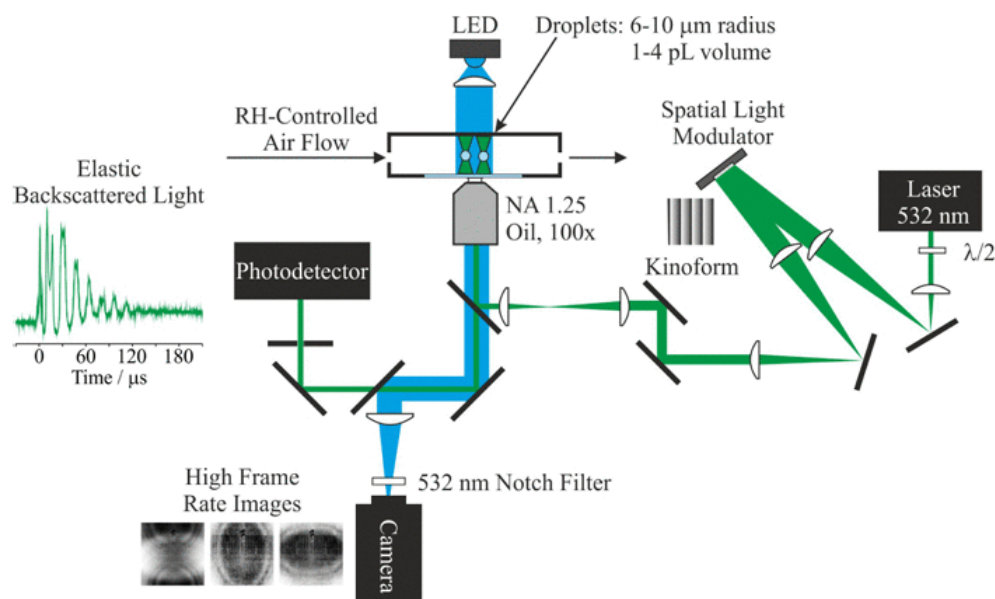


Figure 6.1: A simplified schematic of the optical tweezers used at the University of Bristol.

aperture microscope objective. Dichroic mirrors are used to reflect light from the LED and scattered light onto a photodiode and CCD. A simplified schematic is shown in figure 6.1; it was produced at the University of Bristol.

The trapping laser used was a visible 532 nm laser. The 532 nm laser is known to produce an optical heating effect of 1-10 mK on the aerosol droplet whereas the 1070 nm laser gives a heating effect on the order of 1 K [134]. Previously the coalescence experiment has been compared between a 1070 nm and 532 nm trapping laser [1]. If the 1070 nm laser is used to trap the droplet, then the composite droplet undergoes heating leading to evaporation.

The aerosol flow was generated inside a sealed chamber using a nebulizer (Omron NE U22), the trapping chamber is isolated from the microscope with a cover slide (Chance Glass, # 0

thickness). It was also possible to flow dry and humidified nitrogen into the chamber to control the relative humidity (RH). The RH could then be measured at the outlet of the flow using a capacitance probe. The aerosols viscosity is strongly effected by changes in RH. This allows the coalescence to be recorded at different viscosities.

The spatial light modulator could be used to create two optical traps above the microscope objective. The SLM is controlled in the same way as discussed in chapter four, the position can be adjusted in 3 dimensions at sub-micrometer accuracy. As the SLM is controlled using a computer the position of one trap can be dragged toward the other, once the droplets are sufficiently close together the coalescence process will begin. This could be done so that the coalescence was triggered parallel to the trapping laser or transverse to the propagation of light. The elastic light scattering from the 532 nm laser was then recorded on a high resolution photodiode. The photodiode was connected to an oscilloscope. The oscilloscope was triggered so that once the coalescence process began it would acquire the modulated intensity of the light scattering.

Images could also be recorded using a high frame rate camera (time resolution  $< 10 \mu\text{s}$ )(Vision Research, Phantom v. 7.3), this temporal resolution is shown to be appropriate for high viscosity droplets, but is unable to capture detailed features from low viscosity aerosol. Images were collected, and the contrast of these images was enhanced using the ImageJ software package in order to more clearly show the position and shape of the droplets.

### **6.1.2 Computer simulations**

The finite element procedure described in the introduction chapter has been used to simulate the coalescence of aqueous aerosol. The simulation gives a complete description the dimensions of the droplet over time. It produces coordinates in  $x$  and  $y$  for one quadrant of the compos-

ite droplet. These coordinates are then rotated to produce 3D images, this can be done as the coalescence is equivalent in 2 and 3 dimensions [5].

The oscillation in elastic back scattered light for coalescing optically trapped aerosol droplets is compared to the oscillation in aspect ratio for the simulated coalescence. That is for each time step, the value of  $y$  at  $x = 0$  is divided by the value of  $x$  at  $y = 0$  (in top right quadrant). The code used to calculate the aspect ratio is given in appendix B.

In the high viscosity case, the light scattering measurement is inappropriate to probe the morphological change. Instead images are taken of the coalescence using the high speed camera allowing for a direct comparison of the shape of the droplet. The high speed camera has a time resolution of  $<10 \mu\text{s}$  and so an exact time stamp cannot be specified, therefore the simulated images correspond to the midpoint of the exposure time.

## **6.2 A comparison of mathematical modelling with previous light scattering results**

Firstly, the mathematical modelling techniques will be compared to the coalescence results presented for aqueous aerosol in [1] which were also recorded at the University of Leicester. In [1], an aqueous solution of aerosols were nebulized with an NaCl content of  $35 \text{ gL}^{-1}$ . A droplet was then optically trapped with the 532 nm optical trap. Another droplet was then allowed to flow into the trap freely to induce coalescence.

For water, the values of the physical properties at room temperature governing the coalescence process are given by surface tension  $\sigma=73 \text{ mNm}^{-1}$  and shear viscosity  $1.0 \text{ mPa s}$ . The nebulizer is known to generate droplets of radius  $1\text{-}6 \mu\text{m}$ , the droplets were modelled as having radius  $r =4 \mu\text{m}$ .

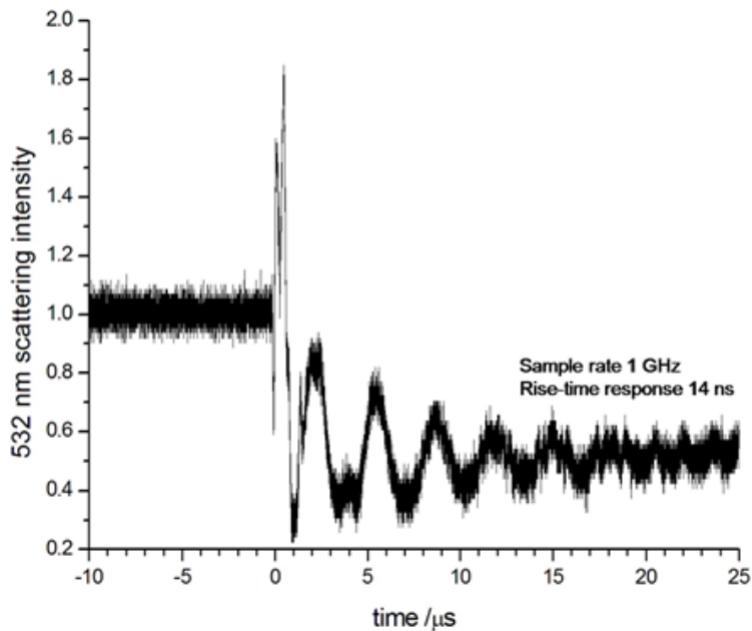


Figure 6.2: The scaled high resolution elastic light scattering of optically trapped aqueous droplets over the coalescence. The light scattering is sampled at 1 GHz with 14 ns rise time, the figure was taken from [1].

Figure 6.2 shows the elastic back scattered light during the coalescence of the two aqueous aerosol droplets as presented in [1]. The light scattering shows approximately 6 periods of the oscillation. The frequency of the oscillation is approximately 2 MHz. The sharp peak seen at  $t = 0$  marks the initial point of contact of the droplets. The initial contact of the two droplets is challenging to resolve in the scattering theory, however, the finite element model can produce images of this stage.

The elastic light scattering and simulated aspect ratio are shown together in figure 6.3. The light scattering trace has been normalized so that the baseline is set to zero to simplify comparisons to mathematical modelling (the original figure showed a baseline of 0.5 V). The initial peak at  $t = 0$  has also been removed as this stage cannot be resolved using light scattering. The simulated

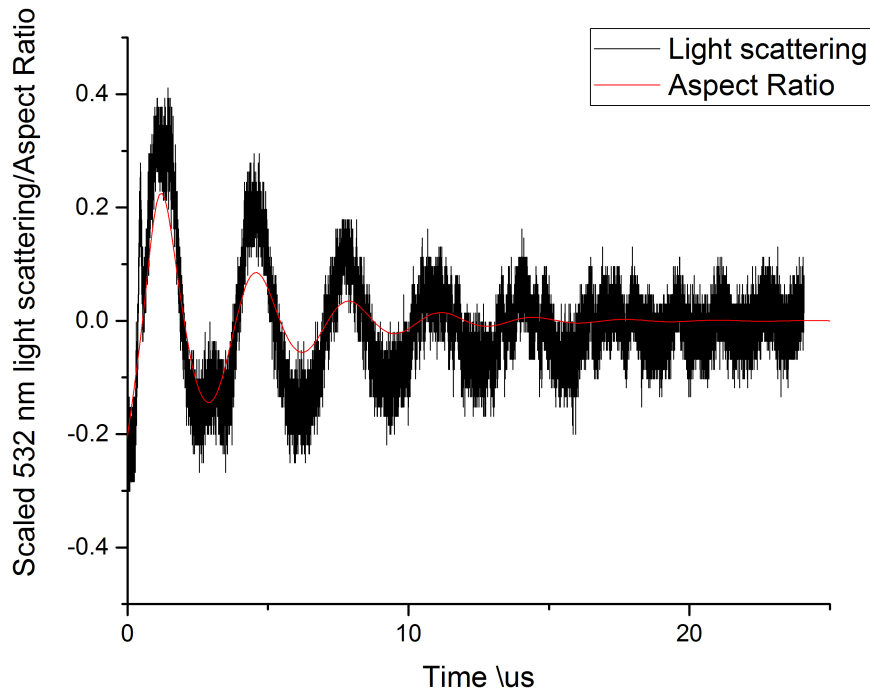


Figure 6.3: The simulated aspect ratio and light scattering trace plotted over each other. The aspect ratio has been scaled so that it may be fitted over the light scattering data.

aspect ratio has been normalized so that it may be fitted over the light scattering trace. The first periods of the oscillations are then fitted together. From the figure, it is clear that the oscillation in simulated aspect ratio corresponds to the oscillation in back scattered light.

Images of the coalescence of  $4 \mu\text{m}$  radius droplets are shown in figure 6.4. A video showing the full evolution is available at [135]. One frame of the video corresponds to  $0.27 \mu\text{s}$  and there are 20 frames per second. The oscillation in aspect ratio is clear. The composite droplet oscillates between a prolate and oblate sphere.

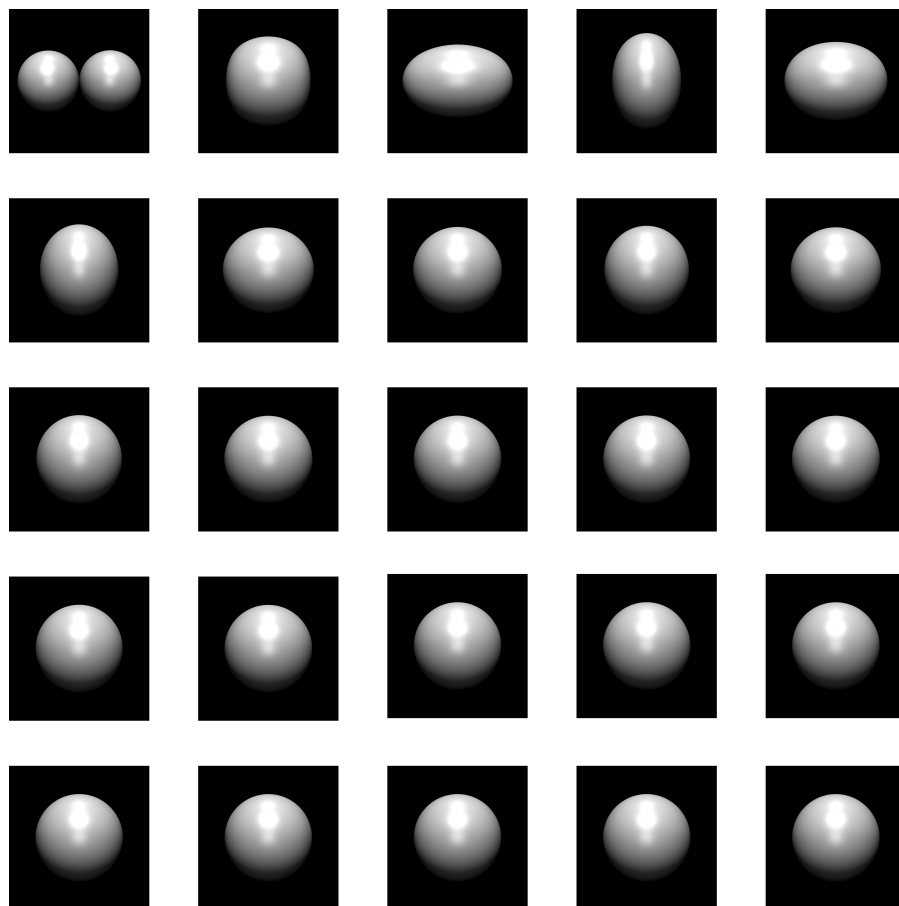


Figure 6.4: Images of the simulated coalescence of aqueous aerosol droplets. There are 20 timesteps between each image.

### 6.3 Results and discussion

Elastic light scattering measurements were taken for the coalescence of high and low viscosity droplets. The intensity of the light scattering was shown to be in strong correlation with finite element based simulations of the aspect ratio and radius of the droplet. The intensity of the back scattered light is dependant on the orientation of the droplet in the optical trap. The mathematical modelling allows the coalescence to be viewed from any orientation and hence can be compared to the two orientations we consider. As the finite element simulations gives all coordinates of

the oscillating droplet, these results could also be compared with images of the high viscosity droplets taken on the high time resolution camera.

### **6.3.1 Analysis of low viscosity droplets, the affect of droplet orientation**

As discussed in the introduction, Egger's showed that the coalescence phenomena for spheres is equivalent in two and three dimensions, i.e. the oscillating droplet is a surface of revolution. Therefore, the intensity of light scattering could potentially be affected by the orientation of the merging droplet. This is illustrated in figure 6.5. The direction of back scattered light is considered to be along the  $y$  axis and is shown by the green arrow. The left image shows a coalescence transverse to the direction of scattered light. The position of this composite droplet relative to the optical traps is dependant on the initial size of the droplets [136]. As the droplets are assumed to be of equal size, it can be assumed that the composite droplet lies approximately equidistant between the optical traps. The right image shows a coalescence transverse to the back scattered light. The figure shows that in each case the beam is probing different areas of the droplet. In the transverse case the laser probes the meniscus which is driving the coalescence. In the parallel case, the laser probes the expanding and contracting circular region of the droplet.

The effect of the droplet's orientation within the optical trap has been considered experimentally and computationally. Figures 6.6 and 6.7 present images and light scattering traces for the merging droplet in the transverse and parallel direction. Figure 6.6 shows high frame rate images ( $8 \mu\text{s}$  time resolution) of the oscillation induced by the coalescence in the transverse direction. At time  $t < 0$ , the two precursor droplets are visible at the top and bottom of the image. The image has been cropped so that only the region of interest is included. After time  $t = 0$ , the composite droplet is observed to oscillate in shape, with the distortion decreasing with time until the droplet

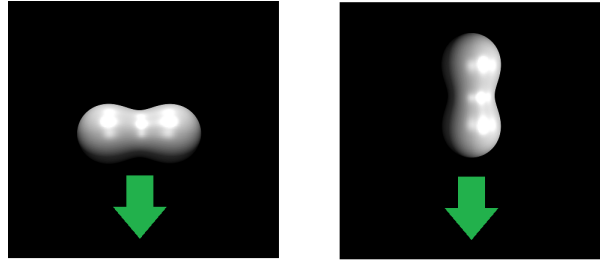


Figure 6.5: Two possible orientations for a merging droplet in an optical trap, the green arrow shows the direction of the back scattered light. In the left image the coalescence is transverse to the laser beam, the right image the coalescence is parallel to the beam.

achieves a spherical shape at  $t \approx 60 \mu\text{s}$ . The progression in shape indicates the dominance of the  $l = 2$  oscillation mode, which corresponds to an oscillation between oblate and prolate shape (see introduction). Additionally, the location of the composite droplet is at a position approximately equidistant from the original droplets. A movement of the composite droplet away from the optical traps supports a conclusion that optical forces are much smaller than the forces driving coalescence [137]. Time-dependent aspect ratios ( $\frac{a_y}{a_x}$ ) for the composite droplet shown in a) are plotted in b). They illustrate the damped oscillator form of the shape relaxation.

The elastic back scattered light measured by the oscilloscope for the same coalescence event is shown in b). The oscilloscope records data with a time resolution of  $\sim 100 \text{ ns}$ , which is nearly two orders of magnitude improvement over the resolution provided by the high frame rate camera. A correspondence is clear between the aspect ratio and light scattering intensity, the aspect ratio is shown by the red circles. The maximum of the light scattering corresponds to the frames where the droplet is elongated in the  $y$  axis (high aspect ratio), and the minimum corresponds to the frames where the droplet is elongated in the  $x$  axis (low aspect ratio). Note that the optical traps are located at the top and bottom of the image, so a higher light scattering intensity is expected for high aspect ratio droplets. That is in the high aspect ratio case the laser probes a greater area

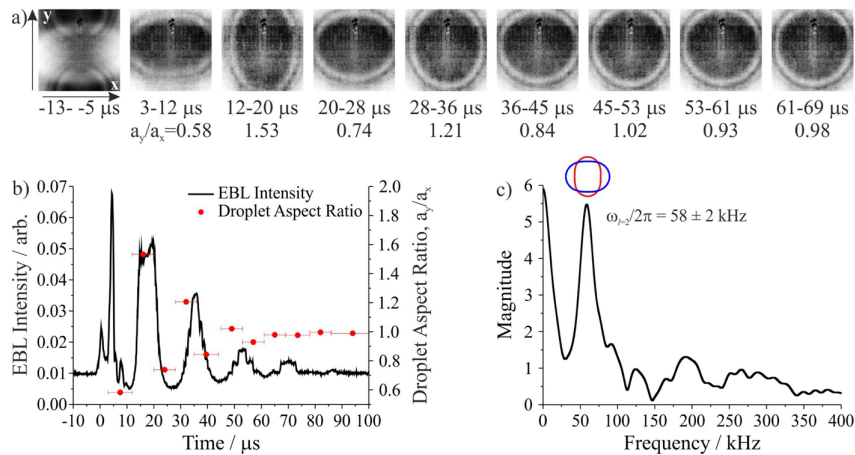


Figure 6.6: Coalescence along an axis transverse to the trapping beam of two sodium chloride droplets doped with the surfactant sodium dodecyl sulfate. (a) High frame rate camera images of the coalescence event. Time ranges underneath each image provide the exposure period during which the image was taken. Aspect ratios are also reported for each image after the coalescence time. (b) elastic back scattered light (EBL) collected after coalescence (left axis, time  $t = 0$  corresponds to the moment of coalescence) and droplet aspect ratios ( $a_y/a_x$ ) determined from high frame rate imaging (right axis). (c) Fast Fourier transform of the light scattering trace gives the frequency of the shape oscillation (the higher order features observed correspond to Fabry-Perot type interference resonances).

of the droplet and so a higher intensity of scattering would be expected.

In c), a fast Fourier transformation is applied to the light scattering trace, this allows the intensity of the modes of the oscillation to be identified. c) shows the fast Fourier transform of the light scattering trace shown in b), giving the frequency of the shape oscillation and confirming that the  $l = 2$  mode is predominately excited upon coalescence. The broad, low intensity peaks at higher frequency correspond to the  $l = 3$  and  $l = 4$  modes.

Figure 6.7 shows a coalescence event where the precursor droplets initially have different heights above the cover slip. As a result, a droplet in one trap migrates onto the axis of the adjacent trapping beam and coalesces with the other droplet along an axis parallel to the trapping beam.

Consequently the images do not capture the oscillation between an oblate and prolate spheroid shown in figure 6.6. The asymmetrical shape distortion of the composite droplet which was seen in the high frame rate images in figure 6.6, occurs in vertical planes parallel to the beam axis. The shape distortion recorded in figure 6.7 a) is symmetrical with a periodically increasing and decreasing radius that is difficult to resolve from the camera images. Although the shape distortion is unclear in the experimental images, it is evident from the variation in light scattering intensity in b).

There are many similarities to the trace shown in figure 6.6 b), most notably the periodic changes in intensity. However, there are two key differences. First, there are fewer additional features in the light scattering trace. This difference probably arises from the fact that, in this geometry, the coalesced droplet is entirely contained within one optical trap. Therefore, interference features present in the transverse coalescence geometry, which results in shape oscillations that intercept the light in both optical traps, are not present. Secondly, the fast Fourier transform of the elastic light scattering intensity (figure 6.7 c) shows that the magnitude of the  $l = 2$  mode is decreased relative to that of the  $l = 3$  and  $l = 4$  modes (at higher frequencies). This difference is likely to be the result of the modest distortion in shape for the  $l = 2$  mode perpendicular to the beam path for axial relative to transverse coalescence geometries. The observation of a coalescence event with an axial geometry enables the existence of higher order modes to be identified in the fast Fourier transform, which are not as clearly resolved in a measurement from a transverse geometry due to the dominance of the  $l = 2$  mode and additional noise from the higher frequency interference features.

The simulated aspect ratio and radius may be measured for composite droplet from both orientations. This is shown in figure 6.8. As expected the aspect ratio for the parallel coalescence shown in b) remains constant at 1. This is because we are recording the aspect ratio of an expanding and

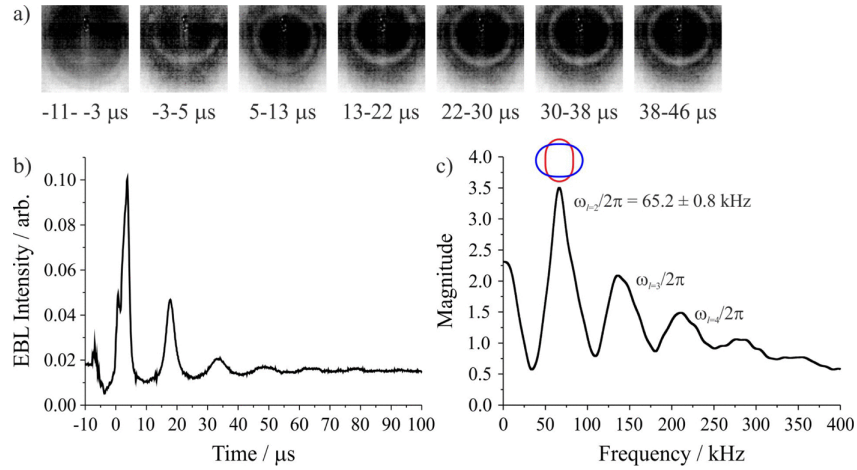


Figure 6.7: Coalescence along an axis parallel to the trapping beam of two sodium chloride droplets doped with the surfactant sodium dodecyl sulfate. (a) High frame rate camera images of the coalescence event. Time ranges underneath each image provide the exposure period during which the image was taken. (b) elastic light scattering collected after coalescence (time  $t = 0$  corresponds to the moment of coalescence). (c) Fast Fourier transform of the light scattering trace gives the frequencies of the shape oscillations.

contracting circle. Instead, the oscillation may be identified with the radius over time which is in phase with the oscillation in aspect ratio. Videos are available for the coalescence viewed from both transverse [135] and parallel directions [138]. The videos and figure show the coalescence for a droplet with  $\eta = 1 \times 10^{-3}$  Pa s,  $\sigma = 72$  mN m $^{-1}$ , and  $\rho = 1$  g cm $^{-3}$ . Each frame of the videos corresponds to a time-step of  $0.27 \mu\text{s}$  with 20 time steps per second. If different values for the physical properties of the fluid (in the under-damped regime) were taken the behaviour would largely be the same. For a higher Reynolds number fluid the frequency and intensity of the oscillation would increase.

For the coalescence examples shown above, the change in shape of the droplet has been shown to occur on a microsecond time-scale, both experimentally and theoretically. The orientation in which it is viewed is shown to affect how elastic scattering probes the coalescence. The initial

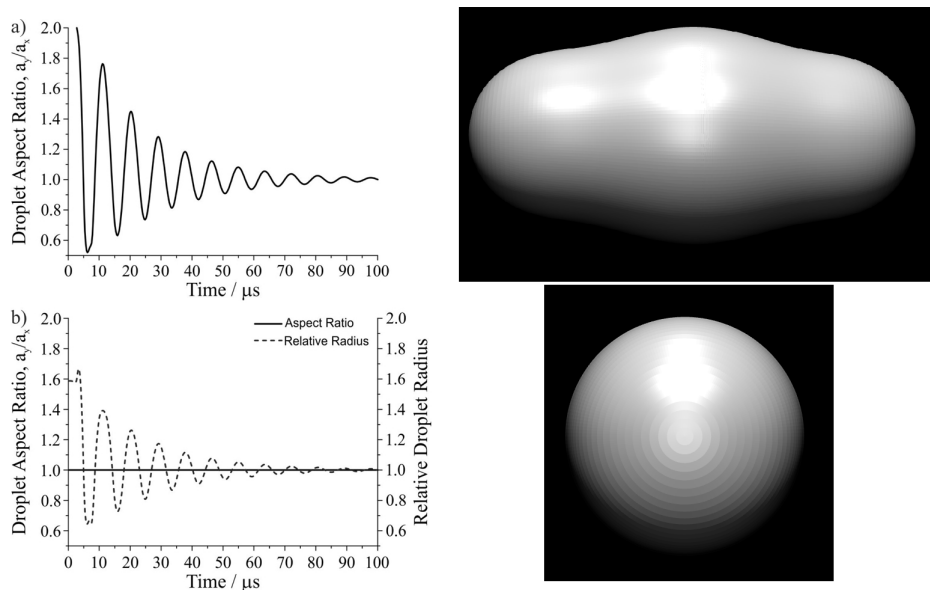


Figure 6.8: The top left shows the aspect ratio of the merging droplet when viewed in the  $x$ - $z$  plane an example image of the merging droplet is shown on the top right. The bottom left shows the aspect ratio and relative radius of the merging droplet over time when viewed in the  $y$ - $z$  plane, an example image of the merging droplet is shown in the bottom right. Simulated droplet properties are  $\eta = 1 \times 10^{-3}$  Pa s,  $\sigma = 72$  mN m $^{-1}$ , and  $\rho = 1$  g cm $^{-3}$ .

position of the droplet within the optical traps also influences the reorientation of the composite droplet. This occurs on a millisecond time-scale. Figure 6.9 shows the light scattering and images of the composite droplet showing processes occurring during the milliseconds before and after coalescence for transverse a) and parallel b) coalescence. In both, the large spike in light scattering at time  $t = 0$  corresponds to the moment of contact where the meniscus forms. For the transverse coalescence a), a gradual decrease in light scattering intensity is observed over the first 2 ms after the end of the shape oscillation (which occurs in between the two optical traps).

From the high frame rate images, it is clear that this gradual decrease results from the recapture of the composite droplet in one of the optical traps. On the other hand, for the coalescence

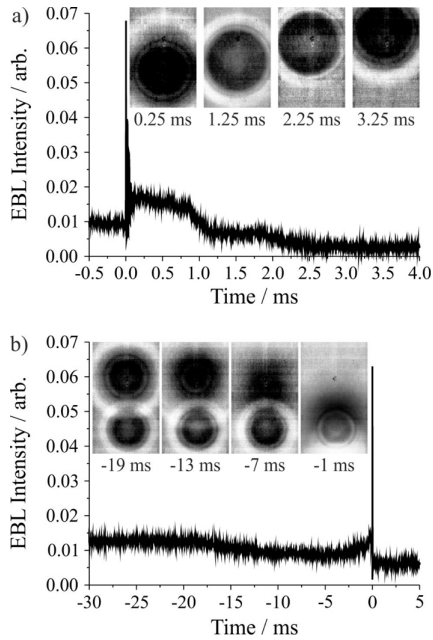


Figure 6.9: Expanded view of the two coalescence events in figures 6.6 and 6.7 to show features of the light scattering that occur on the millisecond time scale. (a) Coalescence transverse to the trapping beam. (b) Coalescence parallel to the trapping beam. Images at different moments during each coalescence are provided as insets.

occurring parallel to the trapping beam b), the droplet coalescence occurs in one of the optical traps. A gradual shift in light scattering intensity is not observed after coalescence because the coalescence occurs when both droplets are already confined within one of the optical traps. However, the light scattering intensity changes before coalescence as a droplet is gradually pulled from one trap into the other, eventually inducing coalescence. This phenomenon is illustrated by the images in b). At 19 ms before coalescence, two droplets are stably trapped. Over the intervening period until coalescence, the droplet located at a higher position is pulled into the axis of the adjacent laser beam, and just before coalescence, it is almost completely obscured by the other droplet located at the beam waist. The trajectory of this droplet gives rise to the slow changes in the light scattering intensity before the coalescence event, similar to the previous

observations of coalescence between a free-flowing and optically trapped droplet [1].

The combination of the two approaches shows that two time scales can be discriminated during coalescence in a dual optical trap. Shape distortion occurs on the microsecond time scale. Migration of the composite droplet into one of the optical traps (coalescence transverse to the trapping beam) or of a precursor droplet from one trap to another (coalescence parallel to the trapping beam) occurs on the millisecond time scale. Understanding and distinguishing these two processes is essential to confidently identify which portion of the light scattering trace is relevant to the coalescence event. Secondly, the coalescence geometry has an impact on the observed form of the elastic light scattering, and this arises due to the location of the coalescence event relative to the positions of the optical traps and the axis along which the shape distortion is viewed. Correctly assigning the origin of the key features in the elastic light scattering permits more confident determination of the oscillation frequency and relaxation time.

### **6.3.2 Viscous aerosol**

The coalescence process is governed by the Reynolds number  $Re = \frac{\sigma r}{\rho v^2}$ , therefore for liquids of different surface tension and viscosity the timing and the intensity of the oscillation can be altered. By decreasing the relative humidity of the trapping chamber the viscosity of the droplets is increased significantly. As an increase in viscosity increases the time taken for the composite droplet to recover it is possible to take several images of the coalescence. The oscillation is also damped by viscosity, by varying the value of viscosity we are able to compare elastic back scattered light, high resolution images, simulated images and simulated aspect ratio to analyse the coalescence process.

The oscillations of a viscous droplet can be divided into two regimes based on the droplet's

viscosity. It has been shown that there is a critical value of viscosity  $\eta_{crit}$  dividing the two regimes [70], where  $\eta_{crit}$  is given by,

$$\eta_{crit} = 0.76 \sqrt{\sigma r \rho}.$$

If the viscosity of the fluid  $\eta$  is less than  $\eta_{crit}$  the droplet oscillates rapidly, the oscillation is eventually damped by viscosity. In the case of  $\eta > \eta_{crit}$  the oscillation is over damped and the droplet slowly deforms into a sphere. If the viscosity of the fluid is similar to  $\eta_{crit}$  the oscillation is said to be critically damped.

Optical trapping has previously been used to analyse the coalescence of viscous aerosol droplets by measuring elastically back scattered light in the over damped, under damped and critically damped cases [139]. The authors estimate the value of  $\eta_{crit}$  to be 0.01 Pa s for droplets of initial radius of approximately 5  $\mu\text{m}$  with surface tension and density similar to water. In this work, for over damped droplets, the use of the high speed camera and mathematical modelling allows images to be taken alongside elastic light scattering traces. Videos have been produced for the simulated coalescence for droplets with surface tension  $\sigma = 72 \text{ mN m}^{-1}$ ,  $r = 8 \mu\text{m}$  and  $\rho = 1 \text{ g cm}^{-3}$  and varying viscosity. The coalescence is shown for droplets of 1 mPas (under damped) [135], 10 mPas (critically damped) [140], 100 mPas (over damped) [141] and 1 Pas [142] (over damped) with each frame corresponding to 0.27  $\mu\text{s}$ . The videos show 20 frames per second.

Figure 6.10 shows images and light scattering of the coalescence of sucrose at 89% RH, where the droplet has a viscosity estimated at 90 mPas, which is reasonably close to the critical value of viscosity. In this case, relaxation to a sphere is very fast, occurring within about 60  $\mu\text{s}$  from coalescence. Indeed, relaxation occurs so quickly that even with a time resolution of 10  $\mu\text{s}$ , only 3-4 images showing a distorted droplet shape are captured. The light scattering intensity shows

a clear initial increase, this is due to the intersection of the two trapping beams. After which there is a rapid decrease in intensity that corresponds to the later stages of droplet relaxation to a sphere. Note that the maximum in light scattering intensity corresponds to a maximum interception of the trapping beams by the distorted droplet surface area. Fitting exponential decays to both the elastic light scattering trace and the droplet aspect ratios gives a relaxation time constant of  $13 \pm 1 \mu\text{s}$  from the light scattering and  $12 \pm 1 \mu\text{s}$  from the images, which is remarkable agreement considering the additional features in the light scattering and the small number of images captured during relaxation (along with the relatively wide time window for each image). The good agreement between the measured relaxation time constants indicates that both approaches are essentially equivalent.

The computation of the relaxation time allows the viscosity of the fluid to be estimated. Previously, physical properties of fluids have been measured by comparing the elastic light scattering over a coalescence with the theory developed by Rayleigh and Lamb [143][139]. If the time constant is taken from the high frame rate images then using the equation for the damping constant in the overdamped regime

$$\tau_l = \frac{2(2l^2 + 4l + 3)r\eta}{l(l+2)(2l+1)\sigma} = \frac{38\eta}{40\sigma} \quad (12)$$

where the viscosity can be estimated. Note here we assumed that the  $l = 2$  is the dominant mode and the droplets radius is  $8 \mu\text{m}$ , the equation was taken from [144]. This gives a value of  $\eta = 113 \text{ mPa s}$  if the relaxation time is given as  $12 \mu\text{s}$ .

A comparison of the aspect ratio given by the finite element model and images from the high speed camera is shown in figure 6.11. The simulated and scaled aspect ratio is shown by the black line and the aspect ratio taken from the high speed camera is shown by the red squares.

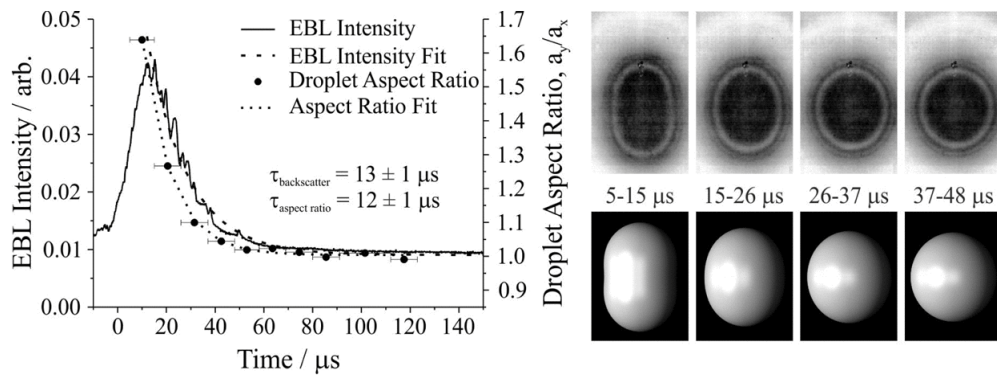


Figure 6.10: Coalescence of sucrose droplets at 89% RH ( $\eta_{est} = 90\text{mPa}\cdot\text{s}$ ). The image on the left is a light scattering trace with black dots showing the aspect ratio of images taken using the camera, the dotted line shows a decay curve fitted to the images aspect ratio. The right shows images of the droplet where the top row were captured using the camera and the bottom row are simulations.

The black line has been shifted to coincide with the triggering of the oscilloscope. Note also that both aspect ratios have been inverted to allow analysis of the earlier stages of coalescence. Largely, there is a clear correspondence between the aspect ratio of the images and the simulated aspect ratio. The first image differs from the curve by approximately 10 microseconds. This can be accounted for by the inaccuracy of the time stamp given to the images. All points were plotted at the average of the range of possible time stamps.

Figure 6.12 shows the coalescence of sucrose droplets at 86% RH, which is considerably more viscous ( $\eta_{est} = 350\text{ mPa}\cdot\text{s}$ ), the droplet can be considered to be in the over damped regime. There is a significant increase in the time-scale of the coalescence relative to figure 6.10. In this case, relaxation occurs over hundreds of microseconds and tens of images are recorded that show the relaxation in droplet shape. A strong agreement is shown between the relaxation time constants fit from the light scattering ( $52\pm 4\ \mu\text{s}$ ) and the droplet aspect ratios ( $48\pm 4\ \mu\text{s}$ ). Equation (12) produces a reasonable estimate of  $454\text{ mPa}\cdot\text{s}$  for the viscosity of the droplet, if the  $\tau$  is taken

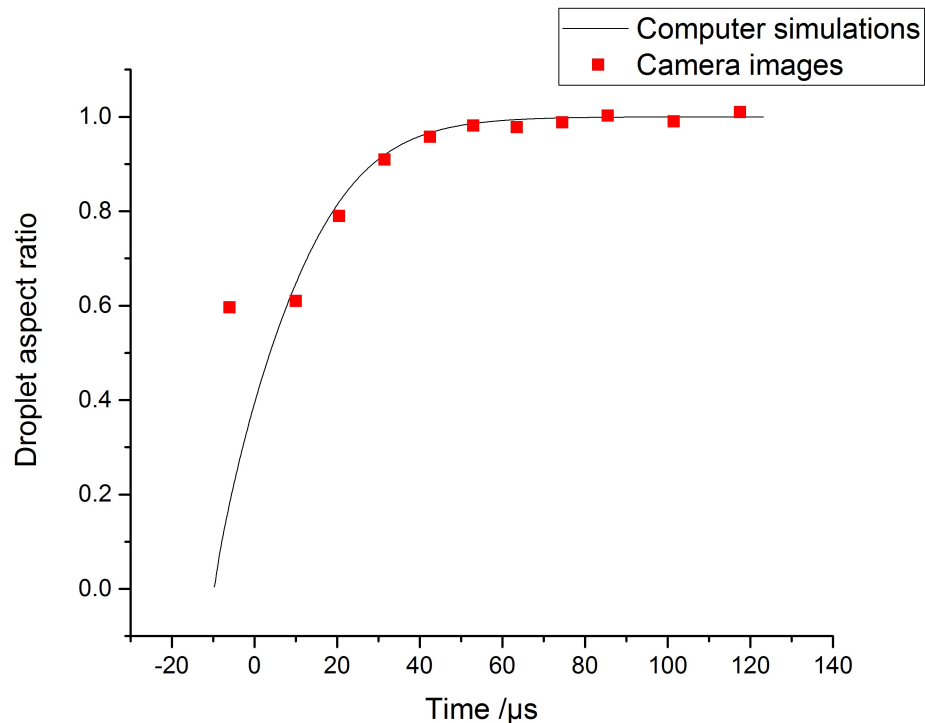


Figure 6.11: The simulated aspect ratio (black line) and aspect ratio of images (red squares) for the coalescence of sucrose droplets at 89% RH ( $\eta_{est} = 90$  mPas).

from the decay in aspect ratio.

The images from the high speed camera have been corresponded to the simulated aspect ratio for the droplets of 350 mPa s, this is shown in figure 6.13. This was fitted in the same way as in figure 6.11. Again there is a strong correspondence between the images and the simulations though the early stages are not completely aligned. This could again be attributed to the inaccuracy of the time stamp from the camera or the challenges in resolving the early stages of coalescence.

Figure 6.14 shows the coalescence of sucrose droplets at 82% RH, which corresponds to droplets with a viscosity about an order of magnitude larger than those shown in figure 6.12. The viscosity was estimated as  $\eta_{est} = 6400$  mPa s. In this case, relaxation occurs over several milliseconds and

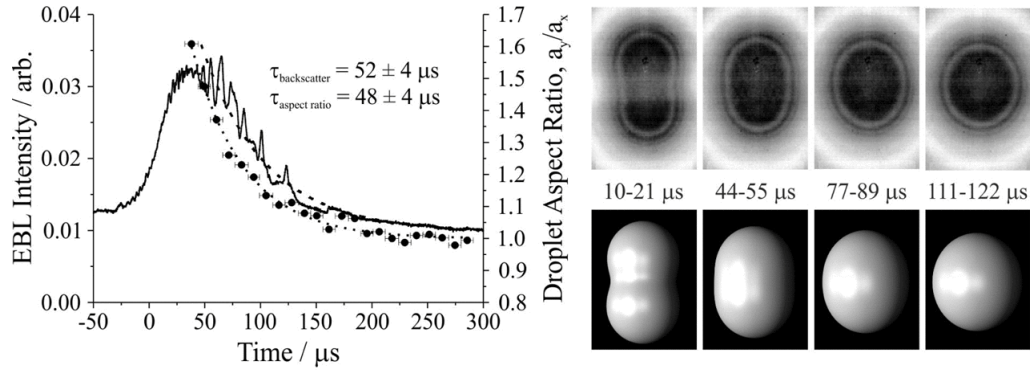


Figure 6.12: Coalescence of sucrose droplets at 86% RH ( $\eta_{est} = 350$  mPa s). The image on the left is a light scattering scattering trace with black dots showing the aspect ratio of images taken using the camera. The right shows images of the droplet where the top row were captured using the camera and the bottom row are simulations.

it is clear that the fit obtained from the light scattering ( $360 \pm 30 \mu\text{s}$ ) does not agree well with that obtained from the droplet aspect ratios ( $870 \pm 60 \mu\text{s}$ ). The reason for this relates to the time-scale of droplet recapture into the optical traps. The coalescence was induced in the transverse direction, as seen from figure 6.9 the recapture of the droplet in the optical trap occurs on a millisecond time-scale. As a result, the coalescence is still occurring while the droplet is being recaptured, significantly complicating the light scattering trace. To separate the two processes in the light scattering trace would be challenging.

The two processes can be distinguished from the experimental images of figure 6.14. Initially (see image at  $661\text{-}678 \mu\text{s}$ ) the composite droplet is located between the two optical traps, which are located at the top and bottom of the image. As the coalescence progresses, the droplet gradually relaxes to a sphere, but the droplet position shifts upwards over the same time period as it migrates to the upper trap (image at  $2113\text{-}2130 \mu\text{s}$ ). Although these are two relatively simple processes to distinguish in the images, they convolute the elastic light scattering, giving

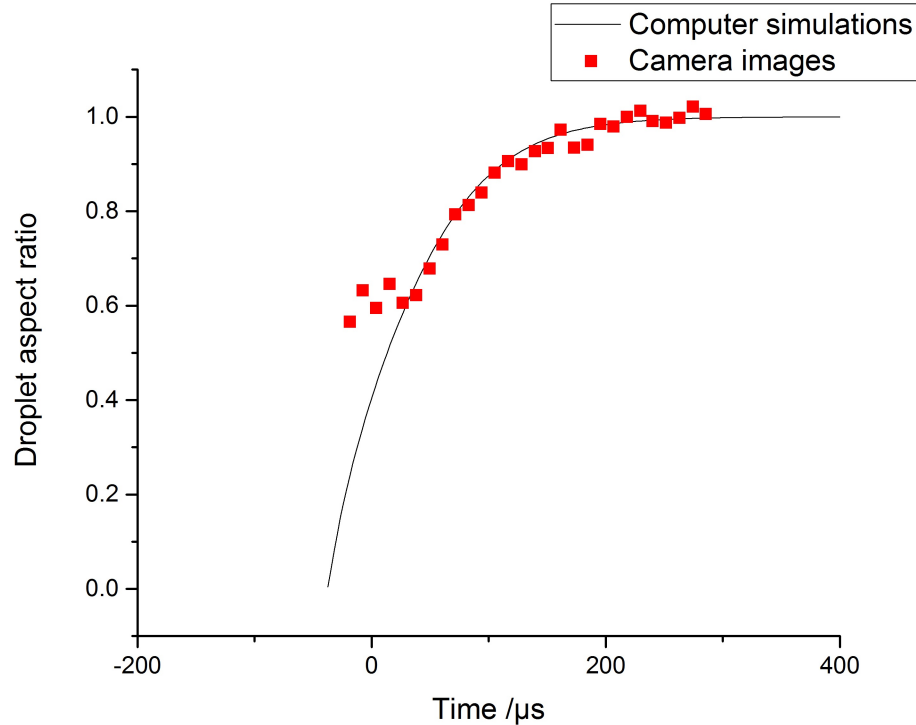


Figure 6.13: The simulated aspect ratio (black line) and aspect ratio of images (red squares) for the coalescence of sucrose droplets at 86% RH ( $\eta_{est} = 350 \text{ mPa s}$ ).

a relaxation time constant that is smaller than that determined from the droplet aspect ratios. In short, these observations indicate that once coalescence times last for more than a millisecond, light scattering is no longer an effective approach to quantitatively infer changes in droplet shape. Though light scattering may be unsuitable for the very high viscosity coalescence the images from the camera can be corresponded with the simulated coalescence. This is shown in figure 6.15. In this case the simulated aspect ratio is in almost perfect alignment with the aspect ratio from the images. This correspondence further validates the use of high frame rate cameras to analyse the coalescence of high viscosity droplets. The aspect ratio of the droplet taken from the images provides an estimated value of approximately viscosity of 8242 mPa s, which is in

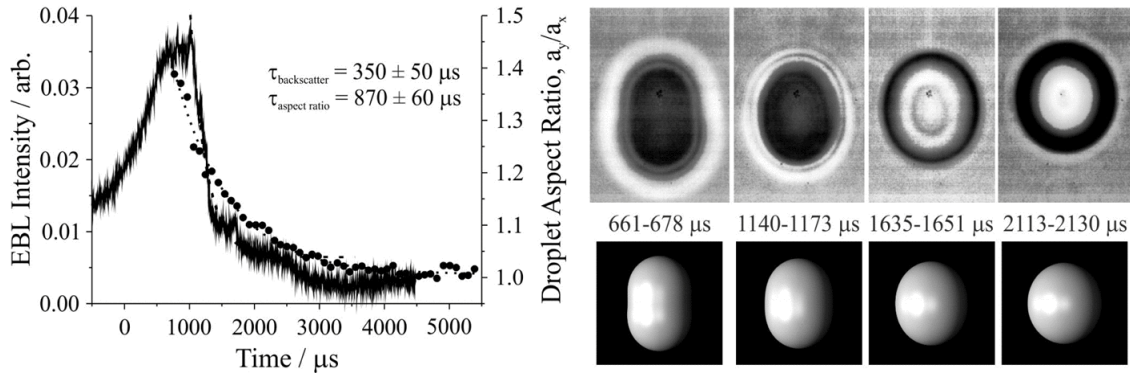


Figure 6.14: Coalescence of sucrose droplets at 82% RH ( $\eta_{est} = 6400 \text{ mPa s}$ ). The image on the left is a light scattering scattering trace with black dots showing the aspect ratio of images taken using the camera. The right shows images of the droplet where the top row were captured using the camera and the bottom row are simulations.

reasonable agreement with the estimated value.

A similar process can be used to analyse coalescence in the under damped regime. By fitting maxima in light scattering intensity and aspect ratio to a decay curve the decay rates can be compared. Figure 6.16 shows the coalescence for droplets with an estimated viscosity of 0.67 mPa s. The black circles show the maxima of aspect ratio of images taken on the high frame rate camera and the green triangles show the maxima of light scattering intensity. The corresponding dotted lines give the best fit of exponential decay for these quantities, the straight line corresponds to the mathematical model.

The agreement between the observed aspect ratio and simulated aspect ratio/light scattering intensity is less strong than for the higher viscosity droplets. This can be accounted for due to the exposure time of the camera. The simulations show that time period for the droplet to deform most prolate to most oblate spheroid is approximately  $5 \mu\text{s}$  which is under the cameras exposure time of  $8 \mu\text{s}$ . As such recording elastic light scattering is a more effective way to determine

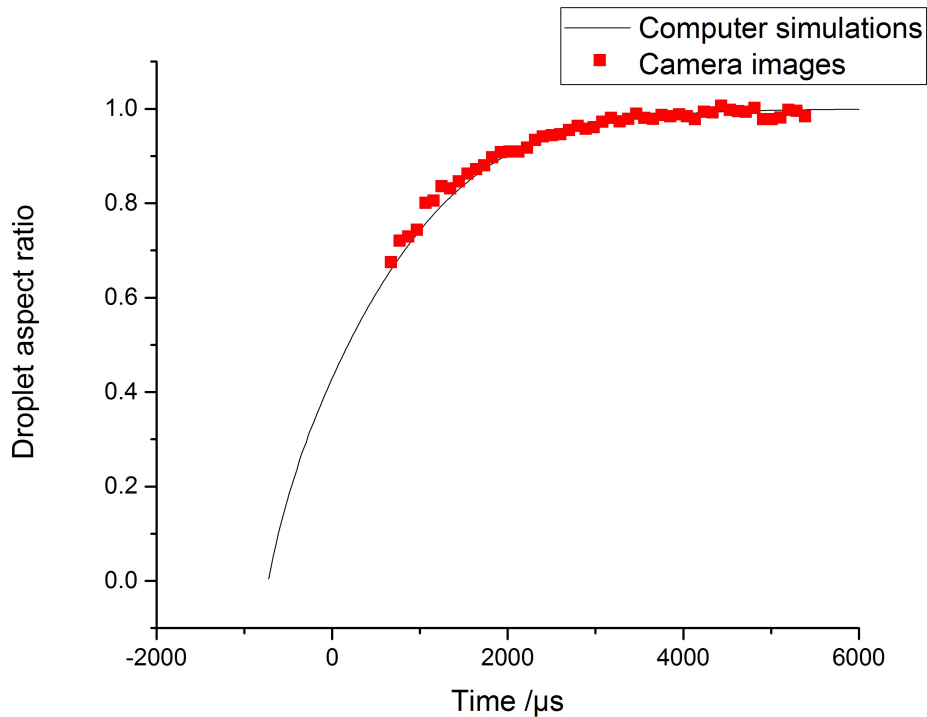


Figure 6.15: The simulated aspect ratio (black line) and aspect ratio of images (red squares) for the coalescence of sucrose droplets at 82% RH ( $\eta_{est} = 6400 \text{ mPa s}$ ).

relaxation time, however there is still a minor difference from the simulation. This difference is caused by broad maxima in light scattering intensity which is due to light scattering being recorded from two optical traps.

## 6.4 Conclusions

The results presented in this chapter show a strong correspondence between elastic light scattering of coalescing aerosol droplets and the aspect ratio of numerical simulations of the coalescence. This has been shown for different values of viscosity. The comparison validates both the assumptions used in the mathematical modelling and the assumption that in the low viscosity

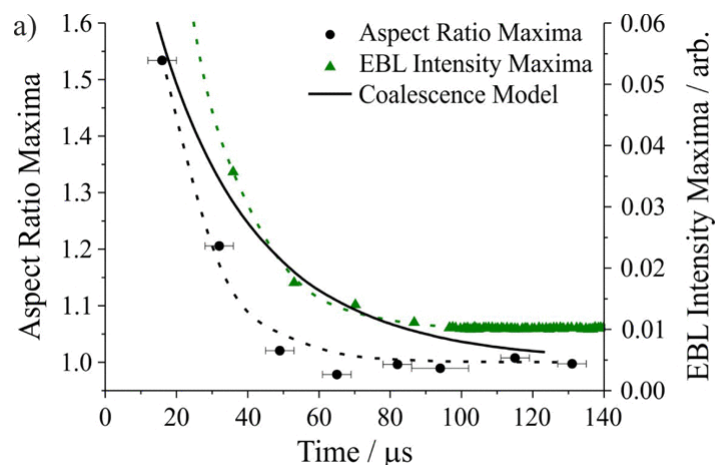


Figure 6.16: Coalescence of the sodium dodecyl sulfate-doped sodium chloride droplets, the viscosity is estimated as 0.67 mPa s. Circles represent droplet aspect ratio maxima (left axis) whereas triangles represent light scattering intensity maxima (right axis). The corresponding dotted line gives the exponential fit for each measurement. The solid line represents the simulated droplet aspect ratios.

case the trapping laser does not interfere with the dynamics of the coalescence. By considering the different possible orientations for the merging droplet in the optical trap we show that the reorientation of the droplet in the optical tweezers occurs on millisecond time-scale, whereas generally, the droplet is fully coalesced after microseconds. An exception to this is the case of a highly viscous droplet, where the coalescence will occur on a millisecond time-scale. In this case light scattering is unsuitable to probe the coalescence, however modern high speed cameras allow for a detailed analysis of the dynamics. The images allow the relaxation to a sphere and movement into an optical trap to be distinguished.

The finite element based model also allowed for high quality images of coalescing droplets to be produced. Classical techniques have been able to model the frequency of the oscillation of the particle, however our approach is also able to produce coordinates for the droplet in three dimensions. In the case of a low viscosity droplet the simulated aspect ratio is shown to oscillate at the

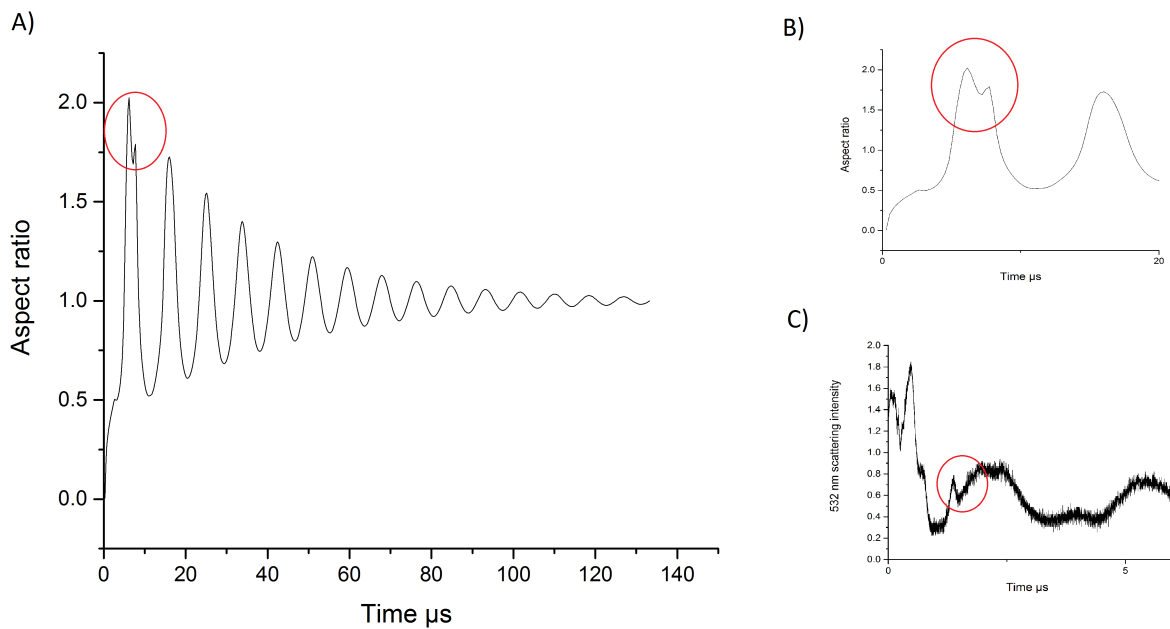


Figure 6.17: A) shows the aspect ratio of a simulated coalescence for droplets with  $\sigma = 72 \text{ mN m}^{-1}$ ,  $r=8 \mu\text{m}$ ,  $\rho = 1 \text{ g cm}^{-3}$ , and viscosity of  $0.67 \text{ mPa s}$  (left). B) shows the aspect ratio over the first 20 microseconds in greater detail. C) shows the light scattering trace shown in figure 6.2 for the first 6 microseconds.

same frequency of the elastic scattering. In the over damped case the fall in light scattering also corresponds with the fall in simulated aspect ratio. By comparison with equation 12, values for viscosity can be recovered for the fluid, shown to be in reasonable agreement with the estimated value.

The high speed camera is able to capture images of the droplet over the coalescence. In the under damped regime the camera does not record images at sufficient time resolution to completely record the oscillation, although 4-5 images of the oscillating droplet are shown in figure 6.6. In the over damped regime several images can be captured so that the early stages where a bridge forms connecting the two droplets can be viewed.

As well as supporting an analysis of the coalescence of high viscosity droplets and droplet position the mathematical modelling techniques have been used to look at the aspect ratio of lower viscosity droplets. The left side of figure 6.17 shows the aspect ratio over time for a coalescence with initial droplets having  $\sigma = 72 \text{ mN m}^{-1}$ ,  $r=8 \text{ }\mu\text{m}$ ,  $\rho = 1 \text{ g cm}^{-3}$ , and viscosity of  $0.67 \text{ mPa s}$ . As well as the oscillation shown in figure 6.2, the graph shows an additional feature on the first period of the oscillation, it is highlighted by the red circle. The region of interest is shown inset, in the top right of the figure and is labelled B). The otherwise gradual decline in aspect ratio over this period is disturbed by a small rise. A video (at  $45^\circ$  to the collision axis) showing this phenomena is available at [145], each frame corresponds to  $0.267 \text{ }\mu\text{s}$  and there are three frames per second. The effect can be seen between approximately the seventh and eighth second of the video.

A similar feature can also be identified in the light scattering data shown in figure 6.2, between approximately  $1 \text{ }\mu\text{s}$  and  $2 \text{ }\mu\text{s}$ . An expanded view of this region has been reproduced in figure 6.17C and highlighted with a red circle. A similar shoulder peak can be seen in both figures. Potentially, a complete analysis of this behaviour could be undertaken by coalescing droplets of lower viscosity (or alternatively higher surface tension). Theoretically this should exaggerate this effect and therefore the feature would become clearer in the light scattering.

# **Chapter Seven - The simple factor dressing of the k-noid**

## 7 The simple factor dressing of the k-noid

In this chapter the transformations described in chapter 3 are applied to the  $k$ -noid and the geometric properties of the resultant surfaces are investigated. The Jorge-Meeks  $k$ -noid was first described by Jorge and Meeks in 1983 [146], it is a minimal surface with  $k$  catenoidal ends. They proved that it is a complete minimal surface with finite total curvature. In this chapter we investigate the Lopez-Ros deformation and simple factor dressing of the  $k$ -noids.

The chapter is structured so that the first section provides an explanation of how the  $k$ -noid is parametrized and constructed from its symmetries. This has been implemented as an extension of the surface lab [91] so that the value of  $k$  may be adjusted. The second section investigates the periodicity of the newly constructed minimal surfaces. The  $k$ -noid is globally defined on  $S^2 \setminus \{p_1 \dots p_k\}$ , where  $p_j$  are the catenoidal ends, whereas its conjugate is doubly periodic. In general simple factor dressings of the  $k$ -noid are doubly periodic, however under certain restrictions singly periodic minimal surfaces in  $\mathbb{R}^3$  can be constructed. The third section investigates the symmetries of the newly constructed surfaces. Finally, some concluding remarks and ideas for future work are discussed.

### 7.1 Constructing the k-noid

In topological terms the  $k$ -noid is a sphere with  $k$  punctures which correspond to catenoidal ends, that is, a minimal, conformal immersion  $f : S^2 \setminus \{p_1, \dots, p_k\} \rightarrow \mathbb{R}^3$ , where the points  $p_i$  correspond to catenoidal ends.

We will consider the  $k$ -noid defined by its simplest Weierstrass data.

**Theorem 7.1.1.** *The Weierstrass data  $g(z) = z^{k-1}$  and  $\omega(z) = \frac{1}{(z^k-1)^2}$  where  $z \in \{\mathbb{C} \cup \infty\} \setminus$*

$\{p_1, \dots, p_k\}$  with  $p_j = e^{\frac{2\pi ij}{k}}$ , and  $k \geq 2$  generates a  $k$ -noid.

Recall from Example 3.1.1 that  $S^2$  is a Riemann surface described by charts as stereographic projections and  $r(z) = \frac{1}{z}$  as a transition map.

Using this Weierstrass data we obtain the holomorphic null curve  $\Phi = \begin{pmatrix} \Phi_1 \\ \Phi_2 \\ \Phi_3 \end{pmatrix}$  with

$$\Phi_1(z) = \frac{1}{2} \int \frac{1 - z^{2k-2}}{(z^k - 1)^2} dz, \quad \Phi_2(z) = \frac{i}{2} \int \frac{1 + z^{2k-2}}{(z^k - 1)^2} dz, \quad \Phi_3(z) = \int \frac{z^{k-1}}{(z^k - 1)^2} dz.$$

We shall consider this Weierstrass data in terms of both charts. Firstly note that for a holomorphic one form  $\omega(z)dz$  described by a local coordinate  $z$ , if we wish to make a change of coordinates  $z = z(w)$ , then  $\omega(z)dz = \omega(z(w))z'(w)dw$ . In our case we have that  $\omega(z) = \frac{dz}{(z^k-1)^2}$  which under change of coordinates  $z \rightarrow \frac{1}{z}$  is given by  $\omega\left(\frac{1}{z}\right) = -\frac{1}{z^2} \frac{dz}{\left(\frac{1}{z^k}-1\right)^2}$ . Therefore we may compute the holomorphic null curve under the change of coordinates  $r(z) = \frac{1}{z}$  by considering Weierstrass data  $g\left(\frac{1}{z}\right)$  and  $\omega\left(\frac{1}{z}\right)$ , we compute that the holomorphic null curve is given by

$$\Phi\left(\frac{1}{z}\right) = \begin{pmatrix} \Phi_1(z) \\ -\Phi_2(z) \\ -\Phi_3(z) \end{pmatrix}.$$

The Weierstrass representation above given in terms of coordinate  $z$  can be integrated to give a parametrization for the  $k$ -noid in terms of the hypergeometric function:

**Theorem 7.1.2.** *The holomorphic null curve of the  $k$ -noid is given by:*

$$\begin{aligned}\Phi_1(z) &= \frac{-1}{2kz(1-z^k)} \left( (k-1)(z^k-1) {}_2F_1\left(1, \frac{-1}{k}, \frac{k-1}{k}, z^k\right) - (k-1)z^2(z^k-1) {}_2F_1\left(1, \frac{1}{k}, \frac{1+k}{k}, z^k\right) \right. \\ &\quad \left. - kz^k + z^2 + k - 1 \right), \\ \Phi_2(z) &= \frac{i}{2kz(1-z^k)} \left( (k-1)(z^k-1) {}_2F_1\left(1, \frac{-1}{k}, \frac{k-1}{k}, z^k\right) + (k-1)z^2(z^k-1) {}_2F_1\left(1, \frac{1}{k}, \frac{1+k}{k}, z^k\right) \right. \\ &\quad \left. - kz^k - z^2 + k - 1 \right), \\ \Phi_3(z) &= \frac{1}{k(1-z^k)}.\end{aligned}$$

Here  ${}_2F_1$  is the hypergeometric function given by

$${}_2F_1(a, b, c, z) = \sum_{n=1}^{\infty} \frac{a^{(n)} b^{(n)} z^n}{c^{(n)} n!},$$

and  $q^{(n)}$  is the rising Pochhammer symbol given by:

$$q^{(n)} = \begin{cases} 1 & \text{if } n = 0, \\ q(q+1)\dots(q+n-1) & \text{if } n > 0. \end{cases}$$

Note that we write  $q^{(n)}$  to distinguish the Pochhammer symbol  $q^{(n)}$  from the standard exponentiation  $q^n$ . We also have that

$${}_2F_1(1, b, c, z) = \sum_{n=1}^{\infty} \frac{b^{(n)}}{c^{(n)}} z^n, \quad (13)$$

since  $1^{(n)} = n!$ . To compute the parametrization later on we will also need to consider the falling Pochhammer symbol  $q_{(n)}$ .

$$q_{(n)} = \begin{cases} 1 & \text{if } n = 0, \\ q(q-1)\dots(q-n+1) & \text{if } n > 0. \end{cases}$$

*Proof.* To show that the parametrization given above is indeed formed from the Weierstrass data  $(\frac{1}{(z^k-1)^2}, z^{k-1})$  we must now integrate  $\Phi'$ . To integrate  $\Phi'_3$  is a straightforward substitution using  $u = z^k$ , however integrating  $\Phi'_1$  and  $\Phi'_2$  is more challenging. To obtain  $\Phi_1$  and  $\Phi_2$  we decompose their integrands into a part that can be easily integrated and a part that can be expanded binomially and then integrated to a hypergeometric function. For  $\Phi_1(z)$  this is

$$\Phi_1(z) = \frac{1}{2} \int \frac{k(-z^{2k} + z^{k+2} + z^k - 1) + (-z^2 - 1)(z^k - 1)}{kz^2(z^k - 1)^2} - \frac{(k-1)(z^2 + 1)}{kz^2(z^k - 1)} dz.$$

Firstly recall Newton's binomial formula [147] in terms of the falling Pochhammer symbol given by

$$(x+y)^r = \sum_{n=0}^{\infty} \frac{r_{(n)}}{n!} x^{r-n} y^n.$$

In our case let  $x = -1$  and  $z^k = y$  and consider,

$$\begin{aligned} \frac{(z^2 + 1)}{z^2(z^k - 1)} &= \frac{1}{(z^k - 1)} + \frac{1}{z^2(z^k - 1)} \\ &= \sum_{n=0}^{\infty} \left( \frac{(-1)_{(n)}}{n!} (-1)^{-1-n} z^{ni} \right) + \frac{1}{z^2} \sum_{n=0}^{\infty} \left( \frac{(-1)_{(n)}}{n!} (-1)^{-1-n} z^{ni} \right). \end{aligned}$$

Since  $(-1)_{(n)} = \frac{1^{(n)}}{(-1)^n}$  we can rewrite the above as

$$\frac{(z^2 + 1)}{z^2 (z^k - 1)} = - \left( \sum_{n=0}^{\infty} z^{ni} + \sum_{n=0}^{\infty} z^{ni-2} \right).$$

We are now able to integrate the expression above, that is

$$\begin{aligned} \int \frac{(z^2 + 1)}{z^2 (z^k - 1)} &= - \left( \sum_{n=0}^{\infty} \left( \frac{1}{ni + 1} z^{ni+1} \right) + \sum_{n=0}^{\infty} \left( \frac{1}{ni - 1} z^{ni-1} \right) \right), \\ &= - \left( z \sum_{n=0}^{\infty} \frac{1}{ni + 1} z^{ni} + \frac{1}{z} \sum_{n=0}^{\infty} \frac{1}{ni - 1} z^{ni} \right). \end{aligned}$$

To write the above function in terms of the hypergeometric function we wish to express  $\frac{1}{ni+1}$  and  $\frac{-1}{ni-1}$  in terms of the rising Pochhammer symbol. It can be easily verified that

$$\frac{1}{ni + 1} = \frac{(\frac{1}{k})^{(n)}}{(\frac{1+k}{k})^{(n)}}, \quad \frac{-1}{ni - 1} = \frac{(\frac{-1}{k})^{(n)}}{(\frac{k-1}{k})^{(n)}}.$$

This gives, recalling (13),

$$\begin{aligned} \int \frac{(k-1)(z^2 + 1)}{kz^2 (z^k - 1)} &= - \frac{z(k-1)}{k} \sum_{n=0}^{\infty} \frac{(\frac{1}{k})^{(n)}}{(\frac{1+k}{k})^{(n)}} z^{ni} + \frac{(k-1)}{kz} \sum_{n=0}^{\infty} \frac{(\frac{-1}{k})^{(n)}}{(\frac{k-1}{k})^{(n)}} z^{ni} \\ &= - {}_2F_1\left(1, \frac{1}{k}, \frac{1+k}{k}, z^k\right) \frac{z(k-1)}{k} + {}_2F_1\left(1, -\frac{1}{k}, \frac{k-1}{k}, z^k\right) \frac{(k-1)}{kz}. \end{aligned}$$

Combining this with the remainder of the integral,

$$\int \frac{k(-z^{2k} + z^{k+2} + z^k - 1) + (-z^2 - 1)(z^k - 1)}{2kz^2 (z^k - 1)^2} dz = \frac{-kz^k + k + z^2 - 1}{2kz(1 - z^k)},$$

we compute that

$$\Phi_1(z) = \frac{-1}{2kz(1-z^k)}((k-1)(z^k-1)_2F_1\left(1, \frac{-1}{k}, \frac{k-1}{k}, z^k\right) - (k-1)z^2(z^k-1)_2F_1\left(1, \frac{1}{k}, \frac{1+k}{k}, z^k\right) - kz^k + z^2 + k - 1).$$

A similar argument can be applied to integrate  $\Phi_2'$ . □

### 7.1.1 The behaviour of the poles

The parametrization above defines a  $k$ -noid on the unit disc with  $k$  punctures at the roots of unity, these points correspond to the catenoidal ends. Recall Theorem 3.2.14 that if a pole  $p$  of  $\Phi'$  is of order 2 and that if the residue  $\text{Res}(\Phi', p)$  is real then the minimal surface has an embedded finite total curvature end at  $p$ . If the residue is non-zero the end is catenoidal and if it is zero the end is planar.

We will now calculate the residues for the differential of the holomorphic null curve  $\Phi$  of the  $k$ -noid. Firstly consider the derivative of  $\Phi$

$$\Phi_1'(z) = \frac{1}{2} \frac{(1 - z^{2(k-1)})}{(z^k - 1)^2}, \quad \Phi_2'(z) = \frac{i}{2} \frac{(1 + z^{2(k-1)})}{(z^k - 1)^2}, \quad \Phi_3'(z) = \frac{z^{k-1}}{(z^k - 1)^2}. \quad (14)$$

Let  $p = e^{\frac{2\pi ij}{k}}$  be a  $j^{\text{th}}$  root of unity where  $j \in \{0, \dots, k-1\}$ , these points are the poles of the derivative of the holomorphic null curve (of order 2). Noting,

$$(z^k - 1) = (z - p) \sum_{j=0}^{k-1} z^j p^{k-j-1},$$

we will use the following function

$$w(z) = \sum_{j=0}^{k-1} z^j p^{k-j-1},$$

to apply the Cauchy integral formula to calculate the residue of  $\Phi'$  at  $p$ , so that

$$\Phi'(z) = \left( \begin{array}{c} \frac{1}{2} \frac{(1-z^{2k-2})}{(z-p)^2 w(z)^2} \\ \frac{i}{2} \frac{(1+z^{2k-2})}{(z-p)^2 w(z)^2} \\ \frac{z^{k-1}}{(z-p)^2 w(z)^2} \end{array} \right).$$

The derivative of  $w$  is given by,

$$w'(z) = \sum_{j=1}^{k-1} j z^{j-1} p^{k-j-1}.$$

If we put  $p$  into  $w(z)$  and  $w'(z)$  it is straightforward to see that

$$w(p) = kp^{k-1}, \quad w'(p) = p^{k-2} \sum_{j=1}^{k-1} j = p^{k-2} \frac{k(k-1)}{2}.$$

To apply the Cauchy integral formula consider

$$\psi(z) = \left( \begin{array}{c} \frac{1}{2} \frac{(1 - z^{2(k-1)})}{w(z)^2} \\ \frac{i}{2} \frac{(1 + z^{2(k-1)})}{w(z)^2} \\ \frac{z^{k-1}}{w(z)^2} \end{array} \right). \quad (15)$$

Note that  $\psi(z) = (z-p)^2 \Phi'(z)$  and  $\psi'(z)$  is given by

$$\psi'(z) = \begin{pmatrix} -\frac{(k-1)z^{2(k-1)-1}}{w(z)^2} - \frac{(1-z^{2(k-1)})w'(z)}{w(z)^3} \\ \frac{i(k-1)z^{2(k-1)-1}}{w(z)^2} - \frac{i(z^{2(k-1)}+1)w'(z)}{w(z)^3} \\ \frac{(k-1)z^{k-2}}{w(z)^2} - \frac{2z^{k-1}w'(z)}{w(z)^3} \end{pmatrix}.$$

Finally evaluating at  $p = e^{\frac{2\pi ij}{k}}$  gives

$$\psi'(p) = \begin{pmatrix} -\frac{(k-1)p^{-2k-1}(p^{2k}+p^2)}{2k^2} \\ \frac{i(k-1)p^{-2k-1}(p^{2k}-p^2)}{2k^2} \\ 0 \end{pmatrix} = \begin{pmatrix} -\frac{\cosh(\frac{2\pi ij}{k})(k-1)}{k^2} \\ i\frac{\sinh(\frac{2\pi ij}{k})(k-1)}{k^2} \\ 0 \end{pmatrix} = \begin{pmatrix} -\frac{\cos(\frac{2\pi j}{k})(k-1)}{k^2} \\ -\frac{\sin(\frac{2\pi j}{k})(k-1)}{k^2} \\ 0 \end{pmatrix}. \quad (16)$$

Here we applied the identities  $\cosh(iz) = \cos(z)$  and  $\sinh(iz) = i \sin(z)$ .

We can evaluate now the residue of  $\Phi'$  at  $p$  using the Cauchy integral formula. Let  $e^{\frac{2\pi ij}{k}} = p$  where  $j \in \{0 \dots k-1\}$  and  $\lambda$  be a circular closed curve around  $p$ . Then,

$$\text{Res}(\Phi', p) = \frac{1}{2\pi i} \oint_{\lambda} \Phi'(z) dz = \frac{1}{2\pi i} \oint_{\lambda} \frac{\psi(z)}{(z-p)^2} dz = \psi'(p) = \begin{pmatrix} -\frac{\cos(\frac{2\pi j}{k})(k-1)}{k^2} \\ -\frac{\sin(\frac{2\pi j}{k})(k-1)}{k^2} \\ 0 \end{pmatrix}. \quad (17)$$

Therefore,  $\text{Res}(\Phi', p)$  is always real and thus using Theorem 3.2.14, we have proved:

**Theorem 7.1.3.** *The  $k$ -noid has  $k$  catenoidal ends at the roots of unity.*

Recall that the translational period of the conjugate surface is given by  $2\pi \text{Res}(\Phi', p)$ . Therefore

the conjugate surface has periods,  $\tau_j^* = \begin{pmatrix} -\frac{2\pi \cos(\frac{2\pi j}{k})(k-1)}{k^2} \\ -\frac{2\pi \sin(\frac{2\pi j}{k})(k-1)}{k^2} \\ 0 \end{pmatrix}$ . If  $k > 2$ , then  $\tau_0$  and  $\tau_1$  form a basis for

$\{\tau_j\}$  and the conjugate surface is a doubly periodic surface. In the case of  $k = 2$ , the catenoid the

conjugate surface (the helicoid) is singly periodic since  $\tau_0 = -\tau_1$  in this case.

### 7.1.2 The geodesics of the k-noid

The series of the hypergeometric function  ${}_2F_1(a, b, c, z)$  is not defined for  $|z| > 1$ , however  ${}_2F_1$  can be analytically extended to the whole complex plane. For  $k$ -noids this can be understood in terms of the reflection principle. Recall that the reflection principle states that a minimal surface containing a planar geodesic may be extended by reflection across the plane. On the conjugate surface this corresponds to a 180 degree rotation around the corresponding straight line. To visualize the  $k$ -noid we use the reflection principle extensively and therefore will need to show which curves are planar geodesics. To show a curve on the  $k$ -noid is a planar geodesic we will show that the corresponding curve on the conjugate is a straight line (that is, has vanishing curvature).

**Lemma 7.1.4.** *Let  $f$  be a  $k$ -noid. Then the image  $\lambda_j(t) = f(te^{\frac{ij\pi}{k}})$ ,  $t \in \mathbb{R} \setminus \{1\}$ ,  $j \in \{1, \dots, 2k-1\}$ , of the straight line connecting 0 and  $e^{\frac{ij\pi}{k}}$  under  $f$  is a planar geodesic. Moreover, the image  $\gamma(t) = f(e^{\frac{in\pi}{k}})$ ,  $t \in \mathbb{R}$ ,  $t \neq 2j$ , of the unit circle under  $f$  is a planar geodesic.*

*Proof.* Firstly let us show that  $\lambda_j(t) = f(te^{\frac{\pi ij}{k}})$  are planar geodesics. To do so we will show that the corresponding curves on the conjugate,  $\lambda_j^*(t) = f^*(te^{\frac{\pi ij}{k}})$  are straight lines, that is the curvature  $\kappa^* = \frac{\|\lambda^{*'} \times \lambda^{*''}\|}{\|\lambda^{*'}\|^3}$  is equal to zero. Since  $\lambda_j(t) + i\lambda_j^*(t) = \Phi(te^{\frac{\pi ij}{k}})$  and recalling (14) we have that

$$\frac{d}{dt}\Phi(te^{\frac{\pi ij}{k}}) = e^{\frac{\pi ij}{k}}\Phi'(te^{\frac{\pi ij}{k}}) = \left( \begin{array}{c} e^{\frac{inj}{k}} \left( 1 - \left( te^{\frac{inj}{k}} \right)^{2(k-1)} \right) \\ \frac{((-1)^j t^k - 1)^2}{ie^{\frac{inj}{k}} \left( 1 + \left( te^{\frac{inj}{k}} \right)^{2(k-1)} \right)} \\ \frac{((-1)^j t^k - 1)^2}{2(-1)^j t^{k-1}} \\ \frac{2(-1)^j t^{k-1}}{((-1)^j t^k - 1)^2} \end{array} \right),$$

which has imaginary part

$$\lambda_j^{*'}(t) = \text{Im} \left( \frac{d}{dt} \Phi \left( t e^{\frac{\pi j}{k}} \right) \right) = \begin{pmatrix} \frac{\sin\left(\frac{\pi j}{k}\right)}{\left((-1)^j t^k - 1\right)^2} + \frac{t^{2k-2} \sin\left(\frac{\pi j}{k}\right)}{\left((-1)^j t^k - 1\right)^2} \\ \frac{\cos\left(\frac{\pi j}{k}\right)}{\left((-1)^j t^k - 1\right)^2} + \frac{t^{2k-2} \cos\left(\frac{\pi j}{k}\right)}{\left((-1)^j t^k - 1\right)^2} \\ 0 \end{pmatrix} = \frac{1 + t^{2k-2}}{\left((-1)^j t^k - 1\right)^2} \begin{pmatrix} \sin\left(\frac{\pi j}{k}\right) \\ \cos\left(\frac{\pi j}{k}\right) \\ 0 \end{pmatrix}.$$

Since  $\lambda_j^{*'}(t) = v(t) \begin{pmatrix} \sin\left(\frac{\pi j}{k}\right) \\ \cos\left(\frac{\pi j}{k}\right) \\ 0 \end{pmatrix}$  with  $v(t) = \frac{1+t^{2k-2}}{\left((-1)^j t^k - 1\right)^2}$  we have that  $\lambda_j^{*'} \times \lambda_j^{*''} = 0$ , and  $\lambda_j^*$  is a straight line.

Using Theorem 3.2.17 we see that  $\lambda_j$  is a curve in the plane perpendicular to  $\begin{pmatrix} \sin\left(\frac{\pi j}{k}\right) \\ \cos\left(\frac{\pi j}{k}\right) \\ 0 \end{pmatrix}$ .

By the same method we will show that  $\gamma$  is a planar geodesic. Consider  $\Phi \left( e^{\frac{i\pi t}{k}} \right) = \gamma(t) + i\gamma^*(t)$ ,

$$\frac{d}{dt} \Phi \left( e^{\frac{i\pi t}{k}} \right) = \frac{i\pi}{k} e^{\frac{i\pi t}{k}} \Phi' \left( e^{\frac{i\pi t}{k}} \right) = \begin{pmatrix} \frac{i\pi e^{\frac{i\pi t}{k}} \left( 1 - \left( e^{\frac{i\pi t}{k}} \right)^{2k-2} \right)}{k \left( -1 + \left( e^{\frac{i\pi t}{k}} \right)^k \right)^2} \\ \frac{\pi e^{\frac{i\pi t}{k}} \left( 1 + \left( e^{\frac{i\pi t}{k}} \right)^{2k-2} \right)}{k \left( -1 + \left( e^{\frac{i\pi t}{k}} \right)^k \right)^2} \\ \frac{2i\pi \left( e^{\frac{i\pi t}{k}} \right)^k}{k \left( -1 + \left( e^{\frac{i\pi t}{k}} \right)^k \right)^2} \end{pmatrix} = \begin{pmatrix} -\frac{\pi \csc^2\left(\frac{\pi t}{2}\right) \sin\left(\frac{\pi(k-1)t}{k}\right)}{2k} \\ \frac{\pi \csc^2\left(\frac{\pi t}{2}\right) \cos\left(\frac{\pi(k-1)t}{k}\right)}{2k} \\ -\frac{i\pi \csc^2\left(\frac{\pi t}{2}\right)}{2k} \end{pmatrix}$$

which has imaginary part,

$$\gamma^{*'}(t) = \operatorname{Im}\left(\frac{i\pi}{k}e^{\frac{it}{k}}\Phi'(e^{\frac{it}{k}})\right) = \begin{pmatrix} 0 \\ 0 \\ -\frac{\pi \csc^2\left(\frac{\pi t}{2}\right)}{2k} \end{pmatrix},$$

thus  $\gamma^{*'}(t) \times \gamma^{*''}(t) = 0$  and  $\gamma^*(t)$  is a straight line parallel to the  $z$  axis.  $\square$

As  $\gamma^*$  is parallel to the  $z$  axis we see that  $\gamma(t)$  is contained in the  $x - y$  plane and therefore the  $k$ -noid may be extended by reflection across the  $x - y$  plane. This shows that the Weierstrass data given by Theorem 7.1.1 can be extended to  $\mathbb{C} \setminus \{p_j\}$ .

For the implementation of the  $k$ -noid we will restrict to smaller domains and use the additional symmetries given by the curves  $\lambda_j$ . Since  $\lambda_j$  is a planar geodesic in the plane orthogonal to

$\begin{pmatrix} \sin\left(\frac{\pi j}{k}\right) \\ \cos\left(\frac{\pi j}{k}\right) \\ 0 \end{pmatrix}$ , we know that  $f(D)$  is invariant under matrices of the form,

$$R_j = \begin{pmatrix} \cos\left(\frac{2j\pi}{k}\right) & -\sin\left(\frac{2j\pi}{k}\right) & 0 \\ -\sin\left(\frac{2j\pi}{k}\right) & -\cos\left(\frac{2j\pi}{k}\right) & 0 \\ 0 & 0 & 1 \end{pmatrix}.$$

Clearly the reflection in the  $x - y$  plane is given by

$$T = \begin{pmatrix} 1 & 0 & 0 \\ 0 & 1 & 0 \\ 0 & 0 & -1 \end{pmatrix},$$

which we also know  $f(D)$  to be invariant under. Therefore if the  $k$ -noid is given by  $f: M \rightarrow \mathbb{R}^3$

then  $R_j f$  and  $T f$  are equivalent to  $f$ . We are now able to construct the  $k$ -noid from its symmetries.

We therefore can restrict to implementing a fundamental piece of the  $k$ -noid and obtain the remainder of the surface by applying  $2k + 1$  reflections. For the conjugate surface we need to implement the periods giving three stages to the implementation of a  $k$ -noid.

- (i) Implement a fundamental piece of the  $k$ -noid.
- (ii) Use the reflection principle to complete the  $k$ -noid and its conjugate.
- (iii) Add multiple periods of the conjugate.

The following subsection will provide a detailed description of how each stage is implemented. The code used to generate images of the  $k$ -noid can be found in the appendices of this thesis.

### 7.1.3 Constructing the $k$ -noid from its symmetries

As discussed, the  $k$ -noid is defined on  $S^2 \setminus \{p_j\} = (\mathbb{C} \setminus \{p_j\}) \cup \{\infty\}$  where  $\{p_j\}$  are the roots of unity  $p_j = e^{\frac{2\pi i j}{k}}$ , with  $j \in \{0, \dots, k - 1\}$ . The  $k$ -noid has  $2k + 1$  symmetries, on  $(\mathbb{C} \setminus \{p_j\}) \cup \{\infty\}$ . The punctured unit circle gives a geodesic on the  $k$ -noid and thus, the image of  $D = \{z \in \mathbb{C} \mid |z| < 1\}$  can be reflected across the plane orthogonal to the  $z$  axis. However, for the conjugate surface the image of the arcs  $A_j = \{z \in \mathbb{C} \mid z = e^{i\theta}, \text{ where } \frac{2\pi j}{k} < \theta < \frac{2\pi(j+1)}{k}\}$  are  $k$  different straight lines parallel to the  $z$  axis.

Therefore, the punctured unit disc has to be split into  $2k$  pieces using the lines passing through the origin and  $z_j$ . These pieces are then reflected across the unit circle, giving a total of  $4k$  domains. Figure 7.1 shows lines corresponding to the symmetry planes on the unit disc for the 4-noid, a neighbourhood has also been removed around the poles  $p_j$ .

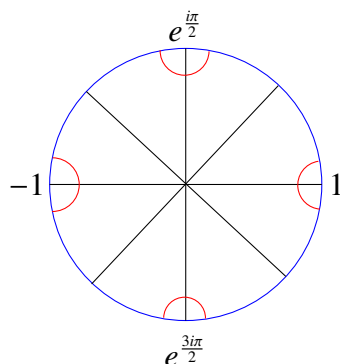


Figure 7.1: The domain on which the  $k$ -noid has been implemented for  $k = 4$ . An open disc around the poles is indicated by the red arc. For the general  $k$ -noid the domain is given by  $\Omega = \{\mathbb{C} \cup \infty\} \setminus \{B_\varepsilon(1), B_\varepsilon(e^{\frac{2\pi i}{k}}), \dots, B_\varepsilon(e^{\frac{(2k-2)\pi i}{k}})\}$ .

For implementation, we need our parameters to have positive distance to the punctures. Therefore, we take as the domain for a fundamental piece of the  $k$ -noid a segment of the unit disc with an open disc around the puncture removed, it is shown in figure 7.3. To fit with the requirements of the surface lab [91], we need a rectangular domain  $U_1^\varepsilon = [\varepsilon, 1] \times [0, \frac{\pi}{2}]$ , which will be mapped to the annulus  $U_2^\varepsilon = \{z \in \mathbb{C} \mid z = ue^{iv}, (u, v) \in U_1^\varepsilon\}$  by polar coordinates. Now, we use the map  $v : U_2^\varepsilon \rightarrow \mathbb{C}$  given by,

$$v(u, v) = \frac{1 - u^2 - v^2}{v^2 + (1 + u)^2} + i \frac{2v}{v^2 + (1 + u)^2},$$

where  $z = u + iv \in U_2^\varepsilon$ . The map  $v$  is the restriction of the map whose image of a punctured unit disc is an open disc around  $z = 1$ . The radius  $\varepsilon$  of the disc can be calculated as follows,

$$\varepsilon = v(0, 0) - v(\varepsilon, 0) = 1 - \frac{1 - \varepsilon}{1 + \varepsilon} = \frac{2\varepsilon}{1 + \varepsilon}.$$

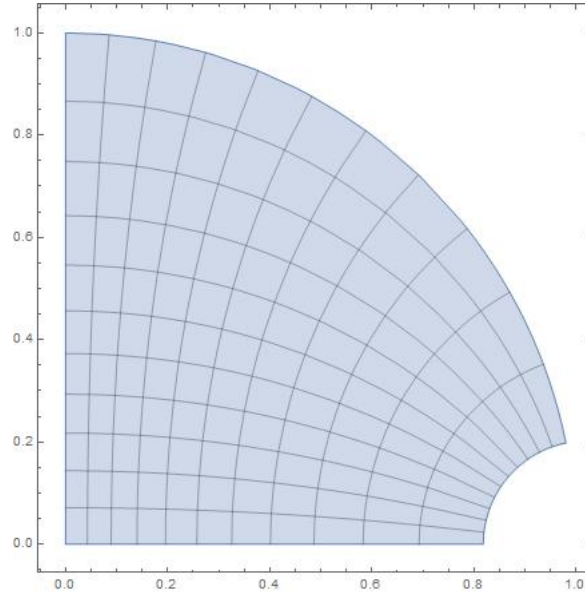


Figure 7.2: The image of the map  $\nu$  for  $z \in U_2^\varepsilon$ . The image was generated using Mathematica.

We will only consider  $z = \nu(u, v)$  with  $\arg(z) \leq \frac{\pi}{k}$ . This gives our fundamental domain  $D_0$ , where

$$D_0 = \{re^{i\theta} \in \mathbb{C} \mid 0 \leq r \leq 1, 0 \leq \theta \leq \frac{\pi}{k}\} \setminus B_\varepsilon(1),$$

and  $B_\varepsilon(1)$  is a ball of radius  $\varepsilon$  around 1. This is shown in figure 7.3. This allows us to now generate a fundamental piece of the  $k$ -noid given by  $f(D_0)$ , for  $k = 3$  this shown in figure 7.4.

The  $k$ -noid is defined on  $(\mathbb{C} \setminus \{p_j\}) \cup \{\infty\}$  where  $\{p_j\}$  are the roots of unity  $p_j = e^{\frac{2\pi i j}{k}}$ , with  $j \in \{0, \dots, k-1\}$ . This means we require a domain

$$\Omega = \{\mathbb{C} \cup \infty\} \setminus \{B_\varepsilon(1), B_\varepsilon(e^{\frac{2\pi i}{k}}), \dots, B_\varepsilon(e^{\frac{(2k-2)\pi i}{k}})\},$$

so that balls of equal radii are removed around the roots of unity  $p_j$ . This can be achieved by applying the reflection principle to  $f(D_0)$ . As  $f(te^{\frac{ij\pi}{k}})$ ,  $t \in \mathbb{R} \setminus \{1\}$ ,  $j \in \{0, \dots, 2k-1\}$ , and  $f(e^{\frac{m\pi i}{k}})$ ,

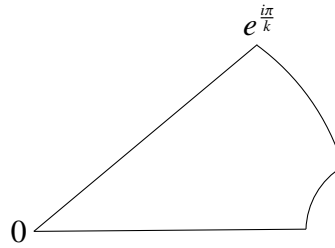


Figure 7.3: The fundamental domain  $D_0$  of the  $k$ -noid.

$t \in \mathbb{R}, t \neq 2j$ , are planar geodesics,  $f(D_0)$  may be reflected to define  $f$  on  $\Omega$ . This will be described in detail below.

The construction of the completed trinoid is shown in figure 7.5. For the general  $k$ -noid, the fundamental piece  $f(D_0) = P_1$  is reflected in the plane containing the geodesic which is the image of the straight line connecting 0 and 1. Recall that,  $G_j = f(te^{i\frac{j\pi}{k}})$ , with  $t \in (0, 1)$  and  $j \in \{0, \dots, 2k - 1\}$  are planar geodesics of the  $k$ -noid. We shall refer to the reflection of surface piece  $P$  in the plane containing planar geodesic  $G$  as  $\text{Ref}(P, G)$ . Note that the plane containing

$G_0$  is orthogonal to  $\begin{pmatrix} 0 \\ 1 \\ 0 \end{pmatrix}$ . The reflection of the fundamental piece  $P_1, P_2$  where  $P_2 = \text{Ref}(P_1, G_0)$

creates a pair of fundamental pieces as shown in the centre of the top row of figure 7.5 (for  $k = 3$ ), which we shall refer to as  $Q_1 = P_1 \cup P_2$ . To create the second pair of fundamental pieces  $Q_2, Q_1$  is then reflected in the plane containing the geodesic  $G_1$  that is  $Q_2 = \text{Ref}(Q_1, G_1)$ ,  $Q_2$  is shown in the top right of figure 7.5. To create the  $j^{\text{th}}$  pair of fundamental domains  $Q_j$  the original pair is reflected in a series of planes so that

$$Q_j = \text{Ref}(\dots \text{Ref}(\text{Ref}(Q_1, G_1), G_3) \dots G_{2j-1}).$$

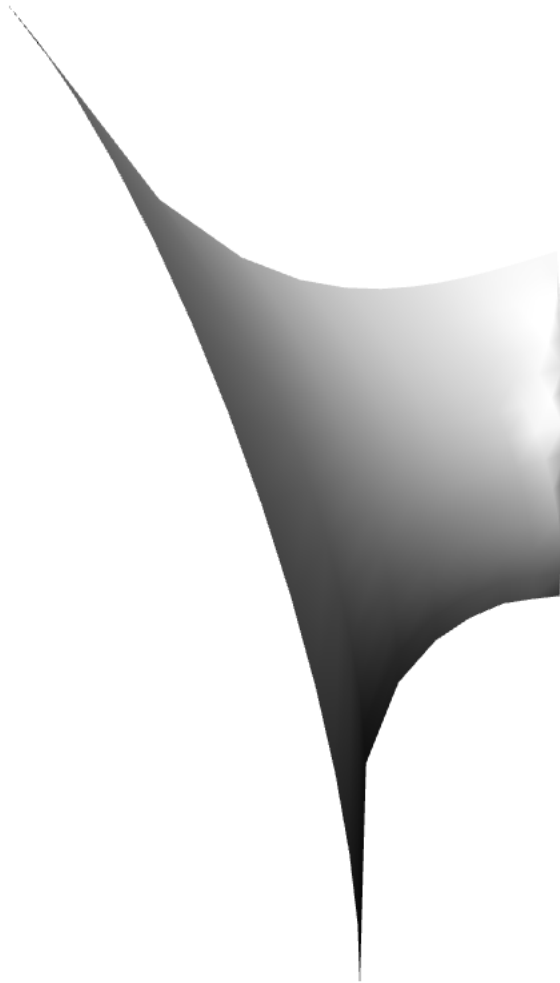


Figure 7.4: A fundamental piece of the trinoid.

To complete one half of the  $k$ -noid shown in the bottom left of figure 7.5, the reflection,

$$Q_k = \text{Ref}(\dots \text{Ref}(\text{Ref}(Q_1, G_1), G_3) \dots G_{2k-1}),$$

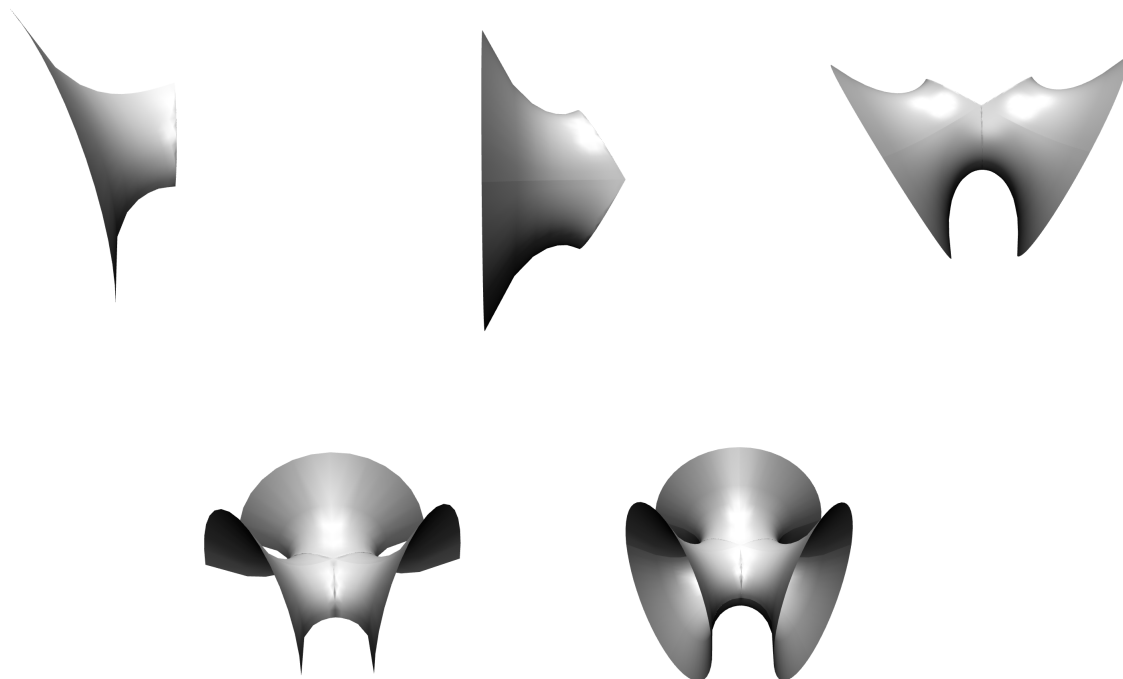


Figure 7.5: The construction of the trinoid from one fundamental piece.

is used, so that the one half of the  $k$ -noid  $T_1 = Q_1 \cup Q_2 \dots \cup Q_k$ .

The planar geodesics  $f(e^{\frac{ti}{k}})$ ,  $t \in \mathbb{R}$ ,  $t \neq 2j$ , all lie in a single plane orthogonal to the  $z$  axis.

Therefore, to complete the  $k$ -noid the set of fundamental pieces  $T_1$  is reflected in the plane

orthogonal to  $\begin{pmatrix} 0 \\ 0 \\ 1 \end{pmatrix}$ . That is,  $T_2 = \text{Ref}(T_1, \tilde{G})$ , where  $\tilde{G} = f(e^{\frac{ti}{k}})$ , with  $t \in (0, 2)$ . The completed

trinoid  $T_1 \cup T_2$  is shown in the bottom right of figure 7.5.

A goal of this work was to implement the  $k$ -noid in the surface lab so that the value of  $k$  may be adjusted on a slider. Images of the  $k$ -noid for  $k = 3, 4, 5, 6$  are shown in figure 7.6.

The part of the conjugate surface which corresponds to the upper half of the  $k$ -noid is shown on

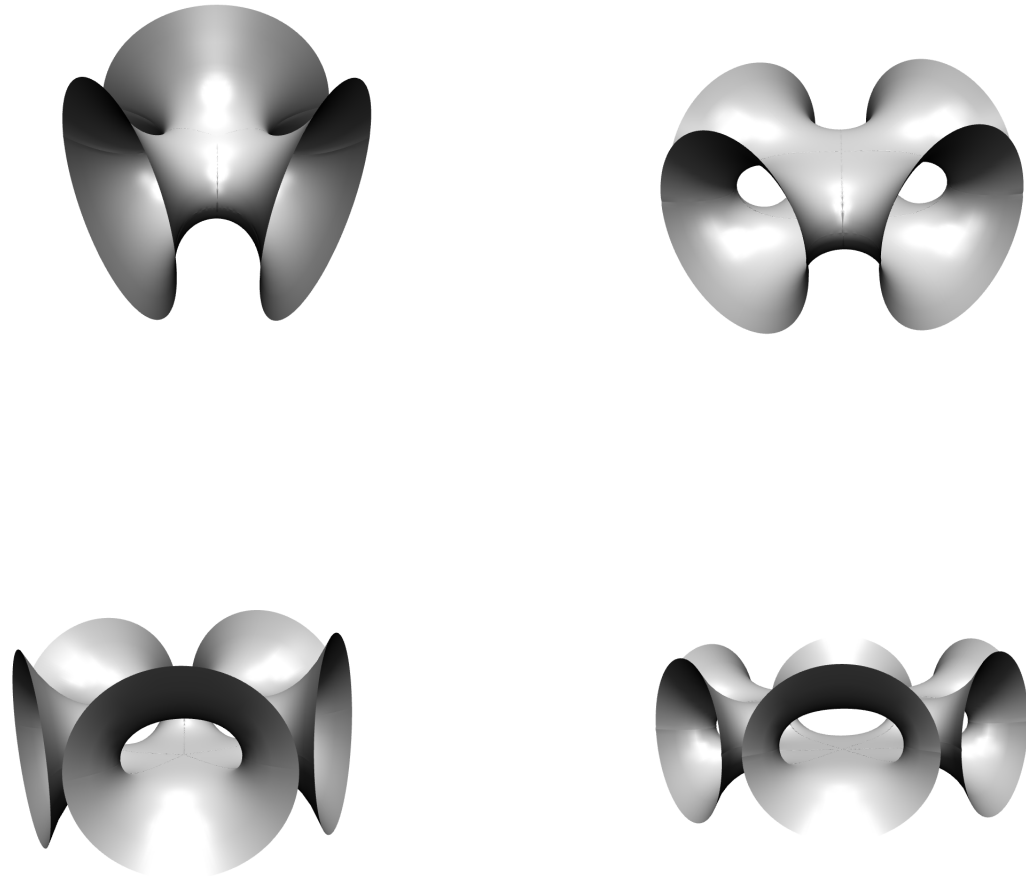


Figure 7.6: The  $k$ -noid for  $k = 3$  (top left),  $k = 4$  (top right),  $k = 5$  (bottom left), and  $k = 6$  (bottom right).

the left of figure 7.7. We will denote this part of the conjugate surface by  $T_1^* = f^*(D_{int})$ , where

$$D_{int} = \{re^{i\theta} \in \mathbb{C} \mid 0 \leq r \leq 1, 0 \leq \theta \leq 2\pi\} \setminus \{B_\varepsilon(1), B_\varepsilon(e^{\frac{2\pi i}{k}}), \dots, B_\varepsilon(e^{\frac{(2k-2)\pi i}{k}})\}.$$

For the  $k$ -noid, the curves  $G_j = f(te^{\frac{ij\pi}{k}})$ ,  $t \in \mathbb{R} \setminus \{1\}$ ,  $j \in \{0, \dots, 2k-1\}$  are planar geodesics, for the conjugate surface  $L_j = f^*(te^{\frac{ij\pi}{k}})$ ,  $t \in \mathbb{R} \setminus \{1\}$ ,  $j \in \{0, \dots, 2k-1\}$  are straight lines perpendicular to the  $z$  axis. The part  $T_1^*$  of the conjugate surface corresponding to the top half  $T_1$  of the  $k$ -noid is created in a similar way as  $T_1$  where the reflections in the plane containing  $G_j$  are replaced with 180 degree rotations around  $L_j$ . We will refer to pairs of fundamental pieces of the conjugate as  $Q_j^*$  with  $j \in \{1, \dots, k\}$  and the fundamental pieces are referred to as  $P_j^*$  with  $j \in \{0, \dots, 2k-1\}$  with  $Q_j^* = P_{2j+1}^* \cup P_{2j}^*$ .

To create the bottom half of the  $k$ -noid  $T_2$ , a single reflection was used. We will denote the corresponding part of the conjugate by  $T_2^*$ . Note that  $T_2$  and  $T_2^*$  are defined on

$$D_{ext} = (\{\frac{1}{r}e^{i\theta} \in \mathbb{C} \mid 0 < r \leq 1, 0 \leq \theta \leq 2\pi\} \cup \{\infty\}) \setminus \{B_\varepsilon(1), B_\varepsilon(e^{\frac{2\pi i}{k}}), \dots, B_\varepsilon(e^{\frac{(2k-2)\pi i}{k}})\}.$$

To create  $T_2$ , a single reflection can be used since the geodesics, which are the images of the arcs on the unit disc connecting the poles, all lie in the same plane. For the conjugate this is not the case. Each path between  $e^{\frac{2j\pi i}{k}}$  and  $e^{\frac{2(j+1)\pi i}{k}}$  on the unit circle corresponds to a distinct straight line on the conjugate. This is due to the fact that  $k$  poles lie on the unit disc and there is a discontinuity when the curve crosses a pole.

We will denote the straight lines as  $W_j = f^*(e^{\frac{tj\pi i}{k}})$ ,  $t \in (2j, 2(j+1))$ , where  $j \in \{0, \dots, k-1\}$ . The straight lines are found numerically within the implementation. That is,  $W_j$  is the line passing through  $f^*(e^{\frac{(2j+1)\pi i}{k}})$  which is parallel to the  $z$  axis.

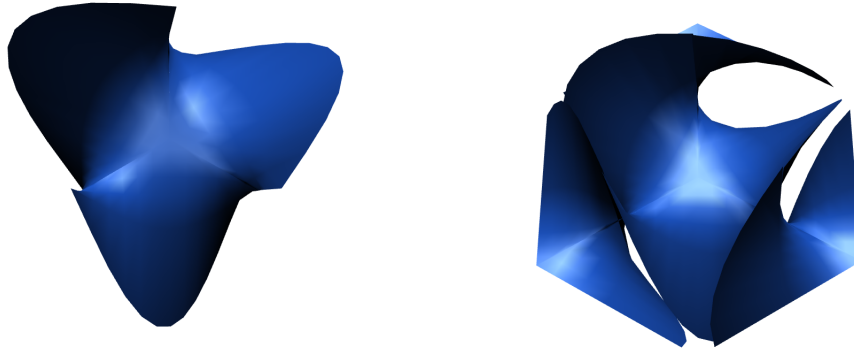


Figure 7.7: The interior of the conjugate surface to the  $k$ -noid (left) and both the interior and exterior parts (right).

To complete the exterior of the conjugate surface we will need to consider the set of pairs of fundamental pieces  $\{Q_1^*, \dots, Q_k^*\}$  as a set of fundamental pieces  $\{P_1^*, \dots, P_{2k}^*\}$ , where  $Q_j^* = P_{2j-1}^* \cup P_{2j}^*$ . A pair of fundamental pieces  $P_{2j}^* \cup P_{2j+1}^*$  are rotated around the straight line  $W_j$  to give a pair of exterior pieces  $R_j^*$ . The set of pieces  $R_1^* \cup R_2^* \dots \cup R_k^*$  is equal to  $T_2^*$ . Therefore,  $\{Q_1^*, \dots, Q_k^*\} \cup \{R_1^*, \dots, R_k^*\} = T_1^* \cup T_2^*$  is the whole conjugate surface shown on the right of figure 7.7.

From the figure it is clear that the conjugate could be extended by further rotations. Rather than rotating part of the conjugate around one of the straight lines parallel to the  $z$  axis, the interior surface could be rotated. This would create a doubly periodic surface in the  $x$  and  $y$  directions. We have already shown using the residue of the holomorphic null curve that the conjugate is doubly periodic.

For the case of  $k = 3$ , the process to create a ring of trinoid conjugates is shown in figure 7.8. The interior part is shown in the top left of the figure, this can then be rotated around any of the straight lines formed from the paths connecting the 3 poles. In the figure, the straight line

chosen is the one formed from the arc connecting 1 and  $e^{\frac{2\pi i}{3}}$ . This then produces two new straight lines which an interior part can be rotated around, hence the surface could be extended infinitely. Therefore a ring of conjugate trinoids can be produced as shown in the bottom left of the figure. This can then be further extended by rotating the ring of conjugates around one of the remaining straight lines, as shown in the bottom right.

This now gives us a complete implementation of the  $k$ -noid and its conjugate which the simple factor dressing can be applied to, as well as all transformations discussed in Chapter 3. We will now investigate the surfaces created by applying these transformations to the  $k$ -noid. The implementation will allow use to visualize these surfaces.

As an example, the Lopez-Ros deformation with  $\lambda = 2$  of the  $k$ -noid is shown in figure 7.9, where the conjugate has the same number of periods as shown in figure 7.8. The bottom right of the figure shows that the Lopez-Ros deformation of the  $k$ -noid is a doubly periodic surface. Recall from Theorem 3.3.12 that calculating the translational periods of the simple factor dressing of a minimal surface is equivalent to substituting the translational periods of  $f$  and  $f^*$  into the simple factor dressing.

For the Lopez-Ros deformation,  $f_\lambda: \tilde{M} \rightarrow \mathbb{R}^3$  then the translational periods of  $f_\lambda$ , are given by  $\tau_\lambda = 2\pi \text{Res}(\Phi_\lambda, p_j)$ . Therefore, we may calculate the translational periods  $\tau_\lambda$ , for the Lopez-Ros

deformation  $f_\lambda: \tilde{M} \rightarrow \mathbb{R}^3$ , using  $\tau_j^* = \begin{pmatrix} -\frac{2\pi \cos(\frac{2\pi j}{k})(k-1)}{k^2} \\ -\frac{2\pi \sin(\frac{2\pi j}{k})(k-1)}{k^2} \\ 0 \end{pmatrix}$ ,

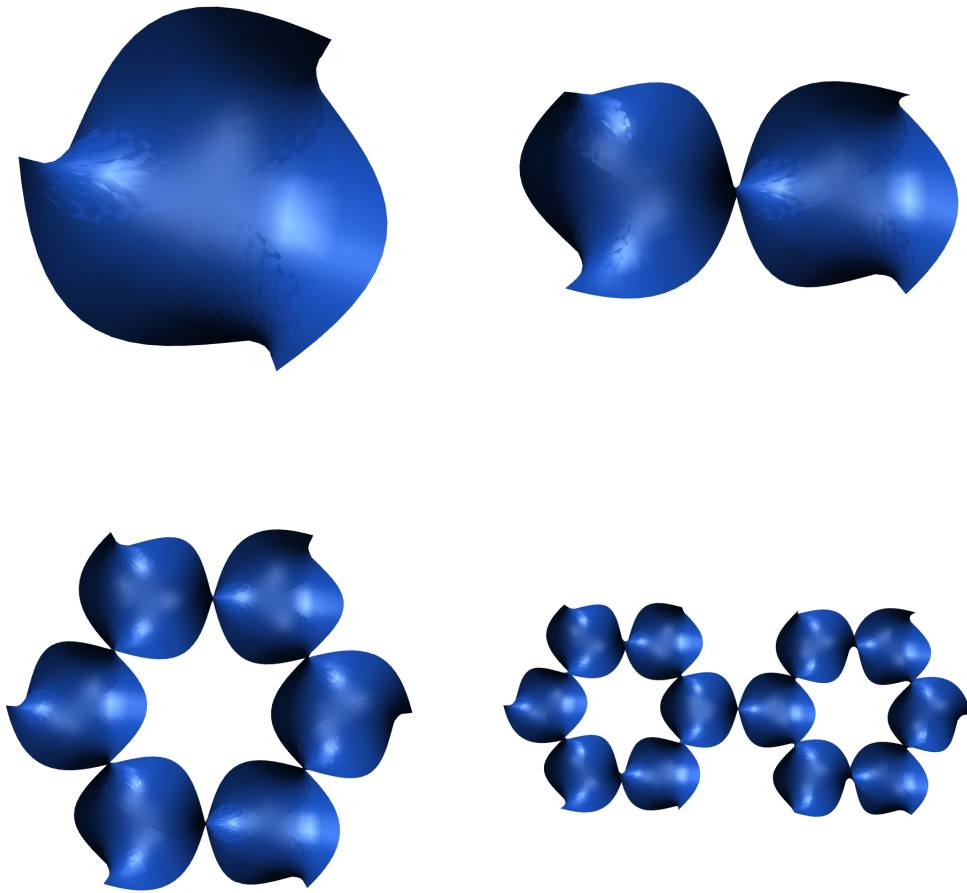


Figure 7.8: The construction of the periodic conjugate surface using its rotational symmetries.

$$\tau_\lambda = \begin{pmatrix} \cos(t)(\tau_1 \cosh(s) - \tau_2^* \sinh(s)) \\ \cos(t)(\tau_2 \cosh(s) + \tau_1^* \sinh(s)) \\ \tau_3 \end{pmatrix} = \begin{pmatrix} -\cos(t)\tau_2^* \sinh(s) \\ \cos(t)\tau_1^* \sinh(s) \\ 0 \end{pmatrix} = \begin{pmatrix} \cos(t) \sinh(s) \frac{2\pi \sin(\frac{2\pi j}{k})(k-1)}{k^2} \\ -\cos(t) \sinh(s) \frac{2\pi \cos(\frac{2\pi j}{k})(k-1)}{k^2} \\ 0 \end{pmatrix}.$$

Thus, we see that the Lopez-Ros deformation of the  $k$ -noid is a doubly periodic surface for  $s \neq 0$  and  $k > 2$ .

## 7.2 The periodicity of the simple factor dressing of the $k$ -noid

In this section the periodicity and the behaviour of the catenoidal ends of the  $k$ -noid under the simple factor dressing is considered. We have already seen from Theorem 3.2.15 that the periodicity of the conjugate of a minimal surface is determined by the value of the residue at the poles. From Theorem 3.2.14, we see that a catenoidal end at  $p_j$  is mapped to a catenoidal end under the simple factor dressing if the residue of  $\hat{\Phi}'$  remains real and non-zero. Put differently, if the simple factor dressing of the  $k$ -noid has no periods at end  $p_j$ , then the simple factor dressing of the  $k$ -noid has an end at  $p_j$  and it is catenoidal.

Let us first find the simple factor dressings which preserve at least one of the catenoidal ends of the  $k$ -noid. First, note that for the simple factor dressing of a minimal surface

$$\text{Res}(\hat{\Phi}, p_j) = R^{-1}AR \text{Res}(\Phi, p_j), \quad (18)$$

where  $R$  is a rotation matrix and  $A$  is the matrix representation, see Theorem 3.3.10 of the simple factor dressing with parameter  $\mu$ . This allows us to prove the following theorem.

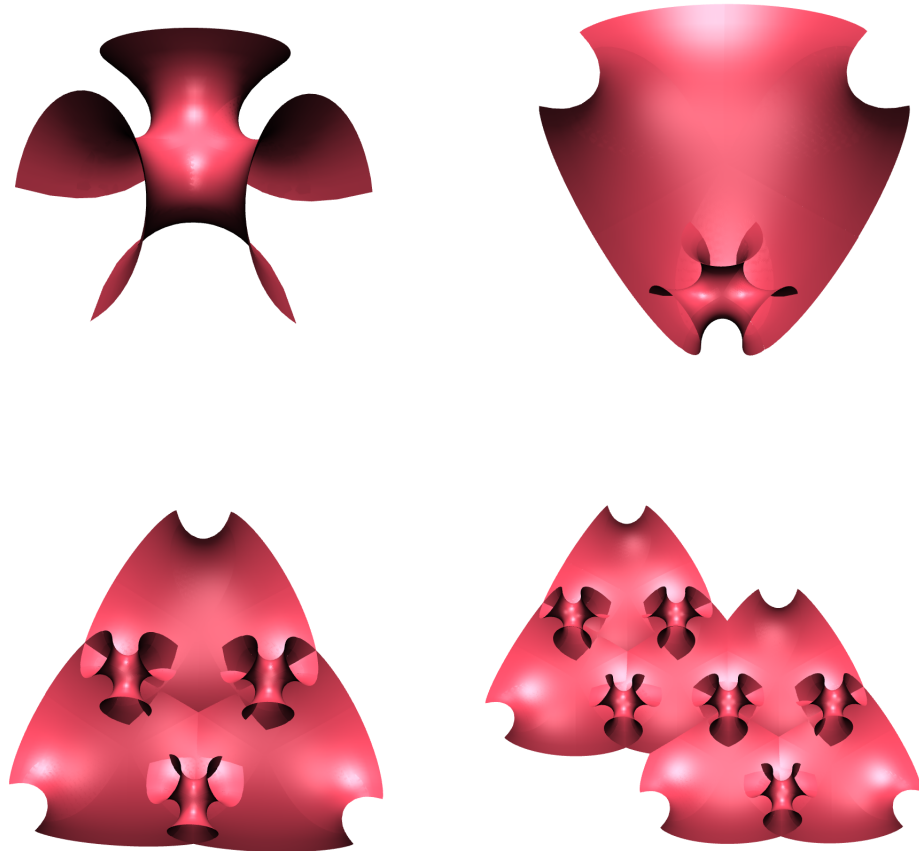


Figure 7.9: The Lopez-Ros deformation of the  $k$ -noid with  $\lambda = 2$  with multiple periods shown.

**Theorem 7.2.1.** *The simple factor dressing of the  $k$ -noid in  $\mathbb{R}^3$  will preserve at least one catenoidal end of the  $k$ -noid if and only if  $m = m_1 + (m_1(\cot(\frac{2\pi j}{k}) + \csc(\frac{2\pi j}{k})))\mathbf{k}$ , where  $m_1 \in \mathbb{R}$ . If  $k$  is odd then only the end at  $e^{\frac{2\pi ji}{k}}$  is preserved. If  $k$  is even the ends at  $e^{\frac{2\pi ji}{k}}$  and  $e^{\frac{(2\pi j+k\pi)i}{k}}$  are preserved. In both cases the simple factor dressing is independent of the choice of  $m_1$ .*

*Proof.* Consider the translational period of the simple factor dressing of the  $k$ -noid in  $\mathbb{R}^3$ , note that we calculate  $\hat{\tau}$  from (18),

$$\hat{\tau}_j = 2\pi \begin{pmatrix} \frac{2(k-1) \sinh(s) \sin(\frac{2\pi j}{k})(m_1 m_3 - m_2 m_4)}{k^2(m_1^2 + m_2^2 + m_3^2 + m_4^2)} \\ - \frac{2(k-1) \sinh(s) \cos(\frac{2\pi j}{k})(m_1 m_3 - m_2 m_4)}{k^2(m_1^2 + m_2^2 + m_3^2 + m_4^2)} \\ \frac{(k-1) \sinh(s) (\sin(\frac{2\pi j}{k})(m_1^2 + m_2^2 - m_3^2 - m_4^2) - 2 \cos(\frac{2\pi j}{k})(m_1 m_4 + m_2 m_3))}{k^2(m_1^2 + m_2^2 + m_3^2 + m_4^2)} \end{pmatrix},$$

where  $m = m_1 + m_2\mathbf{i} + m_3\mathbf{j} + m_4\mathbf{k}$  and  $m_1, m_2, m_3, m_4 \in \mathbb{R}$ . Solving the equation  $\hat{\tau}_j = 0$  gives,  $m = m_1 + m_1(\cot(\frac{2\pi j}{k}) + \csc(\frac{2\pi j}{k}))\mathbf{k}$  or  $m = m_1 + m_1(\cot(\frac{2\pi j}{k}) - \csc(\frac{2\pi j}{k}))\mathbf{k}$  as a solution. Note that both of these produce the same simple factor dressing, and do not depend on the choice of  $m_1$ . A simple factor dressing with  $s = 0$  would also solve  $\hat{\tau}_j = 0$ , however this would generate the  $k$ -noid so we do not include it.

Therefore the simple factor dressing in  $\mathbb{R}^3$  with  $m = m_1 - (m_1(\cot(\frac{2\pi j}{k}) + \csc(\frac{2\pi j}{k})))\mathbf{k}$  preserves the catenoidal structure of the end at  $e^{\frac{2\pi ji}{k}}$ . If  $k$  is even then the catenoidal end at  $e^{\frac{(2\pi j+k\pi)i}{k}}$  is also preserved, due to the trigonometric identity that  $\csc(\theta + \pi) = -\csc(\theta)$ .

The simple factor dressing with  $m = n = m_1 + (m_1(\cot(\frac{2\pi j}{k}) + \csc(\frac{2\pi j}{k})))\mathbf{k}$  is independent of the choice of  $m_1$  for all minimal surfaces  $f: M \rightarrow \mathbb{R}^3$ . It is straightforward to compute that for general quaternion  $f$ , we have that  $m((m^{-1}fm)^\mu m^{-1})$  does not depend on  $m_1$ .  $\square$

So in the case of  $k$  being an odd number the simple factor dressing with  $m = m_1 + m_1((\cot(\frac{2\pi j}{k}) +$

$\csc(\frac{2\pi j}{k})\mathbf{k}$  will preserve one catenoidal end at  $e^{\frac{2\pi ij}{k}}$ . This is shown in figure 7.10 for the trinoid with  $\mu = \frac{1}{2}$  and  $j = 1, 2, 3$ .

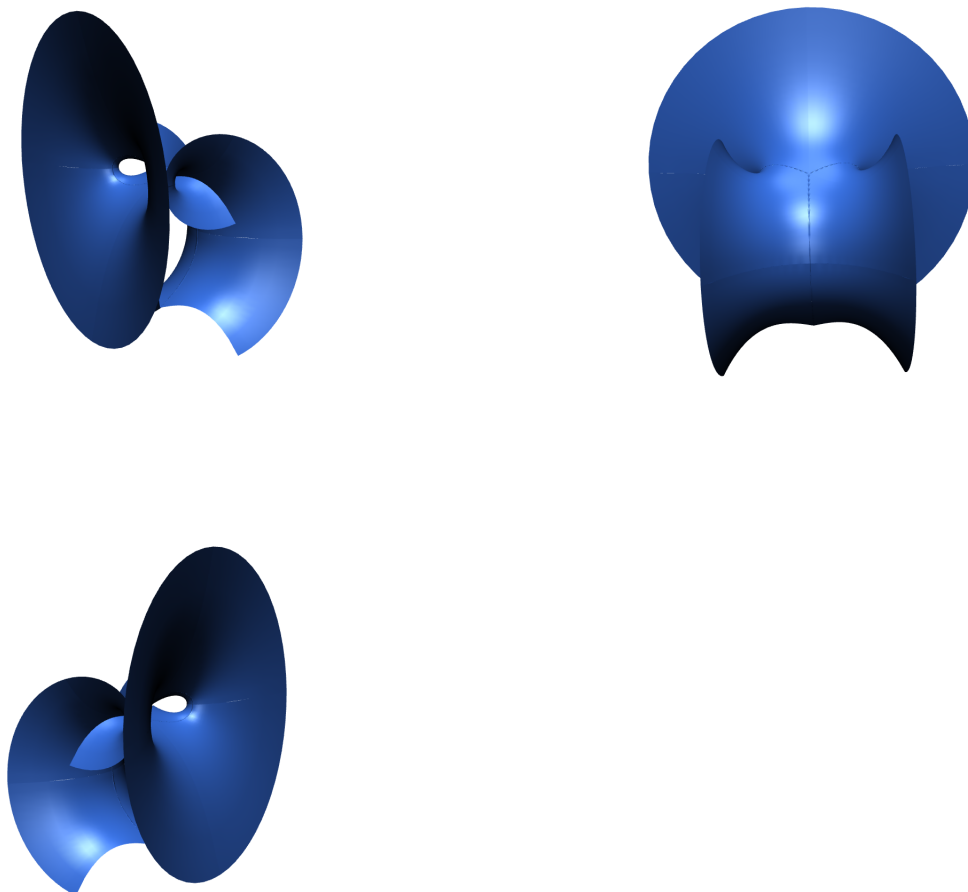


Figure 7.10: The simple factor dressing of the trinoid with  $\mu = \frac{1}{2}$  and  $m = m_1 + (m_1(\cot(\frac{2\pi j}{k}) + \csc(\frac{2\pi j}{k}))\mathbf{k}$ , for  $j = 1$  (top left),  $j = 2$  (top right) and  $j = 3$  (bottom).

In the case of  $k$  being even two ends are preserved by the simple factor dressing with  $m = m_1 + (m_1(\cot(\frac{2\pi j}{k}) + \csc(\frac{2\pi j}{k}))\mathbf{k}$ . It is shown in figure 7.11 for  $\mu = \frac{1}{2}$  and  $j = 1, 2, 3, 4$ .

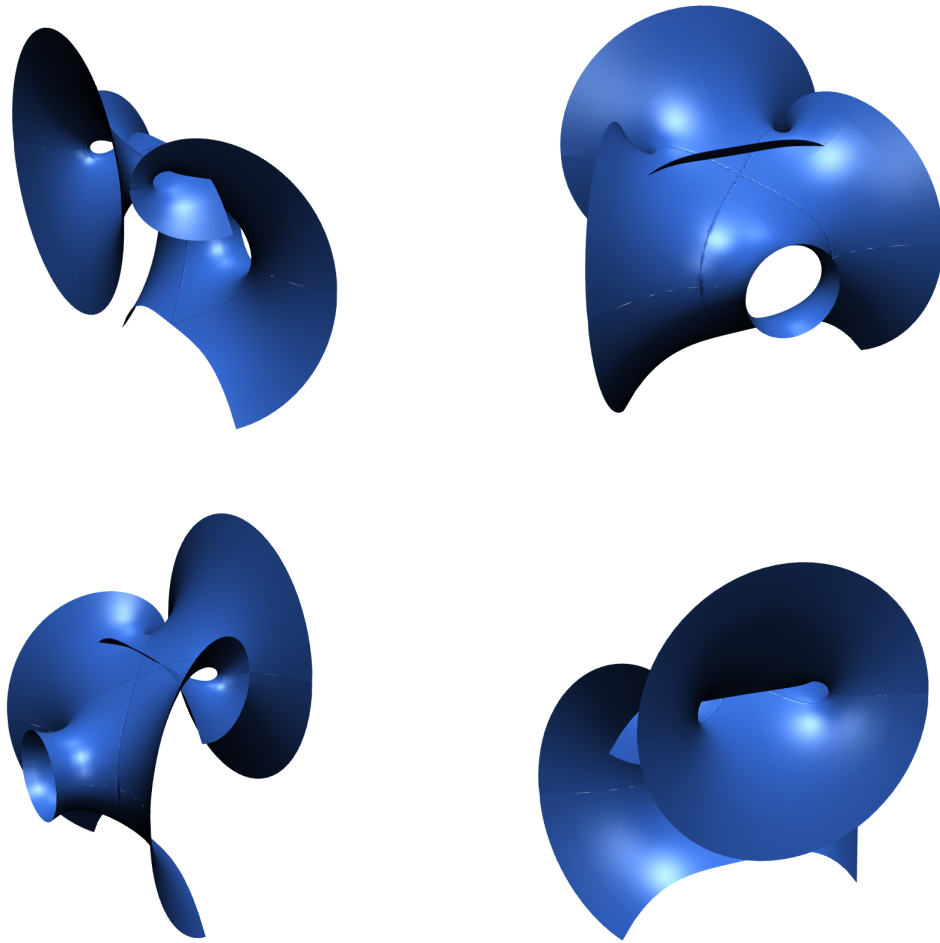


Figure 7.11: The simple factor dressing of the 4-noid with  $\mu = \frac{1}{2}$  and  $m = m_1 + (m_1(\cot(\frac{2\pi j}{k}) + \csc(\frac{2\pi j}{k})))\mathbf{k}$ , for  $j = 1$  (top left),  $j = 2$  (top right),  $j = 3$  (bottom left) and  $j = 4$  (bottom right).

From the figures we see that in this case that the simple factor dressing with  $m = m_1 + (m_1(\cot(\frac{2\pi j}{k}) + \csc(\frac{2\pi j}{k})))\mathbf{k}$  of the  $k$ -noid does not depend on  $j$  up to a rotation of the surface. This will become clear from the symmetry relations on  $f$  and  $f^*$ . Consider  $\text{Re}((m^{-1}\Phi m)^\mu)$ , where  $\Phi = f + if^*$ ,

$$\operatorname{Re}((m^{-1}\Phi m)^\mu) = \begin{pmatrix} f_2 \sin\left(\frac{2\pi j}{k}\right) - f_1 \cos\left(\frac{2\pi j}{k}\right) \\ f_3^* \sinh(s) - \cosh(s) \left( f_1 \sin\left(\frac{2\pi j}{k}\right) + f_2 \cos\left(\frac{2\pi j}{k}\right) \right) \\ f_3 \cosh(s) - \sinh(s) \left( f_1^* \sin\left(\frac{2\pi j}{k}\right) + f_2^* \cos\left(\frac{2\pi j}{k}\right) \right) \end{pmatrix}.$$

As  $f$  and  $f^*$  are both invariant under a rotation of  $\frac{2\pi j}{k}$  around the  $z$  axis, we see that  $\operatorname{Re}((m^{-1}\Phi m)^\mu)$  is the same surface for all  $j$  up to rotation and hence so is the simple factor dressing with  $m = m_1 + (m_1(\cot(\frac{2\pi j}{k}) + \csc(\frac{2\pi j}{k})))\mathbf{k}$ .

We have already seen that a minimal surface has a catenoidal end at point  $p_j$  if the residue at pole  $p_j$  of the derivative of the holomorphic null curve  $\operatorname{Res}(\Phi', p_j)$  is real and non zero. Moreover, the translational period of the conjugate is given by  $2\pi \operatorname{Res}(\Phi', p_j)$ . Therefore, if  $\lambda_j$  is a curve around  $p_j$  generating the translational period  $\tau_j$  and if there is a catenoidal end at  $p_j$ , then the translational period of the surface vanishes. If one translational period has been closed and a catenoidal end at  $p_j$  has been preserved it is a natural question to ask how the other catenoidal ends at  $p_l$  where  $l \in \{1, \dots, k\} \setminus \{j\}$  and their translation periods  $\tau_l$  behave. It is straightforward to calculate that for the simple factor dressing with  $m = m_1 + (m_1(\cot(\frac{2\pi j}{k}) + \csc(\frac{2\pi j}{k})))\mathbf{k}$  the residue of  $\hat{\phi}'$  at  $p_l$  is,

$$\operatorname{Res}(\Phi', p_l) = \begin{pmatrix} 0 \\ -\frac{(k-1) \sinh(s) \sin\left(\frac{2\pi j}{k} + 2\pi l + t\right)}{k^2} \\ \frac{(k-1) \sinh(s) \cos\left(\frac{2\pi j}{k} + 2\pi l + t\right)}{k^2} \end{pmatrix},$$

which does not depend on  $l$ . We also see that multiple periods cannot be closed at the same time and therefore no non-periodic minimal surfaces can be generated in  $\mathbb{R}^3$  from a simple factor dressing of the  $k$ -noid. The simple factor dressing of the trinoid with  $m_4 = 0$  (i.e.  $j = 3$ ) is shown

in figure 7.12, where extra periods have been added.



Figure 7.12: The simple factor dressing of the trinoid with  $\mu = \frac{1}{2}$  and the first period has been closed by setting  $m_4 = 0$ . The transformation does not depend on  $m_1$ .

### 7.3 Symmetries of the simple factor dressing of the $k$ -noid

We have already discussed the symmetries of the  $k$ -noid and its conjugate by considering the geodesics and applying the reflection principle. We will now consider the symmetries of the Lopez-Ros deformation and simple factor dressings of the  $k$ -noid in  $\mathbb{R}^3$ . From the images shown in this chapter, it is clear that the symmetries of these surfaces are dependent the choice of the quaternion  $m$ . For instance, recall that figure 7.9 shows the Lopez-Ros deformation. Figure 7.9 shows a highly symmetric surface, however, the simple factor dressing with parameter  $\mu$  shown in figure 7.12 appears to have one reflective symmetry.

We will now consider the symmetries of the simple factor dressing and investigate under what conditions they are preserved. Firstly consider the definition of an isometry on the Riemann surface  $M$ .

**Definition 7.3.1.** *If  $M$  and  $\tilde{M}$  are Riemannian manifolds the map  $\alpha : M \rightarrow \tilde{M}$  is said to be a isometry if the metric is preserved that is for  $X, Y \in T_p M$  we have*

$$g_p(X, Y) = \tilde{g}_{\alpha(p)}(d\alpha(X), d\alpha(Y)).$$

In the case of  $S^2 \setminus \{p_1, \dots, p_k\}$ , the functions

$$\alpha_j(z) = e^{\frac{2\pi ij}{k}} z, \quad \beta_j(z) = e^{\frac{\pi ij}{k}} \bar{z}, \quad \gamma(z) = \frac{1}{z},$$

are the only automorphisms, since the set of punctures must be preserved under an automorphism. The following theorem of Meeks and Hoffman [148] allows us to relate the symmetries of a minimal immersion to the symmetries of the domain.

**Theorem 7.3.2.** *If  $f : M \rightarrow \mathbb{R}^3$  is a minimal immersion and  $A \in O(3)$  is a symmetry of  $f$  then an automorphism  $\alpha$  is induced on  $M$ , that is*

$$f \circ \alpha = Af.$$

That is, if  $A$  is a symmetry on  $f(M)$  an automorphism  $\alpha$  must exist on  $M$ . We will consider the rotation symmetries of the simple factor dressing of the  $k$ -noid, that is  $\hat{f}(e^{\frac{2\pi ij}{k}} z)$ . We will prove the following:

**Theorem 7.3.3.** *If  $\hat{f} : \tilde{M} \rightarrow \mathbb{R}^3$  is the simple factor dressing of the  $k$ -noid then  $\hat{f}$  preserves all rotational symmetries of the  $k$ -noid if and only if*

$$m = m_1 + m_2 \mathbf{i} - m_1 \mathbf{j} + m_2 \mathbf{k},$$

with  $m_1, m_2 \in \mathbb{R}$ .

*Proof.* To prove the above recall from section 7.1.2 that  $f$  and  $f^*$  have the same symmetry relations  $f(e^{\frac{2\pi ij}{k}} z) = R_j f(z)$  and  $f^*(e^{\frac{2\pi ij}{k}} z) = R_j f^*(z)$  where  $R_j$  is a matrix representing a rotation by  $\frac{2\pi j}{k}$  around the  $z$  axis, and note  $\Phi(e^{\frac{2\pi ij}{k}} z) = R_j \Phi(z)$ . Consider the matrix representation of the simple factor dressing  $\hat{f}$  of  $\alpha_j(z) = e^{\frac{2\pi ij}{k}} z$ ,  $\text{Re}(M^{-1} B M \Phi(e^{\frac{2\pi ij}{k}} z))$ , where  $B$  represents the simple factor dressing with parameter  $\mu$  and  $M$  is a rotation in  $\mathbb{R}^3$ . Note we only need to consider  $\text{Re}(B M \Phi(e^{\frac{2\pi ij}{k}} z))$ , then,

$$M \hat{f}(e^{\frac{2\pi ij}{k}} z) = \text{Re}(B M \Phi(e^{\frac{2\pi ij}{k}} z)) = \text{Re}(B M R_j \Phi(z)) = \text{Re}(C B M \Phi(z)) = \text{Re}(C) M \hat{f} - \text{Im}(C) M \hat{f}^*,$$

where,  $C = BMR_jM^{-1}B^{-1}$ . We wish to find under what conditions  $\text{Re}(C)M\hat{f} - \text{Im}(C)M\hat{f}^*$  is a rigid motion of  $M\hat{f}(e^{\frac{2\pi ij}{k}}z)$ . Therefore, we require that  $\text{Im}(C) = 0$  and  $\text{Re}(C)$  is an orthogonal matrix, as  $\text{Im}(C)M\hat{f}^*$  cannot be written in terms of  $\hat{f}$ , as  $\hat{f}$  is not self-conjugate. It is straightforward to compute that we require that

$$m = m_1 + m_2\mathbf{i} - m_1\mathbf{j} + m_2\mathbf{k},$$

completing the proof. □

Recall from theorem 3.3.13 that the Lopez-Ros deformation is the simple factor dressing in  $\mathbb{R}^3$  with  $m = \frac{1-\mathbf{i}-\mathbf{j}-\mathbf{k}}{2}$ . Therefore, putting  $m_1 = \frac{1}{2}$  and  $m_2 = -\frac{1}{2}$  we see that the Lopez-Ros deformation satisfies the conditions of the previous theorem:

**Corollary 7.3.4.** *The Lopez-Ros deformation preserves the rotational symmetries of a  $k$ -noid.*

## 7.4 Conclusions

In this chapter we have applied the simple factor dressing to the  $k$ -noid and investigated the resulting minimal surfaces. To do so, the Jorge-Meeks  $k$ -noid was implemented as an extension of the surface lab which was developed using the JReality software package. This type of implementation allows for a high degree of control and transformations can easily be applied to the surface. The  $k$ -noid required multiple domains to be created to allow the conjugate surface to be correctly implemented. This allowed for the simple factor dressing to be visualized.

Our first interest was in the periodicity of the resulting surfaces, this is defined by the value of

the residue at the poles. The  $k$ -noid is defined on the punctured sphere whereas the conjugate surface in general is doubly-periodic. For an appropriate choice of the parameter  $m$  of the simple factor dressing, we have shown that the simple factor dressing is singly-periodic.

Finally, we investigated the symmetries of the simple factor dressings. In particular, we proved that the Lopez-Ros deformation preserves the rotational symmetries of the  $k$ -noid. Looking forward, the reflective symmetries of the simple factor dressing could also be investigated. Figure 7.11 indicates that a single reflective symmetry could be preserved, dependant on the value of  $j$ .

Additionally to the Jorge-Meeks  $k$ -noid a similar process to that described in this chapter could be used to investigate other minimal surfaces. For example one could investigate the simple factor dressing of  $k$ -noids of higher genus or lower symmetry, see [149] for work on these surfaces. Since the relationship between the genus and number of catenoidal ends of a minimal surface has been of particular interest [150], potentially by investigating a  $k$ -noid of arbitrary genus and its simple factor dressing a better understanding of this relationship could be developed.

# Chapter Eight - Conclusions

## 8 Conclusions

This chapter will conclude and summarise this thesis. Potential future work is also discussed. The work presented in this thesis analyses temperature-induced transitions in lipid bilayers, coalescence of aqueous aerosol droplets and transformations of minimal surfaces. Resultant morphology changes were analysed using optical tweezers, light scattering, mathematical modelling and visualization techniques. The initial goal of the project was analyse the coalescence of micrometer sized liquid droplets both experimentally with optical tweezers and theoretically. This was achieved by comparing elastic light scattering over the coalescence with simulations of the composite droplets aspect ratio. Additionally, we wished to explore the capability of the optical tweezers and spectroscopic detection to analyse morphological changes in biological membranes. The optical tweezers were configured to analyse temperature-induced transitions in micron sized liposomes using elastic and inelastic scattering techniques.

Initially, for the coalescence, it was hoped that by modelling the precursor and composite droplet as constant mean curvature surfaces coordinates for the composite droplets could be produced as it coalesces. A literature search revealed that this type of model would be inappropriate, though analytic techniques have given expressions for the shape of the meniscus connecting the precursor droplets. To produce coordinates for the coalescing droplet numerical methods are required. A finite element process was used to solve the Navier-Stokes type equations governing the process. The work on constant mean curvature surfaces lead us to investigate the related class of minimal surfaces ( $H = 0$ ). A  $k$ -noid was implemented using the JReality package allowing for high quality images of the surface to be produced. The simple factor dressing was then applied to the  $k$ -noid to create new families of minimal surfaces. The symmetry and periodicity of these surfaces was then analysed.

In chapter 5, elastic and Raman scattering was used to probe temperature-induced transitions in lipid bilayers. For the main gel-to-liquid crystalline transition of a single optically trapped liposome a sharp change in the intensity of elastically scattered light was recorded over the main transition. Previous work on liposome suspensions showed a gradual transition occurring over approximately 1 °C, we are able to probe the transition of a single liposome over a temperature difference of 1 m°C. An analysis of the diffraction pattern allow us to conclude that this change in scattering can be attributed to a loss of rigidity of the bilayer as it enters the fluid phase. Raman spectra were recorded in the C-H region for a single optically trapped liposome in the gel, fluid and ripple phases. The spectra are understood to show a decrease in molecular packing order as would be expected over the temperature ramp.

Other temperature sensitive behaviour was induced by the intercalation of cholesterol and sphingomyelin on the lipid bilayer. Transitions from an ordered bilayer to a disordered bilayer with ordered microdomains, and a disordered bilayer with ordered microdomains to a uniform disordered bilayer were considered. The change in rigidity of the bilayer was recorded using elastic scattering. Again this showed a sharp change in rigidity of the bilayer on the scale of m°C. The multicomponent lipid bilayers were also analysed using Raman spectroscopy. Sets of spectra were recorded for single optically trapped liposomes over the temperature ramp showing a gradual change in molecular ordering.

The results demonstrate the capability of optical trapping to analyse physical change in liposomes. Potentially, a complete study of temperature transitions for single optically trapped liposomes could be undertaken for liposomes with different physical properties. To do so a more refined system for controlling temperature would be required. Outside of temperature transitions, the use of microfluidic devices is now being investigated as a means to expose liposomes to another solution. This would allow several phenomena including liposome fusion and the infection

of a liposome to be analysed using spectroscopic methods.

The coalescence of liquid droplets is analysed in chapter 6 using both experimental and computational techniques. A finite element based procedure was used to model coalescence. The model was contrasted with experimental results recorded at the University of Bristol using holographic optical tweezers. The coalescence process was analysed for variable viscosity fluids and for differently orientated composite droplets within the optical trap using mathematical modelling, elastic light scattering and a high speed camera.

Coalescence was induced both parallel and transverse to the direction of propagation of light. The mathematical modelling was used to illustrate both cases. From the videos, it becomes clear that the light scattering probes significantly different regions of the composite droplet in either case. In the transverse case, the coalescence takes place in between the two optical traps, supporting the conclusion that forces driving coalescence are stronger than those of the optical trap. Higher order modes of the oscillation become clearer in the elastic scattering when coalescence is induced in the parallel direction. This behaviour can also be analysed by considering the aspect ratio of the simulated composite droplet. In the transverse case, the laser is probing the region of high curvature around the meniscus, whereas in the parallel case the laser probes an expanding and contracting spherical region.

Viscosity of the droplet could be increased by adjusting the relative humidity of the chamber. The dynamics of coalescence are determined by the Reynolds number, which describes the ratio of inertial to viscous forces. There is a critical value of viscosity at which the oscillation in shape is overdamped by viscosity. In this case, the mathematical model shows a coalescence where the predominant feature is the evolution of the meniscus.

Experimentally, the aspect ratio of images taken using the high speed camera could be compared

to the elastic light scattering and simulated aspect ratio. For lower viscosity droplets, where the coalescence occurs on a microsecond time-scale, the high frame rate images and elastic scattering are essentially equivalent. For higher viscosity droplets, where the coalescence occurs on a millisecond time-scale the elastic scattering is distorted by the repositioning of the composite droplet in an optical trap. However images taken using the high speed camera may still be compared to simulated images, validating the approach.

Overall we have demonstrated the ability of the finite element procedure to analyse several different types of coalescence dependant on viscosity and the droplets orientation. Looking further, simulated results for a low viscosity fluid (or equivalently higher surface tension) suggest additional features may be present in the coalescence. An complete analysis of coalescence of such a fluid could be undertaken experimentally to explore these features further.

In chapter 7 the simple factor dressing is applied to the  $k$ -noid. The  $k$ -noid and its conjugate surface have been implemented using the JReality software package allowing for the simple factor dressing to be visualized. The conjugate surface is a doubly periodic minimal surface. However, for some choices of the parameter of the simple factor dressing the resulting surfaces is a singly periodic surface in  $\mathbb{R}^3$ . The symmetry of simple factor dressings in  $\mathbb{R}^3$  is also considered.

Apart from the Jorge Meeks  $k$ -noid there are other minimal surface classes this work could be applied to. For example, it is possible to create a  $k$ -noid of higher genus or with less symmetries. There are several open problems in the theory of minimal surfaces relating to the possible number of catenoidal ends and genus of a minimal surface. Potentially, by investigating transformations of a higher genus  $k$ -noid a better understanding of these problems could be developed.

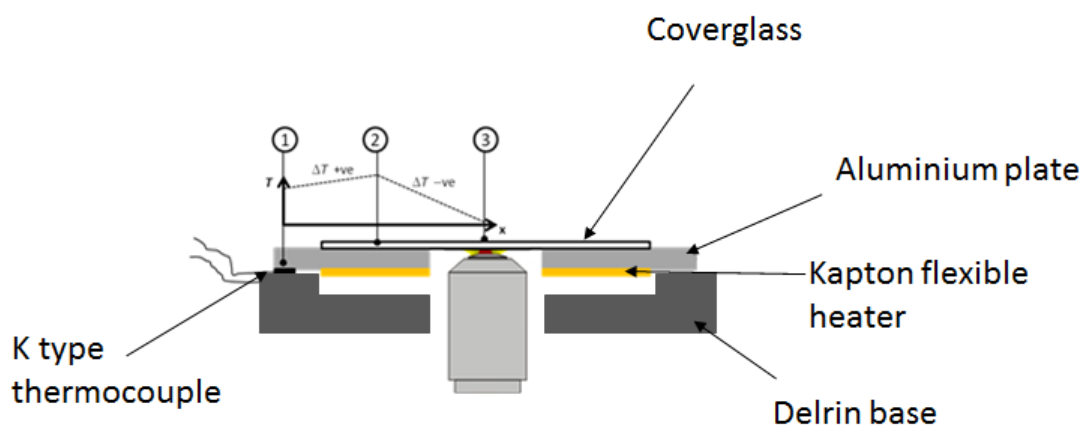


Figure A.1: Schematic of the heating plate.

## Appendices

### A Customised heating stage plate

A custom built delrin and aluminium plate was used to heat samples dispensed onto the microscope stage. The plate consisted of a rectangular delrin base of dimensions  $10 \times 5 \times 1$  cm with a rectangular alluminum heating plate  $8 \times 4 \times 0.5$  cm attached. Both plates had a 4 cm diameter aperture in the centre. Between the delrin and aluminium layer a ring-shaped kapton-insulated flexible heater (50 mm-outer diameter, 25 mm-inner diameter; Minco Products Inc.) was bonded onto the lower surface. The temperature was monitored with a K-type thermocouple on the edge of the aluminium plate. The thermocouple was connected to the computer and by a LabView programmes.

A schematic of the heating plate is shown in figure A.1. A limitation of the design is that an accurate temperature cannot be measured at the precise position of an optically trapped particle.

In our experiments, the temperature is reported based on a measurement with a contact K-type thermocouple positioned at the edge of the heated aluminium plate. The profile of the temperature across the aluminium plate, and the coverglass on which the sample is dispensed is considered below.

Figure A.1 shows 3 points on stage, (1) at the thermocouple, (2) directly above the heating element and (3) where the liposome is optically trapped. There was a positive temperature gradient between the edge of the aluminium plate (1) and the surface area of the aluminium plate that was actually in contact with the coverglass (2); this area of the aluminium plate is directly above the bonded-Kapton flexible element. Furthermore, there was a negative temperature gradient between the area of the coverglass in contact with the heating plate (2) and the centre of the coverglass (3); the liposome was optically-trapped at a height of  $50\ \mu\text{m}$  above the centre of the coverglass.

An estimate of the magnitude of the temperature difference,  $\Delta T_{(1,3)}$  between (1) and (3), when the bonded thermocouple at the edge of the aluminium plate reports a temperature,  $T_3$ , of  $44\ ^\circ\text{C}$  can be made; i.e. the temperature at which the main phase transition of the DPPC liposomal bilayer was observed.

Firstly we measure the temperature difference between (1) and (2),  $\Delta T_{(1,2)}$  by placing a 2nd (non-bonded) K-type thermocouple in contact with the upper surface of the aluminium plate at (2). When the bonded thermocouple reported a temperature of  $44.0\ ^\circ\text{C}$  at (1), the non-bonded thermocouple reported a temperature of  $42.2\ ^\circ\text{C}$  at (2). Thus,  $\Delta T_{(1,2)}$  is  $1.8\ ^\circ\text{C}$ , when  $T_1 = 44\ ^\circ\text{C}$ .

The coverglass can be assumed to be in good thermal contact with the aluminium plate, and the surface of the coverglass at (2) is at the same temperature as the aluminium plate. The temperature difference between (2) and (3)  $\Delta T_{(2,3)}$  is estimated from measurement of temperature at (2)

and (3) using a non-contact IR thermometer. Absolute temperature values cannot be measured directly by the IR thermometer because the emissivity  $e$  of the surface and of the coverglass is unknown. A linear dependence was assumed between  $\Delta T_{(1,2)}$  and the magnitude of  $T_1$  above room temperature; i.e.  $T_2 = T_1 + 1.8 \frac{(T_1 - 22)}{22}$ . The emissivity of the coverglass surface was estimated by assuming the energy  $E$  radiated by the surface, per second per unit area, follows Stefan Boltzmanns law,  $E = \sigma e T_2^4$ , where  $\sigma$  is Stefan-Boltzmanns constant.  $\Delta T_{(2,3)}$  can now be determined from the difference in energy radiated by surface of the coverglass at (2) and (3).

The actual temperature at (1) (Al plate) and (2) (centre of coverglass) is shown in figure A.2 as a function of the temperature reported by the bonded thermocouple. The literature value for the main transition in DPPC bilayers (41.6 °C see table 5.1) is shown relative to the reported temperature of 44 °C at (1). The precision of a temperature measurement by the infrared thermometer at (2) was  $\pm 0.5$  °C. The error reported in figure A.1 for  $T_3$  takes into account the uncertainty in the emissivity value and the precision of  $T_2$ .

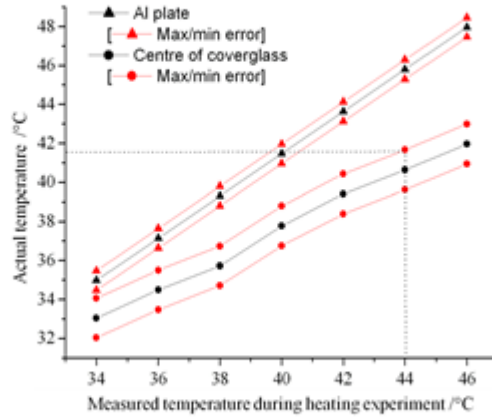


Figure A.2: Comparison of the temperature recorded at the thermocouple and the estimated temperature of the sample.

As the plate is heated, thermal expansion will result in the upward displacement of the sample relative to the objective. To compensate for this the adjustable stage was lowered a further 60 micrometres below the focus of the laser after the liposome had been optically trapped. This means that during the course of the experiment, the liposome is first located at approximately 110  $\mu\text{m}$  above the surface of the cover glass, and is finally located at a height of approximately 30  $\mu\text{m}$  above the surface of the cover glass.

## B Code relating to coalescence of aqueous droplets

The following piece of code recovers the simulated aspect ratio for the imported points.

```
public static void main(String [] args){  
double []x=new double [125501];  
double []y=new double [125501];  
x=GetXPoints ();  
y=GetYPoints ();  
  
for (int i=1;i<500;i++){  
System.out.println(x[(i)*251+1]/y[i*251]);  
}  
}
```

The code below produces images of the coalescence using the JReality software.

```
int rot=200;  
int p = (int) domain.getMinY ();  
double []x=new double [50602];  
double []y=new double [50602];  
x=GetXPoints ();  
y=GetYPoints ();  
IndexedFaceSetFactory psf= new IndexedFaceSetFactory ();  
double [][] vertices = new double [202*(rot+2)][3];  
for (int j=0;j<rot+2;j++){  
for (int i=0;i<201;i++){  
    if (i<101){  
        vertices [i+j*202][0]=10*Math.cos(j*2*Math.PI/(rot))*x[(p*101)-i+101];  
        vertices [i+j*202][1]=10*Math.sin(j*2*Math.PI/(rot))*x[(p*101)-i+101];  
        vertices [i+j*202][2]=10*-y[(p*101)-i+101];  
    } else {  
        vertices [i+j*202][0]=10*Math.cos(j*2*Math.PI/(rot))*x[(p*101)+i-99];  
        vertices [i+j*202][1]=10*Math.sin(j*2*Math.PI/rot)*x[(p*101)+i-99];  
        vertices [i+j*202][2]=10*y[(p*101)+i-99];  
    }  
}  
}  
  
int [][] faceIndices = new int [201*(rot+1)][4];  
  
for (int i=0;i<201*(rot+1);i++){  
    faceIndices [i][0]=i;  
    faceIndices [i][3]=i+1;
```

```
        faceIndices [ i ][ 1 ] = i + 202;
        faceIndices [ i ][ 2 ] = i + 203;

    }
    psf . setVertexCount ( 202 * ( rot + 2 ) );
    psf . setVertexCoordinates ( vertices );
    psf . setFaceCount ( 201 * ( rot + 1 ) );
    psf . setFaceIndices ( faceIndices );
    psf . setGenerateEdgesFromFaces ( true );
    psf . setGenerateFaceNormals ( true );

    psf . update ();
    c . setGeometry ( psf . getGeometry ( ) );
```

## **C An implementation of the $k$ -noid**

The following piece of code creates the holomorphic null curve generating the  $k$ -noid and its conjugate.

```

public Complex[] HvalueAt(double u, double v) {

    int nods=(int) getNumberOfCatenoidalEnds ();
    //the k-noid required 4k domains
        double k=nods*.25;

        int realnod=nods*(nods/4)+1;
        setNumberOfDomains (realnod);
        nos=getAerosolNumberOfSphere ();

    Complex FirstHypGeom=new Complex(),SecondHypGeom=new Complex ();
    Complex i = new Complex(0,1.0);
        Complex a = new Complex(), b = new Complex(), c =new Complex ();
        Complex aref = new Complex(), bref = new Complex(),
            cref =new Complex ();
        Complex z = new Complex(u, v);
        Complex Bound=
            new Complex(Math.cos(Math.PI/k),Math.sin(Math.PI/k));
    //Lines below transform unit circle to punctured unit circle
        if (nos%2==0)

            {
                double p= (1-u*u-v*v)/(v*v+(1+u)*(1+u));
                double q= -2.0*v/(v*v+(1+u)*(1+u));
                z.assign(p,q);
            }

    else

        {
            v=-v;
            double p= (1-u*u-v*v)/(v*v+(1+u)*(1+u));
            double q= -2.0*v/(v*v+(1+u)*(1+u));
            z.assign(p,q);}
        //Numerical methods re-shape the domain to the
        required punctured circle segment
    if (nos%2==0) {
    if (z.arg()>Math.PI/k){
        double length=z.abs();
        z.assign(Bound);
        z.assignTimes(length);
    }}

    else

```

```

{ if (z. arg() < -(Math.PI/k)) {

    double length=z. abs ();
        z. assign (Bound);
        z. assignTimes (length);
        z. im=z. im*( -1.0);
    }}
//Lines below create the holomorphic null curve
Complex a1= new Complex(1,0), a2= new Complex(-1.0/k,0),
    a3= new Complex((k-1.0)/k,0), a4 = new Complex(1.0/k,0),
    a5=new Complex(1.0+(1/k),0);
Complex apart1 = new Complex(), apart2 = new Complex();
Complex bpart1 = new Complex(), bpart2 = new Complex();
i. assign (0,1.0);
Complex zpowk = new Complex();
zpowk. assign (z);
zpowk. assignPow (k);

FirstHypGeom. assign (de. jtem. mfc. specialFunctions .
HyperGeometric2F1. evaluateSeries (a1 ,a4 ,a5 ,zpowk));
SecondHypGeom. assign (de. jtem. mfc. specialFunctions .
HyperGeometric2F1. evaluateSeries (a1 ,a2 ,a3 ,zpowk));

Complex kz=new Complex ();
kz. assign (k);
kz. assignTimes (z);

Complex kzpowerk=new Complex ();
kzpowerk. assign (k);
kzpowerk. assignTimes (z. pow (k));

Complex zsquared=new Complex ();
zsquared. assign (z);
zsquared. assignTimes (z);

Complex zpowerkminus1 = new Complex ();
zpowerkminus1. assign (zpowk);
zpowerkminus1. assignMinus (1);

Complex zpowerkminus1timeskminus1 = new Complex ();
zpowerkminus1timeskminus1. assign (zpowerkminus1);
zpowerkminus1timeskminus1. assignTimes (k-1);

```

```
Complex zpowerkminus1timeskminus1zquared = new Complex();
zpowerkminus1timeskminus1zquared . assign (zpowerkminus1timeskminus1);
zpowerkminus1timeskminus1zquared . assignTimes (z . pow (2));
```

```
Complex oneminuskpowz = new Complex();
oneminuskpowz . assign (1);
oneminuskpowz . assignMinus (zpowk);
```

```
Complex FirstFrac = new Complex();
FirstFrac . assign (-.5);
FirstFrac . assignDivide (kz);
```

```
FirstFrac . assignDivide (zpowerkminus1);
```

```
Complex SecondFrac = new Complex();
SecondFrac . assign (i);
SecondFrac . assignDivide (kz);
```

```
SecondFrac . assignDivide (zpowerkminus1);
SecondFrac . assignTimes (.5);
```

```
Complex ThirdFrac = new Complex();
ThirdFrac . assign (1);
ThirdFrac . assignDivide (oneminuskpowz);
ThirdFrac . assignDivide (k);
```

```
apart1 . assign (SecondHypGeom);
apart1 . assignTimes (zpowerkminus1);
apart1 . assignTimes (k-1);
apart2 . assign (FirstHypGeom);
apart2 . assignTimes (zpowerkminus1);
apart2 . assignTimes (k-1);
apart2 . assignTimes (z);
apart2 . assignTimes (z);
apart1 . assignMinus (apart2);
apart1 . assignMinus (kzpowerk);
apart1 . assignPlus (zsquared);
apart1 . assignMinus (1.0);
apart1 . assignPlus (k);
```

```

apart1 . assignTimes ( FirstFrac );
a . assign ( apart1 );

bpart1 . assign ( SecondHypGeom );
bpart1 . assignTimes ( zpowerkminus1 );
bpart1 . assignTimes ( k-1 );
bpart2 . assign ( FirstHypGeom );
bpart2 . assignTimes ( zpowerkminus1 );
bpart2 . assignTimes ( k-1 );
bpart2 . assignTimes ( z );
bpart2 . assignTimes ( z );
bpart1 . assignPlus ( bpart2 );
bpart1 . assignMinus ( kzpowerk );
bpart1 . assignMinus ( zsquared );
bpart1 . assignMinus ( 1.0 );
bpart1 . assignPlus ( k );
bpart1 . assignTimes ( SecondFrac );
b . assign ( bpart1 );

c . assign ( ThirdFrac );

aref . assign ( a );
bref . assign ( b );
cref . assign ( c );

// Holomorphic null curve is evaluated , now rotations
// and reflections are used to give value on other domains
// Lines below translate k noid plane of symmetry to x-y plane
Complex HeightPoint = new Complex ( Math . cos ( Math . PI / k ) ,
Math . sin ( Math . PI / k ) );
Complex [] HeightPointValues = KNoidValues ( k , HeightPoint );
double height = HeightPointValues [ 2 ] . re ;
c . re = c . re - height ;

// Lines below do required reflections and rotations to create top half
// of k-noid and interior of the conjugate

Complex [] mainsurface1 = new Complex [ 3 ];
Complex [] mainsurface2 = new Complex [ 3 ];
Complex [] mainsurface3 = new Complex [ 3 ];
Complex [] mainsurface4 = new Complex [ 3 ];
Complex [] mainsurface5 = new Complex [ 3 ];

```

```

Complex[] Conjugatesurface2=new Complex[3];

double points[]=new double[3];
if(nos%2==1){
if(nos>2){
mainsurface3=surfaxrot(1,k,.9*.9*.9);
mainsurface4=surfaxrot(1,k,.9*.9*.9*.9);
mainsurface5=surfaxrot(1,k,.9*.9*.9*.9*.9);

points=ref(a.re,b.re,c.re,mainsurface3[0].re,
mainsurface3[1].re,mainsurface3[2].re
,mainsurface5[0].re,
mainsurface5[1].re,mainsurface5[2].re,
mainsurface4[0].re,
mainsurface4[1].re,mainsurface4[2].re);

a.re=points[0];
b.re=points[1];
c.re=points[2];
if(nos>4){
points=rot1801(a.re,b.re,c.re,0.0,0.0,0.0,0.0,0.0,-1.0,(double)
((nos-3)*Math.PI/(k)));
a.re=points[0];
b.re=points[1];
c.re=points[2];
}
mainsurface1=surfaxrot((nos-1)/2,k,.9);
mainsurface2=surfaxrot((nos-1)/2,k,.9*.9);
mainsurface3=surfaxrot((nos-1)/2,k,.9*.9*.9);
mainsurface4=surfaxrot((nos-1)/2,k,.9*.9*.9*.9);
mainsurface5=surfaxrot((nos-1)/2,k,.9*.9*.9*.9*.9);
double [] newim=rot1801(a.im,b.im,c.im,
mainsurface2[0].im,
mainsurface2[1].im,
mainsurface2[2].im,
mainsurface2[0].im-mainsurface3[0].im,
mainsurface2[1].im-mainsurface3[1].im,
mainsurface2[2].im-mainsurface3[2].im,
Math.PI);

a.im=newim[0];

```

```

        b.im=newim[1];
        c.im=newim[2];
    }
}
else {

if (nos > 2){

    mainsurface3=surfaxrot(1,k,.9*.9*.9);
    mainsurface4=surfaxrot(1,k,.9*.9*.9*.9);
    mainsurface5=surfaxrot(1,k,.9*.9*.9*.9*.9);

    points=ref(a.re,b.re,c.re,mainsurface3[0].re,
    mainsurface3[1].re,
    mainsurface3[2].re,
    mainsurface5[0].re,
    mainsurface5[1].re,
    mainsurface5[2].re,
    mainsurface4[0].re,
    mainsurface4[1].re,
    mainsurface4[2].re);
    a.re=points[0];
    b.re=points[1];
    c.re=points[2];

if (nos > 4){
    points=rot1801(a.re,b.re,c.re,0.0,0.0,0.0,
    0.0,0.0,-1.0,(double)((nos-4)*Math.PI/(k)));

a.re=points[0];
b.re=points[1];
c.re=points[2];
}
mainsurface1=surfaxrot((nos-2)/2,k,.9);
mainsurface2=surfaxrot((nos-2)/2,k,.9*.9);
mainsurface3=surfaxrot((nos-2)/2,k,.9*.9*.9);
mainsurface4=surfaxrot((nos-2)/2,k,.9*.9*.9*.9);
mainsurface5=surfaxrot((nos-2)/2,k,.9*.9*.9*.9*.9);
double [] newim=rot1801(a.im,b.im,c.im,mainsurface2[0].im,
mainsurface2[1].im,
mainsurface2[2].im,

```

```

mainsurface2 [0].im-mainsurface3 [0].im,
mainsurface2 [1].im-mainsurface3 [1].im,
mainsurface2 [2].im-mainsurface3 [2].im,
Math.PI);
a.im=newim [0];
b.im=newim [1];
c.im=newim [2];
}}
//Lines below create bottom half of k noid and corresponding part of the

if (      nos%nods>(nods/2-1)      )
{      c.re=c.re*-1.0;
if (nos%2==1){
int axis=nos-nods/2;
Conjugatesurface2=conjurfaxrot (axis,k,0);
double [] newim2=rot1801(a.im ,b.im, c.im,
Conjugatesurface2 [0].im,
Conjugatesurface2 [1].im,
Conjugatesurface2 [2].im,
0.0,0.0,1.0,Math.PI);

a.im=newim2 [0];
b.im=newim2 [1];
c.im=newim2 [2];
}

else {
Conjugatesurface2=conjurfaxrot (nos-3,k,0);
double [] newim2=rot1801(a.im , b.im, c.im,Conjugatesurface2 [0].im,
Conjugatesurface2 [1].im,
Conjugatesurface2 [2].im,
0.0,0.0,1.0,Math.PI);

a.im=newim2 [0];
b.im=newim2 [1];
c.im=newim2 [2];}}
//Return the 3 complex numbers giving k-noid and its conjugate
return new Complex[] { a, b,c };
}

```

## References

- [1] R. Power, J. P. Reid, S. Anand, D. McGloin, A. Almohamedi, N. S. Mistry, and A. J. Hudson, "Observation of the binary coalescence and equilibration of micrometer-sized droplets of aqueous aerosol in a single-beam gradient-force optical trap," *Journal of Physical Chemistry A*, vol. 116, no. 35, pp. 8873–8884, 2012.
- [2] L. Rayleigh, "On the capillary phenomena of jets," *Proc. R. Soc. London*, vol. 29, pp. 71–97, 1879.
- [3] A. Ashkin, J. M. Dziedzic, J. E. Bjorkholm, and S. Chu, "Observation of a single-beam gradient force optical trap for dielectric particles," *Optics Letters*, vol. 11, no. 5, pp. 288–290, 1986.
- [4] A. Menchaca-Rocha, A. Martinez-Davalos, R. Nunez, S. Popinet, and S. Zaleski, "Coalescence of liquid drops by surface tension," *Physical Review E*, vol. 63, no. 4, p. 046309, 2001.
- [5] J. Eggers, J. R. Lister, and H. A. Stone, "Coalescence of liquid drops," *Journal of Fluid Mechanics*, vol. 401, pp. 293–310, 1999.
- [6] J. E. Sprittles and Y. D. Shikhmurzaev, "Dynamics of liquid drops coalescing in the inertial regime," *Physical Review E*, vol. 89, no. 6, p. 063008, 2014.
- [7] G. R. Anyarambhatla and D. Needham, "Enhancement of the phase transition permeability of DPPC liposomes by incorporation of MPPC: A new temperature-sensitive liposome for use with mild hyperthermia," *Journal of Liposome Research*, vol. 9, no. 4, pp. 491–506, 1999.
- [8] K. A. Riske, M. J. Politi, W. F. Reed, and M. T. LamyFreund, "Temperature and ionic strength dependent light scattering of DMPG dispersions," *Chemistry and Physics of Lipids*, vol. 89, no. 1, pp. 31–44, 1997.
- [9] H. Matsuki, E. Miyazaki, F. Sakano, N. Tamai, and S. Kaneshina, "Thermotropic and barotropic phase transitions in bilayer membranes of ether-linked phospholipids with varying alkyl chain lengths," *Biochimica et Biophysica Acta (BBA) - Biomembranes*, vol. 1768, no. 3, pp. 479 – 489, 2007.
- [10] K. Larsson and R. P. Rand, "Detection of changes in the environment of hydrocarbon chains by raman spectroscopy and its application to lipid-protein systems," *Biochimica et Biophysica Acta (BBA) - Lipids and Lipid Metabolism*, vol. 326, no. 2, pp. 245 – 255, 1973.
- [11] J. Lagrange, "Essai d'une nouvelle methode pour determiner les maxima et les minima des formules integrales indefinies," *Miscellanea Taurinensia*, vol. 2, pp. 173 –195, 1762.

- [12] K. Weierstrass, “Ueber die Flaechen, deren mittlere Kruemmung ueberall gleich null ist,” *Monatsber. Berliner Akad.*, pp. 612–625, 1866.
- [13] A. Enneper, “Analytisch-geometrische Untersuchungen,” *Z. Math. Phys.* 9, vol. 9, p. 96125, 1864.
- [14] F. J. Lopez and A. Ros, “On embedded complete minimal-surfaces of genus zero,” *Journal of Differential Geometry*, vol. 33, no. 1, pp. 293–300, 1991.
- [15] K. Leschke and K. Moriya, “Simple factor dressing and the Lopez-Ros deformation of minimal surfaces in Euclidean 3-space,” *preprint. arXiv*, 2014.
- [16] A. Ashkin, “Acceleration and trapping of particles by radiation pressure,” *Physical Review Letters*, vol. 24, no. 4, pp. 156–159, 1970.
- [17] A. Ashkin and J. M. Dziedzic, “Optical levitation by radiation pressure,” *Applied Physics Letters*, vol. 19, no. 8, pp. 283–285, 1971.
- [18] A. M. Kaufman, B. J. Lester, and C. A. Regal, “Cooling a single atom in an optical tweezer to its quantum ground state,” *Physical Review X*, vol. 2, no. 4, p. 041014, 2012.
- [19] C. Muldoon, L. Brandt, J. Dong, D. Stuart, E. Brainis, M. Himsworth, and A. Kuhn, “Control and manipulation of cold atoms in optical tweezers,” *New Journal of Physics*, vol. 14, p. 073051, 2012.
- [20] A. Ashkin, “Forces of a single-beam gradient laser trap on a dielectric sphere in the ray optics regime,” *Biophysical Journal*, vol. 61, no. 2, pp. 569–582, 1992.
- [21] J. A. Lock, “Calculation of the radiation trapping force for laser tweezers by use of generalized Lorenz-Mie theory. I. Localized model description of an on-axis tightly focused laser beam with spherical aberration,” *Applied Optics*, vol. 43, no. 12, pp. 2532–2544, 2004.
- [22] W. H. Wright, G. J. Sonek, and M. W. Berns, “Parametric study of the forces on microspheres held by optical tweezers,” *Applied Optics*, vol. 33, no. 9, pp. 1735–1748, 1994.
- [23] A. Ashkin, J. M. Dziedzic, and T. Yamane, “Optical trapping and manipulation of single cells using infrared-laser beams,” *Nature*, vol. 330, no. 6150, pp. 769–771, 1987.
- [24] A. Ashkin and J. M. Dziedzic, “Optical trapping and manipulation of viruses and bacteria,” *Science*, vol. 235, no. 4795, pp. 1517–1520, 1987.
- [25] M. J. Lang and S. M. Block, “Resource letter: LBOT-1: Laser-based optical tweezers,” *American Journal of Physics*, vol. 71, no. 3, pp. 201–215, 2003.

- [26] J. R. Mourant, T. Fuselier, J. Boyer, T. M. Johnson, and I. J. Bigio, "Predictions and measurements of scattering and absorption over broad wavelength ranges in tissue phantoms," *Applied Optics*, vol. 36, no. 4, pp. 949–957, 1997.
- [27] H. J. Butler, L. Ashton, B. Bird, G. Cinque, K. Curtis, J. Dorney, K. Esmonde-White, N. J. Fullwood, B. Gardner, P. L. Martin-Hirsch, M. J. Walsh, M. R. McAinsh, N. Stone, and F. L. Martin, "Using Raman spectroscopy to characterize biological materials," *Nature Protocols*, vol. 11, no. 4, pp. 664–687, 2016.
- [28] L. Rayleigh, "On the light from the sky, its polarization and colour," *Philosophical Magazine*, vol. 41, p. 107120, 1871.
- [29] P. Laven, "Mie scattering software - mieplot," 2017.
- [30] P. Laven, "Simulation of rainbows, coronas, and glories by use of Mie theory," *Applied Optics*, vol. 42, no. 3, pp. 436–444, 2003.
- [31] W. J. Glantschnig and S. H. Chen, "Light-scattering from water droplets in the geometrical-optics approximation," *Applied Optics*, vol. 20, no. 14, pp. 2499–2509, 1981.
- [32] C. V. Raman, "A new radiation," *Indian J. Phys*, vol. 2, p. 387398, 1928.
- [33] M. Diem, M. Romeo, S. Boydston-White, M. Miljkovic, and C. Matthaus, "A decade of vibrational micro-spectroscopy of human cells and tissue (1994-2004)," *Analyst*, vol. 129, no. 10, pp. 880–885, 2004.
- [34] M. Lankers, J. Popp, and W. Kiefer, "Raman and fluorescence-spectra of single optically trapped microdroplets in emulsions," *Applied Spectroscopy*, vol. 48, no. 9, pp. 1166–1168, 1994.
- [35] C. G. Xie, M. A. Dinno, and Y. Q. Li, "Near-infrared Raman spectroscopy of single optically trapped biological cells," *Optics Letters*, vol. 27, no. 4, pp. 249–251, 2002.
- [36] C. M. Creely, G. P. Singh, and D. Petrov, "Dual wavelength optical tweezers for confocal Raman spectroscopy," *Optics Communications*, vol. 245, no. 1-6, pp. 465–470, 2005.
- [37] A. D. Bangham and R. W. Horne, "Negative staining of phospholipids and their structural modification by surface-active agents as observed in the electron microscope," *Journal of Molecular Biology*, vol. 8, no. 5, pp. 660 – 668, 1964.
- [38] J. Y. Shao, G. Xu, and P. Guo, "Quantifying cell-adhesion strength with micropipette manipulation: Principle and application," *Frontiers in Bioscience*, vol. 9, no. S, pp. 2183–2191, 2004.
- [39] A. R. Wheeler, W. R. Throdset, R. J. Whelan, A. M. Leach, R. N. Zare, Y. H. Liao, K. Farrell, I. D. Manger, and A. Daridon, "Microfluidic device for single-cell analysis," *Analytical Chemistry*, vol. 75, no. 14, pp. 3581–3586, 2003.

- [40] J. D. Adams, U. Kim, and H. T. Soh, "Multitarget magnetic activated cell sorter," *Proceedings of the National Academy of Sciences of the United States of America*, vol. 105, no. 47, pp. 18165–18170, 2008.
- [41] A. S. Cans, N. Wittenberg, R. Karlsson, L. Sombers, M. Karlsson, O. Orwar, and A. Ewing, "Artificial cells: Unique insights into exocytosis using liposomes and lipid nanotubes," *Proceedings of the National Academy of Sciences of the United States of America*, vol. 100, no. 2, pp. 400–404, 2003.
- [42] D. Tareste, J. Shen, T. J. Melia, and J. E. Rothman, "SNAREpin/Munc18 promotes adhesion and fusion of large vesicles to giant membranes," *Proceedings of the National Academy of Sciences of the United States of America*, vol. 105, no. 7, pp. 2380–2385, 2008.
- [43] G. Bendas, J. Vogel, U. Bakowski, A. Krause, J. Muller, and U. Rothe, "A liposome-based model system for the simulation of lectin-induced cell adhesion," *Biochimica Et Biophysica Acta-biomembranes*, vol. 1325, no. 2, pp. 297–308, 1997.
- [44] E. Mayhew, D. Papahadjopoulos, Y. M. Rustum, and C. Dave, "Inhibition of tumor cell growth in vitro and in vivo by 1--d-arabinofuranosylcytosine entrapped within phospholipid vesicles," *Cancer Research*, vol. 36, no. 12, pp. 4406–4411, 1976.
- [45] M. D. Moen, K. A. Lyseng-Williamson, and L. J. Scott, "Liposomal amphotericin b: A review of its use as empirical therapy in febrile neutropenia and in the treatment of invasive fungal infections," *Drugs*, vol. 69, no. 3, pp. 361–392, 2009.
- [46] R. Fraley, S. Subramani, P. Berg, and D. Papahadjopoulos, "Introduction of liposome-encapsulated SV40 DNA into cells," *Journal of Biological Chemistry*, vol. 255, no. 21, pp. 431–435, 1980.
- [47] G. J. Charrois and T. M. Allen, "Drug release rate influences the pharmacokinetics, biodistribution, therapeutic activity, and toxicity of pegylated liposomal doxorubicin formulations in murine breast cancer," *Biochimica et Biophysica Acta (BBA) - Biomembranes*, vol. 1663, no. 12, pp. 167 – 177, 2004.
- [48] S. L. Huang and R. C. MacDonald, "Acoustically active liposomes for drug encapsulation and ultrasound-triggered release," *Biochimica et Biophysica Acta-biomembranes*, vol. 1665, no. 1-2, pp. 134–141, 2004.
- [49] A. Yavlovich, A. Singh, R. Blumenthal, and A. Puri, "A novel class of photo-triggerable liposomes containing DPPC:DC<sub>8,9</sub>PC as vehicles for delivery of doxorubicin to cells," *Biochimica Et Biophysica Acta-biomembranes*, vol. 1808, no. 1, pp. 117–126, 2011.
- [50] M. B. Yatvin, W. Kreutz, B. A. Horwitz, and M. Shinitzky, "Ph-sensitive liposomes - possible clinical implications," *Science*, vol. 210, no. 4475, pp. 1253–1254, 1980.

- [51] B. Kneidl, M. Peller, G. Winter, L. H. Lindner, and M. Hossann, "Thermosensitive liposomal drug delivery systems: state of the art review," *International Journal of Nanomedicine*, vol. 9, pp. 4387–4398, 2014.
- [52] F. Szoka, K. E. Magnusson, J. Wojcieszyn, Y. Hou, Z. Derzko, and K. Jacobson, "Use of lectins and polyethylene-glycol for fusion of glycolipid-containing liposomes with eukaryotic cells," *Proceedings of the National Academy of Sciences of the United States of America-Biological Sciences*, vol. 78, no. 3, pp. 1685–1689, 1981.
- [53] S. J. Singer and G. L. Nicolson, "The fluid mosaic model of the structure of cell membranes," *Science*, vol. 175, no. 4023, pp. 720–731, 1972.
- [54] M. Ichikawa and K. Yoshikawa, "Optical transport of a single cell-sized liposome," *Applied Physics Letters*, vol. 79, no. 27, pp. 4598–4600, 2001.
- [55] P. M. Bendix and L. B. Oddershede, "Expanding the optical trapping range of lipid vesicles to the nanoscale," *Nano Letters*, vol. 11, no. 12, pp. 5431–5437, 2011.
- [56] D. Watson, N. Hagen, J. Diver, P. Marchand, and M. Chachisvilis, "Elastic light scattering from single cells: Orientational dynamics in optical trap," *Biophysical Journal*, vol. 87, no. 2, pp. 1298 – 1306, 2004.
- [57] M. Kinnunen, A. V. Bykov, J. Tuorila, T. Haapalainen, A. V. Karmenyan, and V. V. Tuchin, "Optical clearing at cellular level," *Journal of Biomedical Optics*, vol. 19, no. 7, p. 71409, 2014.
- [58] I. Notingher, "Raman spectroscopy cell-based biosensors," *Sensors*, vol. 7, no. 8, pp. 1343–1358, 2007.
- [59] I. Notingher, S. Verrier, S. Haque, J. M. Polak, and L. L. Hench, "Spectroscopic study of human lung epithelial cells (A549) in culture: Living cells versus dead cells," *Biopolymers*, vol. 72, no. 4, pp. 230–240, 2003.
- [60] K. Czamara, K. Majzner, M. Z. Pacia, K. Kochan, A. Kaczor, and M. Baranska, "Raman spectroscopy of lipids: a review," *Journal of Raman Spectroscopy*, vol. 46, no. 1, pp. 4–20, 2015.
- [61] D. P. Cherney, J. C. Conboy, and J. M. Harris, "Optical-trapping Raman microscopy detection of single unilamellar lipid vesicles," *Analytical Chemistry*, vol. 75, no. 23, pp. 6621–6628, 2003.
- [62] K. Kong, C. J. Rowlands, S. Varma, W. Perkins, I. H. Leach, A. A. Koloydenko, H. C. Williams, and I. Notingher, "Diagnosis of tumors during tissue-conserving surgery with integrated autofluorescence and Raman scattering microscopy," *Proceedings of the National Academy of Sciences of the United States of America*, vol. 110, no. 38, pp. 15189–15194, 2013.

- [63] B. Croft, U. Lohmann, R. V. Martin, P. Stier, S. Wurzler, J. Feichter, R. Posselt, and S. Ferrachat, “Aerosol size-dependent below-cloud scavenging by rain and snow in the ECHAM5-HAM,” *Atmospheric Chemistry and Physics*, vol. 9, no. 14, pp. 4653–4675, 2009.
- [64] G. D. Martin, S. D. Hoath, and I. M. Hutchings, “Inkjet printing - the physics of manipulating liquid jets and drops,” in *Engineering and Physics - Synergy for Success*, vol. 105 of *Journal of Physics Conference Series*, 2008.
- [65] R. Vehring, W. R. Foss, and D. Lechuga-Ballesteros, “Particle formation in spray drying,” *Journal of Aerosol Science*, vol. 38, no. 7, pp. 728–746, 2007.
- [66] U. K. Krieger, C. Marcolli, and J. P. Reid, “Exploring the complexity of aerosol particle properties and processes using single particle techniques,” *Chemical Society Reviews*, vol. 41, no. 19, pp. 6631–6662, 2012.
- [67] X. Niu, F. Gielen, A. J. deMello, and J. B. Edel, “Electro-coalescence of digitally controlled droplets,” *Analytical Chemistry*, vol. 81, no. 17, pp. 7321–7325, 2009.
- [68] C. L. Aardahl, W. R. Foss, and E. J. Davis, “The effects of optical resonances on Raman analysis of liquid aerosols,” *Journal of Aerosol Science*, vol. 27, no. 7, pp. 1015–1033, 1996.
- [69] C. L. Aardahl, J. F. Widmann, and E. J. Davis, “Raman analysis of chemical reactions resulting from the collision of micrometer-sized particles,” *Applied Spectroscopy*, vol. 52, no. 1, pp. 47–53, 1998.
- [70] R. M. Power and J. P. Reid, “Probing the micro-rheological properties of aerosol particles using optical tweezers,” *Reports on Progress in Physics*, vol. 77, no. 7, p. 074601, 2014.
- [71] H. Lamb, *Hydrodynamics*. Cambridge University, Cambridge, 1932.
- [72] R. J. Hopkins, L. Mitchem, A. D. Ward, and J. P. Reid, “Control and characterisation of a single aerosol droplet in a single-beam gradient-force optical trap,” *Physical Chemistry Chemical Physics*, vol. 6, no. 21, pp. 4924–4927, 2004.
- [73] L. Mitchem and J. P. Reid, “Optical manipulation and characterisation of aerosol particles using a single-beam gradient force optical trap,” *Chemical Society Reviews*, vol. 37, no. 4, pp. 756–769, 2008.
- [74] J. E. Sprittles and Y. D. Shikhmurzaev, “Coalescence of liquid drops: Different models versus experiment,” *Physics of Fluids*, vol. 24, no. 12, p. 122105, 2012.
- [75] J. Qian and C. K. Law, “Regimes of coalescence and separation in droplet collision,” *Journal of Fluid Mechanics*, vol. 331, pp. 59–80, 1997.

- [76] J. D. Paulsen, J. C. Burton, S. R. Nagel, S. Appathurai, M. T. Harris, and O. A. Basaran, “The inexorable resistance of inertia determines the initial regime of drop coalescence,” *Proceedings of the National Academy of Sciences of the United States of America*, vol. 109, no. 18, pp. 6857–6861, 2012.
- [77] J. E. Sprittles and Y. D. Shikhmurzaev, “The coalescence of liquid drops in a viscous fluid: interface formation model,” *Journal of Fluid Mechanics*, vol. 751, pp. 480–499, 2014.
- [78] J. Eggers, “Nonlinear dynamics and breakup of free-surface flows,” *Reviews of Modern Physics*, vol. 69, no. 3, pp. 865–929, 1997.
- [79] R. W. Hopper, “Plane stokes-flow driven by capillarity on a free-surface,” *Journal of Fluid Mechanics*, vol. 213, pp. 349–375, 1990.
- [80] L. Duchemin, J. Eggers, and C. Josserand, “Inviscid coalescence of drops,” *Journal of Fluid Mechanics*, vol. 487, pp. 167–178, 2003.
- [81] M. M. Wu, T. Cubaud, and C. M. Ho, “Scaling law in liquid drop coalescence driven by surface tension,” *Physics of Fluids*, vol. 16, no. 7, pp. 51–54, 2004.
- [82] J. E. Sprittles and Y. D. Shikhmurzaev, “Finite element framework for describing dynamic wetting phenomena,” *International Journal for Numerical Methods in Fluids*, vol. 68, no. 10, pp. 1257–1298, 2012.
- [83] J. E. Sprittles and Y. D. Shikhmurzaev, “A parametric study of the coalescence of liquid drops in a viscous gas,” *Journal of Fluid Mechanics*, vol. 753, pp. 279–306, 2014.
- [84] R. Enright, N. Miljkovic, J. Sprittles, K. Nolan, R. Mitchell, and E. N. Wang, “How coalescing droplets jump,” *ACS Nano*, vol. 8, no. 10, pp. 10352–10362, 2014.
- [85] J. Jost, *Compact Riemann Surfaces*. Springer, 2002.
- [86] A. Pressley, *Elementary Differential Geometry*. Springer, 2010.
- [87] J. M. Lee, *Introduction to Topological Manifolds*. Springer, 2011.
- [88] A. Newlander and L. Nirenberg, “Complex analytic coordinates in almost complex manifolds,” *Annals of Mathematics*, vol. 65, no. 3, pp. 391–404, 1957.
- [89] S. Kobayashi and K. Nomizu, *Foundations of Differential Geometry I + II*. Wiley, 1963.
- [90] U. Dierkes, *Minimal Surfaces*. Springer, 2010.
- [91] K. Leschke, “Surface lab,” 2014.
- [92] T. U. Berlin, “JReality, <http://www3.math.tu-berlin.de/jreality/jrealityStatic/index.php>.” last accessed 11/03/2018.

- [93] T. U. Berlin, “Java tools for experimental mathematicians, <http://www3.math.tu-berlin.de/jtem/>.” last accessed 11/03/2018.
- [94] J. Kuipers, *Quaternions and Rotation Sequences*. Princeton University Press, 1999.
- [95] F. Burstall, D. Ferus, K. Leschke, F. Pedit, and U. Pinkall, *Conformal Geometry of Surfaces in  $S^4$  and Quaternions*. Lecture Notes in Mathematics, Springer, 2002.
- [96] R. L. Bryant, “A duality theorem for Willmore surfaces,” *J. Differential Geom.*, vol. 20, no. 1, pp. 23–53, 1984.
- [97] M. J. Padgett and R. Bowman, “Optical tweezers software.” <http://www.gla.ac.uk/schools/physics/research/groups/optics/research/>., 2014.
- [98] E. R. Dufresne and D. G. Grier, “Optical tweezer arrays and optical substrates created with diffractive optics,” *Review of Scientific Instruments*, vol. 69, no. 5, pp. 1974–1977, 1998.
- [99] E. R. Dufresne, G. C. Spalding, M. T. Dearing, S. A. Sheets, and D. G. Grier, “Computer-generated holographic optical tweezer arrays,” *Review of Scientific Instruments*, vol. 72, no. 3, pp. 1810–1816, 2001.
- [100] L. Rayleigh, “Xxxi. investigations in optics, with special reference to the spectroscope,” *Philosophical Magazine Series 5*, vol. 8, no. 49, pp. 261–274, 1879.
- [101] V. Weissig, *Liposomes: Methods and Protocols*. No. 2 in Methods in Molecular Biology - Humana Press, Humana Press, 2010.
- [102] A. de Juan and R. Tauler, “Multivariate curve resolution (MCR) from 2000: Progress in concepts and applications,” *Critical Reviews in Analytical Chemistry*, vol. 36, no. 3-4, pp. 163–176, 2006.
- [103] J. Jaumot, A. de Juan, and R. Tauler, “Mcr-als {GUI} 2.0: New features and applications,” *Chemometrics and Intelligent Laboratory Systems*, vol. 140, pp. 1 – 12, 2015.
- [104] J. H. Crowe, F. A. Hoekstra, L. M. Crowe, T. J. Anchordoguy, and E. Drobnis, “Lipid phase-transitions measured in intact-cells with fourier-transform infrared-spectroscopy,” *Cryobiology*, vol. 26, no. 1, pp. 76–84, 1989.
- [105] L. Collard, D. Perez-Guaita, B. H. A. Faraj, B. Wood, R. Wallis, P. W. Andrew, and A. J. Hudson, “Light scattering by optically-trapped vesicles affords unprecedented temporal resolution of lipid-raft dynamics,” *Scientific Reports*, vol. 7, p. 8589, 2017.
- [106] J. R. Silvius, “Thermotropic phase transitions of pure lipids in model membranes and their modifications by membrane proteins,” *Lipid-Protein Interactions*, vol. 2, pp. 239–281, 1982.

- [107] T. C. Lubensky and F. C. Mackintosh, "Theory of ripple phases of lipid bilayers," *Physical review letters*, vol. 71, no. 10, pp. 1565–1568, 1993.
- [108] K. Akabori and J. F. Nagle, "Structure of the DMPC lipid bilayer ripple phase," *Soft Matter*, vol. 11, no. 5, pp. 918–926, 2015.
- [109] A. E. Blaurock and T. McIntosh, "Structure of the crystalline bilayer in the subgel phase of dipalmitoylphosphatidylglycerol," *Biochemistry*, vol. 25, no. 2, pp. 299–305, 1986.
- [110] G. Kong and M. W. Dewhirst, "Hyperthermia and liposomes," *International Journal of Hyperthermia*, vol. 15, no. 5, pp. 345–370, 1999.
- [111] N. Michel, A. Fabiano, A. Polidori, R. Jack, and B. Pucci, "Determination of phase transition temperatures of lipids by light scattering," *Chemistry and Physics of Lipids*, vol. 139, no. 1, pp. 11–19, 2006.
- [112] J. J. Schaefer, C. Ma, and J. M. Harris, "Confocal Raman microscopy probing of temperature-controlled release from individual, optically-trapped phospholipid vesicles," *Analytical Chemistry*, vol. 84, no. 21, pp. 9505–9512, 2012.
- [113] C. B. Fox and J. M. Harris, "Confocal Raman microscopy for simultaneous monitoring of partitioning and disordering of tricyclic antidepressants in phospholipid vesicle membranes," *Journal of Raman Spectroscopy*, vol. 41, no. 5, pp. 498–507, 2010.
- [114] K. K. Halling and J. P. Slotte, "Membrane properties of plant sterols in phospholipid bilayers as determined by differential scanning calorimetry, resonance energy transfer and detergent-induced solubilization," *Biochimica et Biophysica Acta-Biomembranes*, vol. 1664, no. 2, pp. 161–171, 2004.
- [115] R. F. M. de Almeida, A. Fedorov, and M. Prieto, "Sphingomyelin/phosphatidylcholine/c-cholesterol phase diagram: Boundaries and composition of lipid rafts," *Biophysical Journal*, vol. 85, no. 4, pp. 2406–2416, 2003.
- [116] K. Simons and E. Ikonen, "Functional rafts in cell membranes," *Nature*, vol. 387, no. 6633, pp. 569–572, 1997.
- [117] J. F. Hancock, "Lipid rafts: Contentious only from simplistic standpoints," *Nature Reviews Molecular Cell Biology*, vol. 7, no. 6, pp. 456–462, 2006.
- [118] S. Tristramnagle, R. Zhang, R. M. Suter, C. R. Worthington, W. J. Sun, and J. F. Nagle, "Measurement of chain tilt angle in fully hydrated bilayers of gel phase lecithins," *Biophysical Journal*, vol. 64, no. 4, pp. 1097–1109, 1993.
- [119] J. F. Nagle and D. A. Wilkinson, "Lecithin bilayers - density-measurements and molecular-interactions," *Biophysical Journal*, vol. 23, no. 2, pp. 159–175, 1978.

- [120] K. A. Riske, R. P. Barroso, C. C. Vequi-Suplicy, R. Germano, V. B. Henriques, and M. T. Lamy, "Lipid bilayer pre-transition as the beginning of the melting process," *Biochimica et Biophysica Acta-Biomembranes*, vol. 1788, no. 5, pp. 954–963, 2009.
- [121] D. P. Cherney, T. E. Bridges, and J. M. Harris, "Optical trapping of unilamellar phospholipid vesicles: Investigation of the effect of optical forces on the lipid membrane shape by confocal-raman microscopy," *Analytical Chemistry*, vol. 76, no. 17, pp. 4920–4928, 2004.
- [122] Y. Takechi-Haraya, K. Sakai-Kato, Y. Abe, T. Kawanishi, H. Okuda, and Y. Goda, "Atomic force microscopic analysis of the effect of lipid composition on liposome membrane rigidity," *Langmuir*, vol. 32, no. 24, pp. 6074–6082, 2016.
- [123] R. A. Macphail, H. I. Strauss, R. G. Snyder, and C. A. Elliger, "C-H stretching modes and the structure of normal-alkyl chains. 2. Long, all-trans chains," *Journal of Physical Chemistry*, vol. 88, no. 3, pp. 334–341, 1984.
- [124] C. S. Lee and C. D. Bain, "Raman spectra of planar supported lipid bilayers," *Biochimica et Biophysica Acta-Biomembranes*, vol. 1711, no. 1, pp. 59–71, 2005.
- [125] C. B. Fox, R. H. Uibel, and J. M. Harris, "Detecting phase transitions in phosphatidylcholine vesicles by Raman microscopy and self-modeling curve resolution," *Journal of Physical Chemistry B*, vol. 111, no. 39, pp. 11428–11436, 2007.
- [126] P. T. T. Wong, "Raman-spectroscopy of thermotropic and high-pressure phases of aqueous phospholipid dispersions," *Annual Review of Biophysics and Bioengineering*, vol. 13, pp. 1–24, 1984.
- [127] N. Kucerka, S. Tristram-Nagle, and J. F. Nagle, "Structure of fully hydrated fluid phase lipid bilayers with monounsaturated chains," *Journal of Membrane Biology*, vol. 208, no. 3, pp. 193–202, 2005.
- [128] O. Edholm and J. F. Nagle, "Areas of molecules in membranes consisting of mixtures," *Biophysical Journal*, vol. 89, no. 3, pp. 1827–1832, 2005.
- [129] N. V. Surovtsev and S. A. Dzuba, "Flexibility of phospholipids with saturated and unsaturated chains studied by Raman scattering: The effect of cholesterol on dynamical and phase transitions," *Journal of Chemical Physics*, vol. 140, no. 23, 2014.
- [130] G. de Wit, J. S. H. Danial, P. Kukura, and M. I. Wallace, "Dynamic label-free imaging of lipid nanodomains," *Proceedings of the National Academy of Sciences of the United States of America*, vol. 112, no. 40, pp. 12299–12303, 2015.
- [131] P. Meleard, C. Gerbeaud, T. Pott, L. Fernandez-Puente, I. Bivas, M. D. Mitov, J. Dufourcq, and P. Bothorel, "Bending elasticities of model membranes: Influences of temperature and sterol content," *Biophysical Journal*, vol. 72, no. 6, pp. 2616–2629, 1997.

- [132] N. Bag, D. H. X. Yap, and T. Wohland, “Temperature dependence of diffusion in model and live cell membranes characterized by imaging fluorescence correlation spectroscopy,” *Biochimica Et Biophysica Acta-biomembranes*, vol. 1838, no. 3, pp. 802–813, 2014.
- [133] B. R. Bzdek, L. Collard, J. E. Sprittles, A. J. Hudson, and J. P. Reid, “Dynamic measurements and simulations of airborne picolitre-droplet coalescence in holographic optical tweezers,” *Journal of Chemical Physics*, vol. 145, no. 5, p. 054502, 2016.
- [134] R. E. H. Miles, J. S. Walker, D. R. Burnham, and J. P. Reid, “Retrieval of the complex refractive index of aerosol droplets from optical tweezers measurements,” *Physical Chemistry Chemical Physics*, vol. 14, no. 9, pp. 3037–3047, 2012.
- [135] L. Collard, “<https://www.youtube.com/watch?v=-2LY5qwzzw0&feature=youtu.be>.” last accessed 11/03/2018, 2016.
- [136] B. M. Weon and J. H. Je, “Coalescence preference depends on size inequality,” *Physical Review Letters*, vol. 108, no. 21, p. 224501, 2012.
- [137] A. D. Ward, M. G. Berry, C. D. Mellor, and C. D. Bain, “Optical sculpture: controlled deformation of emulsion droplets with ultralow interfacial tensions using optical tweezers,” *Chemical Communications*, no. 43, pp. 4515–4517, 2006.
- [138] L. Collard, “<https://www.youtube.com/watch?v=Pl6ff0kUMoM&feature=youtu.be>.” last accessed 11/03/2018, 2016.
- [139] R. M. Power, S. H. Simpson, J. P. Reid, and A. J. Hudson, “The transition from liquid to solid-like behaviour in ultrahigh viscosity aerosol particles,” *Chemical Science*, vol. 4, no. 6, pp. 2597–2604, 2013.
- [140] L. Collard, “<https://www.youtube.com/watch?v=fHJxKeSAaIs&feature=youtu.be>.” last accessed 11/03/2018, 2016.
- [141] L. Collard, “<https://www.youtube.com/watch?v=9u3Z9sUcpN8&feature=youtu.be>.” last accessed 11/03/2018, 2016.
- [142] L. Collard, “<https://www.youtube.com/watch?v=AXYwSD6Cw1Y&feature=youtu.be>.” last accessed 11/03/2018, 2016.
- [143] B. R. Bzdek, R. M. Power, S. H. Simpson, J. P. Reid, and C. P. Royall, “Precise, contactless measurements of the surface tension of picolitre aerosol droplets,” *Chemical Science*, vol. 7, no. 1, pp. 274–285, 2016.
- [144] S. Chandrasekhar, “The oscillations of a viscous liquid globe,” *Proceedings of the London Mathematical Society*, vol. s3-9, no. 1, pp. 141–149, 1959.

- [145] L. Collard, “<https://www.youtube.com/watch?v=BxqCZ1Y81WY&feature=youtu.be>.” last accessed 11/03/2018, 2016.
- [146] L. P. Jorge and W. H. Meeks, “The topology of complete minimal surfaces of finite total Gaussian curvature,” *Topology*, vol. 22, no. 2, pp. 203 – 221, 1983.
- [147] R. L. Graham, D. E. Knuth, and O. Patashnik, *Concrete Mathematics: A Foundation for Computer Science*. Addison-Wesley Longman Publishing Co., Inc., 1994.
- [148] D. Hoffman and W. H. Meeks, “Embedded minimal-surfaces of finite topology,” *Annals of Mathematics*, vol. 131, no. 1, pp. 1–34, 1990.
- [149] J. Berglund and W. Rossmann, “Minimal surfaces with catenoid ends,” *Pacific Journal of Mathematics*, vol. 171, no. 2, pp. 353–371, 1995.
- [150] W. H. Meeks, J. Perez, and A. Ros, “The geometry of minimal surfaces of finite genus III; bounds on the topology and index of classical minimal surfaces,” *preprint. arXiv*, 2005.